

A Combinatorial Method for Discovery of BaTiO₃-based Positive Temperature Coefficient Resistors

Chen, Yulong

The copyright of this thesis rests with the author and no quotation from it or information derived from it may be published without the prior written consent of the author

For additional information about this publication click this link.

<https://qmro.qmul.ac.uk/jspui/handle/123456789/435>

Information about this research object was correct at the time of download; we occasionally make corrections to records, please therefore check the published record when citing. For more information contact scholarlycommunications@qmul.ac.uk

**A Combinatorial Method for Discovery
of BaTiO₃-based Positive Temperature
Coefficient Resistors**

Yulong Chen

School of Engineering and Materials Science,

Queen Mary, University of London,

London, E1 4NS



A thesis submitted for the degree of Doctor of Philosophy at

University of London

October 2010

Declaration

I hereby declare that all the results presented in this study are my personal unaided work. To the best of my knowledge and belief, this thesis contains no material previously published or written by another person, except where due reference has been made.

Yulong Chen

28/10/2010

Signature: _____

Date: _____

Abstract

The conventional materials discovery is a kind of empirical (“trial and error”) science that of handling one sample at a time in the processes of synthesis and characterization. However, combinatorial methodologies present the possibility of a vastly increased rate of discovery of novel materials which will require a great deal of conventional laboratory work.

The work presented in this thesis, involved the practice of a conceptual framework of combinatorial research on BaTiO₃-based positive temperature coefficient resistor (PTCR) materials. Those including (i) fabrication of green BaTiO₃ base discs via high-throughput dip-pen printing method. Preparation and formulation of BaTiO₃ inks (selection of dispersant and binder/volume fraction) were studied. The shape of drying residues and the morphogenesis control of droplet drying were discussed. (ii) investigation of a fast droplet-doping method, which induced the dopant precursor solution infiltrating into the porous BT base disc. Various characterization methods were used to examine the dopant distribution in the body of disc. (iii) devising a high-throughput electrical measurement system including an integrated unit of temperature control and automatic measurement operation, and an arrayed multi-channel jig. (iv) synthesis of donor-doped BaTiO₃ libraries, which involved lanthanum, erbium, yttrium as donor elements and manganese as an acceptor dopant element respectively. Their temperature dependant resistivities were also explored. The work successfully developed an integrated tool including high-throughput synthesis of a large batch of libraries and high-throughput electrical property measurement for combinatorial research on BaTiO₃-based PTCR ceramics. The

combinatorial method, thus validated, has the potential to deliver dopant-doped BT-based PTCR libraries rapidly with a very wide range of dopant mixtures and concentrations for electrical property measurement and deserves to be applied to other low level dopant ceramic systems. These approaches are novel and paving the way for other new materials selection and materials research.

Publications Resulting from the Thesis

1. **Chen Y., Yang S.** The PTCR effect in donor-doped barium titanate: review of compositions, microstructures, processing and properties. *Advances in Applied Ceramics. Submitted.*
2. **Chen Y., Yang S., Evans J. R. G.** A rapid doping method for high-throughput discovery applied to thick film PTCR materials. *Journal of the American Ceramic Society. To be Submitted.*
3. **Chen Y., Yang S., Evans J. R. G.** Combinatorial screening for BaTiO₃-based PTCR ceramics. *To be Submitted.*

Acknowledgement

Firstly, I want to thank Dr. Shoufeng Yang, my first supervisor, for his generous help, valuable suggestions and guidance. He has helped me overcome many difficulties during the experimental work and provide invaluable advice within discussion about the problems encountered from the work. I also thank Prof. Julian R. G. Evans, my second supervisor, for his insightful help in my work.

I would like to thank Prof. Paul Hogg, Prof. Mike Reece, Prof Julia Shelton, Dr James Busfield, Dr Andy Bushby and other academic staffs in School of Engineering and Materials, for their enormous help during my studying and working in the Department. I also want to thank Mr John Caulfield, Mr Bill Goodwin, Mr Mick Wills, Dr Zofia Luklinska and Dr Rory Wilson, for their help during my work of PhD period.

I would like to express my greatest gratitude to my beloved wife, for her solid support, caring, understanding and loving. Without her constant encouragement and hard work to support the family, I would not get to the finish line of this PhD program. I would also like to thank my new born son. He has given me the courage and determination to complete this program.

Finally I am very grateful to my parents for their support and encouragement. And I dedicate this work to them.

Contents

Abstract.....	i
Publications.....	ii
Acknowledgement.....	iii
Table of Contents.....	iv
List of Figures.....	x
List of Tables.....	xxiii
List of Symbols and Abbreviations.....	xxv
1 Introduction.....	1
1.1 Aims and Objectives	1
1.2 Combinatorial Research in Materials Science.....	2
1.2.1 High-speed Library Synthesis and High-throughput Screening.....	5
1.2.2 Applications of Combinatorial Materials.....	7
1.2.2.1 Superconducting Materials	7
1.2.2.2 Novel Magnetic Materials	8
1.2.2.3 Dielectric and Ferroelectric Materials	9
1.2.2.4 Luminescent Materials	11
1.2.2.5 Heterogeneous Catalysis	12
1.2.2.6 Organic Materials	13
1.2.3 Informatics in Combinatorial Materials Research	14
1.3 Ceramic Film Processing	16
1.3.1 Thin Film Forming Methods.	16
1.3.2 Thin Film Methods in Combinatorial Research.....	17
1.3.3 Thick Film Forming Methods.	22

1.3.4 Thick Film Methods in Combinatorial research.....	25
1.4 Advanced Solid Freeform Fabrication of Ceramics	27
1.4.1 Three-Dimensional Printing (3DP).....	27
1.4.2 Direct Ceramic Ink-Jet Printing (DCIJP).....	29
1.4.2.1 Continuous Ink-Jet Printing.....	30
1.4.2.2 Drop-on-Demand Printing (DOD).....	32
1.4.3 Other Solid Freeform Fabrication methods.....	38
1.4.3.1 Stereolithography (SL).....	38
1.4.3.2 Fused Deposition of Ceramics (FDC).....	39
1.4.3.3 Laminated Object Manufacturing (LOM).....	41
1.4.3.4 Selective Laser Sintering (SLS).....	42
1.5 Droplet Drying Effects and Patterns.....	44
1.5.1 The Evaporation of a Sessile Droplet of a Colloidal Dispersion.....	44
1.5.1.1 Lateral Flow	45
1.5.1.2 Marangoni Flow.....	46
1.5.2 The Control of Sessile Drop Drying Patterns.	48
1.6 Temperature Dependent Resistors: Thermistors.....	53
1.6.1 Negative Temperature Coefficient Resistivity (NTCR) Materials: Compositions and Applications	53
1.6.2 Positive Temperature Coefficient Resistivity (PTCR) Materials: Compositions, Microstructures and Properties.....	56
1.6.2.1 Models of Explanation of PTCR Effect.....	57
1.6.2.2 Effect of Composition of BaTiO ₃ -based Materials on the PTCR Properties.....	66
1.6.2.3 Effect of Processing on the PTCR Properties.....	72

1.6.2.4	Microstructure-PTCR Property Relationships in Donor-doped BaTiO ₃	77
1.6.2.5	Emerging Trend of Research on BaTiO ₃ -based PTCR Materials.....	81
1.7	Liquid Infiltration in Porous Substrate.....	84
2	Experimental Procedures.....	89
2.1	Diagrammatic Representation of the Overall Experimental Design.....	89
2.2	Preparation of Ceramic Inks	90
2.2.1	Characterizing Materials	90
2.2.2	Sedimentation Tests	91
2.3	Control of Shape of Droplet Drying Pattern	95
2.3.1	Drying-induced Forming Agent Selection	95
2.3.2	Characterization of Green BaTiO ₃ Disc after Polymer-burnout	98
2.4	Investigation of Dopant Distribution in Porous BT Base via a Droplet-doping Method	100
2.4.1	Preparation and Characterization of Er-doped BT Using a Droplet Infiltrating Doping Method	100
2.4.2	Investigation of Erbium Distribution	101
2.4.3	Investigation of Yttrium Distribution in Y-doped BT via Droplet-doping Method.....	104
2.5	Heating Control Unit Construction and Furnace Calibration	106
2.5.1	Temperature Control Unit	106
2.5.2	Virtual Control Interface	107
2.5.3	Furnace Calibration	113
2.6	Devising the Arrayed Testing Platform and the Auto-operational	

System.....	117
2.6.1 Device for an Arrayed Testing Kit	117
2.6.2 Operational Interface of the Parallel Electrical Measurement System.....	120
2.6.3 Validity Check of the Parallel Testing System.....	127
2.7 Fabrication and Characterization of La-doped BT Ceramics with PTCR Effect.....	128
2.7.1 Preparation of La-doped BT PTCR Ceramics by Solid-state Reaction (SSR) Method.....	128
2.7.2 Selection of Electrode Materials.....	130
2.7.3 Investigation of La-doped BT PTCR Materials Fabricated by High- throughput (HT) Method.....	131
2.8 Investigation of Er-Mn and Y-Mn Donor-acceptor-codoped BT PTCR Ceramics via HT Method.....	134
3 Results and Discussion	135
3.1 Ceramic Ink Preparation	135
3.1.1 Characterization of Materials	135
3.1.2 Assessment of Dispersion of BaTiO ₃ Ceramic Powder.....	141
3.2 Control of Shape of Droplet Drying Pattern	148
3.2.1 Drying-induced Forming Agent Selection	148
3.2.2 Discussion	154
3.2.3 Characterization of Green BaTiO ₃ Disc after Polymer-burnout.....	158
3.3 Investigation of Dopant Distribution in Porous BT Base via a Droplet- doping Method	163
3.3.1 Droplet-doping Method	163

3.3.2 Characterization of Erbium-doped BaTiO ₃ Ceramics	166
3.3.2.1 STA Measurements.....	166
3.3.2.2 Structures and Microstructures.....	168
3.3.3 Investigation of Erbium Distribution in BT Disc Sample	173
3.3.4 Investigation of Yttrium Distribution.....	182
3.3.5 Discussion	191
3.3.5.1 Effect of Drop Spreading and Imbibition.....	192
3.3.5.2 Effect of Evaporative Drying.....	202
3.4 Furnace Calibration	205
3.5 Testing Platform Examination	213
3.6 Fabrication and Characterization of La-doped BT Ceramics with PTCR Effect	215
3.6.1 Preparation of La-doped BT PTCR Ceramics by Solid-state Reaction Method.....	216
3.6.2 Selection of Electrode Materials.....	231
3.6.3 Investigation of La-doped BT PTCR Materials Fabricated by the High-throughput Method.....	235
3.7 Investigation of Er-Mn and Y-Mn Donor-acceptor-codoped BT PTCR Ceramics via the HT method	247
4 Conclusions.....	258
4.1 Ceramic Ink Preparation.....	258
4.2 Control of Shape of Droplet Drying Pattern.....	258
4.3 Investigation of Dopant Distribution in Porous BT Base via a Droplet- doping Method.....	259
4.4 Heating Control Unit Construction and Furnace Calibration.....	259

4.5 High-throughput Arrayed Testing System.....	260
4.6 Fabrications of La-doped BT Exhibiting PTCR Property.....	260
4.7 High-throughput Fabrication of Donor-acceptor co-doped BT Libraries Exhibiting PTCR Property.....	261
5 Suggestions for Future Work.....	262
6 References	265
Appendix A.....	304
Appendix B.....	305

List of Figures

Figure 1.2.1 Combinatorial materials research: a diverse library containing large numbers of samples with discrete or continuous composition gradients is deposited by automated thin film synthesis methods. Each spatial location represents a different composition or processing history. Parallel high-throughput screening techniques are deployed to search for the lead materials or extract “knowledge” in the form of composition-structure-property relationships. ⁹	4
Figure 1.2.2 Principles of (a) the mix-and-split method and (b) the parallel synthesis method. ¹²	6
Figure 1.2.3a Dopant map for the BaSrTiO ₃ quadrant of a ferroelectric thin-film library; the same map applies to the other quadrants containing different host materials. ³⁹	10
Figure 1.2.3b Dielectric coefficient and loss tangent images of doped BaSrTiO ₃ films with a dopant map as in Figure 1.2.3a. ³⁹	10
Figure 1.2.4 Photograph of a 1024 member combinatorial library of luminescent materials on a 1” x 1” Si chip following thin-film deposition. (a) under ambient light. (b) under short wavelength UV light. ⁴²	12
Figure 1.2.5 Benzene forming droplets in a flow gradient control device. ⁵² ...	14
Figure 1.3.1 Schematic CCS method’s arrangement using co-sputtering of (a) two-component system, (b) three-component system. ⁴	19
Figure 1.3.2 Binary and quaternary masking strategies for combinatorial materials libraries fabrications. ²⁷	19
Figure 1.3.3 The deposition map of library contains multilayer precursors with diverse linear gradients. ¹⁴	21

Figure 1.3.4 Processing flow diagram for basic slip casting process: (a) a porous mould is (b) filled with slurry; (c) superfluous slip is poured out when the desired wall thickness has been achieved and (d) shows the final dried product ready to remove from the mould.....23

Figure 1.3.5 Schematic diagram of the tape casting processing.....25

Figure 1.3.6 General view of the LUSI system. 1: printer table, 2: measurement table, 3: furnace, 1a: slides space, 1b: syringe pumps and controllers, 1c: print head.¹⁰²26

Figure 1.4.1 Schematic structure of the three-dimensional printing process...29

Figure 1.4.2 Schematic diagram of the continuous ink-jet printing system.....32

Figure 1.4.3 Drop formation process of a thermal ink-jet printer.¹²⁵35

Figure 1.4.4 The basic configuration of the piezoelectric printhead.¹²⁵36

Figure 1.4.5 Schematic diagram of acoustic ink-jet printing and time evolution of droplets formation.¹²⁹37

Figure 1.4.6 Schematic diagram of the stereolithography apparatus for fabrication of three-dimensional parts.....39

Figure 1.4.7 Schematic diagram showing the layer-by-layer fabrication in fused deposition of ceramics.....41

Figure 1.4.8 Schematic diagram of the commercial LOM process.....42

Figure 1.4.9 Schematic diagram of the selective laser sintering process43

Figure 1.5.1 Drying profile for a gelcast part, showing the three stages of drying.¹⁴⁷45

Figure 1.5.2 Mechanism of lateral flow during evaporation. Vapour leaves at a rate per unit area (J) and the liquid flow (F) outward to compensate for the

deficit volume. ¹⁵⁸	46
Figure 1.5.3 Streamline plot of the flow field for the Marangoni flow. ¹⁶⁸	47
Figure 1.5.4 Flow field in a drying octane droplet. ¹⁶⁹	47
Figure 1.5.5 (a) Ring deposition pattern from a droplet of water with fluorescent polystyrene particles. (b) Drying pattern from a droplet of octane containing PMMA particles. ¹⁶⁹	50
Figure 1.5.6 Drying pattern of (a) polystyrene in an 80/20 wt.% ethyl acetate/acetophenone mixture on perfluorinated glass ¹⁷⁵ ; (b) silica particle in water/ formamide based ink on a hydrophobic Si wafer. ¹⁷⁶	52
Figure 1.6.1 Electrical characteristics of NTCR effect for Ni-Mn-Co oxides (TA1 represents $\text{Ni}_{1.4}\text{Mn}_{0.6}\text{CoO}_4$, TA2 represents $\text{Ni}_{1.2}\text{Mn}_{0.8}\text{CoO}_4$, TA3 represents NiMnCoO_4) (a) relationship between resistivity (r) and temperature (T); (b) $\log r$ versus $1/T$. ¹⁸³	54
Figure 1.6.2 Typical resistivity-temperature characteristic of a BaTiO_3 -type PTCR material.....	57
Figure 1.6.3 Electrical double layer at a grain boundary. E_s is the electron-trap energy, E_f the Fermi level, N_s the concentration of trapped electrons and b the width of electron depletion layer.....	59
Figure 1.6.4 Ferroelectric domains at the grain boundaries. P is the vector of spontaneous polarization and P_N the normal component of P	61
Figure 1.6.5 Schematic model of the microstructure of the donor-doped BaTiO_3 and its equivalent electric circuit. (replotted from ²³⁷).....	65
Figure 1.6.6 Schematic representation of the room-temperature dc resistivity as a function of La-dopant concentration for BaTiO_3 ceramics sintered in air. (replotted from ²³⁵).....	67

Figure 1.6.7 The effect of isovalent dopant doping on T_c . (replotted from ²⁵³).	71
Figure 1.6.8 r/T curves as a function of cooling rate for donor-doped BaTiO ₃ samples. (replotted from ³²⁹).....	76
Figure 1.7.1 The flow geometry for a porous medium (reproduced from ³⁷⁹)..	84
Figure 2.2.1 Milling equipments: (a) Dyno mill and (b) Vibro mill.....	94
Figure 2.4.1 Schematic diagram of printing the dopant precursor ink on the surface of green BT disc base: solution was printed by (a) a single drop on the central-top surface of the disc; (b) multi-drops evenly on the bottom flat surface of the base.....	102
Figure 2.4.2 Schematic plan for EDS analyses of as-sintered Er-doped BT: (a) upper and lower surfaces; (b) cross section.....	103
Figure 2.5.1 The Carbolite furnace.....	106
Figure 2.5.2 The temperature control box.....	107
Figure 2.5.3 Flow chart of the operational temperature control and monitor system.....	111
Figure 2.5.4 Modules of temperature control system.....	112
Figure 2.5.5 A screenshot of the user interface of the temperature control program: (a) the communication setup page and (b) the temperature control page.....	113
Figure 2.5.6 Block Diagram of program of the temperature control system: (a) overall structure; (b) magnified area in dashed square in (a); (c) the rest of the structure in (a).....	114
Figure 2.5.7 Schematic diagram of the furnace showing: (1) furnace chamber, (2) heating elements, (3) substrate base, (4) sample, (5) thermocouple and (6) control thermocouple.....	116

Figure 2.6.1 Arrayed testing platform views: (a) schematic diagram; (b) assembled platform.	118
Figure 2.6.2 (a) Equivalent circuit of voltammetry arrayed testing. (b) Schematic layout of the automated high-throughput parallel electrical testing.	119
Figure 2.6.3 Flow chart of the high-throughput parallel R (resistance)- T (temperature) measurement processing	122
Figure 2.6.4 Parallel R - T measurement test panel.....	123
Figure 2.6.5 Block diagram of the parallel R - T test operational system.....	124
Figure 2.6.6 The magnified part (furnace heating) of the block diagram as part A in Figure 2.6.5.....	125
Figure 2.6.7 The magnified part (assessment of the reaching thermal equilibrium in furnace) of the block diagram as part B in Figure 2.6.5...125	
Figure 2.6.8 The magnified part (measuring data processing) of the block diagram as part C in Figure 2.6.5.....	126
Figure 2.6.9 The magnified part (channel switch) of the block diagram as part D in Figure 2.6.5.....	126
Figure 3.1.1 SEM image of the as-received BaTiO ₃ powder. Arrows indicate the particle aggregates.....	136
Figure 3.1.2 (a) SEM image of the agglomerates remaining in BaTiO ₃ ink after Dyno-milled, (b) magnified image for the agglomerate arrowed in (a)...138	
Figure 3.1.3 SEM image of the particle distribution in BaTiO ₃ ink after Vibro-milling.....	138
Figure 3.1.4 Particle size distribution by volume of BT powders after Dyno-milling and Vibro-milling respectively.....	140

Figure 3.1.5 Schematic diagram shows the high energy zone at the tip of the ultrasonic probe during dispersion of ceramic powders.....	142
Figure 3.1.6 Cloudy volume fraction of test samples of BaTiO ₃ powder dispersed using ultrasonication and using EFKA series dispersants. They are compared with a Vibro-milled suspension with no dispersant added	146
Figure 3.1.7 Cloudy volume fraction of test samples of BaTiO ₃ powder dispersed using ultrasonication and using non EFKA type dispersants...	146
Figure 3.1.8 Stability of BaTiO ₃ suspensions with different concentrations of EFKA 4540.....	147
Figure 3.1.9 Stability of BaTiO ₃ suspensions with different concentrations of Darvan 821A.....	147
Figure 3.2.1 Binocular microscopy image of the as-dried BaTiO ₃ tablet sample.....	149
Figure 3.2.2 Photograph of as-dried BaTiO ₃ droplet with different solid contents of (a) 40 wt.%, (c) 45 wt.%, (e) 50 wt.%, (g) 55 wt.% and (i) 60 wt.%. The details of their corresponding magnified top surfaces are displayed respectively in image (b), (d), (f), (h) and (j).	154
Figure 3.2.3 Schematic illustration of a drying disc outlining regions of varying saturation: (a) cross-section and (b) top view. ⁴¹²	155
Figure 3.2.4 The pore size distribution of as-dried BaTiO ₃ disc-shaped sample: log differential pore size distribution (A) and cumulative pore size distribution (B).....	162
Figure 3.3.1 Schematic diagram of the BT porous base infiltration with saturated ink of dopant liquid precursor: (a) ideal condition; (b) single drop printing; (c) insufficient ink printing; (d) over saturated ink printing.....	165

Figure 3.3.2 The DTA curve and thermogravimetry for 0.1 mol.% Er-doped BT via droplet doping method.....	167
Figure 3.3.3 The DTA curve and thermogravimetry for 1 mol.% Er-doped BT via droplet doping method.....	167
Figure 3.3.4 The DTA curve and thermogravimetry for 8 mol.% Er-doped BT via droplet doping method.....	168
Figure 3.3.5 The shape of as-sintered Er-doped BT with various concentrations: (a) sintered at 1350 °C for 2h, (b) sintered at 1450 °C for 4h, (c) sintered at 1500 °C for 4h.....	170
Figure 3.3.6 The microstructure of fracture surface of erbium-doped BT sintered at 1350 °C for 2h with the dopant concentration of: (a) undoped (A0), (b) 0.1 mol% (A1), (c) 0.25 mol% (A2), (d) 0.5 mol% (A3), (e) 1 mol% (A4), (f) 2 mol% (A5).....	171
Figure 3.3.7 The SEM images on fracture surface of undoped BT sintered at (a) 1350 °C for 2h (A0), (b) 1350 °C for 4h (B0), (c) 1450 °C for 4h (C0), (d) 1500 °C for 4h (D0).....	172
Figure 3.3.8 5 mol% Er ³⁺ doped BT samples sintered at (a) 1350°C for 4h (B1), (b) 1450°C for 4h (C1) and (c) 1500°C for 4h (D1).....	173
Figure 3.3.9 EDS line-scan image of fracture surface of sample D1. The yellow line at the bottom is scanning path.....	177
Figure 3.3.10 SEM/EDS mapping results for specimen A3: (a) microstructure of cross section, the corresponding element mapping image of O (b), Ti (c), Ba (d) and Er (e).....	178

Figure 3.3.11 SEM/EDS mapping results for specimen A5: (a) microstructure of cross section, the corresponding element mapping image of O (b), Ti (c), Ba (d) and Er (e).....	179
Figure 3.3.12 SEM/EDS mapping results for specimen D1: (a) microstructure of cross section, the corresponding element mapping image of O (b), Ti (c), Ba (d) and Er (e).	180
Figure 3.3.13 SEM/EDS mapping results for as-dried BT sample with Er content of 20 mol.%: (a) microstructure, the corresponding element mapping image of O (b), Ti (c), Ba (d) and Er (e).....	181
Figure 3.3.14 EDS spectrum results for sample D1 under the scanning the plain area (a) and the Er-enrichment (b).....	182
Figure 3.3.15 SEM picture of fracture surface of undoped BT base disk.....	186
Figure 3.3.16 As-dried 1 mol.% Y-doped BT.....	186
Figure 3.3.17 BT doped with 1 mol.% yttrium subjected to slow decomposition (5 °C/min, from room-temperature to 650 °C). Arrows show the decomposed yttrium oxide from the molten nitrate salt during thermal treatment.....	187
Figure 3.3.18 BT doped with 1 mol.% yttrium subjected to fast decomposition (placed in a furnace preheated at 650 °C).....	188
Figure 3.3.19 Optical image of the top surface of the 0.5 mol.% Y-doped BT sample via droplet-doping method sintered at 1380 °C in N ₂ flow.....	188
Figure 3.3.20 Distribution of yttrium for sample printed with unsaturated volume of yttrium nitrate solution measured by WDS vertically and horizontally across the cross-section of Y-doped BT via drop doping,	

broken lines in both Cartesian coordinates indicate the expected dopant level.189

Figure 3.3.21 Distribution of yttrium dopant measured by WDS vertically and horizontally across the cross-section of Y-doped BT via droplet-doping, broken line indicates expected dopant level.190

Figure 3.3.22 Sequence of water spreading and imbibition into green BT porous base. Pictures were captured using high speed camera at 1200 frames per second.....193

Figure 3.3.23 The spreading diameter as a function of time for a water drop on the BT base as in Figure 3.3.22. The pink dash line represents for the diameter of the BT base.....194

Figure 3.3.24 Comparison between modelled and experimentally obtained $V(t)$, the imbibition volume of water as a function of time into the green BT porous base.....195

Figure 3.3.25 Schematic diagram of a porous system.....200

Figure 3.3.26 Different types of piston-like advance. (a) I_0 , all neighbouring throats are filled with water. This is hardly occurred here since the trapped air is incompressible. (b) I_1 , one neighbouring throat is empty. (c) I_{2a} , two of the adjacent throats are filled with water. (d) I_{2o} , two filled throats are opposite each other. (e) I_3 , only one throat is filled with water. The capillary pressures for each mode are ranked: $P(I_0) > P(I_1) > P(I_{2a}) = P(I_{2o}) > P(I_3)$.³⁸⁴201

Figure 3.3.27 (a) the normalized weight compared with the initial value of an over-saturated disc as a function of time measured by a microbalance with sensitivity as 0.1 μg ; (b) the calculated drying rate as a function of time

based on (a).....	203
Figure 3.4.1 Cross-calibration the combination of thermocouples and voltage-to-temperature converters.....	206
Figure 3.4.2 Heating profile of the modified pre-tuning furnace as a function of time.....	207
Figure 3.4.3 Heating profiles of the modified furnace after tuning at 100 °C and 200 °C respectively at a ramp rate as 1 °C/min.....	209
Figure 3.4.4 Temperature profiles of furnace heating by different ramp rates	210
Figure 3.4.5 Furnace temperature and sample surface temperature respectively as a function of time during heating by a ramp rate as: (a) no preset ramp rate, (b) 1 °C/min.....	211
Figure 3.4.6 The temperature gradients between in furnace and on sample surface while heating up the furnace from 20 to 250 °C.....	212
Figure 3.5.1 <i>R/T</i> characteristics of a commercial PTC thermistor: experimental results using in-house system (curve A) and reference values from the supplier (curve B).....	213
Figure 3.6.1 SEM images of the starting materials: (a) as-received BaTiO ₃ powder from PI-KEM, (b) synthesized BT (Ti:Ba=1.01), (c) as-received TiO ₂ powder and (d) as-received La ₂ O ₃ powder.....	218
Figure 3.6.2 Microstructures of the fracture surface of (a) A3, (b) D3 (c) B3, (d) E3, (e) C3 and (f) F3 samples under 500x magnification.....	221
Figure 3.6.3 Microstructures of La-doped BT specimens synthesized by SSR route sintered in air under conditions: (a) A3, (b) D3 (c) B3, (d) E3, (e) C3 and (f) F3.....	222

Figure 3.6.4 Temperature dependence of the electrical resistivity for (a) F3 and (b) F5 sintered at 1380 °C in air.....	223
Figure 3.6.5 r - T characteristics of La-doped BT using SSR method sintered at 1380 °C for 1 hour in N ₂	227
Figure 3.6.6 Microstructures of La-doped BT specimens synthesized by SSR route sintered in N ₂ : (a),(b) NA3; (c),(d) NC3; (e),(f) NF3.....	228
Figure 3.6.7 r - T characteristics of La-doped BT using SSR method subjected to different annealing processing after sintered in N ₂ . The NF3 curve (no annealing) was plotted here for comparison.....	231
Figure 3.6.8 Commercial PTC product with its original electrode. The compositional label above was determined by the EDS results.....	232
Figure 3.6.9 Electrode effects on R / T characteristics of a commercial PTC thermistor: retested results using original electrode (curve A), aluminium electrode by evaporative coating (curve C) and In-Ga alloy electrode (curve D); curve B was replotted from the reference values provided by the supplier.....	234
Figure 3.6.10 The drying of droplets of BT suspension containing: (a) Acrysol 12W; (b) dispersant only. It is thought the thixotropic agent restricts the radial flow of powder during drying. In the insert, schematic drawings were shown for the morphologies of the cross section of as-dried discs.....	235
Figure 3.6.11 An array of unfired as-dried BaTiO ₃ discs.....	236
Figure 3.6.12 Microstructures of La-doped BT specimens synthesized by HT method sintered at 1380 °C in N ₂ : (a) undoped, (b) 0.2 mol.%, (c) 0.3 mol.%, (d) 0.4 mol.%, (e) 0.6 mol.% and (f) 0.8 mol.% La ³⁺	237
Figure 3.6.13 XRD peaks between $2\theta = 35$ and 55° for La-doped BaTiO ₃	




library under the doping concentration of x mol.% sintered at 1380 °C in nitrogen flow.....	238
Figure 3.6.14 Tetragonality parameter (c/a) vs. La donor concentration produced by HT method and sintered in N ₂ at 1380°C for 1 hour.....	239
Figure 3.6.15 The side view of cross section of a BT disc.....	240
Figure 3.6.16 r - T characteristics of 0.3 mol.% La-doped BT using HT method annealed at 1100 °C for various periods after sintering at 1380 °C in N ₂	243
Figure 3.6.17 r - T characteristics of La-doped BT via HT method reoxidized at 1100 °C for 0.5 hour after sintering at 1380 °C in N ₂	244
Figure 3.6.18 Relationship between room-temperature resistivity and PTCR jump of La-doped BT with various donor concentrations via HT method sintered at 1380 °C in N ₂	245
Figure 3.6.19 Comparison of resistivity-temperature curve for combinatorial 0.2 mol.% La-doped BT (fired at 1380 °C) to previously published r - T curve for similar composition. Curves are from ref.:  ³⁶¹ ,  ³¹⁹ ,  ³²²	246
Figure 3.7.1 r - T characteristics of Er-Mn co-doped BT sintered at 1380 °C in N ₂	253
Figure 3.7.2 r - T characteristics of Y-Mn co-doped BT sintered at 1380 °C in N ₂	254
Figure 3.7.3 Relationship between room-temperature resistivity and PTCR jump of Er, Mn co-doped BT with various donor concentrations via HT method sintered at 1380°C in N ₂ flow.....	255

Figure 3.7.4 Relationship between room-temperature resistivity and PTCR jump of Y,Mn co-doped BT with various donor concentrations via HT method sintered at 1380°C in N₂.....256

Figure 3.7.5 Microstructure of doped BT sample containing 0.5 mol.% Y³⁺ and 0.02 mol.% Mn²⁺ sintered at 1380 °C for 1 hour in N₂ (after thermal etching).....257

Figure 5.1 Schematic layout of the fabrication method for high throughput discovery of donor-doped BT PTCR ceramics showing the following stages: droplet-printing (A), drying and debinding (B), droplet-doping (C), sintering (D) application of electrode (E).....264

List of Tables

Table 1.6.1 Summary of aliovalent dopants in BaTiO ₃ (ionic radii data from ²⁴⁸)	68
Table 2.2.1 Chemical and physical characteristics of dispersants.....	94
Table 2.3.1 Chemical and physical characteristics of forming agents.....	97
Table 2.3.2 Composition of BaTiO ₃ inks used for forming agent selection....	97
Table 2.3.3 Inks for investigation on drying pattern effects of changing volumes.....	98
Table 2.3.4 Inks for investigation on drying pattern effects of varying solid contents.....	98
Table 2.4.1 Sintering program of erbium-doped BT.....	102
Table 2.5.1 Modbus addresses for Eurotherm 3216.....	112
Table 2.7.1 La-doped BaTiO ₃ prepared using SSR route sintered in air.....	129
Table 2.7.2 La-doped BaTiO ₃ prepared using SSR route sintered in N ₂ flow	130
Table 2.7.3 Selection of electrode materials.....	131
Table 3.1.1 The results of BET specific surface area.....	139
Table 3.1.2 Particle size distribution of BT powders after various milling processing	140
Table 3.2.1 The configurations of the drying residue of the ink with varying compositions.....	150
Table 3.2.2 The configurations of the drying residue of the ink with different volume.....	151
Table 3.2.3 The porosity of green BT samples by buoyancy method.....	160
Table 3.3.1 EDS analyses for the as-sintered erbium doped BT samples.....	175

Table 3.3.2 EDS analysis for erbium doped BT.....	182
Table 3.4.1 A combination of components of thermocouple and V/T converter	205
Table 3.5.1 Parameters of the PTC thermistor.....	215
Table 3.6.1 Room-temperature resistance of the PTC thermistor with different electrodes.....	233
Table 3.6.2 Measured properties of PTC product with different electrodes...	234

List of Symbols and Abbreviations

α	Temperature Coefficient
γ	The Surface Tension
$\Delta\gamma$	The Surface Tension Difference
ε	The Permittivity
η	Dynamic Viscosity
θ	Contact Angle
κ	The Permeability of the Porous Medium
v	The Filtering Flux or Darcy Velocity in the Medium
\bar{v}	Average Velocity of Particle
ρ	Density
$\Delta\rho$	Density Difference Between the Particles and Solvent
Φ	Volume Fraction of Solids
φ_0	The Potential Barrier
a	The Radius
a_w	The Radius of the Wetting Footprint
b	The Thickness of an Electron Depletion Layer
C_a	Capillary Number
d	The Depth of the Liquid Infiltrating
D	Diffusion Coefficient of Brownian Motion of Spherical Particle
E	The Rate of Evaporation
E_s	The Electron-trap Energy
E_f	The Fermi Level
F	The Liquid Flow
g	The Gravitational Acceleration
h	Height
I	Electrical Current
k	The Eötvös Constant
k_B	Boltzmann Constant
L	The Thickness
M	Marangoni Number

N_s	The Concentration of Trapped Electrons
N_d	The Charge Carrier Concentration
P	The Percentage Porosity
ΔP	The Capillary Pressure
q	The Activation Energy for Electrical Conduction
r	Electrical Resistivity
r_{RT}	Room-temperature Resistivity
R	Electrical Resistance
R_{max}	Maximum Resistance
R_{min}	Minimum Resistance
R_{RT}	Room-temperature Resistance
s	Characteristic Length
t	Time
T	Temperature
T_a	The Absolute Temperature
T_c	The Curie Temperature
T_{ref}	The Reference Temperature
v	Velocity
V	The Volume
V_d	The Total Hg Intrusion Volume Density
U	Electrical Voltage
W	Weight
3DP	Three-Dimensional Printing
BCT	$Ba_{1-x}Sr_xTiO_3$
BT	$BaTiO_3$
BST	$Ba_{1-x}Ca_xTiO_3$
CAD	Computer Aided Design
CCS	Continuous Composition-spread
CVD	Chemical Vapour Deposition
DCIJP	Direct Ceramic Ink-Jet Printing
DOD	Drop-On-Demand Printing
DSS	Discrete Sequential Synthesis
DTA	Differential Thermal Analyses
EDS	Energy Dispersive X-ray Spectroscopy

FDC	Fused Deposition of Ceramics
FDMM	Fused Deposition of Multiple Materials
FGM	Functionally Graded Materials
HT	High-throughput
LMBE	Laser Molecular Beam Epitaxy
LOM	Laminated Object Manufacturing
LUSI	London University Search Instrument
MC	Methyl Cellulose
MOCVD	Metal-organic Chemical Vapour Deposition
NMR	Nuclear Magnetic Resonance
NTCR	Negative Temperature Coefficient Resistivity
PDI	Polydispersity Index
Pe	The Peclet Number
PTCR	Positive Temperature Coefficient Resistivity
PVA	Polyvinyl Alcohol
PVD	Physical Vapour Deposition
Re	Reynolds Number
RF	Radiofrequency
SEM	Scanning Electron Microscopy
SEMM	Scanning Evanescent Microwave Microscopy
SFF	Solid Free-forming Fabrication
SL	Stereolithography
SLS	Selective Laser Sintering
SQUID	Scanning Superconducting Quantum Interference Devices
SSR	Solid-state Route
STA	Simultaneous Thermal Analyzer
TGA	Thermogravimetry Analysis
WDS	Wavelength Dispersive Spectroscopy
We	Weber Number
XPS	X-ray Photoelectron Spectroscopy
XRD	X-ray Diffraction
XRF	X-ray Fluorescence

1 Introduction

1.1 Aims and Objectives

The aim of this project is to realize a protocol for combinatorial research for BaTiO₃-based positive temperature coefficient resistivity materials. This project is a pioneering combinatorial thick film approach to high-throughput donor-doped BaTiO₃ fabrication and to fast parallel electrical screening. The target is set at donor-doped BaTiO₃ PTCR ceramics but once established, it can be used for the general construction of ceramic combinatorial libraries which involve low dopant levels.

The objectives of the project are as follows:

1. To produce a high-throughput library of BaTiO₃ discs by the dip-pen printing method. Formulation of the ink suspension (selection of solid content and polymer additive volume fraction) and the control of the droplet drying pattern need to be investigated.
2. To synthesize libraries of donor-doped BaTiO₃ PTCR discs via a droplet-doping method. The mechanism of dopant ion distribution by impregnating the porous base with a dopant precursor solution, followed by the drying and firing is to be discussed.
3. To devise an high-throughput parallel testing platform for electrical measurements. The testing system is including a furnace control unit and a parallel conducting jig. A computer-operational-interface is also to be developed.
4. To explore the PTCR properties of donor-doped BaTiO₃ materials.

1.2 Combinatorial Research in Materials Science

The development of functional materials has always played a key role in lifting the productivity and advancing the economics and development of mankind. In modern chemistry and materials science, the periodic table forms the basis of inorganic materials formulation. Although there are approximately 24,000 inorganic phases inclusive of 16,000 binary and pseudobinary compounds and 8,000 ternary and pseudoternary compounds known to mankind according to a review by J.C. Phillips at the end of the 1980s,¹ these achievements so far have only discovered a small fraction in the whole scope of materials exploration. If 70 out of 117 elements² in total are chosen from the periodic table to form ternary compounds, then there are around 54,700 possible ternary systems. Therefore, 6 out of 7 of them are still yet to be analyzed. If considering different stoichiometric compositions of each ternary system or increasing the number of components in a system, the number of samples that need to be examined is beyond imaginable capacity. Therefore, the conventional one-by-one trial-and-error method begins to fail to be competent in building the map of the structure-composition-property relationships of compounds. New strategies are needed to fulfil the ambition to achieve the capabilities of high-throughput synthesis and screening. Combinatorial methods were realized with a view to solving such problems. Combinatorial research was originally invented to meet the demands of increasing the rate of mapping of phase diagrams as pioneered by Kennedy.³ It was adapted by Hanak⁴ for finding high-temperature superconductors. This method had been used in the field of biochemistry and the pharmaceutical industry for speeding up the drug discovery process. A variety of high-throughput synthesis and rapid screening schemes were invented to increase dramatically the efficiency of the

discovery process for organic compounds.⁵⁻⁸ Such techniques represent a new paradigm for the discovery of molecules and organic polymers.

Similarly, developments and progress in combinatorial research in chemistry are inspiring and promoting systematic methodology in materials science research. In combinatorial materials science, the experimental techniques can be divided into three major interconnected activities: synthesis, rapid property characterization and data mining. All of these procedures are essential to perform a successful combinatorial investigation. The fast fabrication tool is able to guarantee the speed for creating a variety of combinatorial libraries and composition-spread samples. Suitable characterization tools in high-throughput screening processes can be used to measure multiple functionalities and multiple figures of merits for different applications. Furthermore, an integral part of any materials synthesis effort is materials diagnostics. There is always a need to check and confirm the formation and presence of intended phases at intended locations on libraries. Quickly obtaining accurate composition and phase mapping is of paramount importance in establishing the composition-structure-property relationships of materials. Figure 1.2.1 shows a flow chart of the combinatorial materials methods which indicate the massive advantages of spatiality and efficiency in exploring a large segment of a particular compositional landscape to help to find an optimum around lead compositions.

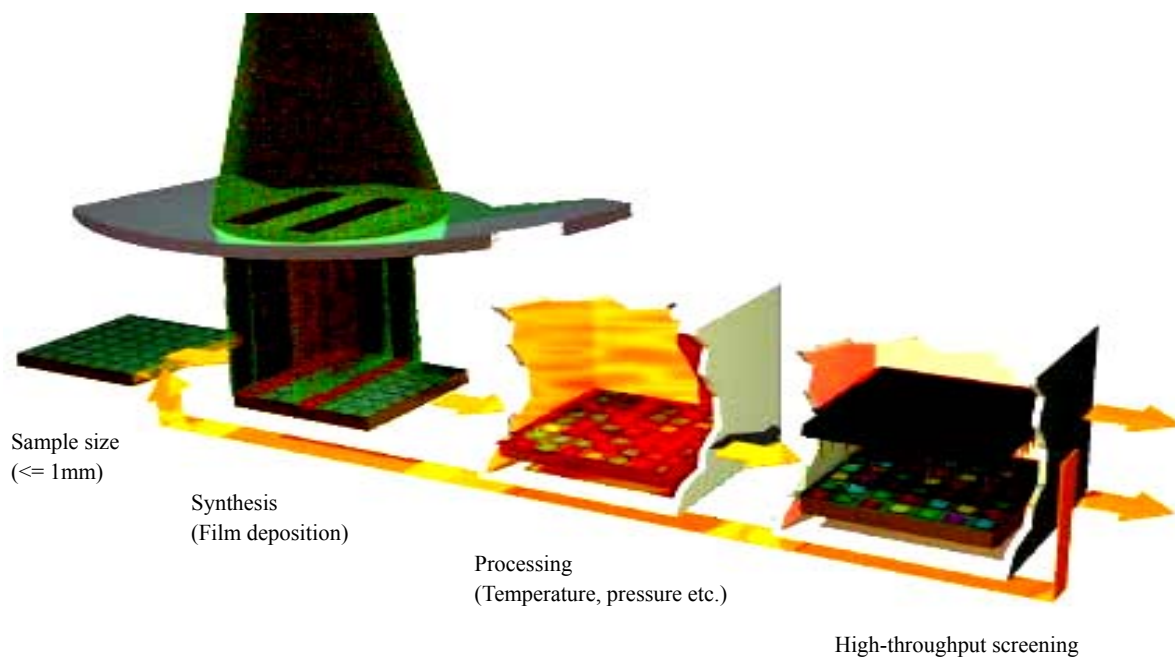


Figure 1.2.1 Combinatorial materials research: a diverse library containing large numbers of samples with discrete or continuous composition gradients is deposited by automated thin film synthesis methods. Each spatial location represents a different composition or processing history. Parallel high-throughput screening techniques are deployed to search for the lead materials or extract “knowledge” in the form of composition-structure-property relationships.⁹

1.2.1 High-speed Library Synthesis and High-throughput Screening

It has long been desirable to increase the rate of new materials synthesis. The first report of the rapid, automated synthesis of diverse organic molecules appeared in the late 1960s.¹⁰ At that time, pioneers like Gutte and Merrifield¹⁰ used polypeptide-synthesis machines to automate the rapid production of diverse amino acid sequences. Soon two methodologies including the mix-and-split technique and the parallel synthesis technique (their schematic structures are displayed in Figure 1.2.2) were developed in order to speed sample production in combinatorial research.¹¹

Figure 1.2.2(a) illustrates the mix-and-split method in which the carriers' pool has been equivalently divided into several portions according to the amount of reaction groups within the same category. The overall products after reaction are mixed together and then evenly split into several groups again which is in accordance with the numbers of compounds for further reaction. This post-reaction mix-and-split procedure is repeated until all variable samples have been synthesized. The parallel synthesis strategy has the advantage of easier manipulation of samples since all reaction products are kept in separate reactors. At the first stage, compounds in the same family are added in corresponding rows of the samples' array. Afterwards, compounds in another family are added in different columns of the same array. More components could be added by using additional arrays or duplicating rows and columns from the first stage. Both parallel and split-pool synthetic strategies explained above which were initially widely used in the pharmaceutical industry have also been well adopted in synthesis of functional inorganic materials.¹² Furthermore, vapour deposition and solution-dispensing are the most common methods for high-speed synthesis of inorganic materials libraries.

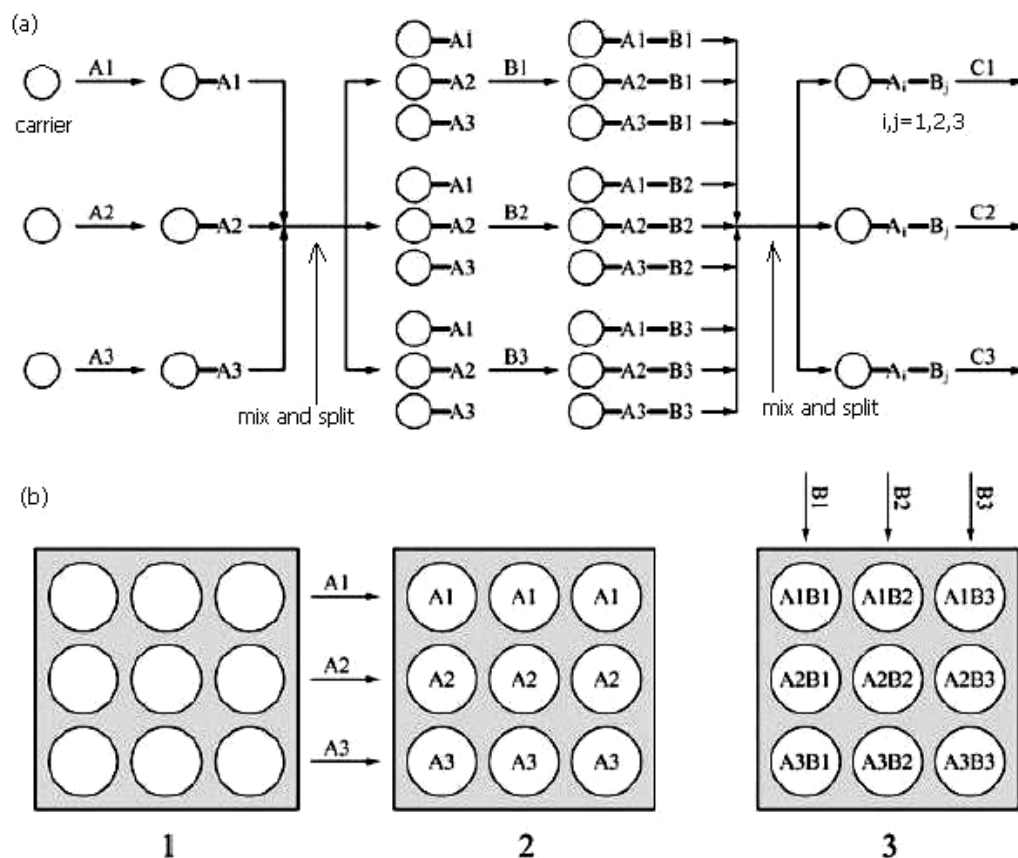


Figure 1.2.2 Principles of (a) the mix-and-split method and (b) the parallel synthesis method. (replotted from¹²)

The number of samples in a library for combinatorial research can be in the range of thousands. A split-and-mix liquid-phase library might even include 10^5 or more different compounds. Therefore, parallel automated measurement setups are needed to achieve high throughput to meet the challenge of rapid characterization of a large number of samples with very small sample volumes (tens to hundreds of microlitre). The concept of automated and high-throughput chemical screening was first realized in the medical field decades ago since it was driven by the need to test thousands of clinical specimens each day in single-site facilities and relative simplicity in screening body-fluid samples.¹³ Nowadays various high-throughput characterization tools for inorganic materials applications have been developed. Generally speaking,

optical imaging and spectroscopic methods are relatively easy to deploy in studying luminescent materials.^{14, 15} Comparably, methods for high-throughput scanning mass spectrometry¹⁶ and parallel calorimetry¹⁷ have been successfully devised for quickly and automatically screening large numbers of catalytic materials. Furthermore, other nondestructive and high-throughput tools such as X-ray diffraction for structural characterization,¹⁸⁻²⁰ scanning-tip microwave near-field microscopy for microwave dielectric properties,²¹ scanning evanescent microwave microscopy (SEMM) for mapping electrical impedance²² and scanning superconducting quantum interference devices (SQUID),²³ the scanning hall probe^{24, 25} and magneto-optical techniques²⁶ for mapping magnetic properties have also been developed recently in order to cope with the fast growing speed of sample fabrication. However, those characterization methodologies are still not keeping pace with the increase of library density due to limitations on testing speed or spatial resolution. Therefore, novel and powerful high-throughput characterization tools are still in urgent and high demand.

1.2.2 Applications of Combinatorial Materials

1.2.2.1 Superconducting Materials

One of the first implementations of combinatorial research in materials exploration involved preparing libraries of superconducting thin-film materials. Xiang *et al.*²⁷ first used sequential radio-frequency (RF) sputtering method through binary masks to build Ba-Cu-Y oxide systems and evaluated the superconductivity of each sample by measuring its resistance as a function of temperature with an array of small four-point probes which analyzed 64 samples at a time. By their novel methods, films of BiSrCaCuO_x, BiPbCaSrCuO_x and YBa₂Cu₃O_x were successfully identified along with their superconducting characteristics which had critical temperatures in the

range of 80-90K. Although the profiles of resistance versus temperature of those film samples displayed distinct characteristics in terms of deposition sequences and annealing conditions which were hence different from those via conventional bulk synthesis methods,²⁸ this methodology has been proven effective and efficient. Recently, a similar superconducting thin-film $\text{La}_{2-x}\text{Sr}_x\text{CuO}_4$ library was also developed.²⁹

1.2.2.2 Novel Magnetic Materials

Magnetic semiconductors are important materials because of their spin-dependent electronic functionality and they are broadly used in the computing industry especially in memory and recording products. Discovering new systems of magnetic semiconductors including room-temperature ferromagnetic semiconductors and colossal magnetoresistance materials has been driven by combinatorial research since the mid-90s.^{30, 31} Dietl *et al.*³² first predicted room-temperature ferromagnetism in manganese doped GaAs and ZnTe, soon followed by the discovery of cobalt-doped TiO_2 anatase by a laser molecular beam epitaxy method.³¹ Recently, Tsui *et al.*³³ discovered new Ge-based magnetic semiconductors by combinatorial methods. In particular, the compound $\text{Co}_{0.1}\text{Mn}_{0.02}\text{Ge}_{0.88}$ was found to have a Curie temperature as high as 280K and large magnetoresistance effects. In addition, Takeuchi *et al.*³⁴ mapped a bifunctional diagram of the Ni-Mn-Ga system in a search of ferromagnetic shape-memory alloys by using the thin-film compositional spreads method.

Colossal magnetoresistance materials were first found only in Mn-based perovskites, $(\text{La,R})_{1-x}\text{A}_x\text{MnO}_{3-d}$, where R = rare earth, and A = Ca, Sr, Ba. Briceno *et al.*³⁰ have found via combinatorial methods a new family that are Co-containing, for example

$\text{La}_x(\text{Ba},\text{Sr},\text{Ca})_y\text{CoO}_\delta$, which has large magnetoresistance. The magnetoresistance of the Co-containing compounds increases as the size of the alkaline earth ion increases in sharp contrast to Mn-containing compounds, in which the magnetoresistance effect increases as the size of the alkaline earth ion decreases.

1.2.2.3 Dielectric and Ferroelectric Materials

Ferroelectric materials are being widely used in the development of new microwave devices such as frequency agile filters, phase shifters and tunable high-Q resonators. $(\text{Ba}_x\text{Sr}_{1-x})\text{TiO}_3$ (BST) compounds have been studied intensely for such applications owing to their low loss and high dielectric coefficients. Combinatorial approaches in such areas have been applied by Xiang from the Lawrence Berkeley Laboratory.^{35, 36} Four libraries of 256 differently doped thin films of $(\text{Ba}_x\text{Sr}_{1-x})\text{TiO}_3$ where $x = 1, 0.8, 0.7$ and 0.5 were generated on a $2.5\text{cm} \times 2.5\text{cm}$ LaAlO_3 substrate using multistep thin-film RF sputtering together with a quaternary masking strategy with four physical shadow masks. These four hosts were then doped with different combinations of up to three out of nine different metallic elements with each dopant added in excess of 1 mol% with respect of the BST host. Details are displayed in Figure 1.2.3a below. The maps with the values of the dielectric coefficient and loss tangent of the corresponding samples in the libraries are plotted in Figure 1.2.3b.

Van Dover *et al.*³⁷ used the composition-spread technique to discover new dielectric thin-film materials ($\text{Zr}_{0.15}\text{Sn}_{0.3}\text{Ti}_{0.55}\text{O}_{2-\delta}$) which find their way into the node capacitors of prototype dynamic random-access memories. They found that the properties of $\text{Zr}_x\text{Sn}_y\text{Ti}_z\text{O}_{2-\delta}$ thin-film depend strongly on the deposition conditions. Recently, they have investigated the Zr-Si-O dielectric compounds by using similar

tactic.³⁸

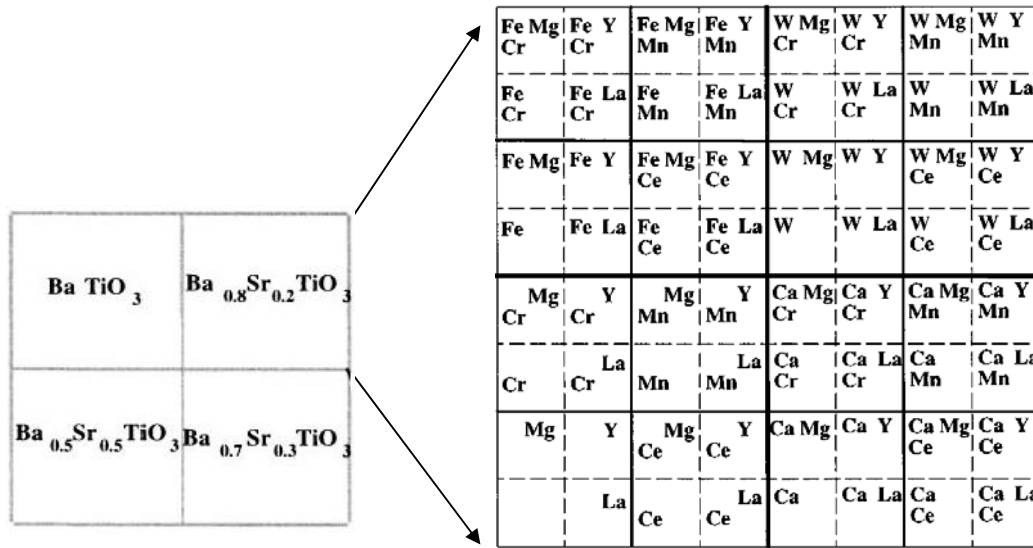


Figure 1.2.3a Dopant map for the BaSrTiO₃ quadrant of a ferroelectric thin-film library; the same map applies to the other quadrants containing different host materials.³⁹

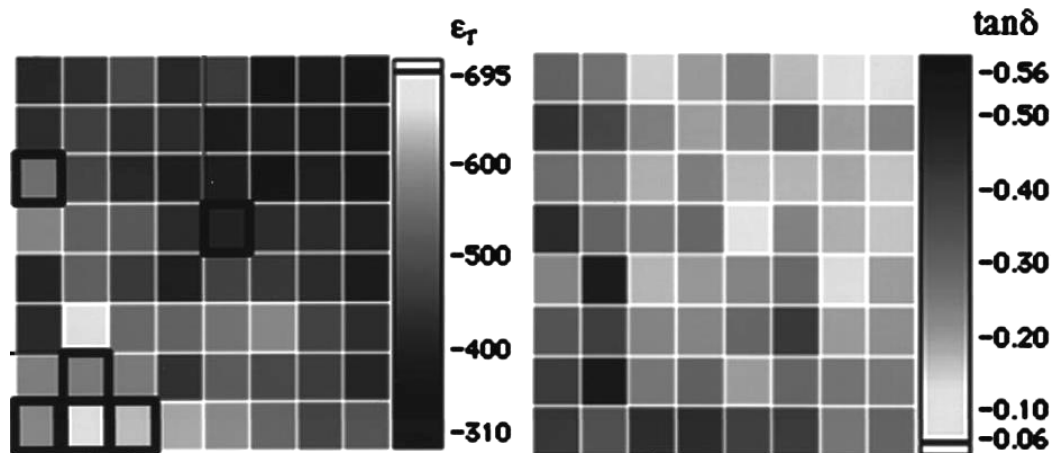


Figure 1.2.3b Dielectric coefficient and loss tangent images of doped BaSrTiO₃ films with a dopant map as in Figure 1.2.3a.³⁹

Recently, Pullar *et al.*⁴⁰ used an automated high-throughput ink-jet printer successfully produced the Ba_xSr_{1-x}TiO₃ libraries with varying compositions of x=0-1 in steps of 0.1. Dielectric measurements showed the measured permittivity results

and Curie temperature values of the samples in the library corresponded well to previously published bulk BST data.

1.2.2.4 Luminescent Materials

Phosphor materials with high quantum efficiencies find applications in display technologies such as cathode ray tubes and are of great importance for developing improved plasma, field emission and electroluminescent flat panel displays as well as lighting. However, after many years of intensive research, fewer than 100 useful commercial phosphor materials have been discovered through conventional one-at-a-time synthesis and testing. Phosphors are normally inorganic powders that consist of a polycrystalline host doped with ions of a rare earth and/or a transition metal. The combinatorial libraries were used to survey a wide range of oxide compositions under a variety of processing conditions. Danielson *et al.*¹⁴ found a new red phosphor, $Y_{0.845}Al_{0.07}La_{0.06}Eu_{0.025}VO_4$, in a library of 25,000 different compositions produced by electron-beam evaporation to deposit thin-film on a silicon wafer. Also following his work, a novel luminescent oxide, Sr_2CeO_4 , was discovered showing blue-white emission.¹⁵ New luminescent systems were also investigated by using combinatorial methods. For instance, several 128-member libraries such as Gd-Zn, Gd-Ga oxide doped with rare earth activators have developed and evaluated the phosphorescence of all the specimens simultaneously by photographing the entire library under broad wavelength UV light.^{41, 42} Figure 1.2.4 displays the photographs of a luminescent materials library under ambient light and short wavelength UV light respectively. Furthermore, a scanning multi-inkjet printer can be used to fabricate a library of phosphors based on rare-earth-activated refractory metal oxides by a solution-phase synthesis technique. The results of samples generated in the ink-jet library are found

to be identical to those in the library deposited by RF sputtering.⁴³ Recently, red phosphors which are in Gd-Al⁴⁴ and Y-Eu⁴⁵ oxide systems were fabricated by high-throughput synthesis method.

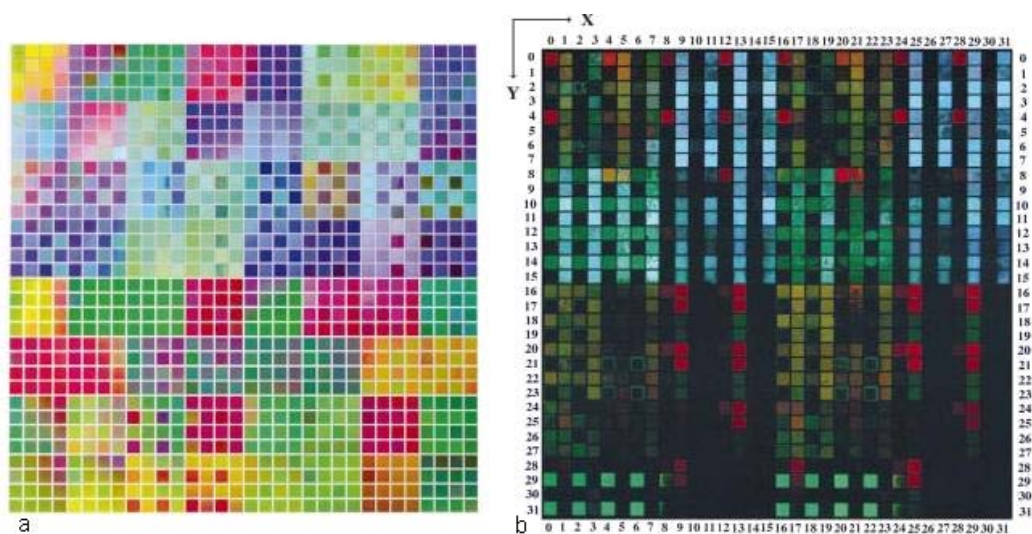


Figure 1.2.4 Photograph of a 1024 member combinatorial library of luminescent materials on a 1'' x 1'' Si chip following thin-film deposition. (a) under ambient light. (b) under short wavelength UV light.⁴²

1.2.2.5 Heterogeneous Catalysis

The screening of catalytic materials via high-throughput techniques started in the 1980s.⁴⁶ Heterogeneous catalysts are multifunctional materials composed of several active components, promoters, and a high surface-area support material. The compositional parameter space associated with them is therefore very large. In addition, there is a wide variety of processing and reaction conditions to which catalysts may be subjected, which results in the total number of possible experimental combinations being even more.

Combinatorial searches for catalysis are often limited not by synthesis but by the lack of efficiency in simultaneously screening many compositions. High-throughput studies of heterogeneous catalysts consist of three components: rapid catalyst synthesis, high-throughput testing of catalyst materials, appropriate data processing and information mining techniques, which feedback into the synthesis. A good example for the application of statistical design for high-throughput experimentation is the work on the development for Pt/Ba/Fe-based nitrous oxide (NO_x) storage and reduction (NSR) catalysts.^{47, 48} It is difficult to reduce NO_x under the oxidizing conditions present in the exhaust of lean-burn gasoline and diesel engines. NSR catalysts are designed to store NO_x during a fuel-lean cycle and reduce the stored NO_x during a subsequent fuel-rich cycle. Furthermore, recently, Vijay *et al.*⁴⁹ have disclosed a noble-metal-free system for NSR catalysts developed entirely using a high-throughput approach. They found that an Al₂O₃-supported catalyst containing 5 wt.% Co and 15 wt.% Ba is just as effective as conventional NSR catalyst that contained platinum.

1.2.2.6 Organic Materials

The early adoption of combinatorial methods by the pharmaceutical industry resulted in a strong foundation of parallel organic synthetic routes and techniques for the rapid screening of organic molecules for drug activity. This has inspired researchers to develop new polymers and organic materials or rapidly optimize the reaction parameters (temperature, catalysts, etc) for specific products.⁵⁰ Microfluidic technology for polymer library synthesis has been devised by Cabral *et al.*⁵¹ for automated control of radical polymerization. A continuous gradient control method has also demonstrated by Cygan *et al.*⁵² to produce arrays of polymer microdroplets

displayed in Figure 1.2.5. In addition such techniques can be used to synthesis libraries of surface-grafted polymers and graded polymer films. The combinatorial approach was recently also used for fast screening of organic light emitting diode (OLED) materials.⁵³

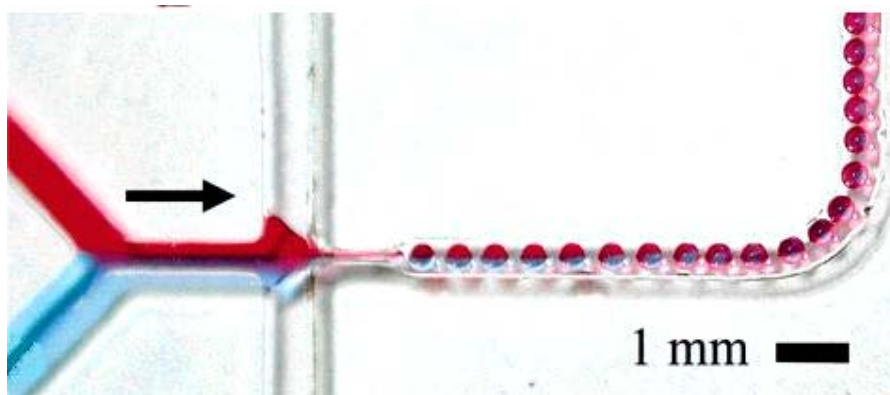


Figure 1.2.5 Benzene forming droplets in a flow gradient control device.⁵²

For organic electronic materials, ink-jet printers are widely used for combinatorial library creation,⁵⁴ including spot or line arrays, multilayers and collection of device prototypes. Besides the applications that adopting combinatorial concepts described above, many other fields have also been widely used combinatorial methods for fabrications or characterizations, which among them are including solid-state battery materials,⁵⁵⁻⁵⁷ fuel-cell materials,^{58, 59} coating materials,⁶⁰ and sensors⁶¹⁻⁶³.

1.2.3 Informatics in Combinatorial Materials Research

Seeking structure-property relationships and optimizing the composition and processing parameters are paradigms in materials science. Driven by the development in high-throughput synthesis and characterization techniques, scientist to date have better understanding of the underlying science governing the behaviour

of many materials. However, there is a bigger challenge that requires scientists to find new materials property relationships and interpret patterns by sifting through huge databases efficiently. Because combinatorial experiments often represent exploration of colossal multidimensional data stream, data mining techniques can play a key role in isolating and identifying ‘hidden trends or variables’ in experiments. Thus the results may be able to uncover new materials behaviour as well as prediction of new compounds.^{64, 65} The scope of materials informatics is extensive but much remains to be developed and fully demonstrated. Therefore, full realization of the combinatorial methodology will require the integration of chemistry, physics, engineering and informatics, to enhance the probability of finding materials with desired properties. Scott *et al.*⁶⁶ are pioneers in building an informatics system which integrated combinatorial experiments particularly in electroceramic materials discovery.

1.3 Ceramic Film Processing

Products in the form of ceramic films and coatings are used for an enormous and diverse set of functional and structural applications. According to the thickness of ceramic samples, the film methods can be distinguished as thin film methods ($\leq 1\mu\text{m}$) and thick film methods ($>1\mu\text{m}$).⁶⁷

1.3.1 Thin Film Forming Methods

There are many thin-film deposition technologies which form layers with thickness in the range of a few nanometers to about one micrometer. Solid ceramic thin films can be prepared by deposition from the gas, liquid or solid phase.

Chemical vapour deposition (CVD) is a synthesis process in which a solid film is deposited from a vapour phase by chemical reaction on a substrate. The main advantages of CVD are its versatility for synthesizing both simple and complex compounds and its ability for tailoring the chemical composition and physical structure of the deposited film by changing the reaction chemistry and deposition conditions. For example, it generally creates amorphous structures when the temperature of the substrate is below 600 °C, grows single-crystal structures when above 1000 °C and produces polycrystalline films when the temperature is between 600 and 1000 °C. Several kinds of CVD processes have been developed including plasma-enhanced CVD, laser-enhanced CVD and metal-organic chemical vapour deposition (MOCVD).⁶⁸ The chemical reaction might involve pyrolysis, oxidation, reduction or compound formation.

In physical vapour deposition (PVD) processes, films are generated from a solid source by heat-induced vaporization or momentum transfer in which evaporation or sputtering directs vapour to a target substrate on which the film is grown in a vacuum chamber.⁶⁹

CVD and PVD are the most common vapour deposition techniques in thin film methods. In spite of their unique merits including capabilities for precise control of structure and composition of films, the low deposition rate (lower than $4 \text{ nm}\cdot\text{s}^{-1}$) and complicated devices required have restrained their applications. Apart from those vapour deposition techniques, other methods such as dip-coating,⁷⁰ spin coating⁷¹ and inkjet-based printing^{72, 73} can also be used to produce ceramic thin films.

1.3.2 Thin Film Methods in Combinatorial Research

Thin film methods have been widely used in combinatorial materials research and they can fabricate most libraries.⁷⁴⁻⁷⁶ The compositional landscape of a library made by thin film synthesis can be achieved by a masking scheme or photolithography techniques combined with various vapour deposition techniques such as cosputtering,^{77, 78} thermal evaporation,^{79, 80} electron-beam evaporation,⁹ pulsed-laser deposition,^{81, 82} ion-beam implantation,^{83, 84} molecular-beam epitaxy^{85, 86} and chemical vapour deposition.³⁸

In high-density thin film library synthesis, different tactics for making samples with various compositional spread schemes have been developed. The continuous composition-spread (CCS) method was pioneered by Hannak⁴ in 1970s to produce samples with a naturally continuous compositional gradient. The CCS technique

relies on the non-uniform deposition of materials formed by the geometric arrangement between the sources and the substrate. The relative concentration of each component at a specific location on the substrate decreases with the distance from the source. As materials spread from the sources in the vapour state, they mix and are deposited on the substrate creating atomic-level mixing that reduces or eliminates the need for high-temperature post-processing. A schematic diagram of using the CCS method by co-sputtering or co-deposition is shown in Figure 1.3.1. However, these techniques have limited scope for optimizing and exploring systems with more than three independent components due to the lack of precise stoichiometric control, limited compositional range and difficulty in spatial arrangement for sources of multiple elements.

Masking strategies including physical shadow masks,⁸⁷ movable shutters⁸⁸ and photolithography⁷⁶ were hence introduced in order to allow the precise control of the deposition of precursors at a given location on the substrate. Such techniques as the discrete sequential synthesis (DSS) method was first developed by Xiang *et al.*²⁷ Simple binary and quaternary masking methods are the most common strategies in the DSS technique and the process flow is indicated in Figure 1.3.2. In the binary masking strategy, only half of the substrate area is exposed to vapour deposition with different patterns in each step. The number of different compositions after N steps is 2^N , which includes all possible combinations of N elements. Moreover, the quaternary masking strategy has been developed that enables efficient generation of diverse libraries containing materials with very different compositions. In the quaternary masking scheme, deposition is carried out using a series of N different masks that subdivide the substrate into a series of nested quadrant patterns (shown in

Figure 1.3.2). Each mask is used for up to four depositions and each time the mask is rotated by 90°. This process can generate up to 4^N different compositions in just $4N$ steps with N different masks.

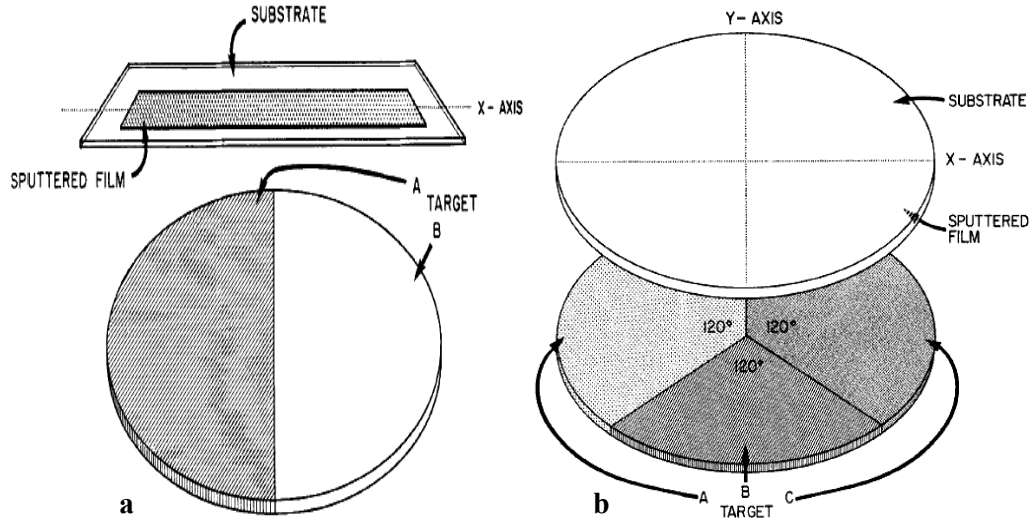


Figure 1.3.1 Schematic CCS method's arrangement using co-sputtering of (a) two-component system, (b) three-component system.⁴

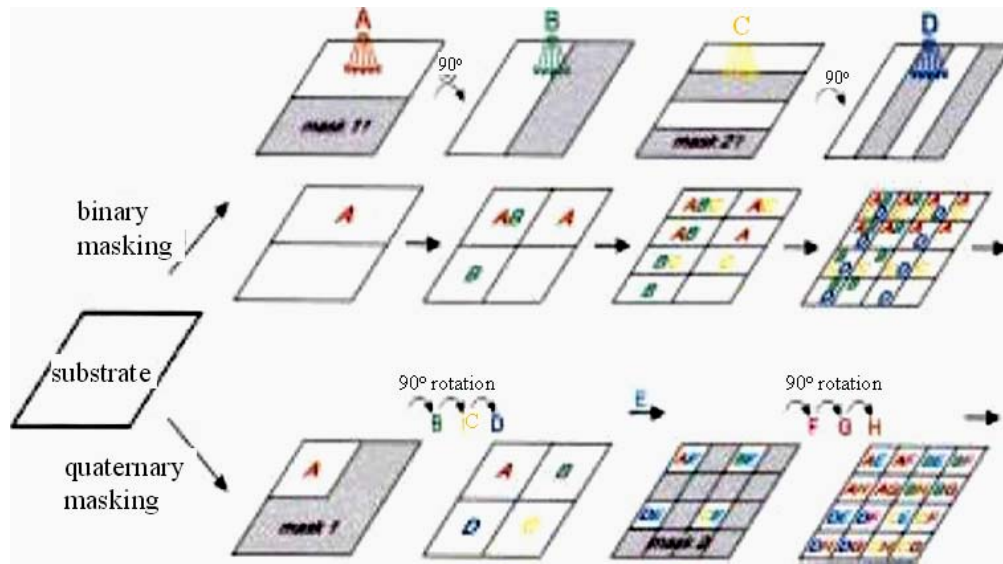


Figure 1.3.2 Binary and quaternary masking strategies for combinatorial materials libraries fabrications.²⁷

In the DSS method, the composition control in the library is determined by the

sequence of masking, time and rate of deposition. The design of masks and sequence is crucial since it dictates the arrangement of compositional landscape; however, the number of compounds that can be simultaneously synthesized by this technique is still limited by the spatial resolution of the masks and detectors and by the degree to which synthesis can be carried out on a microscale. Alternatively, photolithographic lift-off methods rather than physical shadow masks can be adopted to generate high density libraries because of their higher spatial resolution and alignment accuracy capabilities.^{42, 89} The advantage of the DSS technique is that a full phase diagram of multiple components could be prepared with a fixed interval (e.g. 10 at.%) on a single substrate⁵⁸ compared with the CCS technique which is unable to yield a full phase diagram in a single run for cases of more than three components. Furthermore, by using movable shutters, multiple layers of precursor can be deposited onto a small substrate sequentially with a linear thickness gradient. The library in Figure 1.3.3 was fabricated by using two movable masks with different geometrical parameters. Four columns were deposited first with constant thickness of SnO₂, V, Al₂O₃ + V (15:8 molar ratio) and Al₂O₃. Four rows with linearly varying thickness of La₂O₃, Y₂O₃, MgO and SrCO₃ were then layered on the columns to divide the substrate into 16 host lattice sub-regions. Finally, within each sub-region, columns of rare earth Eu₂O₃, Tb₄O₇, Tm₂O₃ and CeO₂ were deposited in linearly varying thickness on the top of the substrate.

Having equilibrium crystallized structures, samples with either discrete or linearly continuous compositional gradients can be created by these masking techniques after subjecting the library to an appropriate annealing treatment.^{39, 88} This compares well with samples that have multiphase non-equilibrium crystallized structure or even

those in an amorphous state that are made from cosputtering or codeposition methods.³⁸

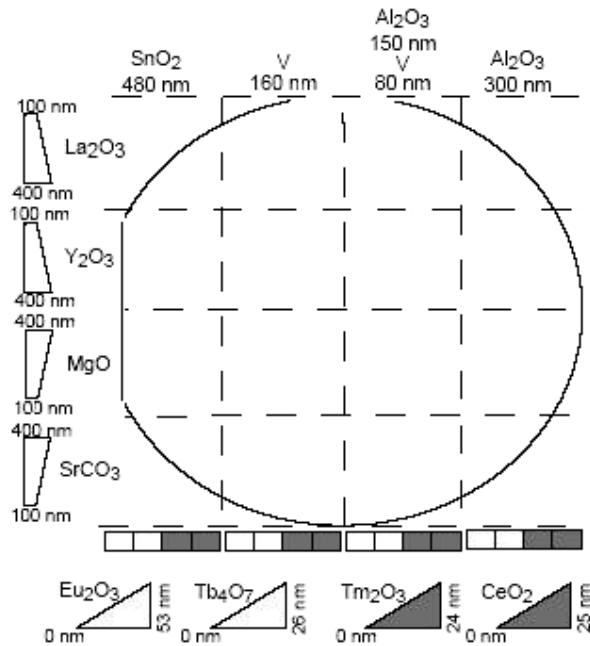


Figure 1.3.3 The deposition map of library contains multilayer precursors with diverse linear gradients.¹⁴

For many materials like ceramics, polymers and polycrystalline phosphors, their syntheses are best accomplished by using solution-phase methods which can fabricate a large number of libraries at a significantly lower capital investment compares with using automated vapour deposition equipment. One significant complication associated with materials discovery in thin-film format is the occasional lack of correlation with bulk properties owing to differences caused by film microstructure, strain and so on. Physical and chemical properties of compounds prepared using solution techniques generally show excellent correlation with bulk properties regardless of the volume of material prepared. Thus, library-based data may be easily confirmed in bulk.

Solution techniques allow mixing at the molecular level, reducing the need for high-temperature interdiffusion and also facilitating the isolation of metastable phases. Ink-jet printing technology has been adapted for combinatorial materials research since 1997. New luminescent materials were prepared by a scanning multi-head inkjet delivery system by Sun *et al.*⁴³ Having accurate and precise aspiration and the capability of delivering nanolitre volumes of reagents, ink-jet printers, particularly drop-on-demand printers, have been deployed for fast automated titration guided by laser-induced fluorescence detection for indicator end points.⁹⁰ In addition, ink-jet printing techniques are still improving for the preparation of thick-film combinatorial libraries for the high-throughput screening of many ceramic compositions.^{91, 92}

1.3.3 Thick Film Forming Methods

Slip casting and tape casting are conventional thick film techniques which have been commonly used to produce ceramic components with mass production capability. In slip casting, a slip or slurry of ceramic is poured into a porous gypsum mould. The liquid in the slurry is absorbed into the mould and particles are compacted on the mould surfaces producing parts with uniform thickness by capillary suction. Subsequently, pressure may be applied to the slurry and/or a vacuum may apply to the mould, or centrifuging may be used in order to increase the casting rate. The procedures of slip casting technique are outline below in Figure 1.3.4.

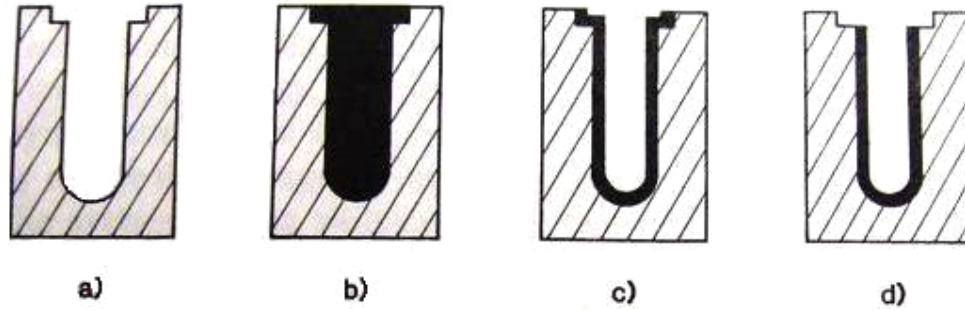


Figure 1.3.4 Processing flow diagram for basic slip casting process: (a) a porous mould is (b) filled with slurry; (c) superfluous slip is poured out when the desired wall thickness has been achieved and (d) shows the final dried product ready to remove from the mould.

The consolidated layer of particles formed on the mould surface occurs by the process of filtration. For uniaxial filtration, the cast thickness L as a function of casting time t is⁹³

$$L = [(2J\Delta Pt / \eta R_c) + (R'_m / R_c)^2]^{0.5} - (R'_m / R_c) \quad \text{Equation 1.3.1}$$

where J is the rate equal to volume of cast/volume of liquid removed, R_c the resistivity of liquid transport in the cast, ΔP the apparent mould suction, η the viscosity of the liquid transported and R'_m the liquid transport resistance in the mould. Equation 1.3.1 is derived based on the assumption that the parameters other than time on the right-hand side of the equation are constant during casting.

According to Equation 1.3.1, the casting rate of the partially coagulated slip is relatively high because the ratio of J/R_c is relatively high. The differential liquid content between the slip and the cast is small. In contrast, the casting rate of well-deflocculated slurry is relatively low because J/R_c is low. However, the completely deflocculated slip is able to produce dense and brittle cast rather than porous, soft

product which is deposited from coagulated slip. Slip casting processes are used to make dense refractories that are of a complex shape, thin-wall products such as crucibles and closed-end tubes, and products having large cross sections. However, the low production rate due to the requirement of long drying period and insufficient dimensional precision of the final product can constrain its applications.

Tape casting is another powerful technique to make ceramic components especially having flat and thin layered structure such as laminated capacitors, varistors, ceramic fuel cell and multilayered piezoelectrics.⁹⁴ The tape casting method is also known as doctor blading or knife coating which was first reported by Glenn Howatt to form ceramic products in 1947.⁹⁵ The process uses a scraping blade, known as the “doctor” for the removal of excess substances from a moving surface being coated. A schematic diagram of tape casting is displayed in Figure 1.3.5. The slip or slurry is poured into a puddle or reservoir behind the doctor blade and the carrier to be cast upon is set in motion. The doctor blade gap between the blade and the carrier defines the wet thickness of the cast tape. The thickness of the slip can be monitored continuously by a gamma-ray back-scatter or X-ray transmission instrument. Thus the gap between the doctor blade and carrier film is adjusted accordingly. Furthermore, thicknesses as low as 5 μm have been reported.⁹⁶ Other important variables that may affect the casting layer properties include reservoir depth, speed of carrier movement, viscosity of the slip and shape of the doctor blade. Drying of the film after being cast is accelerated by induced forced air flow or applied heat.

In tape casting, the dispersion step in the early stage is essential because it determines the homogeneity of the tape which must be very high to obtain

consistently flaw-free laminates. It is also essential to obtain uniform shrinkage in order to maintain the original shape after drying. Tape casting usually adopts non-aqueous solvents to facilitate the drying process which depends on evaporation rather than absorption into a plaster of Paris mould. However, water based tape casting systems are being successfully developed.⁹⁷ Drying is critical because most defects appear during this stage and may lead to the failure.

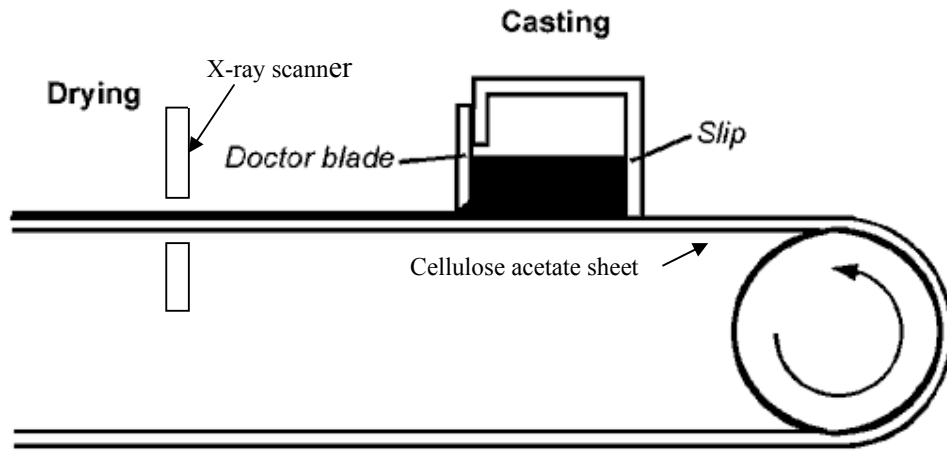


Figure 1.3.5 Schematic diagram of the tape casting processing

Other various methods that can be used for thick film fabrication also include injection moulding, extrusion, printing and novel solid freeforming of which detailed review will be given in the next section.

1.3.4 Thick Film Methods in Combinatorial Research

Libraries of ceramic thick film can be constructed by ink-jet printing method,⁹¹ other solid freeforming (SFF) techniques such as 3-D printing^{98, 99} and dry powder mixing^{100, 101}.

The ink-jet printing method has been employed in ceramic thick film combinatorial library synthesis for a decade but has still not reached a mature stage. The London University Search Instrument (LUSI) was built⁹¹ and modified¹⁰² to print thick film combinatorial libraries of ceramic compositions by mixing ceramic suspensions using stepper-driven syringes to control ink-jet-printing nozzles. The structure of the whole device is shown in Figure 1.3.6. It contains an aspirating-dispensing ink-jet printing station, a gantry robot, a four-zone furnace and a measurement table. LUSI has a potential capability to produce thousands of different ceramic samples in a day. It has synthesized many libraries in searching for novel ionic conductors¹⁰³ and dielectrics.^{40, 104, 105} However, it is less effective in producing compositional uniformity in libraries with trace dopant additives (e.g. < 1 mol.%) by powder mixing. The barriers that constrain the use of ink-jet printing in synthesizing ceramic products are the avoidance of compositional segregation during drying and the structural control of the drying pattern which can severely affect the properties after sintering. The shapes of the drying residue have been studied recently and will be discussed in Section 1.5.

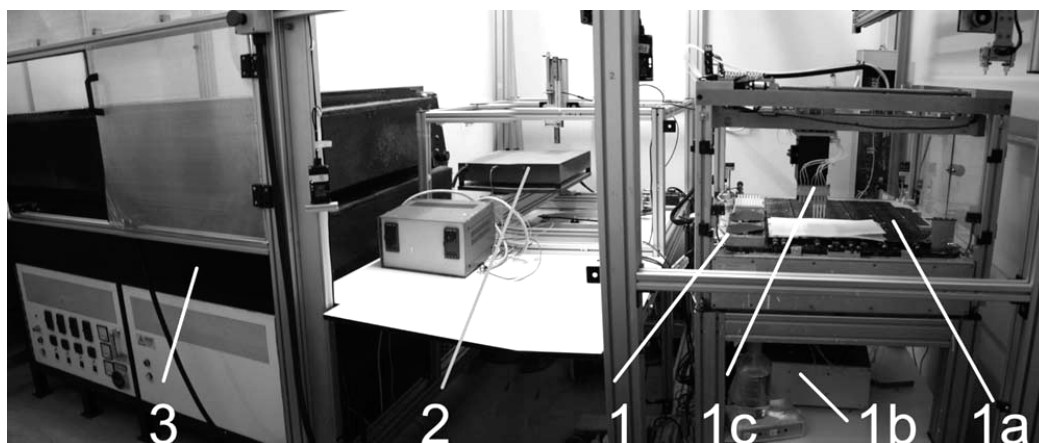


Figure 1.3.6 General view of the LUSI system. 1: printer table, 2: measurement table, 3: furnace, 1a: slides space, 1b: syringe pumps and controllers, 1c: print head.¹⁰²

1.4 Advanced Solid Freeform Fabrication of Ceramics

While the traditional ceramic processing techniques are effective for making products with simple patterns, none of them are feasible for fabrication of samples with complex shapes. Therefore, new manufacturing concepts to fabricate ceramic, metal and polymer components with very high design flexibilities for novel structures and with the possibility of rapid prototyping are needed. Solid Freeform Fabrication (SFF) techniques that provide integrated ways of manufacturing 3-dimensional components from computer aided design (CAD) files have been developed for industrial and engineering purposes. Compared with traditional processing, SFF techniques build parts by additive procedures, rather than by subtractive approaches. Thus, these fabrication technologies are unconstrained by the limitations or costs of conventional tools such as dies, molds and machining operations. Furthermore, any geometrical shape can be built up in a high degree of accuracy. In SFF, three-dimensional objects are created by point, line or planar addition of material without confining surfaces other than a base. Second-generation SFF aims not only to deliver shape but also composition gradients. Hence, functionally graded materials (FGM) can be assembled with effectively stepless gradients by SFF. Current commercial SFF techniques applied to ceramics include stereolithography (SL), fused deposition of ceramics (FDC), laminated object manufacturing (LOM), selective laser sintering (SLS), three dimensional printing (3DP) and direct ink-jet printing including continuous and drop-on-demand printing.

1.4.1 Three-Dimensional Printing (3DP)

Three-Dimensional Printing (3DP) is a process that creates porous objects with

complex-shaped by selectively binding loose powder in a sequential fashion controlled by a CAD file. Any starting materials in the form of powder including ceramic, metals and polymers can be used to form a green body by 3DP. A schematic diagram for a typical 3DP machine is shown in Figure 1.4.1. A thin layer of the powder is spread or roll-compacted evenly in a box where the floor is an adjustable platform moving along the z direction. The organic binder droplets are deposited on selected regions from a printhead which scans the powder bed. To avoid excessive disturbance of the powder when subjected to the impact from the binder drops, it is essential to stabilize the ceramic powder layer by moistening with water beforehand.¹⁰⁶ When one layer is finished, the floor of the powder box steps down by motor control so that a new layer of powder can be spread. These procedures are repeated until all the layers are printed and thereafter heat is introduced in order to set the binder. Loose powder is then removed to reveal the printed green body. Furthermore, the green body is subjected to post-printing processes that are designed to strengthen and densify the components. The resolution of the printed parts depends on the size of the binder droplets and the powder particles, the motion accuracy of the printhead and the mechanism that the binder spreading.¹⁰⁷

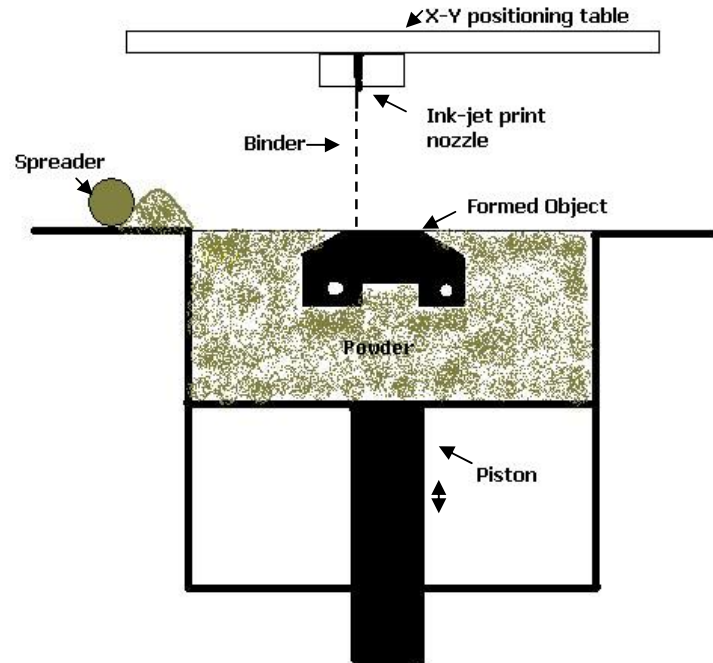


Figure 1.4.1 Schematic structure of the three-dimensional printing process.

1.4.2 Direct Ceramic Ink-Jet Printing (DCIJP)

Direct ceramic ink-jet printing (DCIJP) is a forming process in which droplets of ceramic ink are printed through an array of contactless nozzles onto previous layers. The ceramic ink drops can be deflected or deposited on pre-determined positions on the platform. This technique has been implemented in many different fields and has a wide range of potential applications. Fundamentally, DCIJP is divided into continuous and drop-on-demand ink-jet technologies. Both methods have been used successfully to build ceramic objects of submillimeter-scaled components and multimaterial devices.¹⁰⁸⁻¹¹²

For direct ceramic jet printing techniques, their feasibility is dependent on the availability of suitable inks. Ink chemistry and formulations not only dictate the quality of the printed image, but also determine the drop ejection characteristics and

the reliability of the printing system. The dispersibility of the ceramic powder in the liquid carrier is essential and critical. The powder in the ink must be free from agglomerates or have low agglomerate strength and the ink must resist flocculation. Solvents for the ink are also limited; they must be non-toxic, contain minimal health hazard for prolonged exposure and evaporate fast in order to allow overprinting ceramic components.¹¹³ The best ink should also have low viscosity while maximizing the solids content defined as the volume fraction of ceramic. In order to minimize dimensional shrinkage between the printed part and the final sintered product, it is desirable to use inks with the highest possible solids loading. However, the viscosity of such inks increases rapidly with increasing solids content. Thus the ink viscosity needs to be reduced to a compatible level to let the inks flow at high speed through small nozzles, which are typically 30-120 μm in diameter. The right dispersant, surfactant and other additives are added to improve the performance of the ink. Furthermore, the ink sedimentation stability has to be considered. However, Teng¹¹⁴ suggested that the sediment packing efficiency, rather than the rate of sedimentation,¹¹⁵ indicated the degree of dispersion.

1.4.2.1 Continuous Ink-Jet Printing

The continuous ink-jet printing technique was originally developed for commercial applications such as the date labelling in food packaging etc. A continuous stream of ink is forced under the pressure through a small orifice in the print-head. A piezoelectric vibration is imposed on the nozzle causing the stream of fluid to break into small individual droplets. Subsequently, the strings of ink drops acquire an imparted electric charge while falling through the charging sector that consists of electrodes at a high electric field just beneath the piezoelectric nozzle. Printing is

achieved by deflecting charged drops of ink by subjecting them to high voltage deflector plates. The greater the charge on a drop, the greater the deflection; hence the ceramic ink must be sufficiently conductive for the charge to flow to the jet tip at a rate that allows each drop to be charged fully in the duration of the charging pulse. Ammonium nitrate has been added in the ink to increase the charging ability particularly for ceramic inks. Teng *et al.*¹¹⁶ found that a conductivity of 100 mS/m is sufficient for conventional continuous jet printing. Therefore, the designed pattern is formed by the combined motion of one axis movement of the print table and adjustment of the deflection rate of the inks; furthermore, multiple layers can be built up by over-printing by introducing an optical sensor to guarantee the accurate relocation of the print-table.¹¹⁷ Those drops not required for printing are collected and recycled. A schematic diagram of continuous ink-jet printing device is displayed below in Figure 1.4.2.

The resolution and quality of the printed products are highly dependent on the ink viscosity and surface tension. The key factor in obtaining the stable stream of fluid is determined by whether the ink flow is laminar or turbulent in the nozzle tube. Herein the Reynolds number of the fluid, Re , needs to be considered, which is defined as:

$$Re = \frac{\rho v L}{\eta} \quad \text{Equation 1.4.1}$$

where ρ is the density, v is the fluid velocity, η is the dynamic viscosity and L is the characteristic length. For $Re < 2100$, flow in a circular pipe is considered to be laminar and for $Re > 4000$ to be turbulent. According to Blazdell's¹¹⁸ work, the drop diameter and its kinetic energy ejected from the nozzle have considerable effect on the resolution of the printed object. Higher kinetic energy of each drop and hence larger drop sizes have resulted in coalescence with ink relics on the substrate.

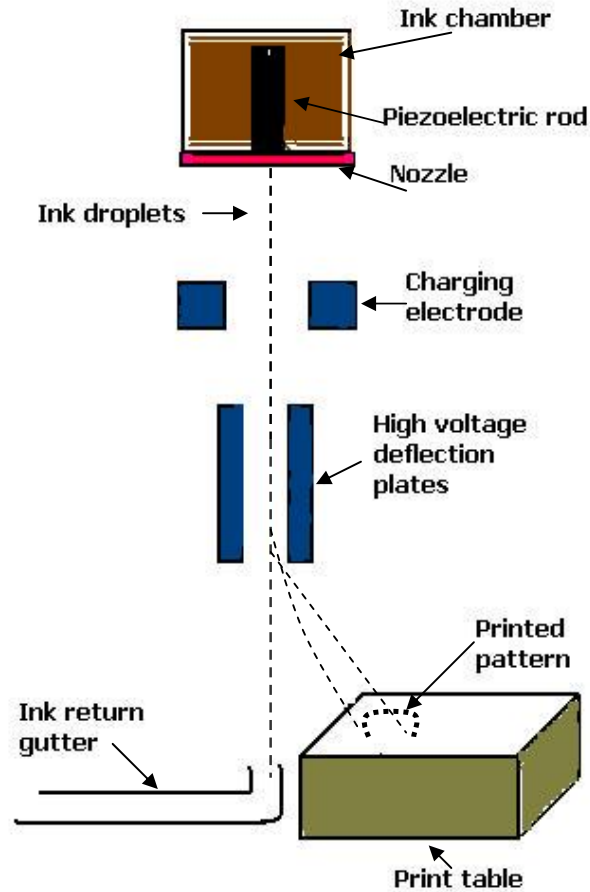


Figure 1.4.2 Schematic diagram of the continuous ink-jet printing system.

Compared with the drop-on-demand printing technique, continuous ink-jet printing has higher ceramic deposition rate owing to faster droplet formation rate which is determined by the high frequency of the piezoelectric actuator driving the vibration. However, its application is constrained by ink selection particularly the requirement for electrical conductivity and this technique has the drawback that changing the ink composition is difficult during printing unless additional print heads and separate ink reservoirs are used.

1.4.2.2 Drop-On-Demand Printing (DOD)

In drop-on-demand printing technology, the ink droplets are ejected from the nozzle

only when required to form the pattern on the substrate. The technique was invented and developed by Zoltan¹¹⁹ and Kyser *et al.*¹²⁰ in the 1970's. The printed drops are generated by a pressure pulse acting on a fluid-filled reservoir immediately behind the nozzle with defined diameter normally in the range of 20-100 μm with a small opening time. There are several principles of ink ejection to produce a drop from the orifice. They include thermal, piezoelectric, electrostatic, acoustic and electromagnetic which are classified according to the drop formation mechanisms. Fromm¹²¹ found an analytical model for the case of the droplet ejection in a DOD ink-jet printer. He used a velocity independent dimensionless ratio containing a group of physical constants shown below which was a representative of the influence of the viscous, inertial and surface-tension forces on fluid flow:

$$Z = \frac{Re}{We} = \frac{(\gamma \rho s)^{1/2}}{\eta} \quad \text{Equation 1.4.2}$$

where Re is Reynolds number, We is the Weber number, γ is the surface tension, ρ is the density, η is the viscosity of the fluid and s is a characteristic length, taken as the diameter of the printer orifice. This ratio, Z , was found in the range of 1 to 10 in commercial drop-on-demand ink-jet printing applications.¹²² When $Z < 1$, the viscous term turns out to have priority in preventing drop ejection unless the pressure pulse is increased. When $Z > 10$, multiple drops form rather than a single defined drop and it also leads to satellite drop formation behind the main drop. A range of aqueous-based¹²² and phase change¹²³ ink systems have been tested and supports these limiting range values of Z .

The drawback of the drop-on-demand printing technique is occurrence of inconsistent fluid flow or nozzle clogging during printing ceramic suspensions. Thus phase-change or hot-melt printing methods have been adapted to eliminate such

flaws. The ceramic ink uses low melting point polymer as a carrier vehicle and the printing process begins at a temperature above its melting point. The molten liquid drops solidify when touching the cooler substrate. Very little spreading and absorption occur during impact on the substrate so that high resolution of the image can be realized and the print quality is almost independent of the substrate properties when comparing aqueous based inks.¹²⁴ Furthermore, this approach eliminates a drying cycle thereby improving the rate when printing samples with multiple layers. It also has greater resistance to printhead clogging.

Compared with the continuous ink-jet printing technique, the drop-on-demand method has the advantage that complex components such as drop charging and deflection hardware as well as the inherent unreliable ink recirculation systems are not required.

A. Thermal Ink-Jet Printer

Most of the DOD printers in the market today use either the thermal or piezoelectric principle. A thermal ink-jet printhead consists of an ink chamber having a small heating device near the nozzle. During the printing action, a bubble in the ink reservoir is created due to superheating the ink above the boiling point by the heater when a short current pulse is applied. For water-based ink, this temperature is around 300°C; hence a water vapour bubble instantaneously expands to force the ink out of the orifice. Once the droplet is ejected, the bubble collapses. The whole process of bubble formation and collapse takes place in less than 10 μ s. The ink then refills by capillarity from the reservoir and the process is ready to start again. Depending on the channel geometry and ink's physical properties, the ink refill time can be varied

from 80 to 200 μs .¹²⁵ The main problem that needs to be tackled in this technique is to avoid clogging of the nozzle by dried ink. This process is illustrated in Figure 1.4.3. Depending on its configuration, a thermal ink-jet print head can be either a roof-shooter where the heater located just behind the orifice or a side-shooter with an orifice on a side located closed to the heater.

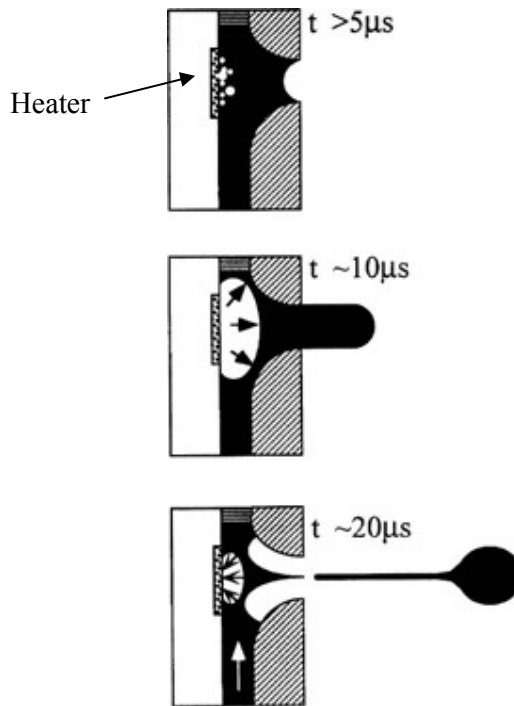


Figure 1.4.3 Drop formation process of a thermal ink-jet printer.¹²⁵

B. Piezoelectric Ink-Jet Printer

In piezoelectric DOD ink-jet printing, the ink is expelled by piezoceramic deformation which is schematically displayed in Figure 1.4.4. Due to the motion driven by the piezoelectric ceramic rod, the volume of the ink chamber behind the orifice is reduced generating a pressure wave that propagates toward the nozzle. The ink drop is formed and ejected from the nozzle when the pressure waves are sufficient to exceed the resistance of the summation of viscous pressure loss in a small nozzle and the surface tension force from ink meniscus. This kind of

technology can be classified into four main types in terms of the way of the mechanical pulse generated by piezoelectric actuation: squeeze, bend, push and shear mode.

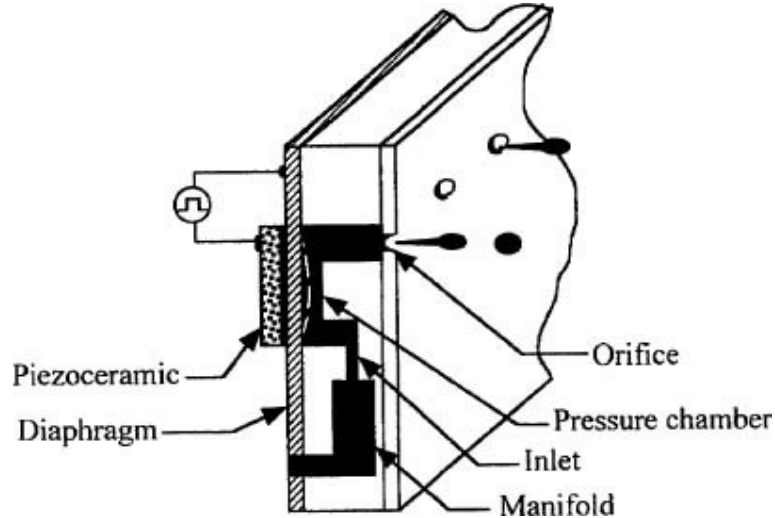


Figure 1.4.4 The basic configuration of the piezoelectric printhead.¹²⁵

C. Electrostatic Ink-Jet Printer

In the electrostatic ink-jet printer, ink drops are generated by the balance between the surface tension force and the electrostatic attractive force at the tip of the nozzle. The drop formation is a very complicated phenomenon of flow dynamics which is a function of applied voltage, nozzle diameter, surface tension of the ink, electrode geometry and position.¹²⁶ When high voltage is applied between the nozzle and the metal electrode, the ink meniscus at the printhead tip is distorted from a spherical shape into an inverted cone-like shape. The tip of the cone is broken subsequently to form very small droplets that are dispersed at wide angle due to the Coulomb repulsive force of charged drops.^{127, 128} The ink-drop frequency increases with applied voltage so that ultra-fine droplets are able to be formed for the potential use of high resolution printing; furthermore, the drops can be synchronized with the

electrical pulse as well by adjusting the pulse voltage to an appropriate range.

D. Acoustic Ink-Jet Printing

Acoustic ink-jet printing is a nozzleless, heatless ink ejection technique. Droplet formation is generated by a high intensity focused acoustic beam. Figure 1.4.5 shows the structure and mechanism that demonstrates how this system works. A series of parallel acoustic waves are generated by the transducer and electrode which are underneath the ink reservoir. The liquid surface level is adjusted to be at the same level of the focal point of the acoustic beam where the maximum acoustic energy burst is most likely to occur. Subsequently, it can drive a water mount that rises up from the liquid surface and a droplet is formed and expelled at a velocity of several meters per second. Elrod and Huang found that they can make the ejected droplets be as small as a few micrometers in diameter as well as stable in size and directionality.^{129, 130}

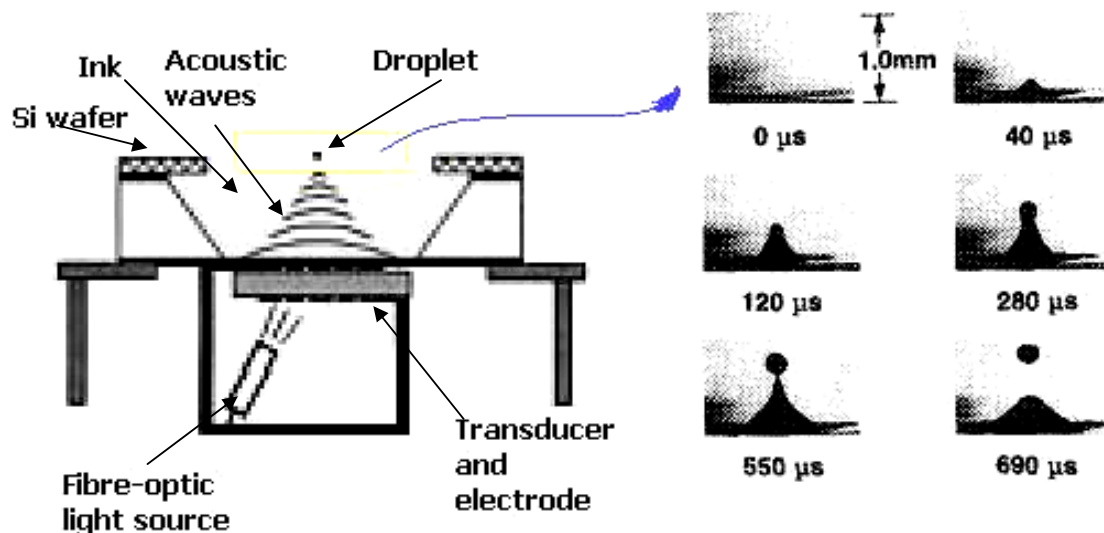


Figure 1.4.5 Schematic diagram of acoustic ink-jet printing and time evolution of droplets formation.¹²⁹

1.4.3 Other Solid Freeform Fabrication Methods

1.4.3.1 Stereolithography (SL)

Stereolithography is one of the earliest SFF technologies. It creates a solid body by scanning an ultraviolet-laser beam over a photo-curable monomer layer, including acrylates and epoxies, curing it in a line-by-line, layer-by-layer process.^{131, 132} SL was invented by Chuck Hull, and was developed by 3D Systems of Valencia, California, USA, founded in 1986. Figure 1.4.6 illustrates a SL machine for fabrication of a 3-dimensional part in a layer-by-layer sequence. It works by taking a computer model and slicing it into many thin layers each 150-200 μm thick. Using the information for each layer, a computer-controlled laser beam scans across the surface of the liquid monomer which contains a highly concentrated suspension of ceramic particles, solidifying the liquid at each point, where the depth of the solidified layer is controlled by the radiation exposure and set to the layer thickness. When the layer is finished, the support platform and the work piece move down by the height of the next layer. A sweeper moves liquid polymer across surface to prepare the next layer. The process is repeated until the whole part is finished. When building is completed, the platform is raised and the solid polymer part emerges from the ceramic suspension pool. After post-curing treatment, the pre-fired part can be given a conventional binder burnout and sintering process.

There is another technique which is very similar to stereolithography called direct photoshaping. The ceramic slurry is photocured layer by layer accomplished by exposing an entire layer to visible light covered by a photomask. A liquid-crystal display or a digital light-processing projection system is induced to irradiate the subsequent layers of slurry to build the three-dimensional green part.¹³³

The advantage of stereolithography, in comparison with other layered manufacturing technologies, is the ability to produce highly complex 3D objects with high surface finish. However, some disadvantages accompanying it such as the following:

- i. The first few cured layers are readily curled due to polymerization shrinkage. Recently this behaviour has been minimized by the control of scanning sequence or space filling routines.
- ii. The ultraviolet-curable materials are normally costly, odorous, toxic and must be shielded from light to prevent premature polymerization.

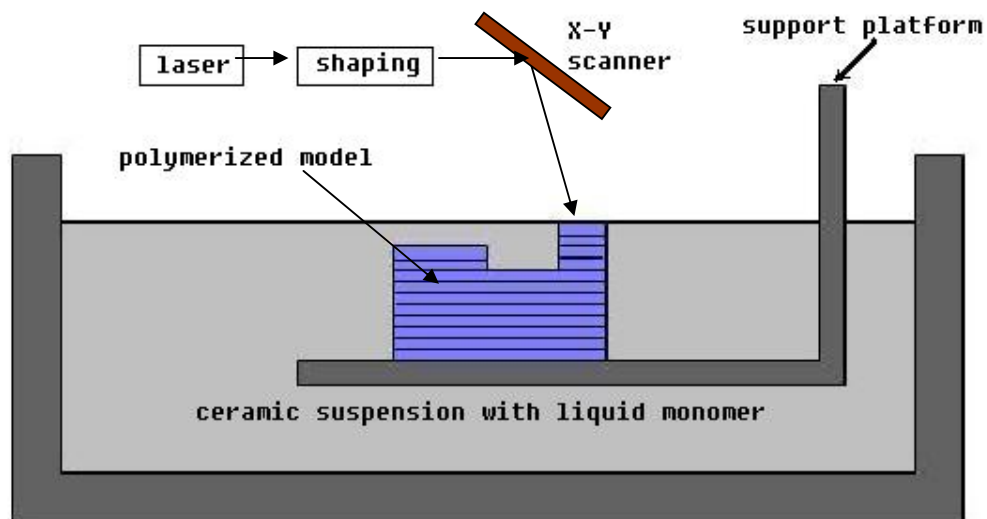


Figure 1.4.6 Schematic diagram of the stereolithography apparatus for fabrication of three-dimensional parts.

1.4.3.2 Fused Deposition of Ceramics (FDC)

Fused Deposition of Ceramics is one of the commercially available SFF techniques that build a 3D object by the process of depositing melted ceramic slurries layer by layer controlled by a CAD file. FDC was developed by StratasysTM Inc. (Eden Prairie, MN) based on the technique Fused Deposition Modeling (FDM).¹³⁴ The filament of the ceramic-loaded thermoplastic polymer passes through a heated liquefier where

the temperature is kept above the melting point of the polymer. A continuous rod or other sections of paste material is extruded through a nozzle from the liquefier and deposited on a fixtureless platform. The movement of the nozzle and liquefier along the X and Y directions is controlled by computer, based on the building strategy designed by the manufacturer. When construction of the first layer has been completed, the platform steps down by the height of the next layer and the second layer is built on the top of the first layer. This process continues until the whole part is completed. Figure 1.4.7 shows the schematic structure of a FDC filament head.

The quality of the feed filament is one of the most important parameters for making successful final products. The critical properties of the feed filaments include the viscosity, flexibility and strength. In order to make the FDC technique feasible, the melt viscosity of the filament in the liquefier must be low enough that the cold feed material can force the molten filament out of the nozzle; otherwise, high external pressure or higher operating temperature or both are required. Other parameters such as the feeding rate and the nozzle diameter also determine the quality of the final products. FDC allows control of both the design of a component macrostructure and the size and phase periodicity of the architecture.¹³⁵ Furthermore, the technique of fused deposition of multiple materials (FDMM) that is able to fabricate components up to four different materials rather than one has also been developed.¹³⁶ However, the application of FDC is restricted by the nozzle size for building fine work, for instance less than 76 μm in diameter, because the filament solidifies too quickly in ambient air after extrusion.¹³⁷ Hence, the solvent-based systems^{138, 139} which can offer more scope for control the fine filament work in such extrusion freeforming processing than the solid-liquid phase change systems are needed.

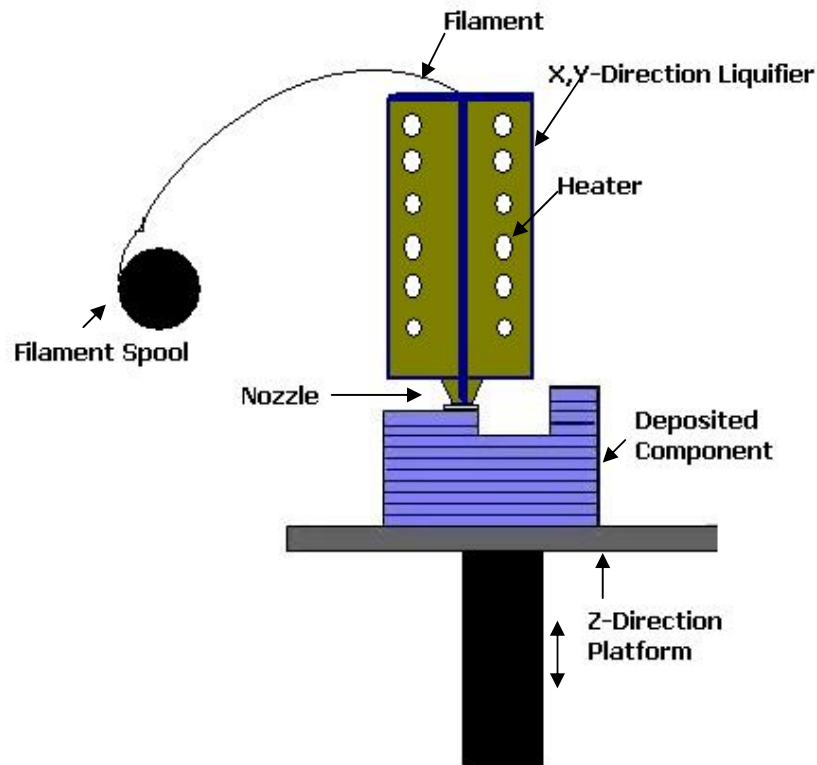


Figure 1.4.7 Schematic diagram showing the layer-by-layer fabrication in fused deposition of ceramics.

1.4.3.3 Laminated Object Manufacturing (LOM)

Laminated Object Manufacturing is a process that uses sheet material such as paper as the laminating material. A sheet coated with a thin layer of thermoplastic adhesive upon its lower side is laminated to the previously laid and bonded layers by a hot roller. The roller applies heat and pressure when it is rolling over the sheet. After a new layer is bonded, a focused laser beam cuts the bonded layer based on a contour instructed by a CAD file. The power of the laser is adjusted to cut through just one layer of the lamination. The unused material is left in place; however, it is diced with crosshatching into tiles for the purpose of easy removal afterwards. The iterative processes of bonding and cutting are repeated until the construction of the final layer

is completed. Then excess material is removed to expose the finished part. A diagram of LOM is showed in Figure 1.4.8.

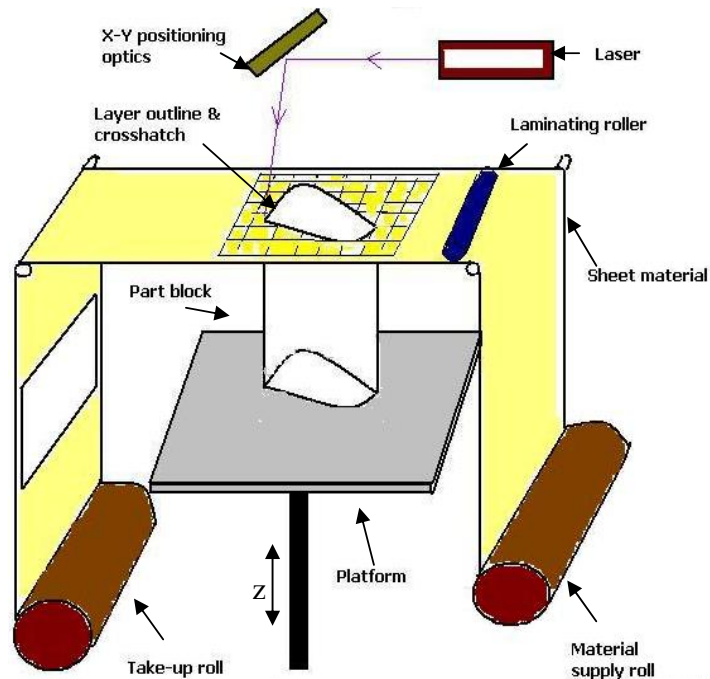


Figure 1.4.8 Schematic diagram of the commercial LOM process.

1.4.3.4 Selective Laser Sintering (SLS)

Selective Laser Sintering is a process invented by Beaman and Deckard¹⁴⁰ where a laser beam scans powders along pre-planned tracks according to a CAD model. Under the heating action of the laser beam, the powders added with bonding agents are softened and melted. After solidification, the whole powder mixture constitutes a solid state bonded skeleton. When one layer is finished, the platform is moved down by a distance determined by the design of the layer thickness. Then the preset amount of powder is placed over the previous sintered layer by the powder layering roller and another selected area on the new slice is scanning by the laser beam. Hence, the parts are built layer by layer. Furthermore, for specific powder mixture systems, to prevent oxidation, the construction cylinder is purged with inert gas. For energy

efficiency considerations, a radiant heater has also been introduced. The schematic structure of the SLS process is showed in Figure 1.4.9. The most important process parameter for SLS is the laser energy density but other parameters like part build orientation, layer thickness, laser beam diameter, powder mixture ratio and post processing also play important roles in influencing not only the mechanical properties but dimensional accuracy of the final sintered products.^{141, 142}

SLS can be used not only in industrial product manufacturing from computer aided design but also in medicine to build models of human anatomy from high resolution multiplanar image data such as computed tomography (CT). Moreover, SLS is chosen by surgeons to fabricate bone models because the sintered products look and feel more like real bone than the products made by other RP techniques.¹⁴³ The feasibilities of fabricating bone models made from polyamide/nylon¹⁴² and porous polycaprolactone scaffolds¹⁴⁴ by SLS have been investigated.

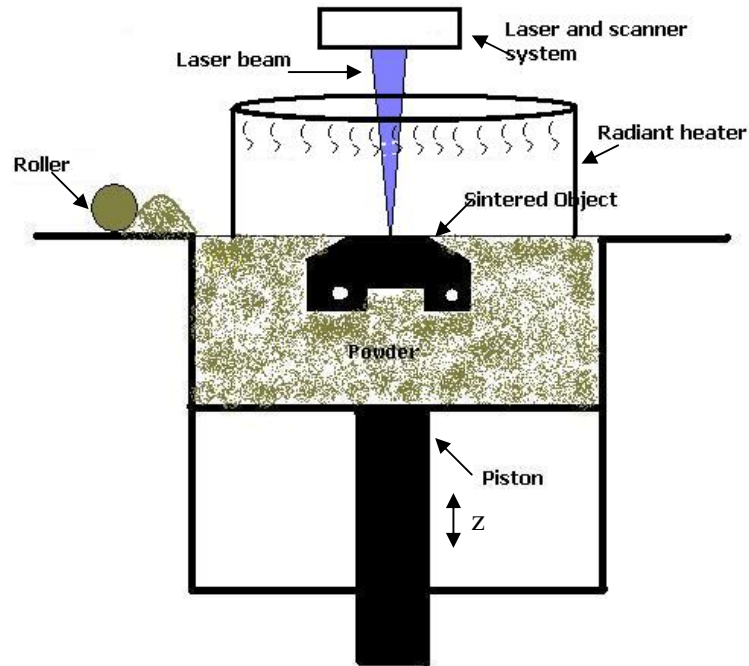


Figure 1.4.9 Schematic diagram of the selective laser sintering process.

1.5 Droplet Drying Effects and Patterns

1.5.1 The Evaporation of a Sessile Droplet of Colloidal Dispersion

The evaporation of a sessile droplet of colloidal suspension is a complex, multiphase transport process. Better understanding of this field is able to help not only controlling the pattern of the drying ink, but also avoiding the occurrence of defects during drying due to residue stresses produced by differential shrinkage or gas pressure.

The rate of evaporation of liquid is dependent on the specifications of ink and substrate and the environment. Three stages have been noted in the drying of ceramic dispersion on a non-porous substrate in open ambient environment (seen in Figure 1.5.1).¹⁴⁵⁻¹⁴⁷ The drying rate, expressed as a weight loss per unit time, keeps constant in the initial part of the drying cycle, which is relatively short. At this stage of drying, liquid is transported via capillary forces from the body to the surface where it evaporates to the atmosphere at a constant rate. There is a non-linear falling rate period following the constant drying rate period, where the evaporation from the menisci of liquid in pores at a stage where there is incomplete coverage of liquid on the external surface. Water vapour diffuses through increasingly longer pore length driven by decreasing concentration gradients hence the mass-loss rate decreases as the time increases. The final drying stage is approximately linear with a very low drying rate arising from the difficulty of the remaining moisture to diffuse through small interparticle voids.

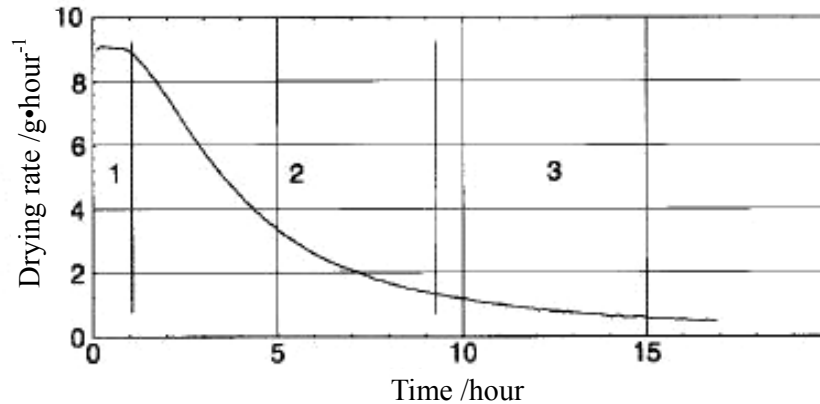


Figure 1.5.1 Drying profile for a gelcast part, showing the three stages of drying.¹⁴⁷

For large objects derived from colloidal suspensions produced by gelcasting or tape casting methods etc, previous studies have focused on the mechanism of occurrence of drying defects including cracks or body deformation which are due to differential shrinkage by stresses inducing during drying.¹⁴⁸⁻¹⁵³ However, the mechanism of aggregation during drying of aqueous particle suspensions for the purpose of drying pattern control still remains poorly understood. There are various capillary-induced flows occurring inside a sessile drop of colloidal suspension which can result in non-uniformity of solute particles during drying.

1.5.1.1 Lateral Flow

Denkov and Adachi found that when drying a thin liquid layer of particulate suspension on a solid substrate, the particles assembled to form particle-arrays at the droplet contact line.^{154, 155} In 1994, Fitzgerald and Woods¹⁵⁶ first observed that the motion of particles in a suspension droplet is from the inside to the boundary during drying. Later Winnik and Feng inferred lateral transport of water from the centre to the edge of the layer by observing nonuniform films after drying a convex layer of a latex dispersion.¹⁵⁷ This so-called “coffee-stain” effect with different corresponding

models has been investigated by many scientists.¹⁵⁷⁻¹⁶⁵

In Deegan *et al.*'s model¹⁵⁸ in Figure 1.5.2, the phenomenon of the “coffee-stain” is due to capillary flow within a sessile droplet of a suspension caused by a pinned contact line of the droplet while drying. Hence, the liquid evaporated from the edge is replenished by liquid from the interior. The resulting outward and radial fluid flow can carry solute to the edge. The spatio-temporal particle motion in a suspension during drying was successfully tracked by the three-dimensional particle tracking velocimetry devised by Ueno *et al.*¹⁶⁶ which dynamically proved the mechanism of lateral flow.

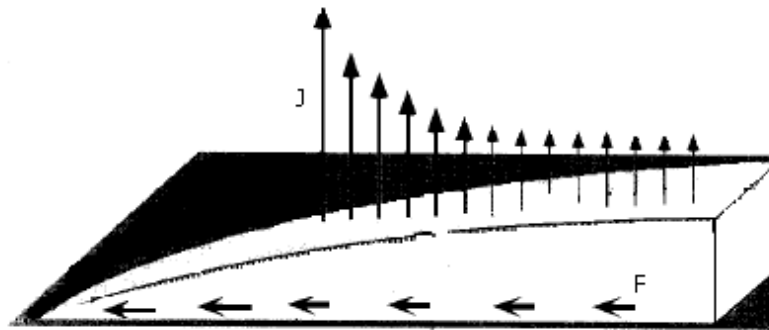


Figure 1.5.2 Mechanism of lateral flow during evaporation. Vapour leaves at a rate per unit area (J) and the liquid flow (F) outward to compensate for the deficit volume.¹⁵⁸

1.5.1.2 Marangoni Flow

Another source of microflow within an evaporating sessile droplet is Marangoni flow named after the Italian physicist who first described the movement of a liquid surface induced by a surface tension gradient along the droplet free surface. The Marangoni effect was first observed as “tears of wine” in the early 19th century.¹⁶⁷ Marangoni flow near the free liquid surface of a droplet is inward toward the top of the droplet

and then plunging downward where the transported particles can be either adsorbed onto the substrate near the centre of the droplet or be carried to the edge where they are recirculated along the free surface back towards the top of the droplet indicated in Figure 1.5.3.

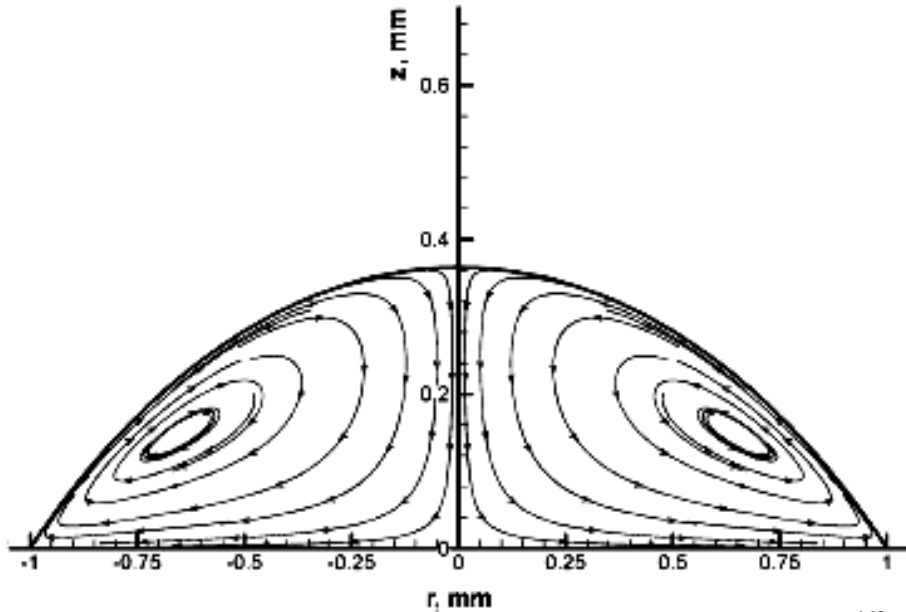


Figure 1.5.3 Streamline plot of the flow field for the Marangoni flow.¹⁶⁸

The flow field driven by Marangoni stresses was successfully traced experimentally by Hu and Larson in 2006 by using PMMA fluorescent particles in an octane droplet shown in Figure 1.5.4.¹⁶⁹

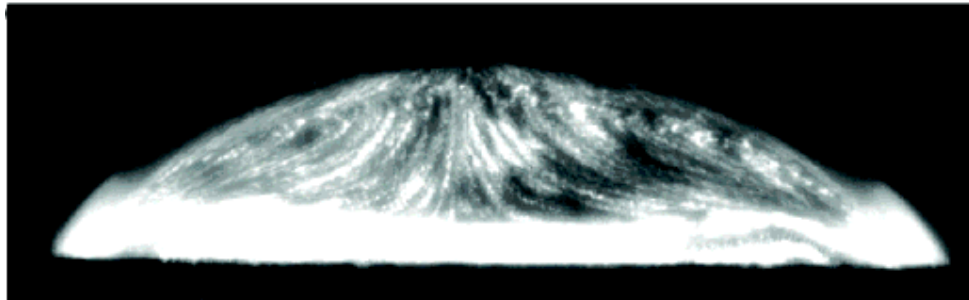


Figure 1.5.4 Flow field in a drying octane droplet.¹⁶⁹

In concentrated suspensions, the field of particles is the result of the competition of

evaporation, particle diffusion and convection which was noted by Yiantsios and Higgins.¹⁷⁰ They studied the film structure formed after the liquid was driven off by evaporation. They used the Peclet number (Pe) which is the rate of particle convection divided by the rate of diffusion in their numerical solution for characterizing the process.

$$Pe = \frac{LE}{D} \quad \text{Equation 1.5.1}$$

where L is the film thickness, E is the rate of evaporation, D the Stokes-Einstein diffusion coefficient which is given by $D=kT/6\pi\eta a$, where kT is the thermal energy, η is the solvent viscosity and a is the particle radius. When $Pe \ll 1$, diffusion is strong and particles are accumulated at the periphery of the droplet, resulting in the formation of a pinhole. When $Pe \gg 1$, convection induced by Marangoni stresses makes vertical concentration gradients exist. A closed packed skin is formed, with low concentration fluid remaining underneath; thereafter, capillary pressure pulls particles in the underlying fluid toward the skin, thus creating voids under the seemingly uniform coating.

However, the Marangoni flow in a single solvent system is readily suppressed by the surface-active contaminants that collected on the free surface of particles particularly in aqueous dispersion. Even a small amount, as little as $300 \text{ molecules}/\mu\text{m}^2$,¹⁶⁸ of contaminated surfactant in a water droplet, can significantly reduce the recirculating flow induced by the Marangoni stresses.

1.5.2 The Control of Sessile Drop Drying Patterns

The understanding of the drying behaviour of a droplet or film on a solid substrate is important for many applications including coating and painting, ink-jet printing¹⁷¹

and the deposition of DNA/RNA microarrays.^{172, 173} The drying pattern of samples in thick film combinatorial research determines not only their dimensional quality but also the feasibility and convenience of property measurement or spectroscopy. Drying patterns of droplets with uniform thickness and homogeneous structure or convex dome shape are preferable in thick film methods.

Drying of a droplet of particle dispersion on a solid substrate is affected by various factors including capillary stress, Marangoni stress and gravity. For fine particles in a stable dispersion, the sedimentation effect due to gravity can be neglected. Deposition of particles occurs preferentially at the centre of the organic fluid droplet due to recirculatory flow driven by Marangoni stress indicated in Figure 1.5.5(b). However, Marangoni flow is readily suppressed by surfactant contamination especially in water. Therefore, a ring-like pattern is often observed after evaporation of an aqueous droplet with solute/particle constituents as displayed in Figure 1.5.5(a). In addition, the coffee-ring pattern can be observed on various substrates (glass, metal, roughened Teflon, polyethylene, ceramic and mica), various solvents (aqueous and non-aqueous), various particle sizes (sugar molecule to 10 μm polystyrene microsphere) and with various solids concentrations (10^{-6} to 10^{-1} in volume fraction).¹⁶⁵ Moreover, other factors such as gravitational effect (comparing pendant and sessile drop), electric field (applying charge needle at various position of droplet) and environmental conditions such as temperature, humidity and pressure could also be varied without affecting the ring pattern. However, Deegan¹⁶⁵ found that the ring pattern can be overcome when drying the droplet on smooth Teflon where the contact line pinning is eliminated. Likewise, the final deposit becomes uniform when evaporation is restricted by covering the drop with a lid that had only a small hole

above the centre of the droplet through which the vapour can escape.

Haw *et al.*¹⁷⁴ found that the inhomogeneity in composition of a drying droplet might be caused not only by flow driven effects, but also rapid phase separation effects according to the studies on the effects of phase behaviour and rheological properties on the evaporative drying of a sessile colloidal droplet. They classified the drying behaviour of a sessile droplet of concentrated colloidal suspension into three regions including gelation, fluid and aggregation in terms of the initial composition of the colloid and polymer in suspension. Homogeneous structure of the final dried residue can be achieved when the drying stage of the droplet is staying in the gelation region.

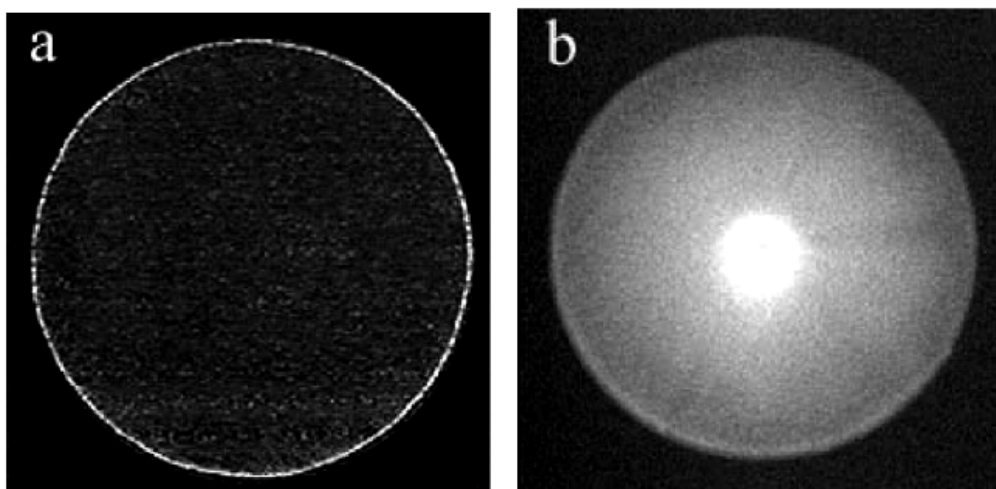


Figure 1.5.5 (a) Ring deposition pattern from a droplet of water with fluorescent polystyrene particles. (b) Drying pattern from a droplet of octane containing PMMA particles.¹⁶⁹

Recently, a new method has been explored to tackle such problems of obtaining uniform residue of drying droplet by the use of solvent mixtures. Gans *et al.*¹⁷⁵ used an ethyl acetate/acetophenone system and Park and Moon¹⁷⁶ used the system of water/formamide. These are low and high boiling point solvent mixtures as well as

having substantial difference in surface tension between them. Both of them successfully obtained homogeneous dome-like patterns from the evaporation of a droplet of colloidal suspension (as seen in Figure 1.5.6). They both believed that the origin of this phenomenon was due to Marangoni flow induced by the use of combined solvents. During the evaporation of a droplet, the local solvent composition near the contact line shifts toward a higher fraction of a high-boiling-point solvent due to increased rate of drying at the periphery. The edge evaporation then slows down, and outward convective flow diminishes. Furthermore, a surface tension gradient is established which can induce Marangoni stress within the droplet. The magnitude of the Marangoni flow is determined by the Marangoni number:¹⁷⁶

$$M = \Delta\gamma L / \eta D_{AB} \qquad \text{Equation 1.5.2}$$

where $\Delta\gamma$ is the surface tension difference, L is the length scale involved, η is the viscosity and D_{AB} is the diffusion coefficient in binary solution. If using typical values for L , η and D , hence M is of the order $10^7\Delta\gamma$. It shows that even a very small surface tension gradient will trigger a Marangoni flow. Schubert and Park also showed that occurrence of recirculation flow caused by Marangoni stresses within a droplet despite directions (inward towards the top of the droplet or inward towards the bottom of the droplet) can both obtain final uniform drying pattern.

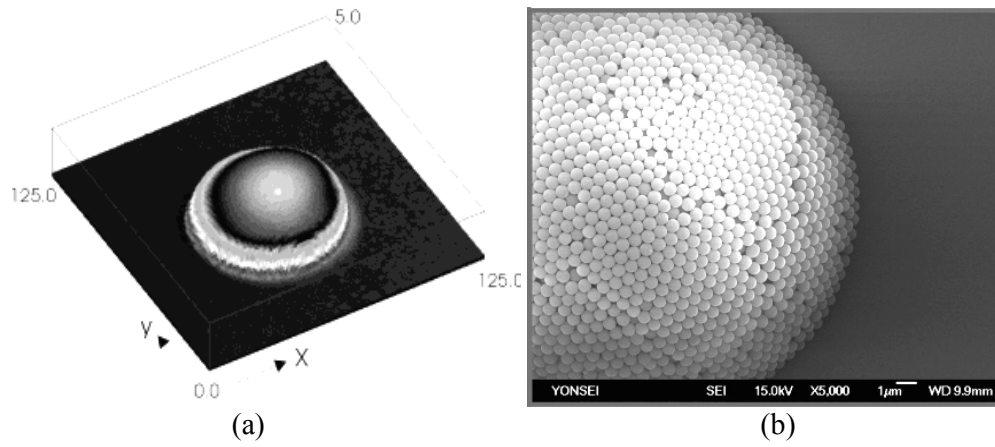


Figure 1.5.6 Drying pattern of (a) polystyrene in an 80/20 wt.% ethyl acetate/acetophenone mixture on perfluorinated glass¹⁷⁵; (b) silica particle in water/formamide based ink on a hydrophobic Si wafer.¹⁷⁶

1.6 Temperature Dependent Resistors: Thermistors

There are wide ranging applications in the electronics industry for temperature-dependent resistors for which their resistances are either negative temperature coefficient (NTC) or positive temperature coefficient (PTC). Both NTC and PTC thermistors can be used as indicators for temperature measurement. PTC units have the advantage that they are unlikely to overheat since an increase in temperature cuts down the power that they need to dissipate because of exponential increase in resistivity. Nevertheless, precautions must be taken with NTC units to ensure that runaway conditions cannot occur; because the internal power increases with temperature resulted from significantly reducing resistivity.

1.6.1 Negative Temperature Coefficient Resistivity (NTCR) Materials: Compositions and Applications

There is a large choice of materials for NTC thermistors but those most used in industry are based on solid solutions of transition metal oxides that exhibit the spinel-type crystal structure with the general formula AB_2O_4 .^{177, 178} Therefore oxides of manganese, nickel and cobalt are preferred for the preparation of a NTC thermistor because their electrical resistivity decreases progressively with increasing temperature. Moreover, some compounds such as $LaCoO_3$ -based materials having perovskite structure can also display the NTCR effect and their working temperature can reach 500 °C.¹⁷⁹ The mechanism of electrical semiconducting properties of those oxides is explained by a phonon-assisted jump of carriers among localized states, the so-called polaron hopping effect.¹⁸⁰ For example, in the nickel manganite systems, the substitution of Ni^{2+} occupies octahedral B sites of the spinel structure and causes

a conversion of Mn^{3+} to Mn^{4+} in order to maintain the charge balance, thus providing a basis for electron hopping and resulting in increase of conductivity.¹⁸¹ Furthermore, their conductivity reaches a maximum when the number of Mn^{3+} ions equals that of Mn^{4+} ions.¹⁸²

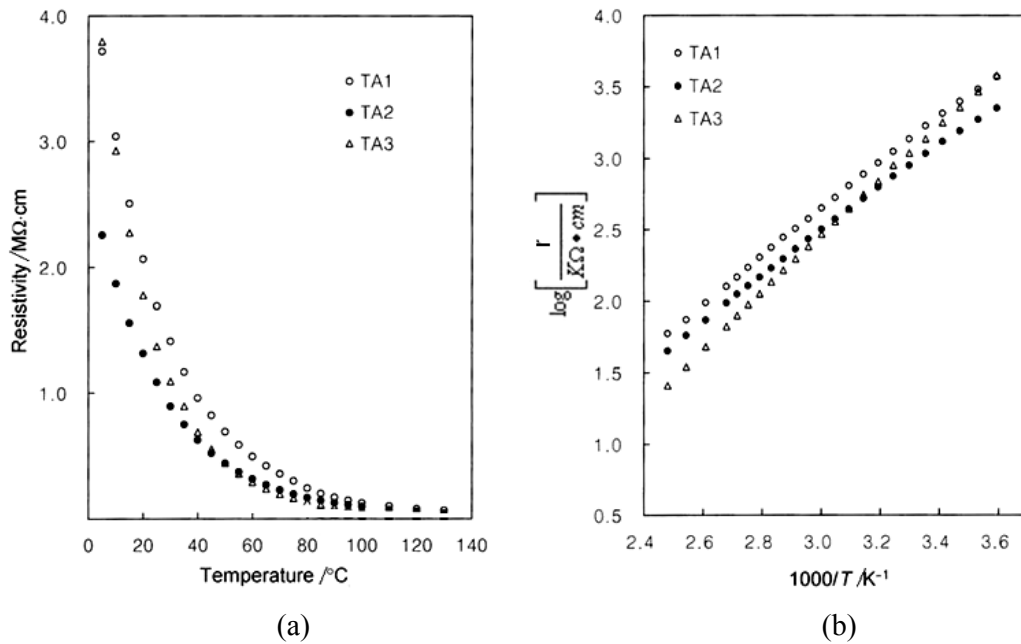


Figure 1.6.1 Electrical characteristics of NTCR effect for Ni-Mn-Co oxides (TA1 represents $\text{Ni}_{1.4}\text{Mn}_{0.6}\text{CoO}_4$, TA2 represents $\text{Ni}_{1.2}\text{Mn}_{0.8}\text{CoO}_4$, TA3 represents NiMnCoO_4) (a) relationship between resistivity (r) and temperature (T); (b) $\log r$ versus $1/T$.¹⁸³

Typical electrical characteristics of a NTCR material are displayed in Figure 1.6.1. Figure 1.6.1(a) shows the direct relationship between the electrical resistivity and temperature for $(\text{Ni}_{2-x}\text{Mn}_x\text{Co}_{1.0})\text{O}_4$ ($0.6 \leq x \leq 0.8$)¹⁸³ and 1.6.1(b) shows their conversion curve using the logarithms of the resistivity, $\log r$, against the reciprocal of the absolute temperature, $1/T$, which has a linear relationship. Furthermore, the slope of the $\log r$ versus $1/T$ curve is taken as a measure of temperature sensitivity,

so-called B constant. The resistivity r can be expressed by the following Arrhenius equation:

$$r = r_0 \exp\left(\frac{B}{T}\right) \quad \text{Equation 1.6.1}$$

where r_0 is the resistivity of the material at infinite temperature, T the absolute temperature and B constant which has the dimensions of temperature in Kelvin is also given by

$$B = \frac{q}{k_B} \quad \text{Equation 1.6.2}$$

where q is the activation energy for electrical conduction and k_B is the Boltzmann constant. The activation energy is the energy primarily for the hopping process from a cation M^{n+} to $M^{(n+1)+}$ on the octahedral sites and hence for the mobility of the cations.¹⁸⁴ Sufficiently high value of the B constant is essential for useful applications because they are more sensitive to the change of temperature, leading to more accurate and smaller variation in temperature measurements.

NTCR ceramics are sintered generally in air at 1000-1300 °C depending on the composition. The NTC thermistors are widely used in a variety of industrial and domestic applications such as elements for the suppression of in-rush current, for temperature measurements and control, for compensation for other circuit elements e.g. in television receivers because the resistance of the beam-focusing coil increases as temperature rises in the cabinet. The electrical properties of NTCR materials strongly depend on the composition and sintering temperature. There are extensive studies on the electrical features of compounds containing multiple transition metals from the oxide pool of Fe, Mg, Cr, Co, Al, Mn, Ni, Cu^{183, 185-189} in order to screen their electrical characteristics in a wide temperature range along with a favourable

combination of resistivity and the coefficient of temperature sensitivity B . New composition systems with novel elements are still attractive to many scientists as a great challenge.

1.6.2 Positive Temperature Coefficient Resistivity (PTCR) Materials: Compositions, Microstructures and Properties

Positive temperature coefficient of resistivity (PTCR) materials are widely used in the electronics industry for, *inter alia*, applications including temperature sensors, time delay circuits and current limiters for overvoltage or overcurrent protection, overheat protection and current stabilizers. There are four main materials groups in the PTCR family: BaTiO₃-based or quasi-BaTiO₃-based ternary perovskite compounds,¹⁹⁰⁻¹⁹⁸ ceramic composites,^{199, 200} polymer composites,^{201, 202} and V₂O₃-based compounds.^{203, 204}

BaTiO₃ is an insulator at room temperature but donor-doped BaTiO₃ with ions such as La³⁺, Y³⁺, Sb³⁺, Nb⁵⁺ presents semi-conducting behaviour at room temperature and an anomalous increase in resistivity near the ferroelectric-paraelectric Curie transition temperature T_c .¹⁸⁰ This PTCR effect (shown schematically in Figure 1.6.2) in barium titanate was first developed in the early 1950s in the Philips Research Laboratories in the Netherlands.²⁰⁵ Over the past 50 years, diverse applications have triggered research efforts directed toward understanding compositional and structural issues that govern the electrical properties. The screening of dopant candidates from the periodic table has been well scrutinized²⁰⁶⁻²⁰⁸ and several models to explain the temperature-resistivity relation have been derived.²⁰⁹⁻²¹³

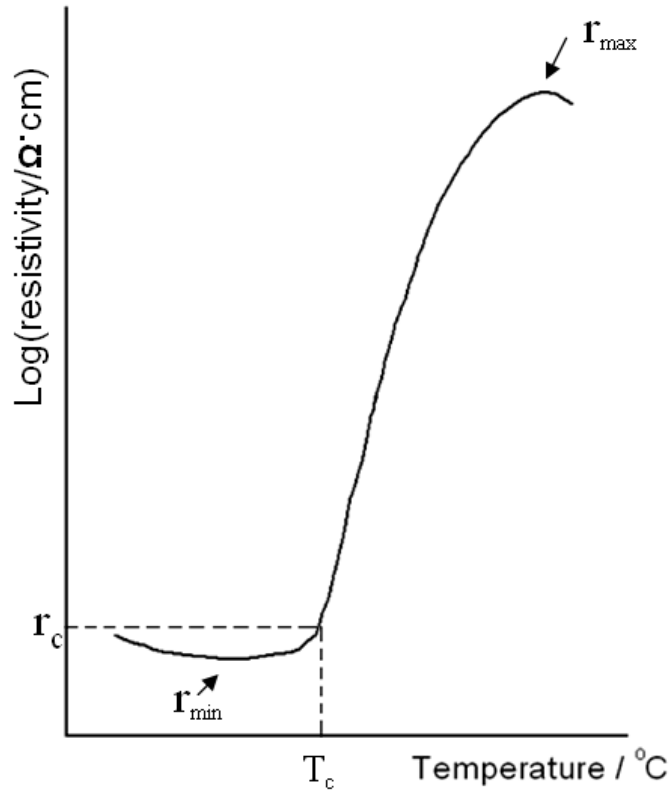


Figure 1.6.2 Typical resistivity-temperature characteristic of a BaTiO₃-type PTCR material.

1.6.2.1 Models of Explanation of PTCR Effect

There is a general agreement that the anomaly in the change of electrical resistivity of donor-doped BaTiO₃ around T_c is due to the grain boundary effect. No PTCR effect has been observed in BaTiO₃ single crystal.²¹⁴ Furthermore, it is clear from impedance-plane analysis that the semiconducting characteristics of bulk grains is independent of either temperature or donor concentration.²¹⁵⁻²¹⁷

A. The Heywang-Jonker model

The most accepted model to explain the PTCR behaviour in donor-doped BaTiO₃ materials is the Heywang-Jonker model proposed by Heywang²¹⁰ and extended by

Jonker.²¹² This model is a fundamental guideline for the understanding of PTC effect in BaTiO₃-based materials. There is a bi-dimensional layer of electron traps, i.e. acceptor states, along the grain boundaries of BaTiO₃ (shown in Figure 1.6.3) exhibiting different electrical properties from those of the bulk phase. The potential barrier ϕ_0 is caused by a two-dimensional electron trap along the grain boundary where acceptor states attract electrons from the bulk resulting in an electron depletion layer with thickness of b . The relation between the density of trapped electrons at the grain boundaries and the thickness of the depletion layer can be expressed as:

$$b = \frac{N_s}{2N_d} \quad \text{Equation 1.6.3}$$

where N_s is the concentration of trapped electrons and N_d is the charge carrier concentration. This depletion layer results in a grain boundary barrier, ϕ_0

$$\phi_0 = \frac{e^2 N_s^2}{8\epsilon_0 \epsilon_{gb} N_d} \quad \text{Equation 1.6.4}$$

where e is the electron charge, ϵ_0 the permittivity of free space and ϵ_{gb} the relative permittivity of the grain boundary region.

The overall resistivity, r , is related to the height of the potential barrier by

$$r = A \exp\left(\frac{\phi_0}{kT}\right) \quad \text{Equation 1.6.5}$$

where A is a geometrical factor and k the Boltzmann constant. Because BaTiO₃ is ferroelectric, the dielectric constant, ϵ , obeys the Curie-Weiss law above its Curie temperature and is given by

$$\epsilon = \frac{C}{T - T_c} \quad \text{Equation 1.6.6}$$

where C is the Curie constant and T the absolute temperature. Incorporating equation 1.6.4 and 1.6.6 into 1.6.5 and rearranging yields:

$$r = A \exp\left\{\frac{e^2 N_s^2}{8\epsilon_0 N_d k C} \left(1 - \frac{T_c}{T}\right)\right\} \quad \text{Equation 1.6.7}$$

Above the Curie point when doped BaTiO₃ is in the paraelectric phase, the grain-boundary permittivity which follows the Curie-Weiss law decreases with increasing temperature. The corresponding potential barrier increases proportionally and results in steeply increasing resistivity which depends exponentially on the potential barrier as denoted by equation 1.6.5. The energy of the trapped electrons in the grain boundary rises with temperature together with the potential barrier. When the energy of the electron traps reaches the Fermi level, trapped electrons start to jump to the conduction band, which can depress the increase in ϕ_0 and r , thus ultimately enhance the conductivity. This also explains the negative temperature coefficient resistivity (NTCR) effect when passing the point r_{\max} (Figure 1.6.2) in the high temperature range.

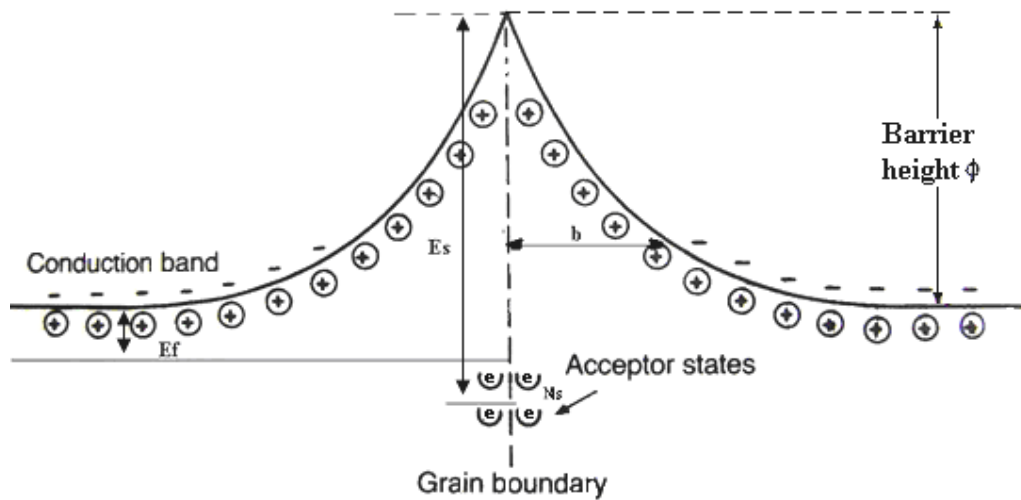


Figure 1.6.3 Electrical double layer at a grain boundary. E_s is the electron-trap energy, E_f the Fermi level, N_s the concentration of trapped electrons and b the width of electron depletion layer.

However, Heywang's model was not able to explain accurately the PTCR behaviour below T_c . Hence Jonker's model²¹² was developed as a refinement. Below the Curie point, BaTiO₃ is ferroelectric with its polarization along the tetragonal crystal axis. The polarization direction is different from grain to grain because each adjacent grain has a different crystal orientation. Therefore, it creates a net polarization vector (P_N) normal to the grain boundaries, producing surface charges at the grain boundaries which are illustrated in Figure 1.6.4. In the areas with negative surface charges, which are around 50% of the grain-boundary area depending on the nature of the ferroelectric material, potential barrier height diminishes or even disappears resulting in the disappearance of the grain boundary resistance. For the other half of the domains containing positive charges, the potential barrier is, of course, getting higher. However, this does not matter as the conducting electrons always follow the path with the lowest barriers so that the material as a whole has low resistivity. This theory is experimentally supported by Huybrechts' work.²¹⁸ Furthermore, according to the Heywang-Jonker's model, the electrical resistivity profile $r(T)$ above the ferroelectric Curie point of donor-doped barium titanate ceramics can be modelled and was verified successfully using experimentally determined permittivity data reported by Brzozowski *et al.*¹⁹⁷ and Zubair *et al.*²¹⁹.

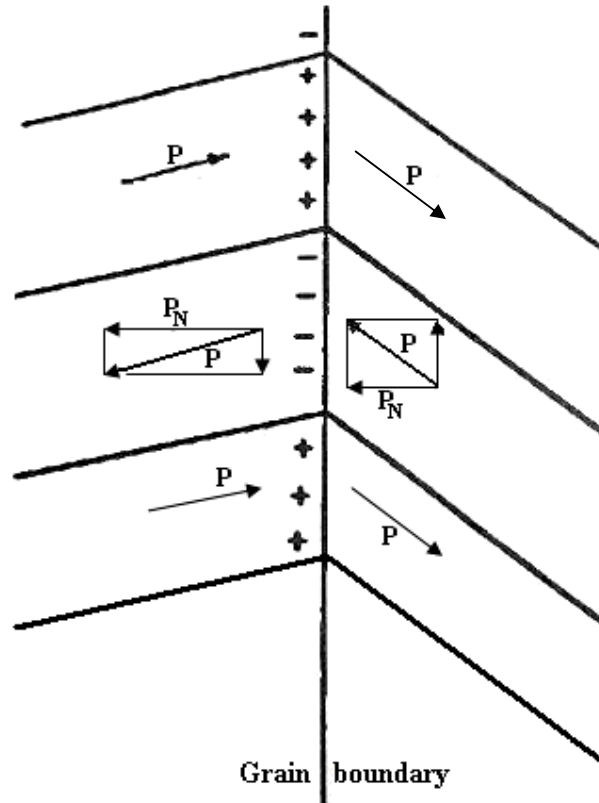


Figure 1.6.4 Ferroelectric domains at the grain boundaries. P is the vector of spontaneous polarization and P_N the normal component of P .

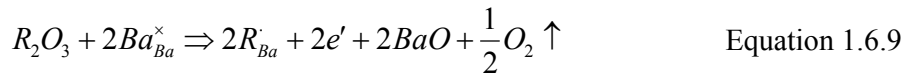
B. Other Theories

In donor-doped BaTiO_3 PTCR ceramics, Heywang-Jonker's model has effectively elucidated the change of resistivity with temperature in PTCR characteristics. Based on this model, the PTCR effect increases with increase of potential barrier by which is affected the trapping of electrons (from ionized donors) by acceptor-type species such as some 3-d elements,²²⁰ chemisorbed gases²²¹⁻²²³ or cation vacancies^{224, 225} at the grain boundary. Those barriers make the grain boundary more resistive than the bulk grain. However, the model does not fully explain the mechanisms by which electrical properties are influenced adding different amounts or kinds of donor dopants or changing the processing parameters.

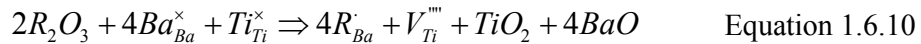
It is believed that, for donor-doped BaTiO₃, the initial drop in resistivity with increasing donor concentration is generally attributed to an electronic compensation mechanism that induces n-type semiconductor characteristics.²²⁴ Choosing a trivalent ion (R³⁺) as a donor dopant, free electrons in the BaTiO₃ lattice can be generated according to equations (written in Kröger-Vink notation):



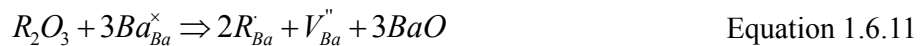
and/or



Based on equation 1.6.8, the free electrons are generated by oxygen deficiency as occurs when sintering at high temperature and/or in reducing atmospheres.²²¹ Based on equation 1.6.9, the electrons are associated with the replacement of barium ion by R trivalent ion. However, if there is a shift to an ionic compensation mechanism (cation vacancy compensation) at high donor contents, this would result in increasing resistivity at room temperature due to the immobility of cation vacancies. It was first suggested by Jonker and Havinga²²⁵ and the corresponding equations are:



and/or



According to equations 1.6.10 and 11, barium vacancies and/or titanium vacancies can be produced at the grain boundaries and diffuse from the grain boundaries into the grains during sintering. Because the diffusion speed of cation vacancies is very slow in grains at high temperature, this results in a sample with heterogeneous electric profiles in grains as the cation vacancies act as electron traps and there is an increase in the potential barrier at the grain boundaries. Chan *et al.*²²⁶ inferred that titanium vacancies were favoured defects compared with barium vacancies in the

ionic compensation scheme according to a microstructural investigation of highly donor-doped BaTiO₃ by TEM. The preference for titanium vacancies is also supported by atomistic simulations which show lower energy of formation than that of barium vacancies.²²⁷

Smyth²²⁸ believed that equations 1.6.9 and 10 can be connected by an exchange reaction:



where the donor centres are charged-compensated by electrons if the extra oxygen is expelled. Clearly, electron compensation is preferred in reducing conditions during sintering resulting from the tendency for oxygen loss, while ionic compensation by generated Ti vacancies is favoured by an oxidation environment. This theory explains well the observation that for light donor-doped BaTiO₃ material processed in air by slow cooling or annealing at a lower temperature may be superficially or completely oxidized to an insulating state but have low resistance at room temperature if cooled rapidly from the sintering temperature because of the ‘frozen-in’ composition, avoiding reoxidation that occurs at lower temperature. For higher donor concentrations, materials can become electrical semi-conducting only if sufficiently reduced. The quantitative analysis²²⁹ of the oxygen exchange of donor-doped BaTiO₃ both under equilibrium and non-equilibrium conditions by the oxygen coulometry method²³⁰ has directly proved that the carrier concentration is equal to the net donor content which is in agreement with the conclusion that the equilibrium conductivity is dependent on the electronic compensation that is proportional to the donor concentration. Furthermore, evidence for precipitation of secondary phases in donor-doped BaTiO₃ when alternated between the oxidizing and reducing environments

during firing support the validity of this charge compensation mechanism.^{231, 232}

There are still some controversies in the well-accepted ideas of charge compensation mechanisms affecting the conductivity of donor-doped BaTiO₃. According to the charge compensation theory, the donor-doped BaTiO₃ should contain an electrically heterogeneous structure regardless of both the composition and subjecting processing parameters because of the cation-stoichiometric difference between the grain core and grain boundary as compared with the electrically homogeneous structure of undoped BT. However, Morrison *et al.*^{233, 234} observed by impedance spectroscopy that there is no semiconducting grain interior in lightly donor-doped BaTiO₃ after sintered in O₂, which suggested that the material was electrically homogeneous. They also announced that there was no finding of change in cation stoichiometry or precipitation of secondary phase in donor-doped BaTiO₃ samples with varied donor concentrations which were sintered in air or argon. Yet it is generally believed that, according to the conventional charge compensation schemes, the appearance of a change in cation stoichiometry is required in donor-doped BaTiO₃ when a switch from insulating to semiconducting and *vice versa* occurs. They²³⁵ hence proposed an alternative explanation: the oxygen nonstoichiometry, which is dependent on the oxidized/reduced state at the grain boundary is the main reason for the semiconducting behaviour of donor-doped BaTiO₃. Furthermore, the production of semiconducting undoped cation-stoichiometric BaTiO₃ which exhibits a modest PTCR effect by losing a small amount of oxygen²³⁶ supports their view.

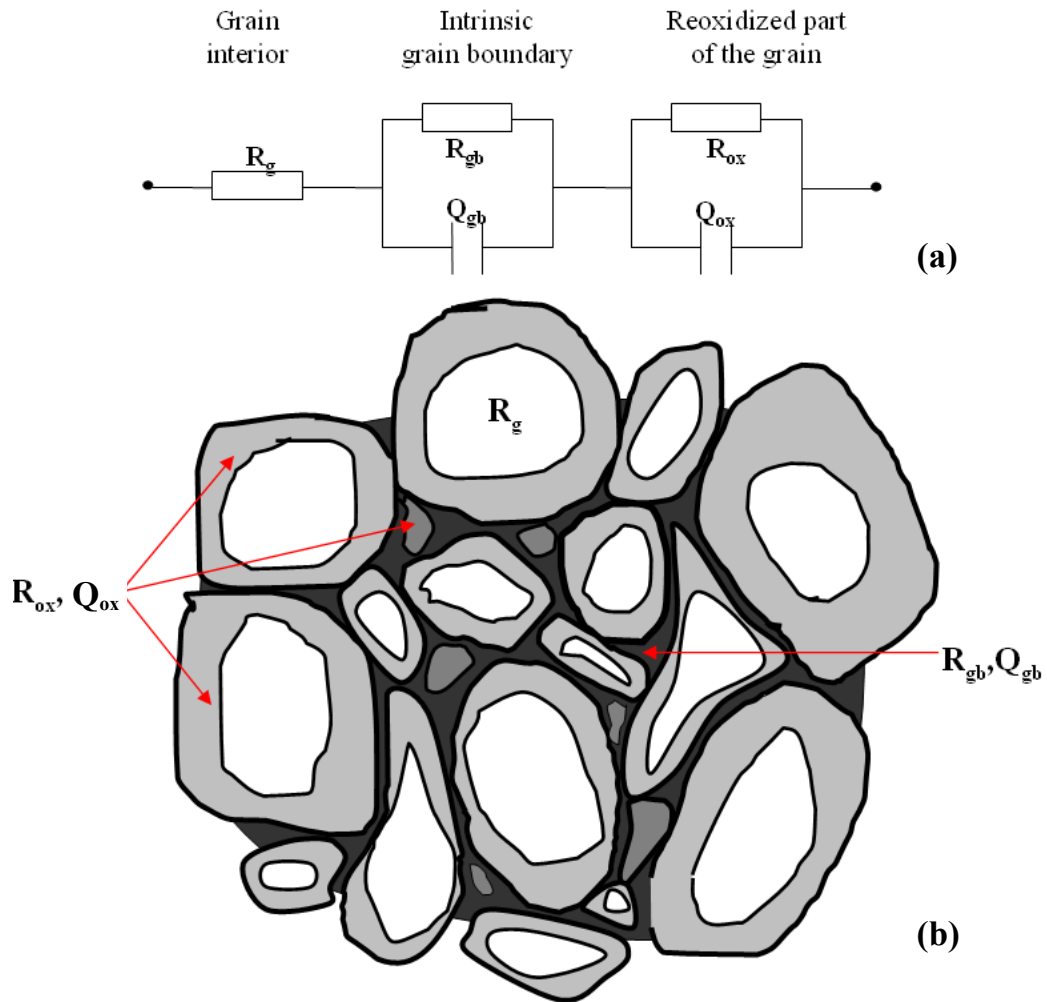


Figure 1.6.5 Schematic model of the microstructure of the donor-doped BaTiO₃ and its equivalent electric circuit. (replotted from²³⁷)

In spite of these discrepancies, there is one common theme that the overall origin of the electrical properties of BaTiO₃-based thermistors is a grain boundary effect and greatly influenced by the defect structure on the perovskite crystal lattice.^{238, 239} The results from the remote electron beam induced current (REBIC) microscopy as a local investigative technique can well support such a view.²⁴⁰ The proposed grain and grain boundary structure of donor-doped BaTiO₃ is schematically displayed in Figure 1.6.5.²³⁷ According to the results of measurements of complex-impedance spectra and microstructural analysis by TEM,^{237, 241} the grain system's structure is postulated

as having three distinct regions (Figure 1.6.5(b)) and its equivalent electric circuit model is shown in Figure 1.6.5(a). The outer layer is an oxidised, insulating grain boundary region; the intermediate layer is reoxidized, semiconducting outer grain region and the inner layer is an oxygen deficient grain interior, again, a semiconducting inner grain region. This heterogeneous structure in the grain system is supported by both the phenomenon of heterogeneous electric structure of donor-doped BaTiO₃ and direct imaging from conductive atomic force microscopy technique.^{242, 243}

1.6.2.2 Effect of Composition of BaTiO₃-based Materials on the PTCR Properties

Pure BaTiO₃ sintered in air is an insulating material at room temperature and no PTCR effect can be observed; however, it turns to a semiconductor at room temperature by doping with various donor dopants such as trivalent ions (e.g. La³⁺, Sb³⁺, Y³⁺) which substitute for the Ba²⁺ site or pentavalent ions (e.g. Sb⁵⁺, Nb⁵⁺, Ta⁵⁺) which substitute for Ti⁴⁺ site at relatively low doping levels. It can revert back to behaving as an insulator when the donor content exceeds the critical concentration (normally less than 1 mol.%) as illustrated in Figure 1.6.6,²³⁵ noting that the solubility limits of most of the dopant elements in BaTiO₃ perovskite lattices are far higher than this critical concentration.²⁴⁴ Moreover, the resistivity versus temperature characteristic is very sensitive to the composition of dopants especially for some 3-d elements acting as acceptors. For example, very small additions ranging between 0.01-0.04 mol.% of Mn can increase the PTCR jump of donor-doped BaTiO₃ as much as nine orders of magnitude in comparison with three to five orders of magnitudes for donor-doped only BaTiO₃.²⁴⁵ In addition, the additives which play a

crucial role in the fabrication of BaTiO₃-based PTC thermistors can be mainly distinguished as two kinds: aliovalent dopants and isovalent dopants.

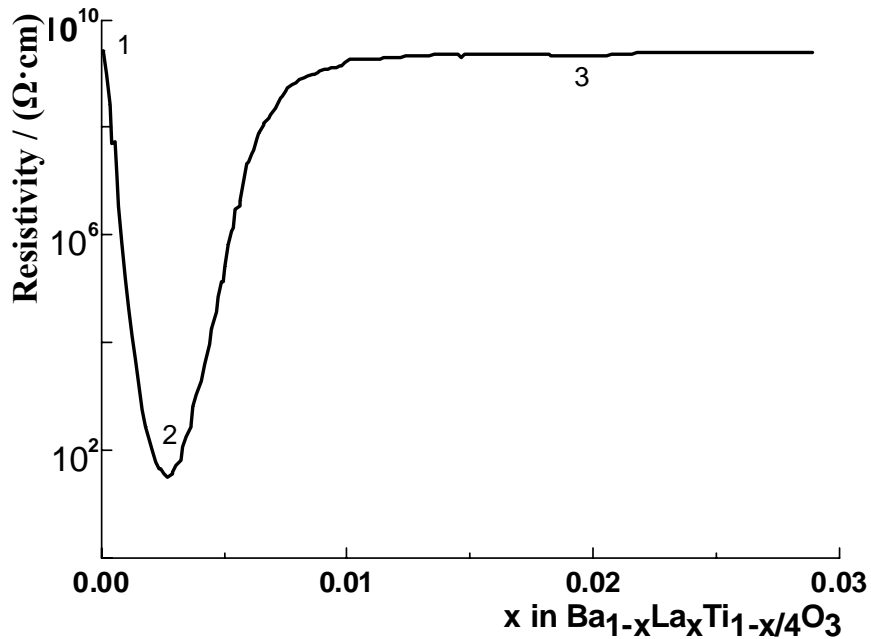


Figure 1.6.6 Schematic representation of the room-temperature dc resistivity as a function of La-dopant concentration for BaTiO₃ ceramics sintered in air. (replotted from ²³⁵)

A. Aliovalent Dopants

The effect of the aliovalent dopant on the bulk electrical conductivity is strongly dependent on its substitution site in the BaTiO₃ perovskite structure. The type of incorporated dopant is determined by the difference in valence charge between the dopant and the replaced host ion. Site replacement in the crystal lattice mainly depends on the dopant's ionic radius.²⁰⁶ Many (*3d*, *4d* and *5d*) elements in Table 1.6.1 which could act as aliovalent dopants in BaTiO₃-based PTC thermistors have been extensively investigated. Among them, the group of rare-earth elements is a rich resource for providing donor dopants.^{207, 208, 246, 247}

Table 1.6.1 Summary of aliovalent dopants in BaTiO₃ (ionic radii data from ²⁴⁸).

Ions	Ionic radius (Å)	Main type of dopant when Ba/Ti=1	Reference
Ba ²⁺	1.35		
Ti ⁴⁺	0.68		
Sb ³⁺	2.45	Donor	249-251
Bi ³⁺	1.20	Donor	252
La ³⁺	1.15	Donor	235, 237, 253
Ce ³⁺	1.11	Donor	254, 255
Nd ³⁺	1.08	Donor	256
Sm ³⁺	1.04	Donor	257
Gd ³⁺	1.02	Donor	258
Dy ³⁺	0.99	Donor	259, 260
Ho ³⁺	0.97	Amphoteric dopant	261-264
Er ³⁺	0.96	Amphoteric dopant	265, 266
Y ³⁺	0.93	Amphoteric dopant	267-269
Yb ³⁺	0.86	Acceptor	191, 206, 270
Ni ²⁺	0.78	Acceptor	271
Cu ²⁺	0.69	Acceptor	272
Cr ³⁺	0.69	Acceptor	245
Mg ²⁺	0.65	Acceptor	273
Fe ³⁺	0.64	Acceptor	274
Co ³⁺	0.63	Acceptor	275
Mn ²⁺	0.80	Acceptor	220, 276, 277
Ta ⁵⁺	0.73	Donor	252, 278
Nb ⁵⁺	0.70	Donor	220, 273, 279-281
W ⁶⁺	0.67	Donor	278
Sb ⁵⁺	0.62	Donor	193
Mo ⁶⁺	0.62	Donor	278

Three regimes of element (expressed in Table 1.6.1) can be identified in terms of site occupancy in BaTiO₃ and are summarized as:

- i.) For small ions, with ionic radii $r \leq 0.09$ nm, dopants preferentially occupy the Ti-site.
- ii.) For intermediate ions, with ionic radii $0.09 \text{ nm} < r < 0.099$ nm, dopants can substitute for either Ti or Ba site depending on dopant concentration, sintering conditions and Ba/Ti molar ratio.^{206, 246, 282, 283}
- iii.) For larger ions, with ionic radii $r \geq 0.099$ nm, dopants preferentially occupy the Ba-site.

The Ba/Ti ratio of the starting materials seems to play a crucial role in affecting the incorporation of dopant elements into the BaTiO₃ lattice. It was observed by electron paramagnetic resonance spectra that Ce³⁺ partially occupied the Ti⁴⁺ sites when Ba/Ti > 1.²⁸⁴ Electrical conductivity measurement has shown that Er-doped BaTiO₃ is weakly semiconducting at room temperature when Ba/Ti = 1. It behaves as an acceptor (preferential substitution at Ti⁴⁺ sites) when Ba/Ti > 1 but as a donor (preferential substitution at Ba²⁺ sites) when Ba/Ti < 1.²⁰⁶ The recent study of Zhi²⁶⁹ on BaTiO₃ with heavily doped Y³⁺ leads to a similar conclusion. Moreover, dopant substitution at the Ti⁴⁺ site can also be enhanced by high dopant concentration partly because the solubility at Ti⁴⁺ sites is higher than that at Ba²⁺ sites.²⁴⁴ For transition metals, like Mn, Co, Fe and Ni, it is well established that they preferentially substitute for the Ti⁴⁺ sites regardless the Ba/Ti ratio. Sintering atmosphere likewise has an effect on the preference of the incorporation site of some donor elements such as holmium.²⁸⁵ Significant substitution of Ho onto Ba sites as a donor occurred in a reducing atmosphere while Ti replacement as an acceptor was preferred when sintered in air.

It is generally observed that the room-temperature resistivity of donor-doped BaTiO₃ rapidly increases beyond the critical donor concentration because donor ions are preferentially segregated at the grain boundaries.^{216, 286} Desu *et al.*^{256, 287} found that at low donor concentration, the donors are compensated electronically, giving a high conductivity. When the donor concentration increases, the donor concentration at the grain boundaries increases even faster due to the segregation until it exceeds a critical level; the compensation mechanism thereafter shifts from electronic compensation to ionic compensation of the donor centre in the grain-boundary region. Hence it creates an insulating layer at the grain boundaries. The total resistivity of the sample can be represented by the grain bulk resistivity and the resistivity from the dopant-segregation-induced insulating region in the grain boundary. The greater the difference in ionic radius between the substitutional dopant and the host ion, the higher is the tendency for such interfacial segregation to occur. Therefore, the difficulty in preparing semiconducting donor-doped BaTiO₃ increases with the radius misfit between the donor and the host ion.²⁵⁶ Furthermore, it was found that when acceptors were added into donor over-doped BaTiO₃ insulating material, in which the concentration of donor had exceeded the critical level, the specimen was able to recover some of its semiconducting property.^{288, 289} This phenomenon might be explained by assuming that those acceptors inhibit donor segregation at grain boundaries.²⁷³ Nevertheless, the nature of the acceptor states is still little known.

B. Isovalent Dopants

Divalent ions such as Pb²⁺, Ca²⁺ and Sr²⁺ are extensively used as additives to substitute the Ba ions in the BaTiO₃ lattice.²⁹⁰⁻²⁹⁴ The replacement by lead can increase the T_c by 4.3°C per percentage atomic replacement, whilst replacement by

strontium reduces the T_c by 3.5°C per percentage atomic replacement (shown in Figure 1.6.7). Since the Curie temperature for BaTiO_3 is $120\text{-}130^\circ\text{C}$, this offers the potential to prepare thermistors with PTCR regions anywhere between -100°C and 250°C . Calcium is frequently used in moderate amount but does not shift the T_c by much, alternatively influencing the grain size of the product.²⁹⁵ On the other hand, tetravalent ions such as Zr^{4+} , Hf^{4+} and Sn^{4+} have been used as substitutes for Ti ions in the BaTiO_3 lattice.²⁹⁶⁻²⁹⁸ All those tetravalent dopants substitutions can significantly reduce T_c and readily make the phase transformation of tetragonal-cubic occur at room temperature. Zirconium added to BaTiO_3 results in lowering the dielectric loss and broadening the dielectric peak near T_c .²⁹⁹ Similarly, Hf and Sn exhibit strong ferroelectric-relaxor behaviour at high contents.³⁰⁰

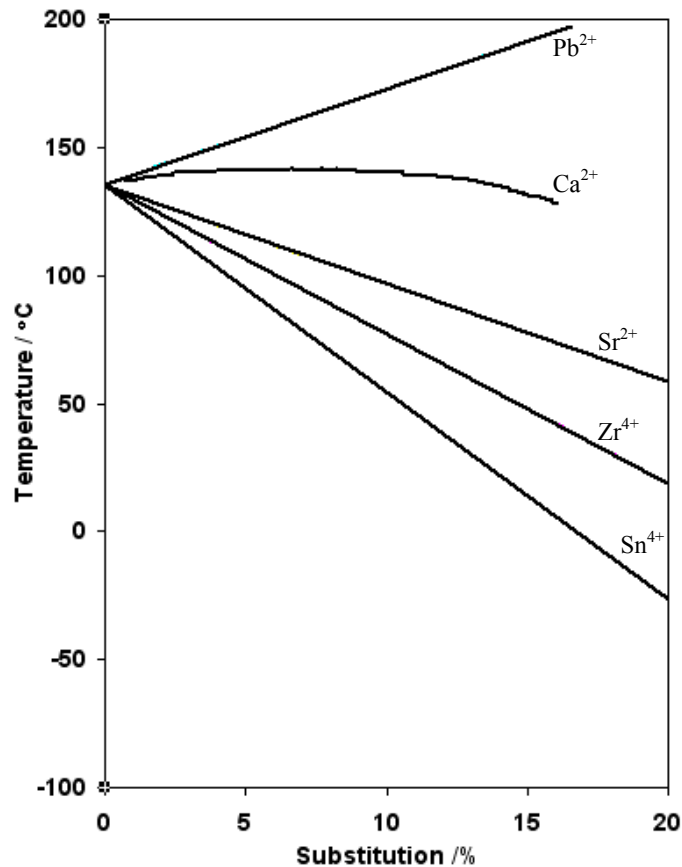


Figure 1.6.7 The effect of isovalent dopant doping on T_c . (replotted from²⁵³)

1.6.2.3 Effect of Processing on the PTCR Properties

It is well known that the impurities and lattice imperfections play an important role in the exhibition of the PTCR effect in doped-BaTiO₃ materials.³⁰¹ Their conductivities are considerably influenced by both the intrinsic defects such as oxygen vacancies as well as cation vacancies and the extrinsic defects produced by adding dopants.²⁸⁸ Furthermore, not only can the equilibrium behaviour of these defects but also the way of defect formation affected by varying sample preparation methods play a crucial role with respect to the semiconducting properties.

A. Effect of Doping Methods

Electrical performance in donor-doped BaTiO₃ ceramics is strongly related to the grain structure. Significant differences in microstructure were observed in samples with the same nominal composition prepared by different doping methods even with the same sintering procedures and hereby different PTCR characteristics were exhibited.³⁰² Hydrothermal synthesis or sol-gel methods can be used to produce donor-doped BaTiO₃ systems contained nano-size grains, with high crystallinity and well-dispersed dopants. However, very high room-temperature resistivities and poor PTCR jumps (r_{\max}/r_{\min} ratio) were observed in materials prepared by such method compared with the conventional solid state reaction route.³⁰³⁻³⁰⁶ A similar phenomenon was observed for donor-doped BaTiO₃ prepared by mixing the donor dopant into BaTiO₃ powder via solution coating method;²⁵⁰ in addition, PTCR ceramics prepared by this doping method has lower critical concentration of donor compared with the same compositional system prepared by the solid state route.²⁵⁰

Besides the different doping methods which cause disparities in PTCR behaviour as

described above, a variety of unique mixing techniques have been investigated in order to obtain a controllable, microstructurally stable, PTCR material. Mukherjee *et al.*³⁰⁷ made a donor-doped BaTiO₃ system by blending Ba-excess BaTiO₃ powder with Ti-excess BaTiO₃ powder in different ratios, finding that these blended systems had homogeneous grain size distribution but lower PTCR jumps than those from stoichiometric non-blended batches. Furthermore, Park *et al.*³⁰⁸ used a seeding technique to produce a heavily niobium-doped BaTiO₃ PTCR material by adding BaTiO₃ seed particles which contained double twins produced via preceding heat treatment. Semiconducting and PTCR characteristics were achieved by this seeding method compared with fine grained and insulating material for Nb-doped BaTiO₃ at the same doping level produced by a conventional, unseeded route.

Some dopants which are commonly used in making PTC thermistors have high vapour pressure particularly at high temperature so that the possibility of incorporating these dopant ions into the barium titanate crystal lattice by vapour phase diffusion exists. A variety of dopants such as Sb³⁺, Mn²⁺, Cd²⁺, Bi³⁺ and Pb²⁺ have been tested using such methods³⁰⁹⁻³¹² and this resulted in more enhancement of the PTCR jump than doping from conventional solid sources. This is partly because, in diffusion doping from a dopant vapour phase, dopant ions can be more effectively distributed at grain boundaries resulting in increasing the potential barrier at grain boundaries and hence increase of resistivity. In addition, diffusion in polycrystalline BaTiO₃ depends on not only the vaporisation rate or vapour pressure of dopants, but also other factors including the sample's porosity, sample's thickness, the nature of grain boundary and grain size.

B. Effect of Fabrication Methods

Not only the various doping techniques, but also the fabrication methods for producing donor-doped BaTiO₃ can alter its PTCR performance. In thin-film forming, the electrical properties of the films are significantly different from the bulk, regardless of the techniques of preparation. For Y-doped BaTiO₃ thin film ($\approx 2 \mu\text{m}$ in thickness) deposited by RF-magnetron sputtering as an example,³¹³ the film has a significant change of PTCR characteristics including a shift to lower T_c and smaller PTCR jump in comparison with the same composition prepared by a solid-state route. Large fluctuations in doping concentration dependent resistivity were also observed among those films themselves with the same composition. Nb-doped BaTiO₃ films prepared by laser molecular beam epitaxy (LMBE) show extremely low resistivity ($\approx 10^{-4}$ - $10 \Omega\text{cm}$);³¹⁴ films grown by metal-organic chemical vapour deposition (MOCVD) exhibit intermediate resistivity ($\approx 10^{-1}$ - $10^7 \Omega\text{cm}$);^{315, 316} similarly, the resistivity is around 10^2 - $10^4 \Omega\text{cm}$ for films deposited by pulse laser deposition³¹⁷. This phenomenon may be due to the significant change in microstructure and phase content of the deposited thin film compared with its target material. In addition, the evidence that donor element segregates to the surface and the amount of dopant is drastically reduced below the near-surface region of the thin film sample indicates that the ineffective doping is the cause of the contrasted resistivity values for thin film form and bulk sample.³¹⁸ BaTiO₃-based PTCR ceramics fabricated by thick film methods such as tape-casting,³¹⁹ slip-casting and roll forming³²⁰ have similar microstructure and PTCR characteristics compared with those made by conventional die-pressing methods; nevertheless samples produced by these thick film techniques have higher room-temperature resistivity which is partly due to the high porosity caused by the burning of larger amount of organic additives which were added to

facilitate the forming processing.

C. Effect of Heat-Treatment

The PTCR effect in donor-doped BaTiO₃ is very sensitive to firing conditions.³²¹⁻³²³ Pure stoichiometric BaTiO₃ which is an electrically insulating material at room temperature after sintering in air can become semiconducting and exhibit a PTCR effect when sintered at 1450°C in nitrogen and subsequently quenched.²³⁶ Unlike the segregation of extrinsic defects introduced from foreign dopant elements accommodating in grains and grain boundaries which change the PTCR profiles directly, changing the sintering parameters can change the PTCR characteristics by introducing intrinsic defects such as oxygen vacancies or cation vacancies. Oxygen from the BaTiO₃ lattice is gradually lost at high sintering temperature resulted in increasing electrical conductivity; however, the oxygen-deficient material rapidly reoxidizes either on reheating at lower temperatures or on cooling slowly in high oxygen partial pressures. Hence applying reducing atmosphere during sintering can facilitate the conductivity of donor-doped BaTiO₃ and enhance the critical donor concentration significantly.^{324,325}

The room-temperature resistivity of donor-doped BaTiO₃ increases with sintering temperature and dwell time which is attributed to an increase in the amount of acceptor-states along grain boundaries.^{326, 327} Kahn³²⁸ and Zubair *et al.*^{329, 330} found that the resistivity of donor-doped BaTiO₃ increases as the rate of cooling is reduced as seen in Figure 1.6.8. The authors claimed that this is due to an increase of the activated surface state density in grain boundaries caused by the oxidation during the cooling cycle. However, LaCourse *et al.*³²³ observed that when quenched the Y-

doped BT from the sintering temperature, the resistivity below T_c was analogous with that of the sample subjected normal cooling rate as $5^\circ\text{C}/\text{min}$ in comparison with the significant lower resistivity exhibited from the sample quenched from 200°C below the sintering temperature. This is due to the immediately solidified liquid phase staying in the grain boundary increases the thickness of insulating grain boundary layer and hence increases the room-temperature resistivity. The heating rate can also have an influence but has a minor impact on the PTCR characteristics.³³¹

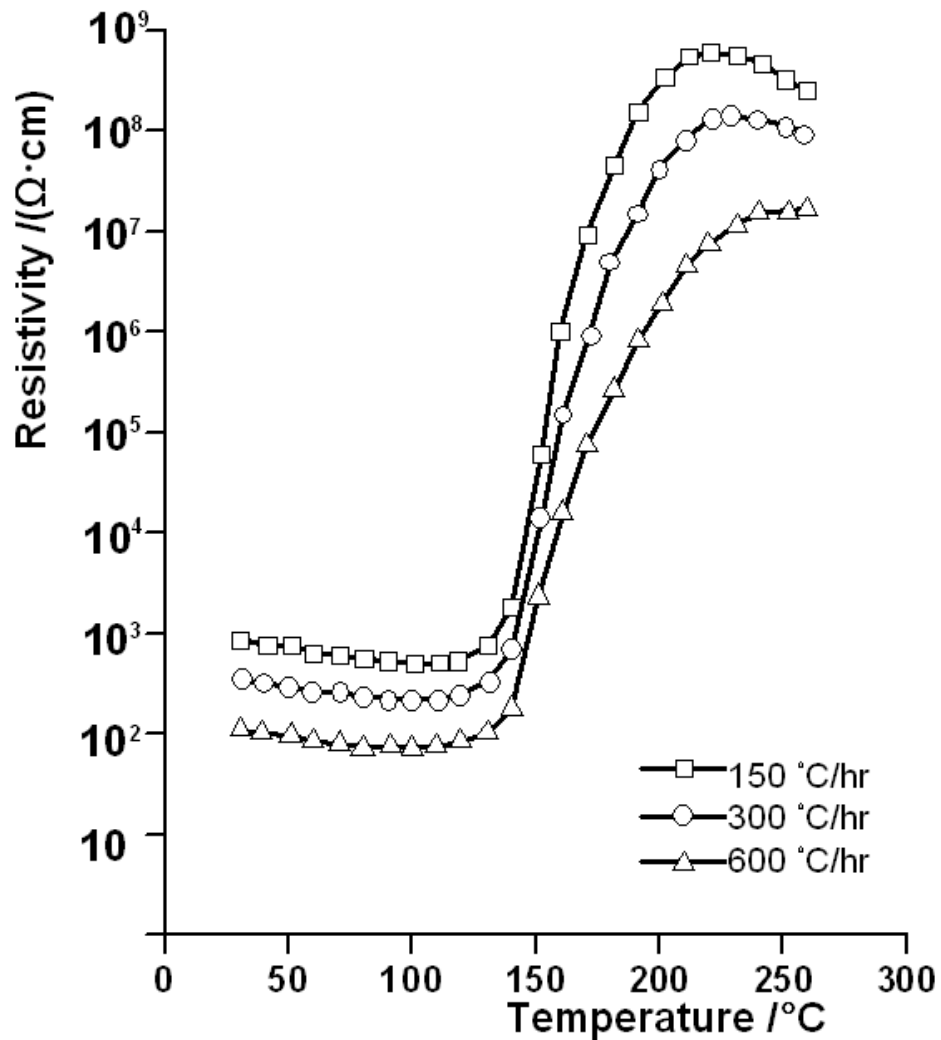


Figure 1.6.8 r/T curves as a function of cooling rate for donor-doped BaTiO_3 samples.

(replotted from ³²⁹)

Liu *et al.*³³² also observed that an improvement of room-temperature conductivity of lightly donor-doped BaTiO₃ can occur when a secondary thermal treatment is used by reheated the sample to 400~650 °C for 20~40 minutes after firing. This results from the relief of internal stress in the crystal lattice through more directional domain alignment thereby reducing the electrical potential barrier. Furthermore, lower room-temperature resistivity of Nb-doped BaTiO₃ is obtained by employing a microwave heating technique compared with ordinary sintering in an electric furnace.³³³ The mechanism of improvement of PTCR characteristics caused by microwave sintering is still under active investigation.

1.6.2.4 Microstructure-PTCR Property Relationships in Donor-doped BaTiO₃

The PTCR behaviour of donor-doped polycrystalline BaTiO₃ ceramics is known to be dependent on microstructural aspects such as grain size, domain orientation, phase profile and porosity. It has been generally observed that the room-temperature resistivities (r_{RT}) are low for donor-doped BaTiO₃ having large grains and the r_{RT} of a doped-BaTiO₃ sample with fine grains is large ($>10^5 \Omega \cdot \text{cm}$).³³⁴ Furthermore, a donor-doped BaTiO₃ sample sintered in a non-reducing environment with very fine grains (less than 1 μm) becomes an insulating material and exhibits no PTCR characteristics. The hypotheses that account for large grains in donor-doped BaTiO₃ facilitating electric conductivity below T_c are:

- i.) As grain boundaries act as insulating layers compared with the internal region of grains, a system with large grains has a lower area fraction of grain boundaries;³³⁵ this suggests that large grain systems contain relatively lower portions of insulating component on the conducting path in the presence of an applied electric field.

- ii.) Based on Daniels' model,³³⁶ the thickness of cation vacancy-rich insulating layers in as-sintered donor-doped BaTiO₃ grains can be up to 3 μm. For BaTiO₃ samples with fine grains, such cation-vacancy layers which act as acceptor-state dominate the electric structures in grains, resulting in overall insulating profile.
- iii.) The high room-temperature resistivity of donor-doped BaTiO₃ with small grains can be also accounted for by the strain effect at grain boundaries. The strain which is caused by interfacial segregation of dopants and formation of cation vacancies at grain boundaries increases the potential barrier and hence increases the resistivity.²⁸⁷ This strain effect becomes more significant for small grain systems and alters its electric properties significantly.
- iv.) The mechanism that causes the electrical insulating behaviour of donor-doped BaTiO₃ with nano-sized grains is more complex. There may be a shift of tetragonal-cubic phase transition temperature due to the size effect. Begg *et al.*³³⁷ reported that when the size of BaTiO₃ particles is below about 190 nm, the cubic rather than the tetragonal phase is thermodynamically preferred at room temperature. Further investigation by Yashima *et al.*³³⁸ confirmed that the T_c of nano-grained BaTiO₃ is suppressed with decreasing particle size and a ferroelectric-paraelectric transition occurs below room temperature leading to disappearance of the PTCR effect above room temperature. Park *et al.*³³⁹ also verified that the crystal phase of the nano-grained BaTiO₃ ceramics is a mixed state of the tetragonal and cubic phases. This may well explain the insulating phenomenon at room temperature for donor-doped BaTiO₃ made by thin-film processing³⁴⁰⁻³⁴² or some sol-gel methods because the BaTiO₃ grains are nano-size.

There is a common observation that the grain size of donor-doped BaTiO₃ decreases rapidly with increasing donor concentration after exceeding the critical concentration and leading to a rapid increase of resistivity. Desu *et al.* believed, based on Auger electron spectroscopy (AES) results, that this phenomenon is due to the impediment of the boundary mobility caused by interfacial segregation of dopants, including donors and acceptors, at the grain boundaries.^{256, 286} As the average donor concentration increases, the excess local concentration of donor at the grain boundary resulting from interfacial segregation would not only retard grain growth but also shift from electronic to ionic compensation, resulting in the formation of highly resistive layers.

Within the same composition, higher PTCR jump is generally achieved in donor-doped BaTiO₃ samples with a heterogeneous grain size distribution and having an optimum porosity, in comparison with materials with large dense grain structures. Kuwabara³⁴³ found that the magnitude of the PTCR jump reaches a maximum at an optimum sintered density ($\approx 75\text{-}85\%$ of theoretical density) and then decreases with increasing density. Those results were partially interpreted that the samples with very dense grain structures, i.e. low porosity indicating containing high level of conducting-grain to conducting-grain contacts, thus have poor PTCR resistivity jump at T_c .³⁴⁴ In addition, the enhancement of the PTCR jump by increase of porosity^{345, 346} from very dense structure may also be due to the assistance for oxygen transport into the ceramic bulk hence facilitating the oxidation of grain boundaries,³⁴⁷ which increases the potential barrier and hence the electrical resistivity. However, it is difficult to specify the optimum combination of the grain size and the porosity of as-sintered donor-doped BT sample in order to satisfy both the need for lowering the

room-temperature resistivity and increasing PTCR jump.

The domain structure within grains of a donor-doped BaTiO₃ can reveal the level of doping. Roseman *et al.*³⁴⁴ claimed that an optimal amount of donor can produce unidirectional domain microstructure and domain randomness is only observed in the near grain boundary regions; nevertheless for under-doped and over-doped cases, the domain orientations and widths are random. This phenomenon is suggested to be associated with the Jahn-Teller effect. The spherically asymmetric defect field of optimally donor-doped BaTiO₃ can be aligned spontaneously by internal stress generated from Jahn-Teller distortion and this type of defect can, therefore, act as nucleation sites for the ferroelectric phase upon cooling through the Curie point. However, for under-doped samples, the distorted defect field does not dominate the domain nucleation sources; in case of over-doped BaTiO₃ samples, the defect compensation mechanism switches to cation vacancy compensation hence the Jahn-Teller distortion no longer exists. As the electron mobility is anisotropic in the tetragonal unit cell in donor-doped BaTiO₃, the aligned domains can facilitate conducting electrons and thus enhance conduction. This can explain why optimal donor-doped BaTiO₃ exhibits the lowest resistivity at room temperature.³⁴⁴

The PTCR properties are strongly controlled by the microstructural aspects of donor-doped BaTiO₃ which is highly sensitive to the cation stoichiometry^{307, 334, 348, 349} and processing parameters.²³¹ Understanding the relationship between microstructure and the PTCR effect and the ways in which microstructure can be changed by chemistry and processing conditions not only help to optimize the performance of PTCR materials but also master potentially the capability for tailoring the PTCR properties

by targetedly adjusting composition and processing parameters.

1.6.2.5 Emerging Trend of Research on BaTiO₃-based PTCR Materials

After half a century's development, the technologies for fabrication of advanced PTCR thermistors have vastly expanded and improved. The requirements for new PTCR sensors are miniaturization, environmental acceptability and optimizing the PTCR effect by reducing r_{\min} , increasing the PTCR jump, decreasing the response time near T_c , increasing T_c and obtaining voltage independence. The single-donor doping system may be inadequate to satisfy all these needs. Multiple-donor systems are considered as potential solutions. Currently double-donor doping systems including $Y_2O_3+Nb_2O_5$ ³⁵⁰ and $Sb_2O_3+Nb_2O_5$ ³⁵¹ have been investigated leading to lower room-temperature resistivity. However, the co-influence of the multiple-donor system still remains poorly understood.

Fabrication of multilayer structures of semiconducting BaTiO₃ ceramics provides another way to decrease the room-temperature resistivity.³⁵² This method has the advantage in substantially reducing the room-temperature resistivity over those that rely on change of composition or heat-treatment parameters because it creates a parallel electric system. However, it is very difficult to co-fire BaTiO₃ having PTCR characteristics with an internal electrode system because the need for an oxidizing atmosphere oxidizes base metal electrodes causing severe deterioration to the ohmic contact with the n-type semiconducting BaTiO₃.³⁵³ On the other hand, if sintered in a reduced atmosphere, the PTCR effect would be substantially compromised.²²³ Therefore, a procedure that prevents oxidation of the internal electrodes without sacrificing the PTCR characteristics during firing is required.

So far, commercially available PTCR thermistors with $T_c > 130^\circ\text{C}$ are mainly based on Pb-doped BaTiO_3 ceramics. Because of the toxicity of lead oxide and detrimental influence on the environment during the preparation of Pb-containing products, considerably effort is devoted to compositional developments of lead-free PTCR ceramics. Recently, an excellent PTCR effect at 170°C has been reported in the La-doped $95\text{BaTiO}_3\text{-}5(\text{Bi}_{0.5}\text{Na}_{0.5})\text{TiO}_3$ (BT-BNT) ceramics.³⁵⁴ Furthermore, without adding any foreign donor dopant, a PTCR effect was found in pure BT-BNT solid solution ceramics with low BNT contents.^{194, 355} The BT-BNT system shows PTCR properties comparable to those of lead-containing BT ceramics. However the noncompetitive PTCR jump and strong sensitivity to the oxygen atmosphere during sintering lag its applications. Research is ongoing to tackle those disadvantages.³⁵⁶⁻³⁵⁸ In addition, similar systems like $\text{BaTiO}_3\text{-}(\text{Bi}_{0.5}\text{K}_{0.5})\text{TiO}_3$ also attract interest.^{359, 360} Other new systems of lead-free, high Curie temperature PTCR ceramics are also in demand.

The PTCR effect in nanograined BaTiO_3 ceramics is not fully realized regardless of composition or processing parameters. This barrier has limited the application of modern nanotechnologies such as using nanoparticles or thin-film fabrication. Recently, a few articles have reported that PTCR characteristics could be found in nanograined BaTiO_3 ceramics synthesized from surface-coated nanopowders.^{339, 361} More work is needed to explore new methods that are able to make very fine grained ($\approx 1\ \mu\text{m}$) BaTiO_3 ceramics exhibiting good PTCR effects which would be a significant step towards creating the next generation miniaturized PTCR devices.

The conventional fabrication methods of PTCR materials are time consuming

especially for making different batches having different dopant concentrations. Hence high-throughput fabrication of PTCR products in applications for both industrial and academic research is desirable. Currently, a freeforming method of making thick-film PTC thermistors by paste extrusion technology combined with laser sintering is reported.³⁶² This technique does not require any high temperature post processing as required for PTC ceramics produced by other methods. This can inspire new applications of PTCR products in rapid-prototyping which has never been reported before. The development of PTCR materials is still very often an empirical (“trial and error”) science. Therefore the high-throughput combinatorial methods are important to speed-up the production of optimized materials. The London University Search Instrument (LUSI) has proved the feasibility of automation for producing and measuring combinatorial libraries of microwave dielectric ceramics including BST⁴⁰ and BCT¹⁰⁵ families. A new study for using such techniques on BaTiO₃-based PTCR ceramics is reported and discussed here.

1.7 Liquid Infiltration in Porous Substrate

Liquid infiltration processing is of great interest for a wide range of applications including soil science,³⁶³⁻³⁶⁶ oil recovery,³⁶⁷⁻³⁶⁹ building materials^{370, 371} and ink-jet printing engineering.³⁷²⁻³⁷⁴ In the engineering ceramics application, using liquid infiltration as a processing method has been applied on the purpose of surface modification and mechanical properties improvement.³⁷⁵⁻³⁷⁸ Therefore, the dynamics of capillary spreading of liquids coupling with their infiltration into the underlying porous substrate has received considerable attention in literature.

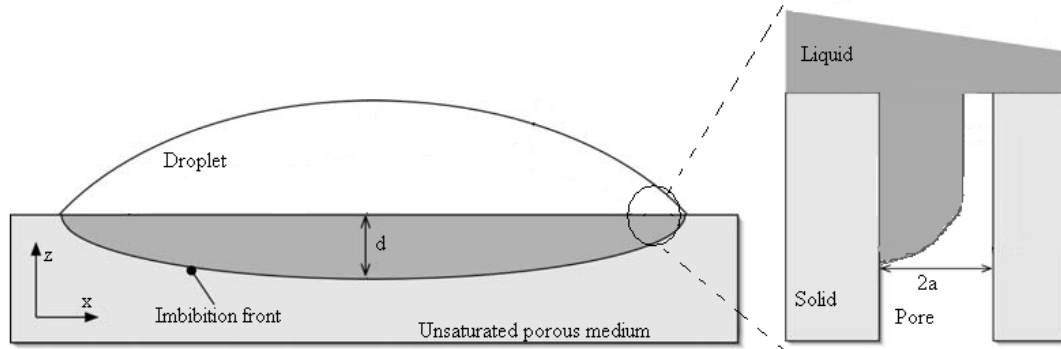


Figure 1.7.1 The flow geometry for a porous medium (reproduced from³⁷⁹)

Figure 1.7.1 shows a droplet infiltrating into a porous substrate which has a simplified cylindrical pore structure. The liquid is assumed with constant density ρ , dynamic viscosity η and surface tension γ . The liquid surface spreading and imbibition processes are determined by the associated surface energy change. Capillary force is the main driving force causes a wetting liquid to flow into the porous medium. From analysis of the wetting of an ideal cylindrical pore of radius a , the capillary pressure is:

$$\Delta P = \frac{2\gamma \cos \theta}{a} \quad \text{Equation 1.7.1}$$

where θ is the contact angle. For a given liquid, it is found that the smaller the pore size and the contact angle, the larger the capillary pressure. In addition, the liquid imbibition into the porous system can be modelled using Washburn's equation:

$$d^2 = \frac{\gamma a t}{2\eta} \quad \text{Equation 1.7.2}$$

where d is the distance of the liquid absorption into the porous substrate and t is the time.

In hydrology and oil recovery field, scientists are more interested in the intrusion and flow of liquid through granular beds. It is generally agreed that some structural features including fractures and crevices within a porous medium can cause the onset of fingering and unstable flows during liquid infiltration. However, even in homogeneous porous system, the liquid displacement proceeding may exhibit a wide range of fluid front morphologies ranging from stable to fingering regime.³⁶⁸ This shows the sensitivity of liquid infiltration front in porous medium to the interactions among driving forces (gravity, capillary and viscous), flow rate and medium properties. The capillary number (C_a) which is a dimensionless ratio of viscous forces to capillary forces at pore level is induced to assess the level of stabilization of fluid displacement front.³⁶⁴

$$C_a = \frac{4\eta v a^2}{\gamma \kappa} \quad \text{Equation 1.7.3}$$

where v is the filtering flux or Darcy velocity in the medium, κ is the permeability of the porous medium. At very low flow rate, the liquid infiltrating into a porous medium with a large capillary number ($>10^{-4}$) performs in a more stable way in terms of the liquid displacement pattern than one with a small value of C_a ($<10^{-6}$) because capillary-driven finger-like flow is less likely to occur.^{380, 381} However, at high flow

rate, viscous forces dominate capillary and gravitational effect. In immiscible two phase flows, e.g. infiltrating water into porous rock sand containing oil, the displacement of water is unstable due to the occurrence of viscous fingering pattern.³⁸² In the opposite case in which the invading fluid is the more viscous one, viscous effects stabilize the front.³⁶⁹ Furthermore, at slow flow rate system, the gravity force can contribute a stabilizing force by reducing the height differences induced by viscous instability or capillary fluctuations hence flattening the wetting front.³⁸³ All the discussion above was based on the modelling of uniform cylindrical pore structure; however, if considered the pore structure effect, the liquid displacement mechanism would be more complicated.³⁸⁴

In ink-jet printing engineering, not only the mechanism of ink imbibition into the underlying porous substrate, but also the simultaneously ink spreading is a fundamental aspect of the study because it determines the resolution of the process. It is generally agreed that the shape of infiltrating droplet on surface can be simplified as a spherical cap, which is considered as starting point for theoretical modelling.³⁸⁵ Starov and co-workers observed that the deposited drop initially spread with the region directly beneath the porous substrate where is immediately saturated. At longer times, the region of saturation extends beyond the edge of the drop and eventually the 'wicking' overpower spreading and causes the droplet to retract.³⁸⁶ They also found that the features of time evolution of the radii of both the drop base and the wetted region on the surface of the porous substrate fell onto universal curves when the spreading of given ink droplet on porous substrates of similar pore size and porosity regardless the materials characters.³⁸⁷

Liquid precursor infiltration and pyrolysis can be useful for processing ceramics and their composites. Lange found that the damage-tolerance of Si_3N_4 sample can be improved when incorporation of second phase by infiltration with Zr-nitrate plus Y-nitrate solution and subsequent pyrolysis.³⁸⁸ In their study, the Si_3N_4 powder compact which was made by pressure-filtering the dispersed aqueous ceramic slurry was immersed in the concentrated Zr-nitrate and Y-nitrate mixed solution. The *in-situ* concentration of incorporated additive was monitored and controlled according to the weight change during the infiltration. They also found that the precursor molecules were enriched near the surface of the powder compact as the precursor solvent was removed during evaporation. However, such heterogeneous distribution of precursor salt can be effectively prevented by gelling prior to drying, *viz.*, by soaking the infiltrated bodies in an aqueous NH_4OH solution.³⁷⁵ Similar attempt was performed by Pratapa *et al.*³⁷⁸ in order to infiltration-process a functionally graded aluminium titanate/zirconia-alumina composite.

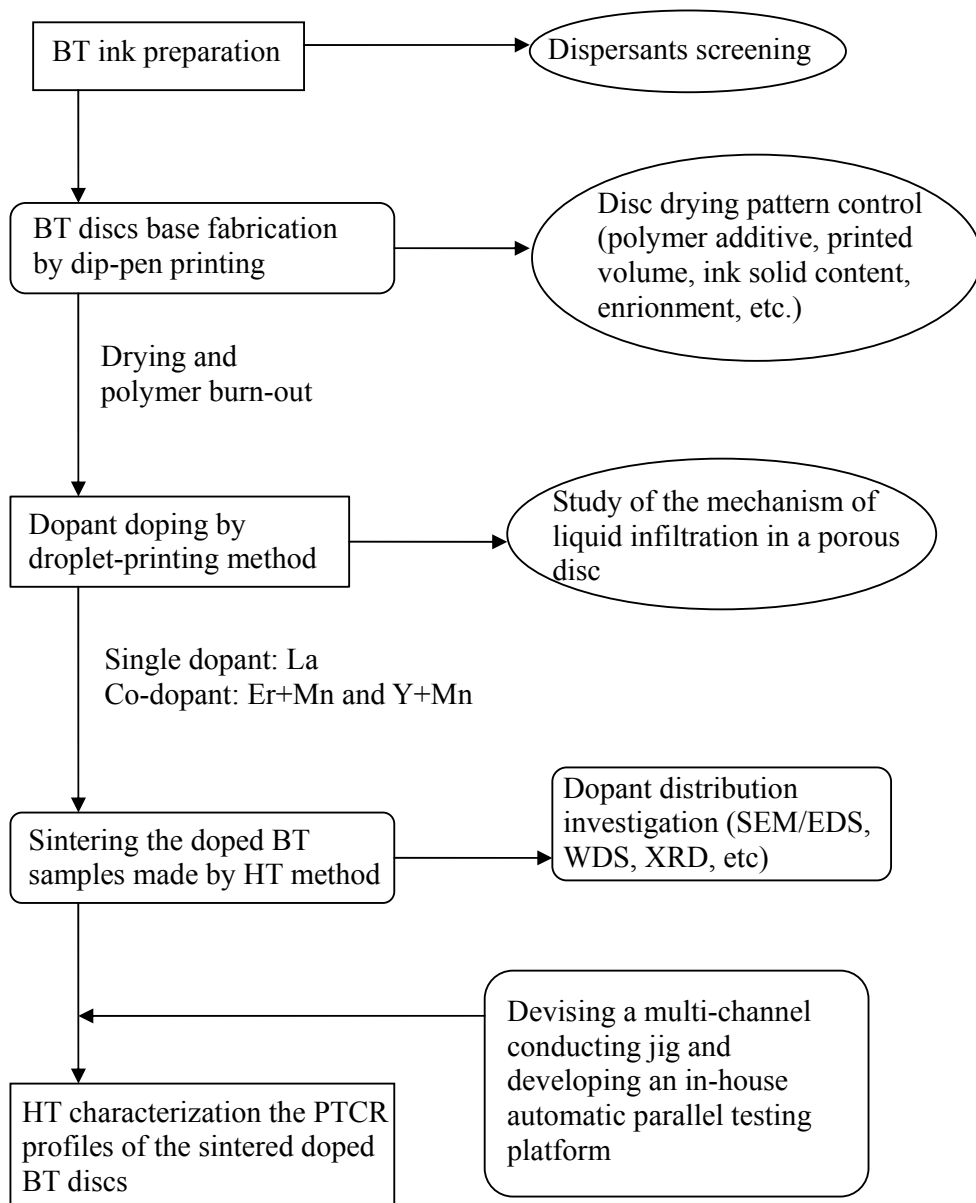
In structural ceramics, the process that allows modifying its external surface plays an important role in improving reliability and performance. There are three major approaches used to modify the surface: solid-state diffusion, ion implantation and liquid infiltration.³⁷⁶ In the liquid infiltration technique, it is possible to intervene earlier in the processing and hence allowing greater control over the depth and composition of the modified surface than that applying the first two techniques. Duh *et al.*³⁷⁶ and Glass *et al.*³⁷⁷ used this infiltration method successfully improve the fracture toughness and thermal stability of ZrO_2 ceramics.

The principle of liquid infiltration in ceramic processing particularly of functional ceramics which is involving low dopant concentration can produce a range of

different dopant levels in ceramics for various functions and properties. This has the potential of significantly increase the speed and efficiency of fabrication of ceramic samples with a broad range of doping concentration in comparison with using conventional ceramic mixing methods. However, there are very few reports on adopting the infiltration technique in functional ceramics processing. The main reasons that block the application of liquid infiltration technique in fabricating ceramics with minor dopant additions might be due to the difficulties in controlling the amount of effective absorption of infiltrant and distributing the precursor solution homogeneously in the body. However, soil researchers have reported that the liquid distribution can be reached uniformly when under the right circumstances, and if the identical individual ceramic green samples as porous substrates can be made, such liquid infiltration method can be used to homogeneously dope porous ceramics. Recently, Darby *et al.*³⁸⁹ successfully produced a calcium-doped yttria stabilised zirconia using an infiltration technique. The resulting dopant distribution showed equivalent homogeneity to the popular ball milling approach for dopant contents below 3 mol.% of Ca²⁺.

2 Experimental Procedures

2.1 Diagrammatic Representation of the Overall Experimental Design



2.2 Preparation of Ceramic Inks

2.2.1 Characterizing Materials

The commercial BaTiO₃ powder with density of 5.85 g·cm⁻³ and purity of 99.95% (provided by the supplier) was supplied by Inframat Advanced Materials, LLC (Farmington, USA) and it was studied by scanning electron microscope (SEM; JEOL, JSM 6300, Tokyo, Japan) as received. To prepare the SEM samples, a small amount of powder was sprayed over one side of a double sided adhesive tape where the other side was attached to an aluminium stub. Vibration and air blowing should be carefully avoided for the purpose of removing loose powders from sample holder because the remaining particle size is selectively left and is not representative of the original powder. The sample powders in the holder were subsequently coated by carbon before SEM studies.

Barium titanate powder was subjected to high energy Dyno-milling (type: KDLA, Glen Creston Ltd., Middx, England) (Figure 2.2.1) and ultra-fine grinding using a Vibro mill (William Boulton, Vibro Energy, Burslem, Stoke-on-trent, England) respectively in order to reduce the size and amount of the aggregates and agglomerates in as-received powder.

A large batch of BaTiO₃ powder was added to distilled water to prepare a suspension. For Dyno-milling, the suspension was slowly pumped using a peristaltic pump (Type 34-505, Glen Creston Ltd., UK) through the rotating Dyno mill chamber where three quarters of the volume was filled with 0.5 mm zirconia grinding media (Y-PSZ, Tosoh Corporation, Tokyo, Japan). The milling processing stopped after the ink

passed thirteen cycles of circulation in the milling chamber which gave a total milling time of ~1 hour.

For the Vibro-milling procedure, the BT suspension was poured into the annular shaped grinding chamber where a vibratory generator was mounted at the base. The chamber was then sealed by a vulcanized rubber gasket underneath the inlet cover and with coil springs mounted around the periphery of the chamber. The Vibro Energy mill employed 10mm cylindrical shaped zirconia grinding media and BaTiO₃ powder was milled for 9 hours. Both of the Dyno milled and Vibro milled BaTiO₃ suspensions were put in an oven in 80 °C for one week and thereafter the dried powders was stored in different plastic bottles.

Various instruments were employed to examine the dried particles of BaTiO₃ powders after Dyno and Vibro milling respectively in order to study and compare the effect of both milling techniques.

- i) The morphologies of the agglomerates in the BaTiO₃ suspensions after Vibro-milling and Dyno-milling processing respectively were examined by SEM. Two specimens of each batch of powder were examined to make sure that the samples were representative. First of all, much diluted inks (< 0.5 g/L) were prepared to ensure the formation of only one layer of dried particles after drying on the sample holder. A few drops of each of those inks which had been subjected to 60 seconds of ultrasonic treatment were placed on different aluminium stubs and the samples were kept desiccated until fully dried before coating by gold for SEM studies.

- ii) The average size and size distributions of powders were analyzed by Zetasizer (Malvern Instruments, Malvern, U.K.). The powder was diluted in distilled water to $< 2\text{g/L}$ and treated ultrasonically before analysis. Each analysis was performed three times.
- iii) The specific surface area of powders including raw BT powder as-received, dried powders after Dyno-milling and Vibro-milling were inspected respectively by a B.E.T. surface area analyzer (model: Micromeritics Gemini 2370, Norcross, Georgia, USA). Samples were first degassed at 200°C for 1 hour. The dried and degassed samples were then analyzed using a five-point nitrogen adsorption method for surface area.

2.2.2 Sedimentation Tests

A variety of dispersants were tested including: EFKA 4540, EFKA 4580, EFKA 5010, EFKA 5071, EFKA 6220, (Ciba Specialty Chemicals, Heerenveen, Netherlands), Dispex A40 (Allied Colloids, Bradford, UK), Solsperse 27000, Solsperse 44000, Solsperse 47000 (Lubrizol, Manchester, England), Darvan 821A (R. T. Vanderbilt Industrial Minerals and Chemicals, Norwalk, Canada). Table 2.2.1 contains the chemical and physical characteristics of dispersants as provided by the suppliers. All those dispersants are water-based.

BaTiO_3 powder after Vibro-milling was prepared for sedimentation tests in order to screen the dispersants. The concentration of BaTiO_3 powder was 0.5 vol.% for every specimen in order to prevent particle-particle interaction during free fall based on the suggestion by Parfitt.³⁹⁰ 3 wt.% of dispersant based on ceramic powder was added in all BaTiO_3 suspensions and the details regarding such sample preparation procedures

are followed below:

- i) The dried BaTiO₃ powder and water were weighed out to obtain 0.5 vol. % of BT suspension in total volume of around 20 mL.
- ii) A high-energy ultrasonic probe (type U-200S-Control, IKA Labortechnik Staufen, Germany) was immersed into the sample suspension just 10 mm above the bottom of the dispersion at 50% of its maximum amplitude and in a continuous mode for 5 minutes.
- iii) The dispersants were weighed and mixed respectively with the previously prepared inks followed by another 5 minutes ultrasonic dispersion with ice surrounding outside the container to prevent heating up.

Those well dispersions were then placed on a roller mixer for 24 hours providing continuous agitation to eliminate bubbles trapped in suspensions before pouring into calibrated glass tubes and left in a tube rack undisturbed for around 300 ks (≈80 hours). Those test tubes were sealed in the upper part to minimize the liquid lost by water evaporation while in the sedimentation test.

After the best candidates were found from the dispersant screening studies, further sedimentation tests were carried out to discover the optimum amount of the dispersant for BaTiO₃ powder.

Table 2.2.1 Chemical and physical characteristics of dispersants

Dispersant	Chemical Composition	Source	Active Ingredient /%	Density $/(g \cdot cm^{-3})$
EFKA 4540	Modified polyacrylate	Ciba	46-48	1.03-1.07
EFKA 4580	Acrylic polymer emulsion	Ciba	39-41	1.03-1.07
EFKA 5010	Acidic polyester polyamide	Ciba	48-52	1-1.04
EFKA 5071	Alkylol ammonium salt	Ciba	51-55	1.08-1.1
EFKA 6220	Fatty acid modified polyester	Ciba	100	1
Dispex A40	Ammonium salt of an acrylic polymer	Ciba	43	1.16
Solsperse 27000	N/A	Lubrizol	100	1.13
Solsperse 47000	N/A	Lubrizol	40	0.9
Solsperse 44000	N/A	Lubrizol	50	1.01
Darvan 821A	Ammonium polyacrylate	R. T. Vanderbilt	40	1.16

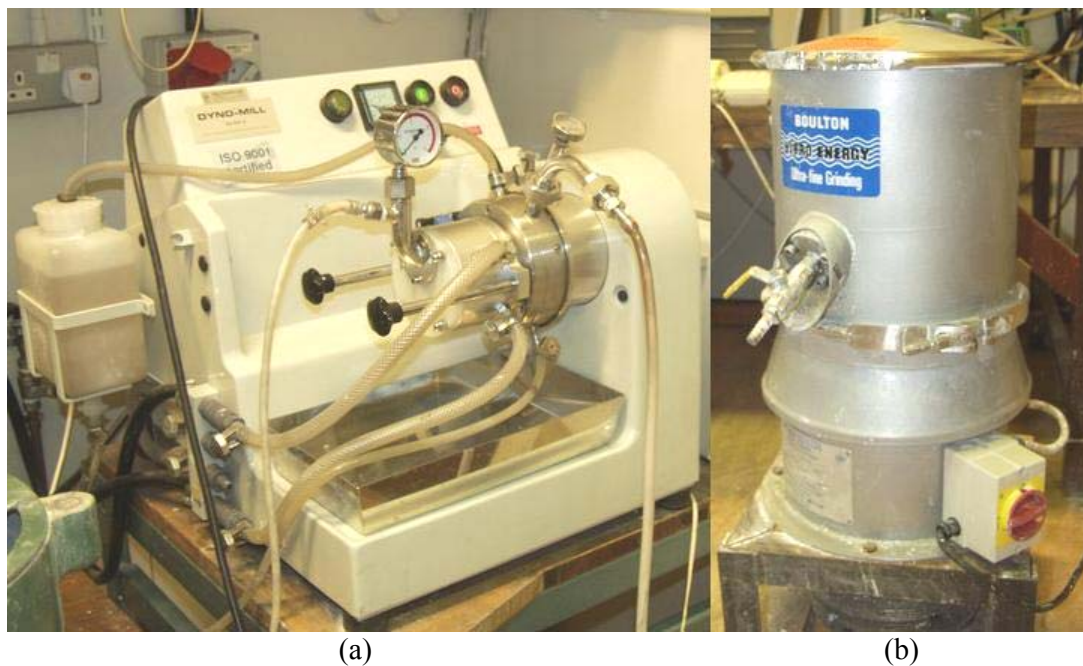


Figure 2.2.1 Milling equipments: (a) Dyno mill and (b) Vibro mill.

2.3 Control of Shape of Droplet Drying Pattern

2.3.1 Drying-induced Forming Agent Selection

Two polymers including polyvinyl alcohol (PVA) ($M_w = 31000$, degree of hydrolysis = 87%) (Fluka, UK) and methyl cellulose (VWR, UK) used as binders were added into $BaTiO_3$ dispersion respectively. Both of them were pre-dissolved in distilled water for subsequent fast mixing. To prepare PVA binder solution, 17.6 g PVA polymer resin was dissolved in 100 mL distilled water at 80 °C in a water bath environment. The mixture which contained 15 wt.% of PVA was then stored in a plastic bottle after cool down by keeping stirring in ambient air. Methyl cellulose (MC) binder solution (4 wt.%) was prepared by mixing the powder with hot water at 85 °C to make a well dispersed system first, then cooled down the solution while stirring and repeated above procedures until the binder fully dissolved in water.

In addition, a thixotropy agent Acrysol RM12W (ROHM and HAAS, UK) was also used to investigate the enhancement of the drying pattern of $BaTiO_3$ inks. All those above polymers' chemical and physical characteristics are listed in Table 2.3.1 as provided by their suppliers.

$BaTiO_3$ slurries with varying forming agents in different compositions as shown in Table 2.3.2 were prepared in a multi-steps processing:

- i) Added an appropriate amount of $BaTiO_3$ (40 wt.%) to distilled water following an ultrasonic actuation for 5 minutes using an ultrasonic probe.
- ii) The dispersant (Darvan 821A) (3 wt.% in the weight of $BaTiO_3$ powder) and an appropriate amount of forming agent solution (following the composition

suggestion in Table 2.3.2) were subsequently added to the as-mixed BT suspension. The overall dispersion was subjected to another 5 minutes' ultrasonic treatment to ensure the well mixture.

- iii) Well-mixed BaTiO₃ dispersion was stored in a capped glass bottle and placed on a rolling table for 48 hours to stabilize the dispersion and remove the trapped air bubbles.

Droplets of the BaTiO₃ inks as described in Table 2.3.2 were deposited respectively in the volume of 30 μL using a digital transfer pipette (Transferpette Brand, Wertheim, Germany) on silicone release paper (Grade SPT50/11, Cotek Papers Ltd., Glos., UK) to which they were non-adherent. All drying experiments were carried out in an ambient environment (298 K and 30-50% RH). The morphologies of the as-dried green samples were visually examined by binocular microscopy.

Various volumes of droplets of the BaTiO₃ dispersion with PVA and Acrysol RM12W as detailed in Table 2.3.3 were printed and the morphologies of their drying residues were examined by the same procedures described above. Furthermore, the drying patterns of BaTiO₃ inks contained Acrysol RM12W with different solid contents from the evaporation of a dip-pen printing droplet with a volume of 100 μL were also investigated (listed in Table 2.3.4). The drying procedure for the last series (inks in Table 2.3.4) was carried out in a covered container with saturated moisture at room temperature.

Table 2.3.1 Chemical and physical characteristics of forming agents

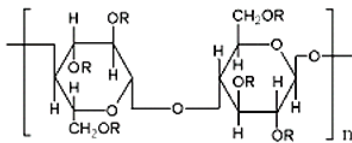
Name	Chemical Composition	Source	Active ingredient /%	Density /($\text{g}\cdot\text{cm}^{-3}$)
PVA	$\text{R} \left[\begin{array}{c} \text{CH}_2 - \text{CH} \\ \\ \text{O} \\ \\ \text{COCH}_3 \end{array} \right]_n \left[\begin{array}{c} \text{CH} - \text{CH}_2 \\ \\ \text{O} \\ \\ \text{COCH}_3 \end{array} \right]_n \text{R}$	Fluka	100	1.27
Methyl Cellulose		VWR	100	1.26-1.30
Acrysol RM12W		Rohm	19	1.04

Table 2.3.2 Composition of BaTiO₃ inks used for forming agent selection.

Ink No.	BT Powder /vol.% (wt.%)	Dispersant /vol.% (wt.%)	Forming Agent /vol.% (wt.%)			Distilled Water /vol.% (wt.%)
			I ^a	II ^b	III ^c	
1	10 (40)	1.2 (1.2)	1.0 (0.8)			87.8 (58)
2	10 (40)	1.2 (1.2)	2.0 (1.7)			86.8 (57.1)
3	10 (40)	1.2 (1.2)	3.0 (2.5)			85.8 (56.3)
4	10 (40)	1.2 (1.2)	4.0 (3.4)			84.8 (55.4)
5	10 (40)	1.2 (1.2)		1.0 (0.8)		87.8 (58)
6	10 (40)	1.2 (1.2)		1.5 (1.2)		87.3 (57.6)
7	10 (40)	1.2 (1.2)			1.0 (0.8)	87.8 (58)
8	10 (40)	1.2 (1.2)			1.5 (1.2)	87.3 (57.6)
9	10 (40)	1.2 (1.2)			2.0 (1.6)	86.8 (57.2)

^a PVA

^b Methyl Cellulose

^c Acrysol RM12W

Table 2.3.3 Inks for investigation on drying pattern effects of changing volumes.

Ink No.	Ink Volume / μ L	BT Powder /vol.% (wt.%)	Dispersant /vol.% (wt.%)	Forming Agent /vol.% (wt.%)		Distilled Water /vol.% (wt.%)
				I ^a	II ^b	
10	50	10 (40)	1.2 (1.2)	1.0 (0.8)		87.8 (58)
11	100	10 (40)	1.2 (1.2)	1.0 (0.8)		87.8 (58)
12	200	10 (40)	1.2 (1.2)	1.0 (0.8)		87.8 (58)
13	50	10 (40)	1.2 (1.2)		1.5 (1.2)	87.3 (57.6)
14	100	10 (40)	1.2 (1.2)		1.5 (1.2)	87.3 (57.6)
15	200	10 (40)	1.2 (1.2)		1.5 (1.2)	87.3 (57.6)

^a PVA

^b Acrysol RM12W

Table 2.3.4 Inks for investigation on drying pattern effects of varying solid contents.

Ink No.	Ink Volume / μ L	BT Powder /vol.% (wt.%)	Dispersant /vol.% (wt.%)	Acrysol RM12W /vol.% (wt.%)	Distilled Water /vol.% (wt.%)
16	100	12.1 (45)	1.4 (1.4)	2.0 (1.6)	84.5 (52)
17	100	14.5 (50)	1.7 (1.5)	2.4 (1.8)	81.4 (46.7)
18	100	17.2 (55)	2.0 (1.7)	2.9 (1.9)	77.9 (41.4)
19	100	20.4 (60)	2.4 (1.8)	3.4 (2.1)	73.8 (36.1)

2.3.2 Characterization of Green BaTiO₃ Disc after Polymer-burnout

The bulk density of as-dried BaTiO₃ disc after polymer burnout by heating at 600 °C for 2 hours was measured by buoyancy method based on Archimedes' principle.³⁹¹

The green BaTiO₃ sample is a porous and fragile material, thus its outer surface was coated with a thin layer of water-resistance wax before measuring its density by buoyancy method in order to prevent it absorbing water. The details of procedures are listed below:

- i) Green dry ceramic sample was first weighed in air (W_1).
- ii) Sample then was covered by a thin paraffin wax coating and weighted again in air (W_2).
- iii) Sample after coating with a thin wax layer was then weighed while fully submerged in water (W_3).

Therefore, the bulk density of the BT disc is determined by the following expression:

$$\rho_s = \frac{W_1}{\frac{W_2 - W_3}{\rho_w} - \frac{W_2 - W_1}{\rho_{wax}}} \quad \text{Equation 2.3.1}$$

where ρ_s is the density of the sample, ρ_w is the density of water, ρ_{wax} is the density of paraffin wax.

The percentage porosity of green BaTiO_3 sample is then found using the following expression:

$$P = \frac{\rho_{th} - \rho_s}{\rho_{th}} \times 100\% \quad \text{Equation 2.3.2}$$

where P is the percentage porosity of the sample and ρ_{th} equal to $6020 \text{ kg}\cdot\text{m}^{-3}$ is the theoretical density of the BaTiO_3 .

In order to obtain the density results and accurate information about the pore profile within the green BaTiO_3 base body, gas pycnometry (Micromeritics AccuPyc 1330 Pycnometer, Norcross, USA) and mercury porosimetry (Micromeritics AutoPore IV, Norcross, USA) methods were also used.

2.4 Investigation of Dopant Distribution in Porous BT Base via a Droplet-doping Method

The group of rare-earth elements is a rich resource for providing donor dopants for BT-based PTCR materials. Among them, Erbium is the only element as a donor candidate that can hold the PTC effect of doped-BT sintered in air in a range up to 8 mol.% in the literature.²⁶⁵ Moreover, in order to investigate the dopant distribution by using EDS/WDS techniques for samples under low doping level, considering the characteristic X-ray energy and associated wavelength of erbium (L α : 6.95 keV and 0.18 nm) along with other elements in the lanthanum (L α : 4.65 keV and 0.27 nm) group is close to that of Ba (L α : 4.47 keV and 0.28 nm) and Ti (K α : 4.51 keV and 0.27 nm) as base elements resulting in the difficulty of quantitative analysis of dopant element especially a trace amount; however, yttrium (K α : 14.93 keV and 0.08 nm)³⁹² which is also a widely used donor element has better distinguishable X-ray energy and associated wavelength compared with that of base elements such as Ba and Ti. Hence Er-doped BT and Y-doped BT were selected for investigation of donor distribution via droplet-doping method.

2.4.1 Preparation and Characterization of Er-doped BT Using a Droplet Infiltrating Doping Method

Droplet-doping was performed by infiltrating the dopant precursor solution into the green BaTiO₃ porous base disc. To achieve the homogeneous dopant distribution in the body of BT disc, the volume of the infiltrating solution must equal to the total pore volume in the disc. For example, to apply droplet-doping for a BT disc with the volume of $\approx 3.3 \times 10^{-8} \text{ m}^3$ (with radius as $4 \times 10^{-3} \text{ m}$ and thickness as $6.5 \times 10^{-4} \text{ m}$) with

55% porosity, the ideal infiltrating volume of dopant solution should be $\approx 18 \mu\text{L}$.

$\text{Er}(\text{NO}_3)_3 \cdot 5\text{H}_2\text{O}$ (99% purity, Sigma-Aldrich) was weighed and dissolved into deionised water to prepare solutions at various concentrations according to the required doping level. In preliminary work, different amount of dopant solution with corresponding concentration was printed using a digital transfer pipette on the surface of the green BaTiO_3 porous base. For example, to incorporate 8 mol.% Er into a BT disc with the volume of $3.3 \times 10^{-8} \text{ m}^3$, the weight of 90 mg and 55% porosity, the concentration of erbium nitrate solution should be prepared as 1.72 M/L to reach the planned doping concentration (8 mol.%) by printing the ‘ideal’ $18 \mu\text{L}$ solution on the base. For lower level of doping, the dopant solution was diluted accordingly.

Erbium doped BT discs with various doping concentrations as detailed in Table 2.4.1 were fabricated by this droplet-doping method. The green BT base was dried from a $100 \mu\text{L}$ sessile droplet of ink 18 by dip-pen printing method as described in section 2.3. The erbium nitrate solution was printed on the central-top surface as illustrated in Figure 2.4.1(a). As-doped samples with various doping levels were dried in an ambient atmosphere (298 K and 30-50% RH) before sintering in air under different firing programmes with heating/cooling rate as $5 \text{ }^\circ\text{C}/\text{min}$ (in Table 2.4.1). Samples with the erbium concentration of 0.1 mol%, 1 mol% and 8 mol% were examined respectively by simultaneous thermal analyzer (STA) (model: PL-STA1500, Rheometric Scientific Inc, NJ, United States). Among them, samples with erbium content of 0.1 mol.% and 8 mol.% were heated up to 1100°C by a rate of $10^\circ\text{C}/\text{min}$ and dwelled for 1 h. Sample contained 1 mol.% erbium was heated up to 1150°C by $5^\circ\text{C}/\text{min}$ and dwelled for 1 h. All STA measurements were carried out in air. The

morphologies of as-sintered Er-doped BT tablets were examined and photographed by a digital camera (Fuji S5600). The microstructures of the fracture surface of as-sintered Er-doped BT ceramics were examined using SEM.

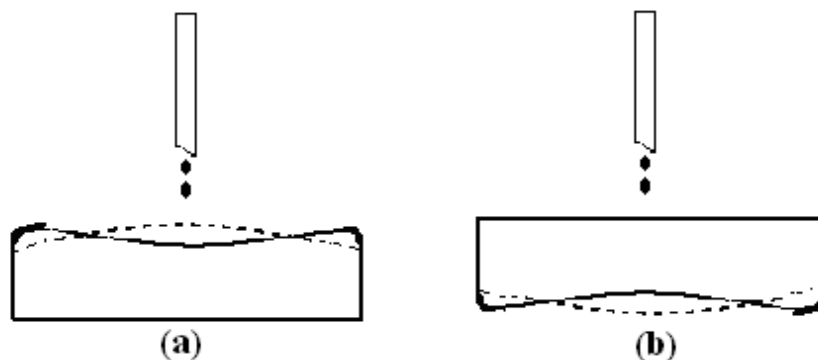


Figure 2.4.1 Schematic diagram of printing the dopant precursor ink on the surface of green BT disc base: solution was printed by (a) a single drop on the central-top surface of the disc; (b) multi-drops evenly on the bottom flat surface of the base.

Table 2.4.1 Sintering program of erbium-doped BT.

Sample No.	Erbium concentration / mol %	Sintering temperature / °C	Dwelling period / h
A0	0	1350	2
A1	0.10	1350	2
A2	0.25	1350	2
A3	0.5	1350	2
A4	1	1350	2
A5	2	1350	2
A6	5	1350	2
A7	8	1350	2
B0	0	1350	4
B1	5	1350	4
C0	0	1450	4
C1	5	1450	4
D0	0	1500	4
D1	5	1500	4

2.4.2 Investigation of Erbium Distribution

Energy dispersive spectroscopy (EDS; Oxford Instruments, UK) was used to analyze the elemental composition of samples after coating the examining surface by carbon. For EDS measurements, cobalt was used as a standard for calibration of the analyzer. Acceleration voltage was chosen as 20 kV. The working distance was adjusted as 10mm and all data were corrected using INCA software (Oxford Instruments). For EDS analyses of as-sintered Er-doped BT, the upper and lower surface of the disc and the cross section of the fracture surface were examined separately. Five measurements were taken on the upper and lower surface and each measurement covered an area approximately $300 \mu\text{m} \times 300 \mu\text{m}$. 12 measurements were taken throughout the cross section and each covered an area approximately $80 \mu\text{m} \times 80 \mu\text{m}$ (seen in Figure 2.4.2). Furthermore, the cross-section of the as-sintered disc was mechanically polished to a $1 \mu\text{m}$ diamond finish before EDS line-scan and area mapping. In addition, an as-dried Er-doped BT sample (T1) at 20 mol.% erbium content was examined by EDS area mapping for comparison.

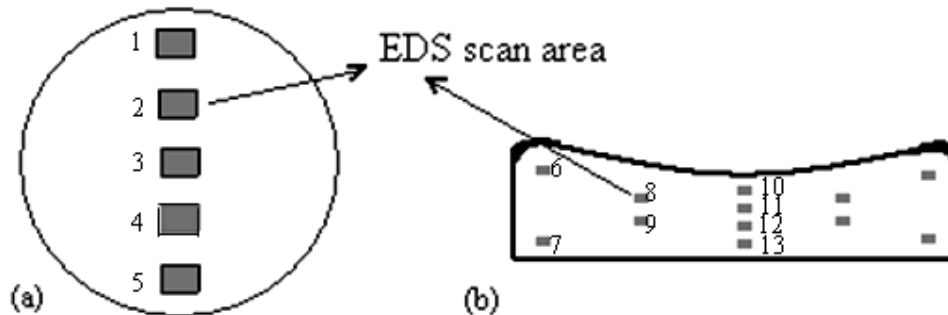


Figure 2.4.2 Schematic positions for EDS analyses of as-sintered Er-doped BT: (a) upper and lower surfaces; (b) cross section.

2.4.3 Investigation of Yttrium Distribution in Y-doped BT via Droplet-doping Method

For Y-doped BT disc, the green BT base was produced by dip-pen printing of 20 μL of concentrated suspension with 50 wt.% using synthesized BT powder. $\text{Y}(\text{NO}_3)_3 \cdot 6\text{H}_2\text{O}$ (99% purity, Sigma-Aldrich) was used to prepare the yttrium dopant solution as detailed in section 2.4.1. Only 0.5 and 1 mol.% Y-doped BT samples were prepared respectively via droplet-doping method by printing the corresponding solution on the bottom flat surface of BT base as illustrated in Figure 2.4.1(b). The as-doped samples were dried first in ambient atmosphere overnight then in a desiccator for two days. The 0.5 mol.% Y-doped discs were rapidly heated to convert the nitrate donor salts to oxide before sintered at 1380 $^\circ\text{C}$ for 1 hour in N_2 flow with a sintering/cooling rate as 5 $^\circ\text{C}/\text{min}$.

The microstructure of as-doped discs with 1 mol.% Y^{3+} content prior to sintering was investigated by SEM (FEI, InspectF, Hillsboro, OR, USA) by surveying their fracture surfaces. The microstructures of as-doped samples after rapidly and slowly pyrolyzed respectively to decompose the nitrate salt to oxide were also compared. The yttrium ion distribution in the as-sintered 0.5 mol.% Y-doped BT was examined by wavelength dispersive spectroscopy (WDS; Oxford Instruments, UK). The cross-section of the dense disc was mechanically polished to a 1 μm diamond finish before subjected to WDS scan. In addition, the droplet-doping volume effect on dopant distribution across the porous body was investigated by WDS. For WDS measurements, cobalt was used as a standard for calibration of the analyzer. The accelerating voltage was set as 20 kV. The slit size for element Ba, Ti and O was 2.5 mm with slit position as 0; while it was 0.63 mm for element Y with slit position as

15. Elements Ba, Ti and O were calibrated using a BaTiO₃ standard compound (Micro-analysis Consultants Ltd, Cambridgeshire, U.K.) before the WDS measurements while element Y was calibrated using a Y₂O₃ standard compound (Micro-analysis Consultants Ltd, Cambridgeshire, U.K.). All data were corrected using INCA software using these calibrations.

The contact angle of water on sintered barium titanate was measured using the goniometer method of Holman *et. al.*³⁷² The as-sintered undoped BT disc was mechanically polished on one side to a 1 µm diamond finish. The polished side was then washed by deionised water and acetone separately. The processed disc was subsequently heated to 600 °C for 2 hours to remove any organic residue that might be carried over from the solvent wash. The contact angle measurement was performed optically using a digital CCD camera (model: STC-C83USB, Sentech, Texas, USA). A 3 µL droplet was deposited onto the surface of the polished side of BT disc using a micropipette. The contact angle was measured on each side of the droplet using MB-Ruler (Freeware, <http://www.markus-bader.de/MB-Ruler/>) and the two numbers were averaged. The results from three different droplets on a disc on a total of three discs were then averaged. The droplet spreading and imbibition on the green porous BT base was investigated by printing a single drop of water with a volume of around 3.6 µL on the flat surface of a BT base. A high-speed video camera (Kodak Z981) was used to capture the resultant images.

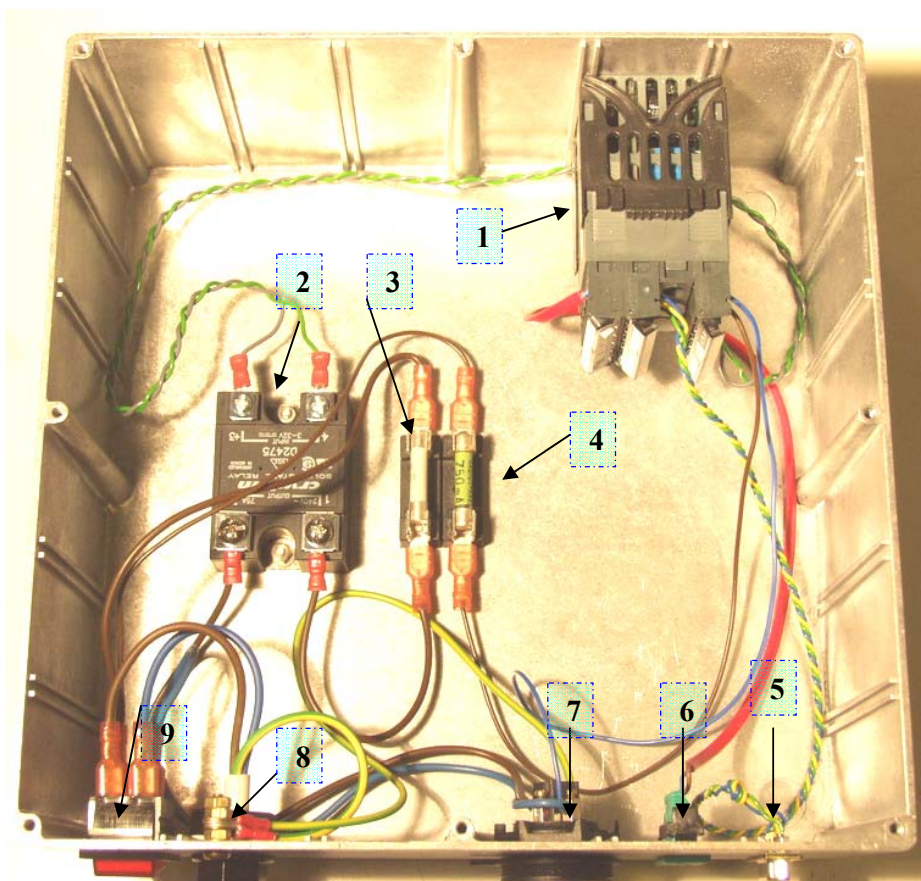
2.5 Heating Control Unit Construction and Furnace Calibration

2.5.1. Temperature Control Unit

A modified furnace (Type: HRF 7/22, Carbolite, Sheffield, England) (in Figure 2.5.1) for which the original temperature control module had been disengaged was used. A new furnace temperature control unit was assembled and photographed in Figure 2.5.2. The temperature control box consists a temperature controller (model 3216, Eurotherm, Eurotherm ltd, UK), a solid state relay (SSR) (model D2475, Crydom, Crydom International ltd, UK) with two fast reaction fuses (Ferraz Shawmut, RS, UK). All components were enclosed in an aluminium box (25cm×25cm×10cm). A RS232 communication module was added to create a connection between this control unit with a computer. A K-type thermocouple with ceramic sheath (model 409-016, TC direct, UK) was used as a control thermocouple with its “hot junction” placed in the central position in furnace chamber.



Figure 2.5.1 The Carbolite furnace



1 Temperature controller (Eurotherm)	6 Thermocouple connector
2 Solid state relay (SSR)	7 Power input
3 Fast reaction fuse (20 A)	8 Power output
4 Fast reaction fuse (750 mA)	9 Power switch
5 RS 232 connector (DB9)	

Figure 2.5.2 The temperature control box.

2.5.2. Virtual Control Interface

A real-time temperature control system was required to satisfy the need for controlling a heat treatment process which contained more than 50 heating segments within a single run. This exceeded the capacity of the self-defined programmer built in most of the existing products in the low-cost temperature controller range.

Figure 2.5.3 and Figure 2.5.4 show the flow chart and core modules of the virtual temperature control operation system respectively. The system was implemented on LabVIEW (Version 7.1, Laboratory Virtual Instrument Engineering Workbench) platform which can use a graphic programming protocol to create an interface between user and machine. The programme contains two phases:

1. The Front Panel which is used for operations and to specify the inputs (controls) and outputs (indicators) of the program.
2. The Block Diagram which defines the actual data flow between the inputs and outputs. It is the actual executable program which is constructed in G (graphical) language.

It is better to construct functional modules as the forms of subVI in LabVIEW program to improve the running efficiency, clear the structure layout and allow easy updating facilities. Furthermore, each subVI can be encapsulated with a well-defined interface. A few subVI were created in terms of different sub-functional modules (seen appendix B).

The temperature control interface consists of two tab sheets including the communication setup page and the temperature control panel respectively. The network between the temperature controller and a computer is created by setting up appropriate communication parameters (as seen in Figure 2.5.5(a)). The digital communication of the temperature controller (Eurotherm 3216) uses the Industry Standard Modbus RTU protocol based on the RS232 standards provided by the supplier. Modbus is an application layer messaging protocol for client/server communication between devices connected on a network. Every operated function in a device (client) that is intended to be communicated with the user (server) by using

Modbus protocol is given a unique address so-called Modbus address. Hence information can be passed between master and slave devices by reading and writing to those addresses registered on the slave devices. Some important Modbus addresses for the temperature controller (Eurotherm 3216) used here are listed in Table 2.5.1 provided by its supplier.

The main temperature control interface is shown in Figure 2.5.5(b). Two rockers were used as switches to activate alarm and heating processes. A toggle-switch was used to select the manual/program mode of the heating process. When manual mode is selected, an individual setpoint can be input in the box below the ‘mode select’ switch with the dwell timer changed by the pointer slide on the left of the window. If program mode is selected, applying setpoint which is determined by the preset heating program will be loaded and display in the thermometer indicator on the right of the panel. When heating is active, a real-time curve of the temperature as a function of time is recorded and displayed in the chart in the centre of the panel and the corresponding data can be acquired and saved as a file in text document format by pressing the “Record graph” button. In addition, the readings of CJC (cold junction compensation) temperature and furnace live temperature measured by the controlled thermocouple can be shown synchronously in the boxes above the chart. Meanwhile, a column indicator beside the chart can illustrate the output utilization rate of the heating capacity. Moreover, a key lock switch is introduced to freeze the operational buttons on the temperature controller in order to prevent changing parameters by incorrect entries particularly while a heating program in progress. The heating process can be manually terminated by pressing the “STOP” button on the top-left of window and the light beside the “STOP” button will turn red as long as the

heating program is stopped.

The overall and partially magnified block diagrams of the temperature control system are shown in Figure 2.5.6. The communication and file creation modules are presented in Figure 2.5.6(b). Figure 2.5.6(c) shows the rest of the modules including PID control, keylock, furnace alarm, data input and output, error report, data displaying and store.

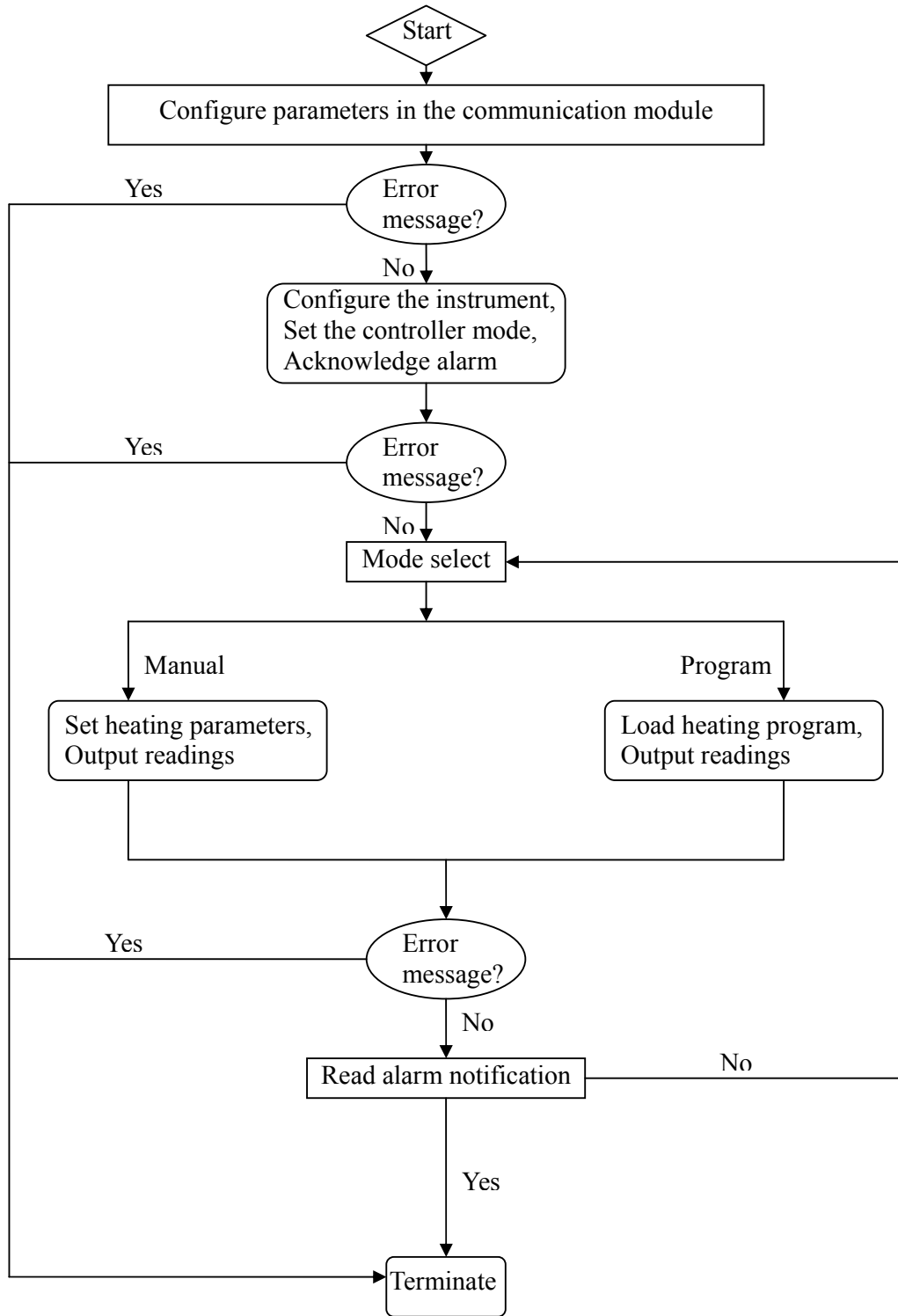


Figure 2.5.3 Flow chart of the operational temperature control and monitor system.

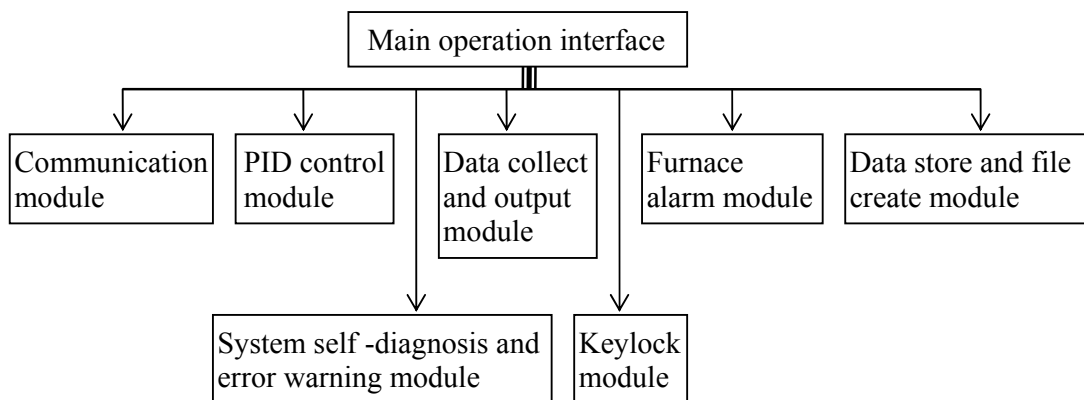


Figure 2.5.4 Modules of temperature control system.

Table 2.5.1. Modbus addresses for Eurotherm 3216*

Number	Parameter Name	Modbus Address
1	Working output	4
2	Setpoint low limit	11
3	Setpoint high limit	12
4	Setpoint 1	24
5	Home display (standard temperature and setpoint display)	106
6	Instrument mode	199
7	CJC temperature	215
8	Alarm status	260
9	Set controller mode	273
10	Acknowledge alarm	274
11	Heat control type	512
12	Allow instrument to be locked via a key input	1104
13	Ramp rate	1282
14	Dwell duration	1280
15	Input sensor type	12290

* provides by supplier

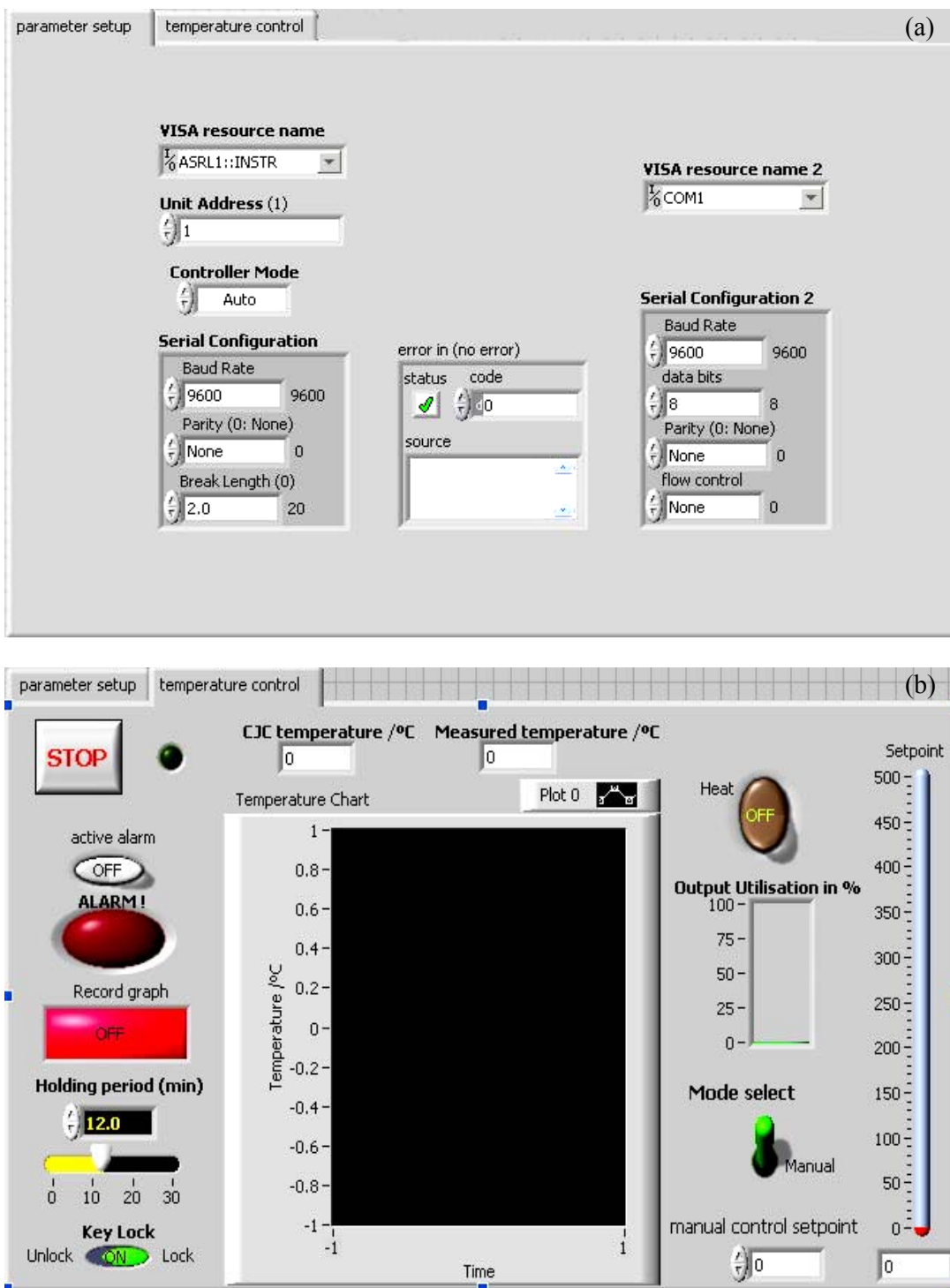


Figure 2.5.5 A screenshot of the user interface of the temperature control program: (a) the communication setup page and (b) the temperature control page.

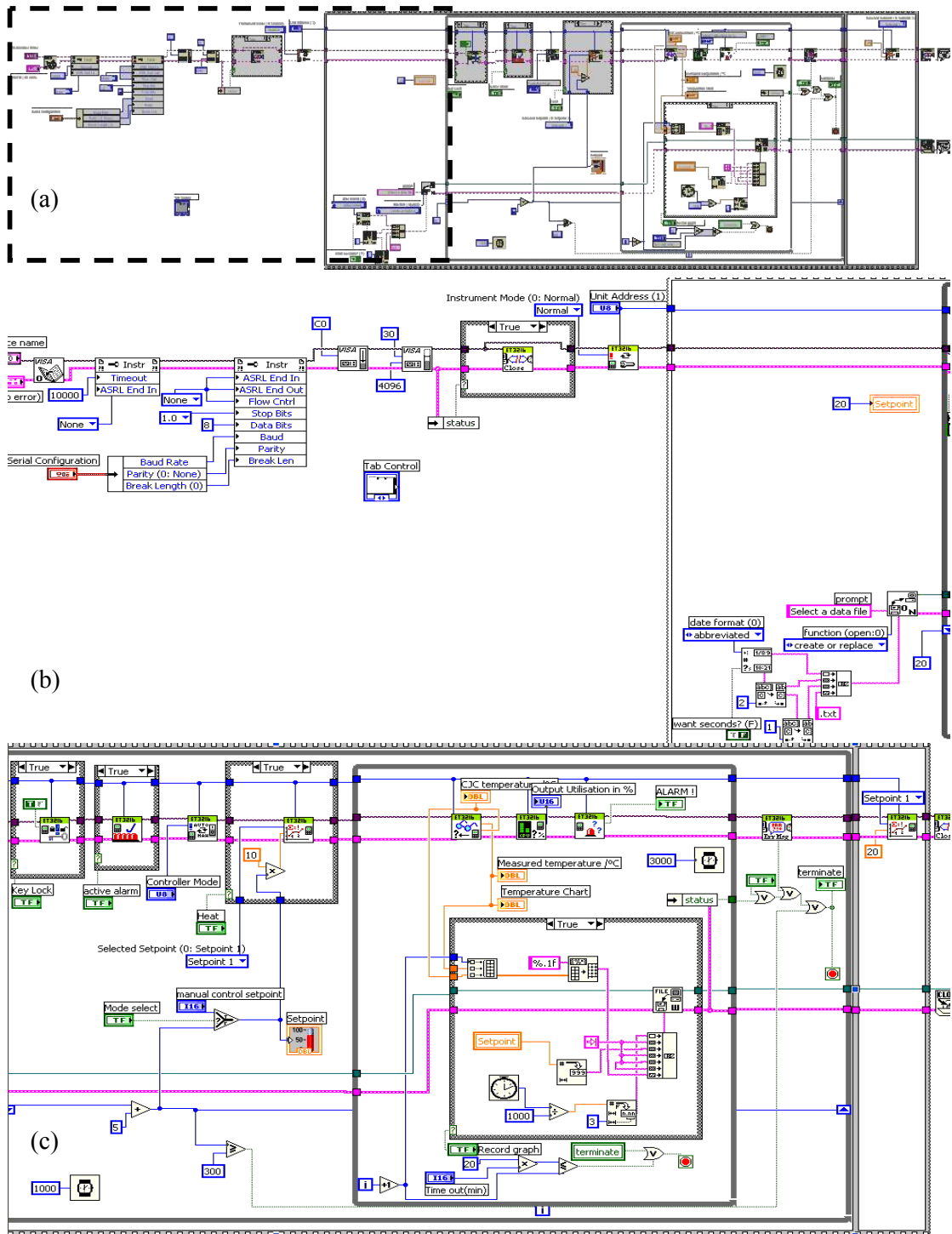


Figure 2.5.6 Block Diagram of program of the temperature control system: (a) overall structure; (b) magnified area in dashed square in (a); (c) the rest of the structure in (a).

2.5.3 Furnace Calibration

The heat treatment furnace is a non-linear, pure-delay system with great inertia, which makes its temperature hard to control. However, the heating process here requires the furnace temperature to rise rapidly and then hold to a specific temperature steadily and accurately. Therefore, the furnace heating parameters need to be calibrated; the actual furnace temperature need to be tracked and compared with the setpoint; as well as the temperature uniformity in both the sample's body and in the furnace need to be investigated. In addition, there are three goals to be achieved:

1. Temperature in furnace should be precisely controlled and monitored.
2. Temperature should not severely fluctuate when it reaches the target setpoint.
3. Period of "heat-up and hold" should be minimized to increase the efficiency of subsequent electrical measurements in a range of temperature.

The temperatures in the heating furnace applying a preloaded heating programme were measured as a function of time. The modified furnace was subjected to tuning at 100 and 200 °C respectively and its heating profiles before/after tuning were recorded and compared. Effects of different ramp rate (1 °C/min or no preset rate) on the heating profile of the furnace were investigated. A dense disc-like barium titanate sample was placed on an alumina substrate and positioned in the central bottom surface in the furnace and a second K-type thermocouple with glass fibre insulation (model KA02, TME, UK) was introduced to measure the surface temperature of the BT sample while furnace heating. The surface temperature readings were obtained via a temperature-to-voltage (T/V) converter (model 80T-150U, Fluke, UK) and a bench-type multimeter (model 1705, TTI, UK) used as a thermocouple indicator for

which the tip of the thermocouple was firmly in contact with the BT disc's top surface (as seen in Figure 2.5.7). Furthermore, the heating profiles of the sample's surface while furnace heating at different ramp rates were measured and compared with those of the furnace. In addition, the temperature gradients between the furnace and the surface of the sample across the heating range of 20 to 250 °C were also investigated.

Before the furnace calibration, both of the thermocouples and their V/T converters were cross-examined by measuring the temperature in a water bath which the reference temperature was measured by a mercury thermometer.

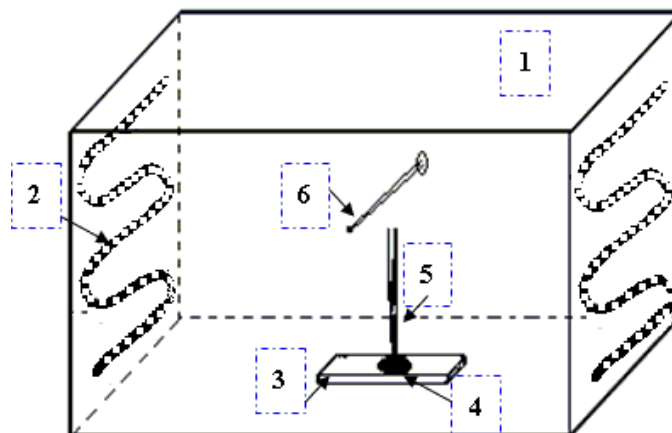


Figure 2.5.7 Schematic diagram of the furnace showing: (1) furnace chamber, (2) heating elements, (3) substrate base, (4) sample, (5) thermocouple and (6) control thermocouple.

2.6 Devising the Arrayed Testing Platform and the Auto-operational System

2.6.1 Device for an Arrayed Testing Kit

The initial objectives in this work were to construct a multi-channel circuit platform to accommodate the array of donor-doped BT samples and to measure electrical performance simultaneously and automatically of the sample array.

A multi-channel measurement jig with a capacity of 16 samples for arrayed testing was designed and assembled for high throughput resistance-temperature measurement. The jig is mainly made of stainless steel as shown in Figure 2.6.1. Electroded samples were mounted between the base plate and copper heads and uniaxial loads were then applied on each sample tablet by the combined forces of gravity of copper heads and stainless steel springs. In order to avoid the short circuit across these parallel circuits during the testing, ceramic tubes were introduced between the copper wires and the stainless steel tubes which provided insulation layers. This arrayed platform was designed to be part of the complete high-throughput parallel testing system as seen in Figure 2.6.2(b). A switch (16-channel relay card, model: PCI2307, Aitai, China) was built in the system by connecting with all parallel circuits. A small DC voltage was applied in the circuit from a triple output power supply (ISO-Tech IPS2250, RS Component Ltd, Northants, UK). The resistances of doped-BT tablets were measured by a digital multimeter (Model 1705, TTI, Huntingdon, England) via voltammetry method as the equivalent circuit diagram is illustrated in Figure 2.6.2(a).

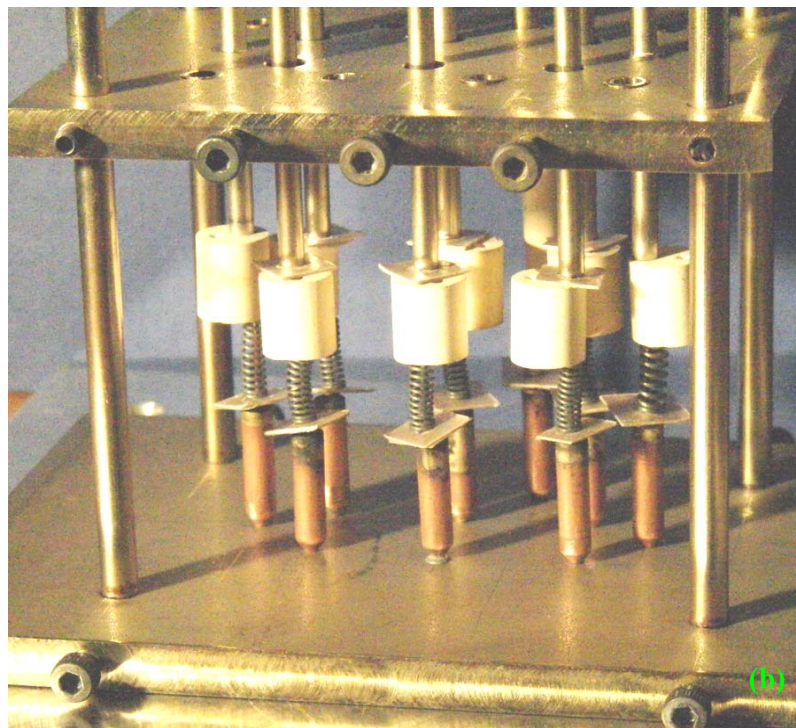
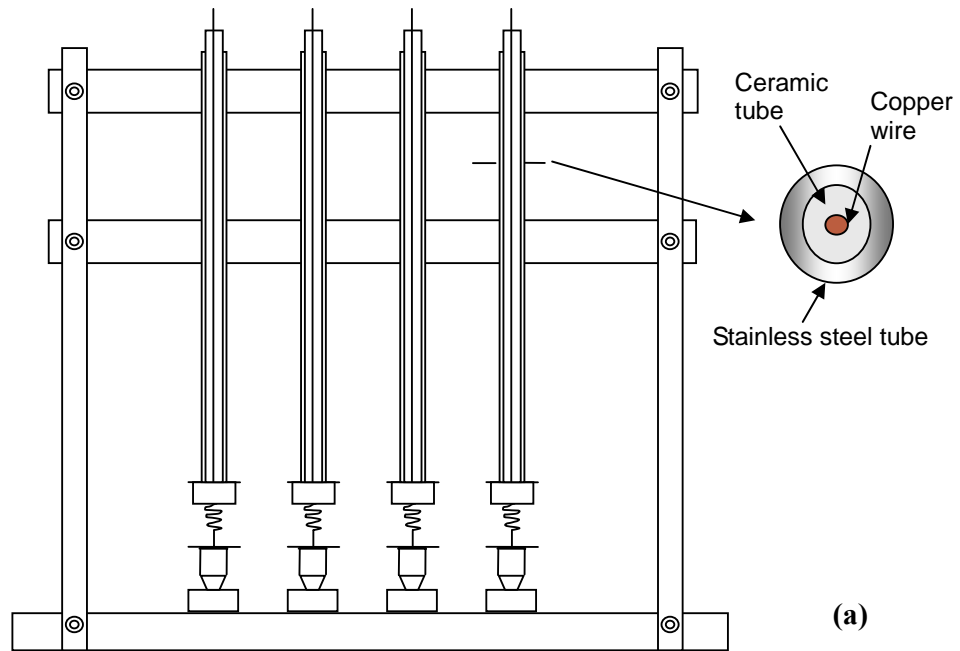


Figure 2.6.1 Arrayed testing platform views: (a) schematic diagram; (b) assembled platform.

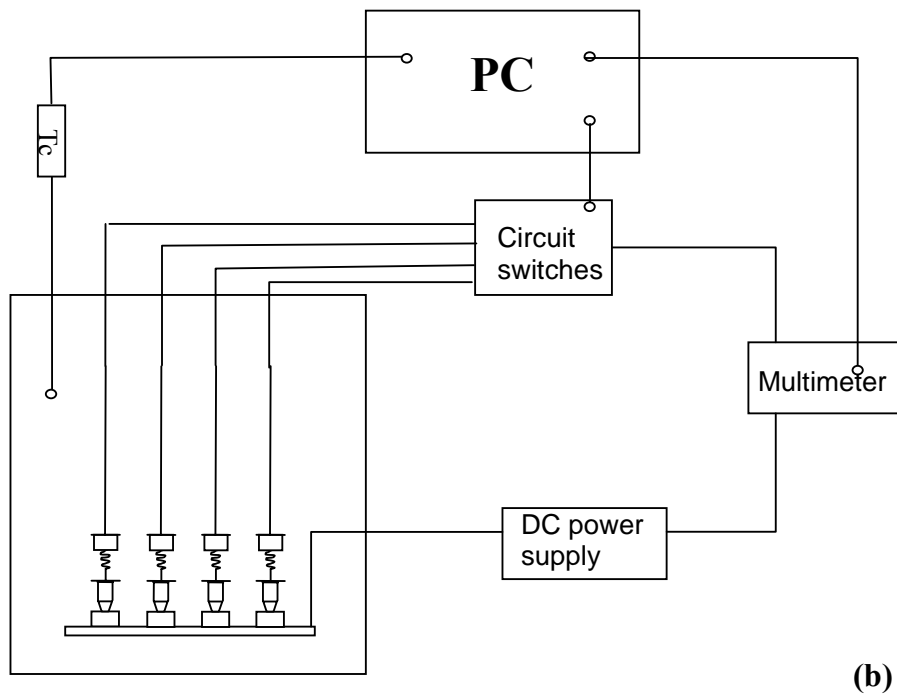
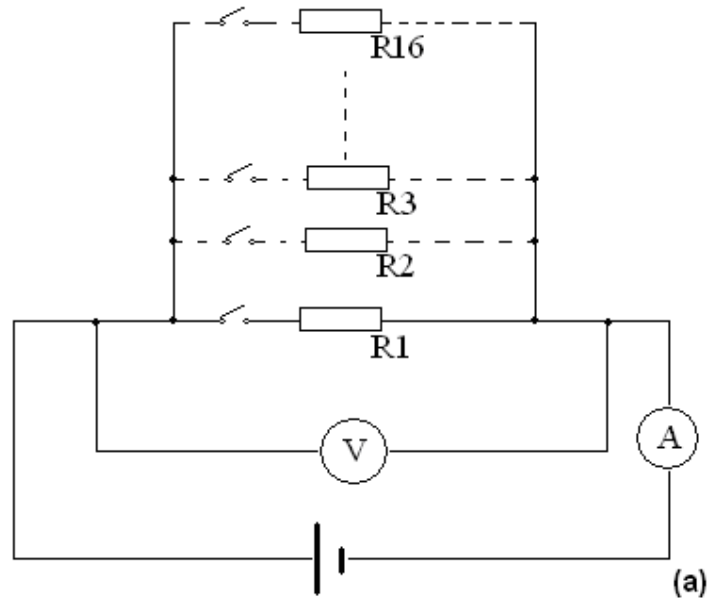


Figure 2.6.2 (a) Equivalent circuit of voltammetry arrayed testing. (b) Schematic layout of the automated high-throughput parallel electrical testing.

2.6.2 Operational Interface of the Parallel Electrical Measurements System

The entire work of testing was controlled automatically by an in-house computing program for which the flow chart of this multi-channel parallel R/T (resistance/temperature) measurement processing is presented in Figure 2.6.3. To obtain the R/T characteristics of a donor-doped BT sample, the values of voltage and current through the sample were measured respectively after the furnace reached thermal equilibrium at the targeted setpoint which was increasing from 20 to 300 °C, at 5 °C intervals.

Figure 2.6.4 displays the operational interface of parallel R-T testing. The capacity of this high-throughput testing system is sixteen channels which are constrained by the size of the arrayed platform and the capacity of the circuit switch (channels in the relay card) installed in the system. Sixteen indicators corresponding to the sequence of samples are arrayed in the centre of the operational panel (in Figure 2.6.4). The individual would turn red when the corresponding electric circuit was switched on by the relay card and the sample's current and voltage results would be displayed respectively in the dialog boxes above those indicators. Three pilot lamps which were located at the right corner of the panel were used to monitor the origin of any likely errors from the reading of the dual measurement multimeter. Once the PTC testing is active by pressing the ON/OFF switch button on the top left of this panel page, an Excel document is created and all measured voltage-current data are placed in the corresponding cells in the Excel sheet. The dial control button on the left of the panel can be used to define the amount of parallel circuit paths (equivalent to the number of testing samples) in the system. Furthermore, the termination indicator light in the bottom of the panel is red when the testing stops.

The block diagram of the parallel R-T testing system is displayed in Figure 2.6.5. Parts A-D in Figure 2.6.5 are the main functions in this operational interface for which the details are shown in Figure 2.6.6-2.6.9. When the furnace starts to heat up (Figure 2.6.6), the assessment of thermal stability in the furnace works reiteratively in comparison with the target setpoint (Figure 2.6.7). When the furnace reaches thermal equilibrium at the target setpoint, the electrical measurement processing activates by opening and switching different electric circuits (Figure 2.6.9) as well as starting data acquisition and saving (Figure 2.6.8). In this high-throughput parallel electrical measurement, only one channel is selected each time thus only one sample is connected into the electric circuit (as seen in Figure 2.6.2). Furthermore, the values of current and voltage were measured 5 times in each measurement step in order to eliminate the influence of data fluctuation. Once all arrayed samples finish testing at a specific temperature, a new target setpoint is applied and the whole process is repeated until samples have been measured over the required temperature range.

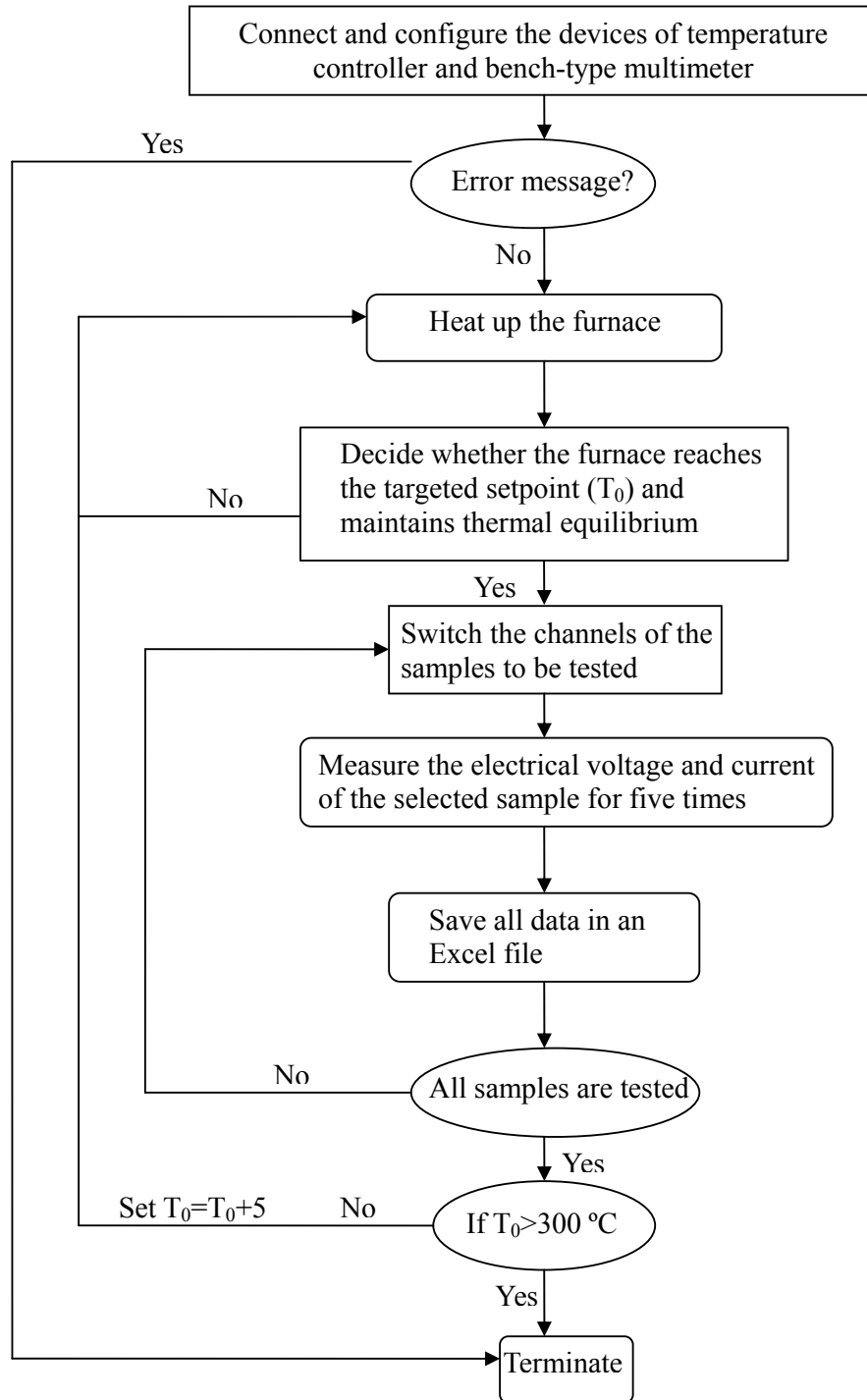


Figure 2.6.3 Flow chart of the high-throughput parallel R (resistance)- T (temperature) measurement processing.

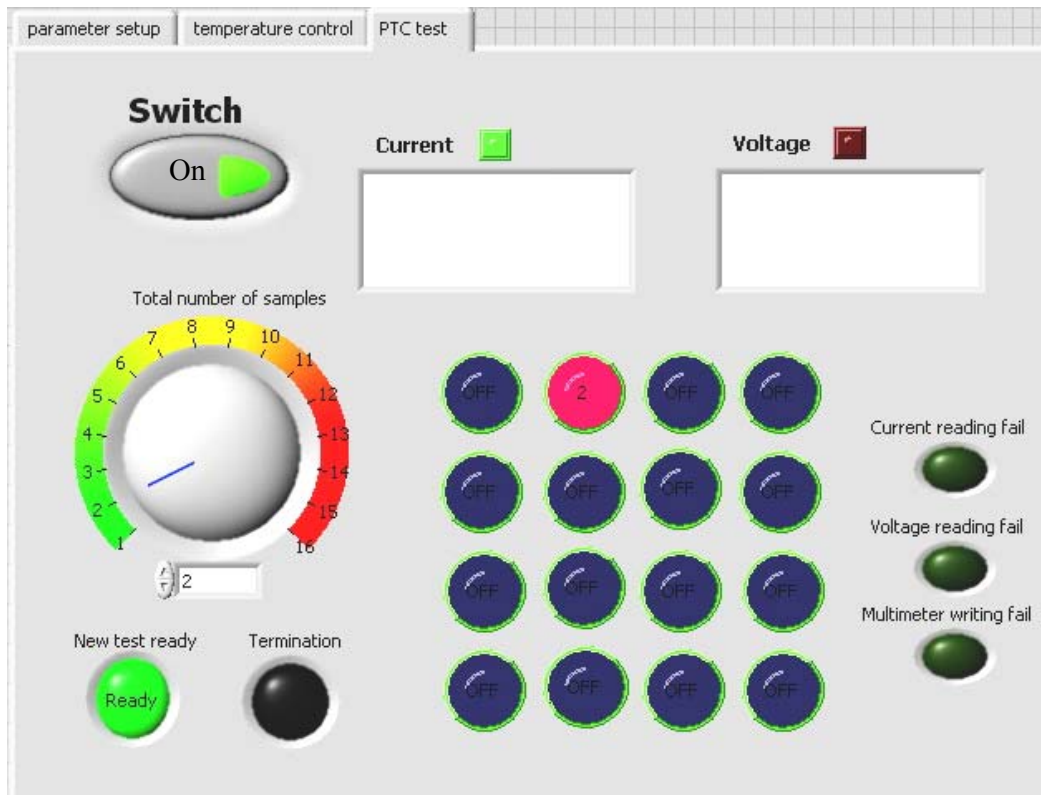


Figure 2.6.4 Parallel $R-T$ measurement test panel.

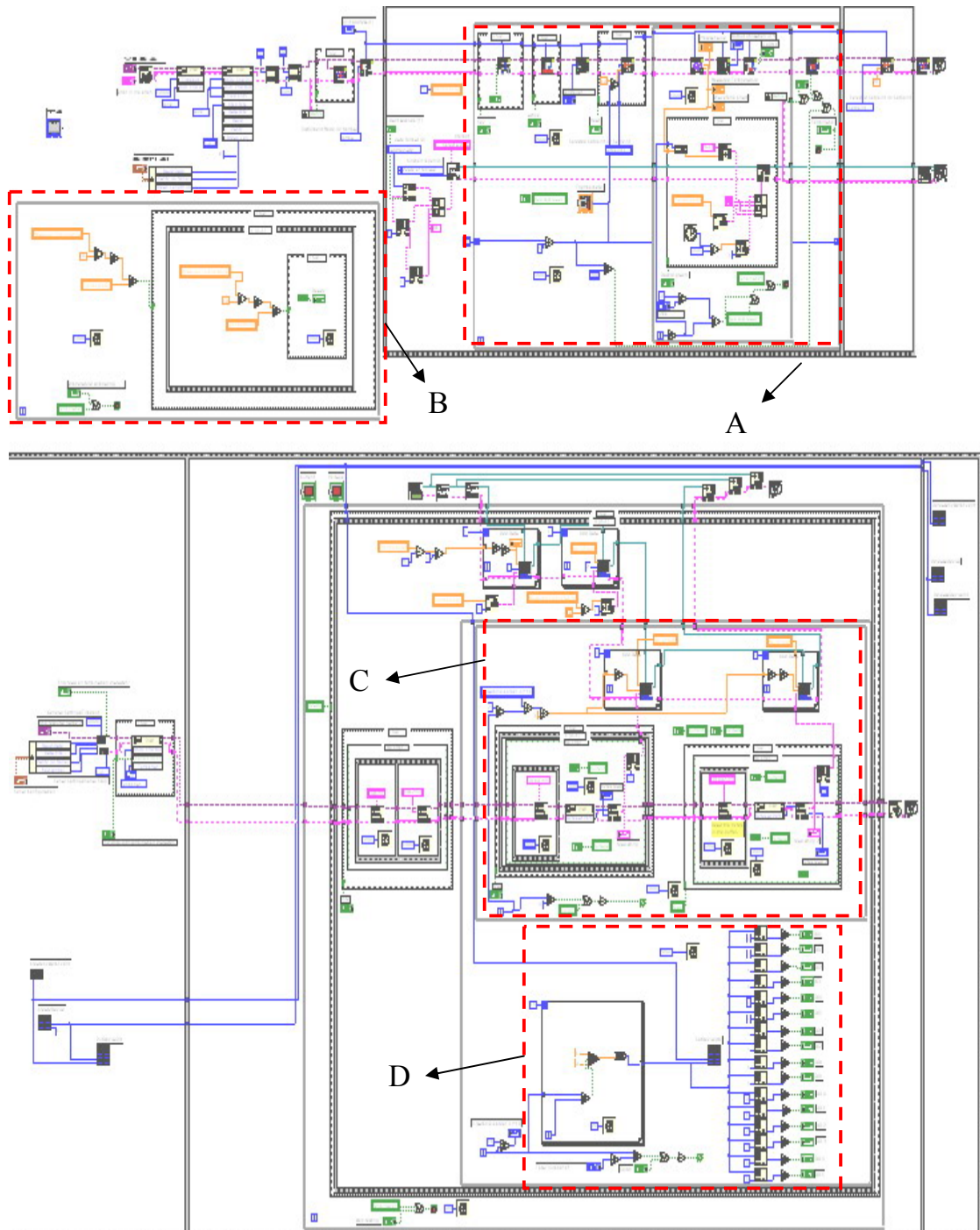


Figure 2.6.5 Block diagram of the parallel $R-T$ test operational system.

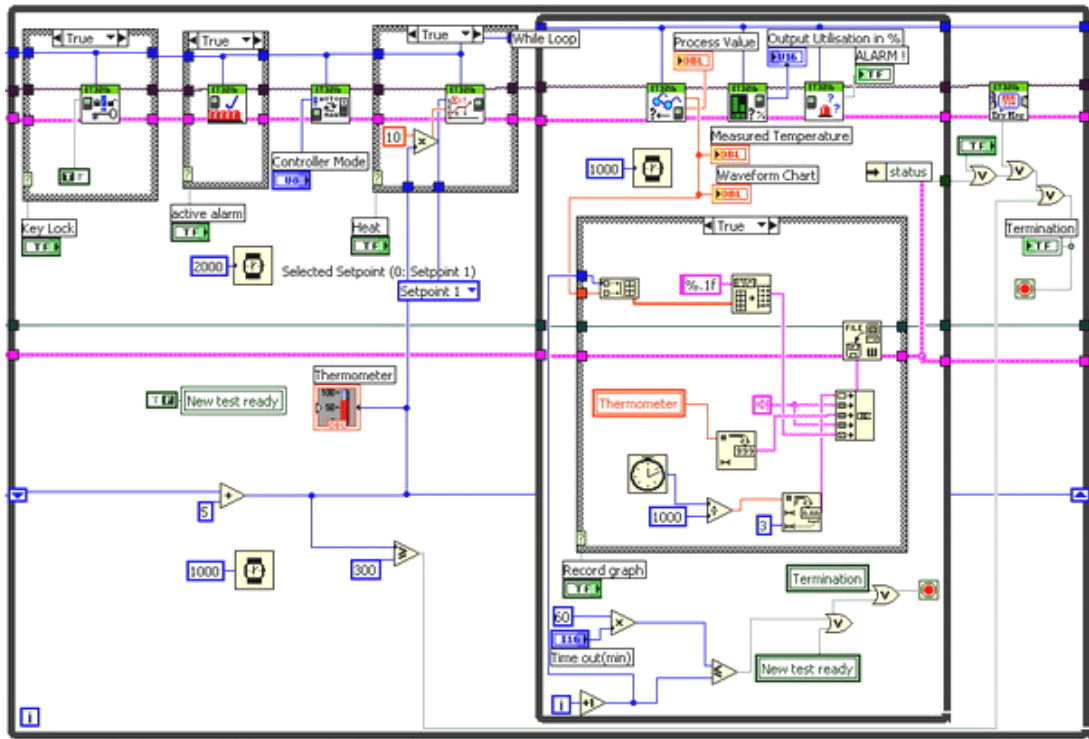


Figure 2.6.6 The magnified part (furnace heating) of the block diagram as part A in Figure 2.6.5.

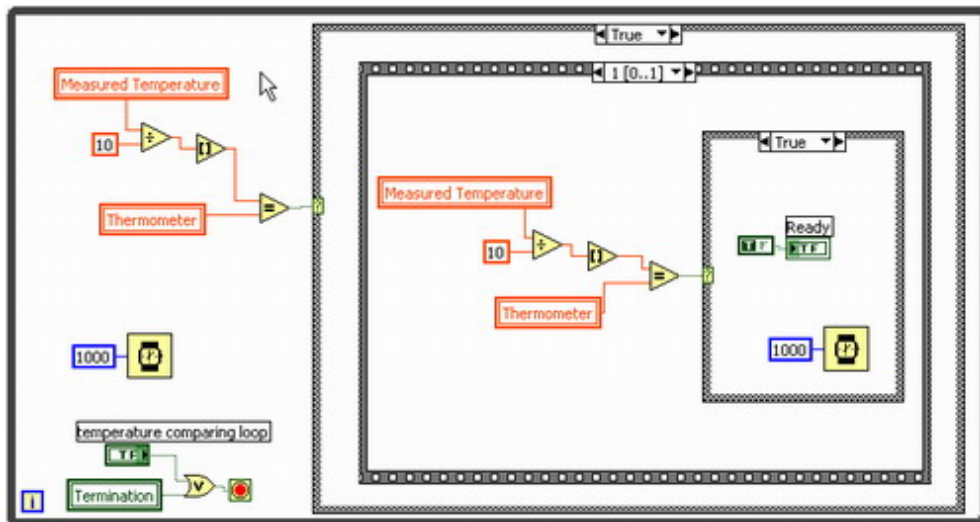


Figure 2.6.7 The magnified part (assessment of the reaching thermal equilibrium in furnace) of the block diagram as part B in Figure 2.6.5.

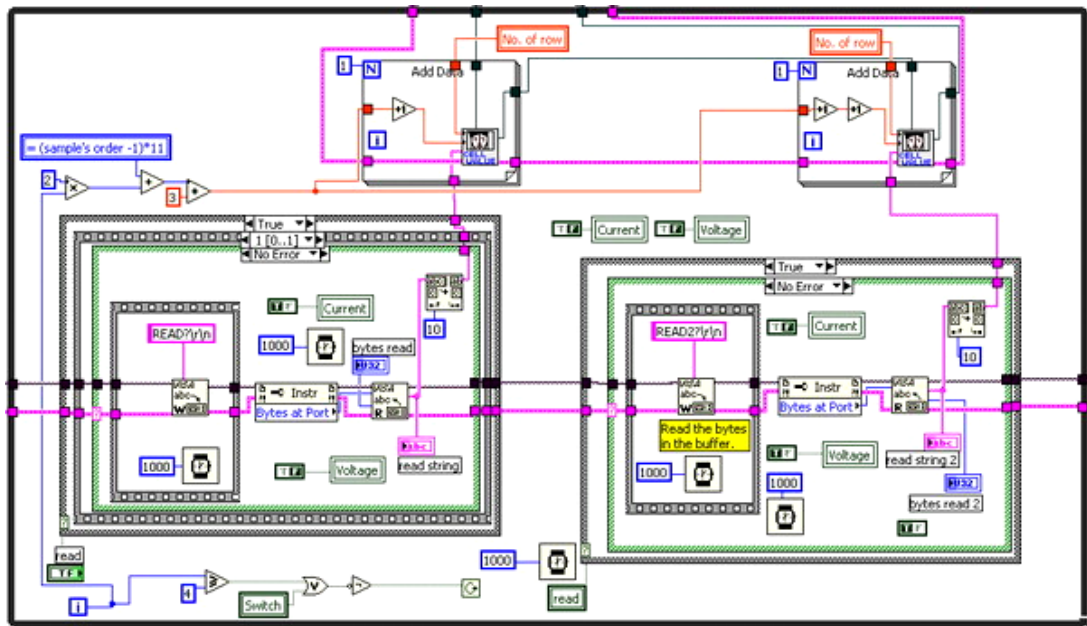


Figure 2.6.8 The magnified part (measuring data processing) of the block diagram as part C in Figure 2.6.5.

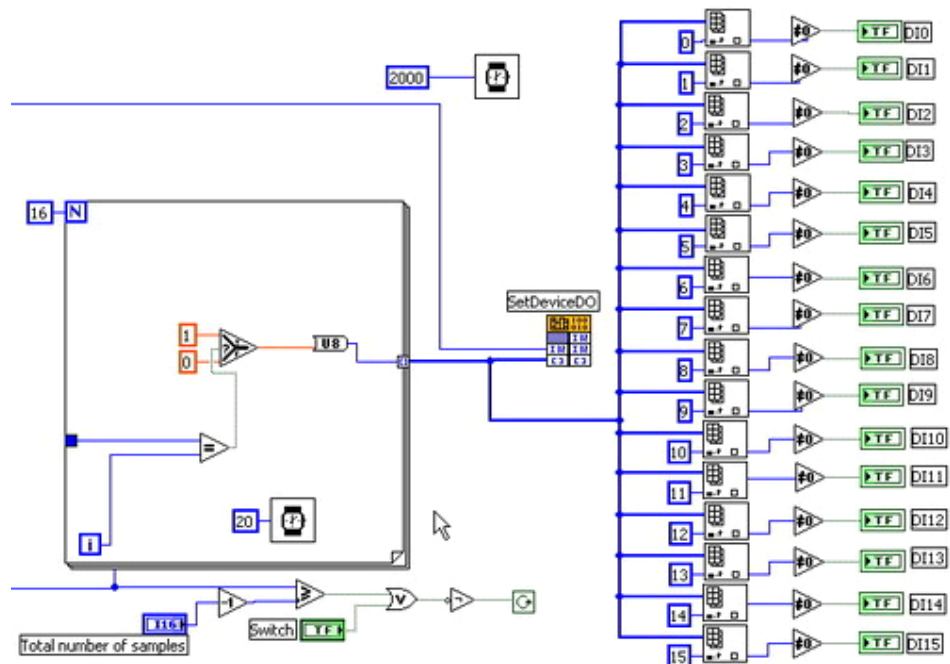


Figure 2.6.9 The magnified part (channel switch) of the block diagram as part D in Figure 2.6.5.

2.6.3 Validity Check of the Parallel Testing System

A commercial PTC thermistor (model: B59985C0120A070, EPCOS, Munich, Germany) was tested via this parallel high-throughput electrical measurement system and the R/T results were compared with the reference curve provided by the supplier.

The testing disc was loaded in the measurement jig after trimming off the metal wires and flattening both surfaces as displayed in Figure 2.6.1. Low-field resistance measurements were carried out in the temperature range of 20-300 °C, at 5 °C intervals, via a two-probe dc technique. The temperature of the furnace was controlled using a temperature/process controller (model 3216, Eurotherm, UK) and RS232 board interfaced to computer. A steady DC voltage ($\approx 0.8V$) was applied in the circuit from a triple output power supply (ISO-Tech IPS2250, RS Component Ltd, Northants, UK). The current passing through the circuit and the voltage applied on the testing sample were measured using a digital bi-channel multimeter (Model 1705, TTI, Huntingdon, England). Resistances at each temperature were calculated by averaging over five measurements. The whole testing system was controlled using an in-house LabVIEW® programme (Figure 2.6.4).

2.7 Fabrication and Characterization of La-doped BT Ceramics with PTCR Effect

2.7.1 Preparation of La-doped BT PTCR Ceramics by Solid-state Reaction (SSR)

Method

La-doped BT samples were prepared by conventional solid-state reaction technology. Various types of BT including as-received BT powders from different suppliers and synthesized BT from the reaction of BaCO₃ (99+% pure, Sigma-Aldrich GmbH, Schnelldorf, Germany) and TiO₂ (99+% pure, Tioxide Europe SA) were used as a starting material. Furthermore, TiO₂ and SiO₂ (99.9% pure, Sigma-Aldrich GmbH, Schnelldorf, Germany) were also used as sintering aids. All reagents were dried for 2 or 3 hours prior to weighing; the barium titanate and carbonate were dried at 150 °C to remove moisture, the titanium dioxide was heated at 800 °C to convert anatase to rutile phase²⁶⁶ and the lanthana (99.9% pure, Sigma-Aldrich GmbH, Schnelldorf, Germany) was heating to 1000°C to decarbonate the La₂(CO₃)₃ and quickly measured to avoid recarbonation.³⁹³ Samples with two different donor (La³⁺) concentrations (0.3 and 0.5 mol.%) were prepared for every batches. Appropriate amounts of those chemicals according to Table 2.7.1 were mixed in ethanol and ball milled with zirconia media in a plastic jar for 8 hours. The mixed powders were then dried and pulverized before calcined in air at 1100 °C for 4 hours. The calcined powder was reground and admixed with about 1.5 wt.% PVA as a binder for 30 minutes with an agate mortar and pestle before being sieved (~350 mesh) to under 40 µm. The powder obtained was then uniaxially pressed into discs with 5 mm diameter in a stainless-steel die at about 200 MPa. The pellets were sintered in air on coarse ZrO₂ sugar bed in an alumina crucible at temperatures ranging from 1350 to 1450 °C

as listed in Table 2.6.1, with a heating rate of 5 °C/min. Pellets sintered at 1450 °C were rapidly cooled (cooling rate \approx 1200 °C/h) and the rest of the samples were cooled at a rate of 5 °C/min.

Table 2.7.1 La-doped BaTiO₃ prepared using SSR route sintered in air.

Sample ref.	BaTiO ₃	Ti/Ba (molar ratio)	SiO ₂ / mol.%	La content /mol.%	Sintering conditions
A3	I ^a	1.02	-	0.3	1350 °C in air for 2 h
A5	I	1.02	-	0.5	1350 °C in air for 2 h
B3	II ^b	1.02	-	0.3	1400 °C in air for 2 h
B5	II	1.02	-	0.5	1400 °C in air for 2 h
C3	II	1.02	2.5	0.3	1400 °C in air for 2 h
C5	II	1.02	2.5	0.5	1400 °C in air for 2 h
D3	I	1.02	-	0.3	1450 °C in air for 9 h
D5	I	1.02	-	0.5	1450 °C in air for 9 h
E3	II	1.02	-	0.3	1450 °C in air for 9 h
E5	II	1.02	-	0.5	1450 °C in air for 9 h
F3	III ^c	1.01	2.5	0.3	1380 °C in air for 1 h
F5	III	1.01	2.5	0.5	1380 °C in air for 1 h

^a BaTiO₃ (as-received, 99.95% pure, Inframat Advanced Materials) after vibro-milling treatment

^b BaTiO₃ (as-received, 99.8% pure, PI-KEM)

^c BaCO₃ (99+% pure, Sigma-Aldrich GmbH, Schnelldorf, Germany) + TiO₂

Samples in batches A, C and F were also sintered at 1380 °C for 1 h in a reducing atmosphere environment by providing consistent flow of N₂ with a heating/cooling rate of 5 °C /min (Table 2.7.2). Among them, reoxidation effect was investigated by annealing the BT samples with 0.3 mol.% of La³⁺ in various batches in Table 2.7.2 at 1100 °C for 4 hours after sintering. Sample NA3 was also reoxidized at 1000 °C for 30 minutes for comparison.

Aluminium was deposited by evaporative coating (High vacuum evaporator, model E306A, Edwards Ltd, Crawley, U.K.) on both the surfaces of all sintered SSR sample discs to form electrodes for electrical measurements.³⁰⁷ The room-temperature

resistance was measured by a digital multimeter (Model 1705, TTI, Huntingdon, England). The resistivity as a function of temperature from room temperature to 300 °C was measured using a two-probe method via an in-house parallel high-throughput testing system as detailed in section 2.6.3. The microstructures of the La-doped BT samples in different batches via SSR route were analyzed using SEM by scanning its fracture surface. The electrical profiles of samples with and without annealing after reduced sintering were also compared.

Table 2.7.2 La-doped BaTiO₃ prepared using SSR route sintered in N₂ flow.

Sample ref.	BaTiO ₃	Ti/Ba (molar ratio)	SiO ₂ / mol.%	La content /mol.%	Sintering conditions
NA3	I	1.02	-	0.3	1380 °C in N ₂ flow for 1 h
NA5	I	1.02	-	0.5	1380 °C in N ₂ flow for 1 h
NC3	II	1.02	2.5	0.3	1380 °C in N ₂ flow for 1 h
NC5	II	1.02	2.5	0.5	1380 °C in N ₂ flow for 1 h
NF3	III	1.01	2.5	0.3	1380 °C in N ₂ flow for 1 h
NF5	III	1.01	2.5	0.5	1380 °C in N ₂ flow for 1 h

2.7.2 Selection of Electrode Materials

The electrode of a commercial PTC thermistor (mode: B59985C0120A070, EPCOS, Munich, Germany) was examined by SEM/EDS after polishing its cross section to a 1 μm diamond finish. Various electrode materials were tested as presented in Table 2.7.3 to form electrode layers on both sides of the PTC thermistor after eliminating the preceding electrode layer by grinding away using sandpaper. ‘Edwards’ high vacuum evaporator (Edwards Ltd., Crawley, U.K.) was used for evaporative coating of the electrode layers on samples surfaces. The details regarding the coating thickness and annealing parameters for different electrode materials are listed in Table 2.7.3. The heat treatments for the electrode layers after evaporative coating are required to enable the consolidation of the deposited electrode films and provide

strong electrodes with Ohmic contact. In-Ga amalgam (45:55 wt.%; In, ex BDH Chemicals, England and Ga, ex MCP group, Northants, England) was also used to form electrodes by rubbing it on opposite samples' surfaces.

Table 2.7.3 Selection of electrode materials

No.	Electrode materials	Deposition method	Thickness / nm	Annealing
1	Silver paste	brushing	--	600 °C for 30 min
2	Al	evaporative coating	120	180 °C for 30 min
3	Ni-Fe alloy (30:70 wt.%)	evaporative coating	100	240 °C for 30 min
4	Cr/Au	evaporative coating	30/120	--
5	In-Ga amalgam	rubbing	--	--

Room-temperature resistance of the thermistor with different electrodes was measured by a multimeter. The characteristics of R-T curves were also measured for the thermistor with Al and In-Ga electrodes respectively using the in-house test station with temperature control as detailed in chapter 2.6.3. Data were corrected for overall disc geometry so as to relate to a geometric factor of unity.

2.7.3 Investigation of La-doped BT PTCR Materials Fabricated by High-throughput (HT) Method

The synthesized TiO₂-excess non-stoichiometric BaTiO₃ powder formed by solid state reaction using BaCO₃ and TiO₂ with molar ratio 1:1.01 was used as the starting material. The mixed powder was calcined at 1100°C for 2 hours in air after ball-milling for 8 hours with ethanol. The calcined powder was easily dispersed by vigorously stirring in deionized water using magnetic stirrers. A suspension with solids content of 50 wt.% was prepared by adding 1.5 wt.% of dispersant (Darvan

821A) and 2 wt.% of thixotropic agent (Acrysol RM12W), as described in section 2.3.1. Droplets of dispersed BT ink with a volume of 20 μL were printed on to silicone release paper by a digital transfer pipette. The as-printed samples were dried under ambient conditions and then heated in air at 600 $^{\circ}\text{C}$ for 2 hours to burn out all organic polymers. These green BT discs were used as base materials for subsequent doping.

Lanthanum dopant was mixed into BT powders by infiltrating the lanthanum salt solution into the porous BT base by a droplet-doping technique, as detailed in section 2.4. BT discs doped with a variety of La donor concentrations between 0.1 to 0.8 mol.%, at 0.1 mol.% as a increment, were produced. Solutions of $\text{La}(\text{NO}_3)_3 \cdot 6\text{H}_2\text{O}$ (99% purity, Sigma-Aldrich) were prepared with deionised water at various concentrations according to the required doping level. In preliminary work, the amounts of dopant solution with corresponding concentrations were printed on the flat surface of green BT base discs using a digital transfer pipette. As-doped samples were dried in an ambient atmosphere overnight then in a desiccator for two days. Then the samples were rapidly heated to convert the nitrate donor salts to oxide before sintered at 1380 $^{\circ}\text{C}$ for 1 hour in nitrogen with a heating/cooling rate of 5 $^{\circ}\text{C}/\text{min}$. The reoxidation effect on PTCR properties of samples with 0.3 mol.% of La^{3+} content was investigated by annealing the as-sintered samples in air at 1100 $^{\circ}\text{C}$ for 0.5, 4 and 24 hours respectively.³⁹⁴

Phase analysis of the as-sintered La-doped BT specimens via this HT method combined with the dip-pen printing for the base and droplet-doping for the dopant distribution was performed by X-ray diffraction (XRD): samples were crushed in an

agate mortar and measurements were conducted on a Siemens D5000 (Karlsruhe, Germany) using Cu K α radiation (40 mA filament current, 45 kV accelerating voltage) and a step size of $0.0334^\circ 2\theta$. The microstructures of the samples' fracture surfaces were examined using SEM.

Electrodes for electrical property measurements were prepared by rubbing a thin layer of In-Ga amalgam to provide Ohmic contacts at room temperature on both surfaces of as-sintered La-doped BaTiO₃ samples via HT method. An in-house multiple sample measurement system was used to measure their r - T characteristics using a two-probe method in the temperature range of 20 to 300 °C as described in section 2.6.3.

2.8 Investigation of Er-Mn and Y-Mn Donor-acceptor-codoped BT PTCR Ceramics via HT Method

The donor-acceptor-codoped BT PTCR libraries were prepared via a high-throughput fabrication method in which the BT base was made by dip-pen printing as detailed in section 2.6.3 and the dopant was doping into BT by the droplet-doping method as described in section 2.4. $\text{Y}(\text{NO}_3)_3 \cdot 6\text{H}_2\text{O}$ (99% purity, Sigma-Aldrich), $\text{Er}(\text{NO}_3)_3 \cdot 5\text{H}_2\text{O}$ (99.9% purity, Sigma-Aldrich) and $\text{Mn}(\text{NO}_3)_2 \cdot 4\text{H}_2\text{O}$ (98% purity, Alfa-Aesar) were used to prepare dopant precursor solutions with deionised water at various concentrations according to the required doping level. Libraries of yttrium-manganese-codoped and erbium-manganese-codoped BT in a donor doping range between 0.1 to 0.8 mol.%, at 0.1 mol.% as increment and with a fixed 0.02 mol.% Mn^{2+} content as an acceptor concentration were produced. As-doped samples were dried in ambient atmosphere overnight then in a desiccator for two days. Then the samples were rapidly heated to convert the nitrate dopant salts to oxide before sintered at 1380 °C for 1 h in nitrogen gas flow atmosphere with a heating/cooling rate as 5 °C/min. Samples were subsequently annealed in air at 1100 °C for 0.5 hours.

The opposite sides of as-sintered samples were rubbed with a layer of In-Ga alloy to form Ohmic contact electrodes. The characteristics of r - T were measured using a two-probe method from room temperature up to 300 °C with an in-house multiple sample measurement system, as described in section 2.6.3. The microstructure of 0.5 mol.% Y + 0.02 mol.% Mn doped BT disc was observed by SEM. Measurement was conducted after thermal etching the polished cross section for 20 minutes at 1250 °C.

3 Results and Discussion

3.1 Ceramic Ink Preparation

One of the main objectives for this project is to fabricate libraries of donor-doped BaTiO₃-based positive temperature coefficient resistivity (PTCR) materials via a high-throughput method which is combined with the dip-pen printing and droplet-doping techniques. BaTiO₃ tablets used as a base material were produced by a dip-pen printing method and this was followed by rapid droplet-doping by printing the dopant precursor solution on the surface of the porous base prepared previously. In order to satisfy the requirement of high-throughput screening for PTCR features, a disc-like or dome-shape of sample is required initially. As is the case for a drop-on-demand ink-jet printer for printing green BaTiO₃ discs, the quality of the ink dispersion is critical in determining not only the stabilization of the ink while printing but also the shape of the drying residue after printing. Therefore, the primary task was focused on finding the optimum dispersion of barium titanate powder.

3.1.1 Characterization of Materials

Both the as-received BT powder and as-dried powder from a diluted aqueous BT dispersion after the powder had been subjected to a fine milling processing contained powder agglomerates and aggregates as seen by SEM. The morphology and the size of the as-received BaTiO₃ powder were revealed in Figure 3.1.1. The mean primary particle size is 320 nm with a standard deviation of 50 nm by measuring around 100 individual particles using a line intercept method. Uniformity of size grading of the primary particles is acceptable; however, large numbers of big aggregates and

agglomerates were spotted as shown in Figure 3.1.1. The size of the agglomerates and aggregates of the as-received BaTiO₃ powder varied in a broad range as observed by SEM study. Furthermore, the chemical analysis of the as-received BaTiO₃ powder examined by energy dispersive X-ray spectroscopy (EDS) revealed that it may contain excess Ba content, as a result of which the average Ba/Ti ratio is 1.2. However, considering the peaks of characteristic EDS energies for elements Ba (L α = 4.4663) and Ti (K α = 4.5089) are strongly overlapping, the quantitative measurement by EDS cannot be considered to be accurate enough and so other characterization techniques such as X-ray photoelectron spectroscopy (XPS) or X-ray fluorescence (XRF) for compositional characterization might be needed.

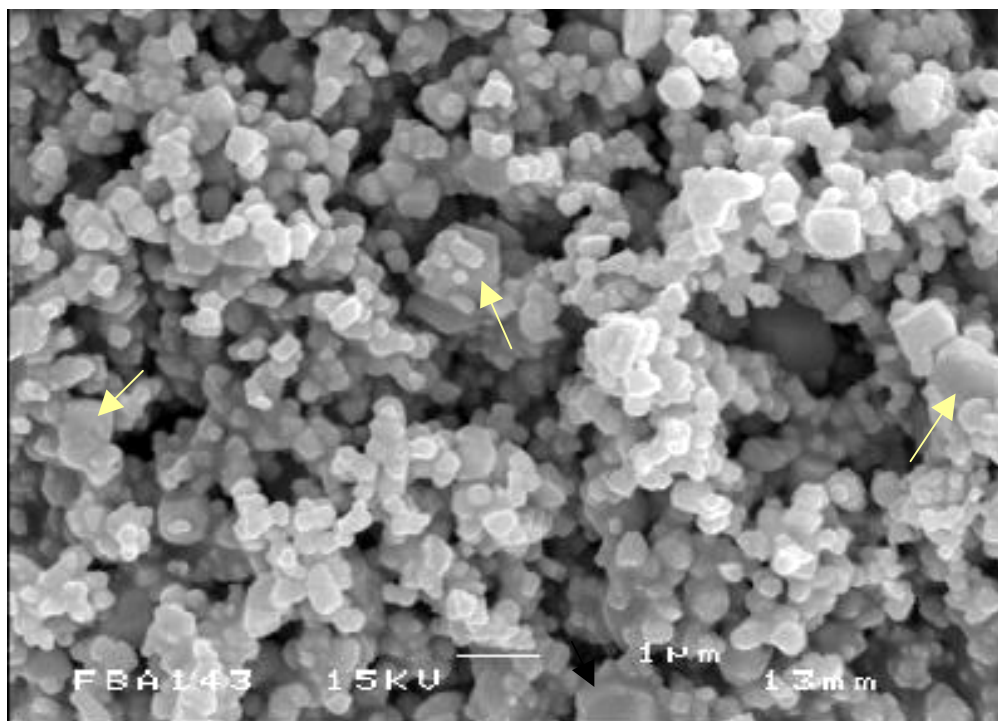


Figure 3.1.1 SEM image of the as-received BaTiO₃ powder. Arrows indicate the particle aggregates.

It was found that the unbroken agglomerates which can cause severe heterogeneous

particles size distribution in a ceramic dispersion can not only significantly influence the stability of inks prepared for ink-jet printing but also cause a gradient structure during ink settlement after printing.³⁹⁵ In order to disperse the aggregates and agglomerates whose strength is dependent upon the mechanism of interparticle bonding, different milling processes were used and their outcomes were also compared. As-received BaTiO₃ powder was prepared with distilled water by Dyno Milling after thirteen passes and by Vibro-milling for 9 hours respectively. Both slurries separately prepared by Dyno-milling and Vibro-milling were dried in an oven. The morphologies of the as-dried BaTiO₃ powders from the diluted suspensions after different milling processes were examined by SEM again. To obtain an ideal sample for SEM, much diluted suspension (<0.01 vol.%) was prepared in order to reduce the possibility of particle contacts; furthermore, 60 second ultrasonication was used to break the weak agglomerates which might reform after milling. If these conditions are not achieved, unbroken and reformed agglomerates may not be distinguishable under the microscope.

It was observed that most of the agglomerates were broken by the physical external forces generating from milling but the average size of the remaining particles was still in the micrometer scale rather than a few hundred nanometre as is the ultimate primary particle size scale. The size of BaTiO₃ particles after Dyno-milling varied up to 10 µm as displayed in Figure 3.1.2 while the size of BaTiO₃ particles reground by the Vibro-mill was reasonably even with the diameter around 1 µm as shown in Figure 3.1.3. Therefore, the Dyno-milling is not powerful enough to be employed here for regrinding the as-received BaTiO₃ powder; the Vibro-milling processing is preferable.

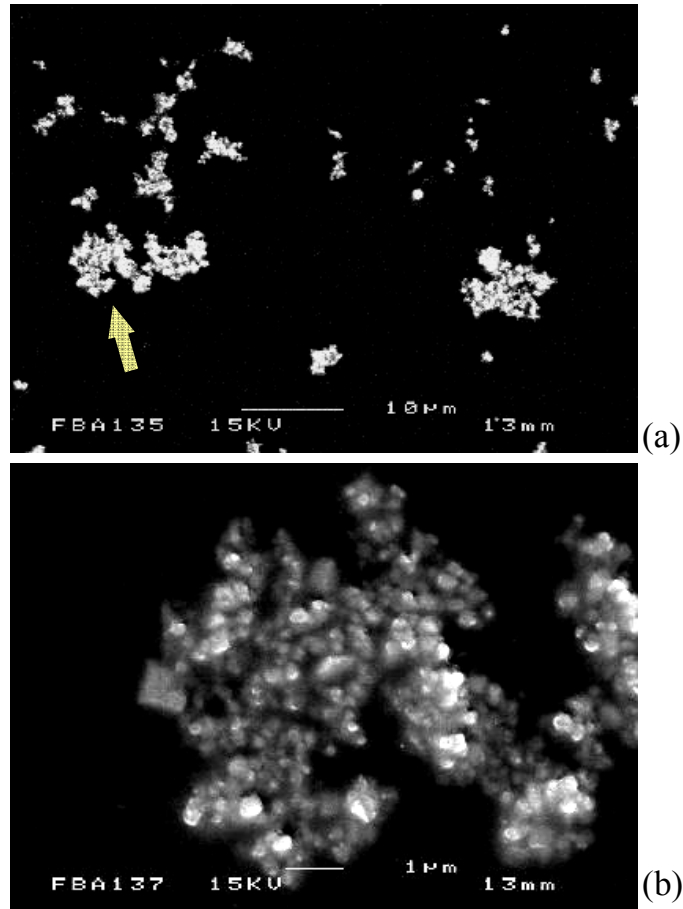


Figure 3.1.2 (a) SEM image of the agglomerates remaining in BaTiO₃ ink after Dyno-milling, (b) magnified image for the agglomerate arrowed in (a).

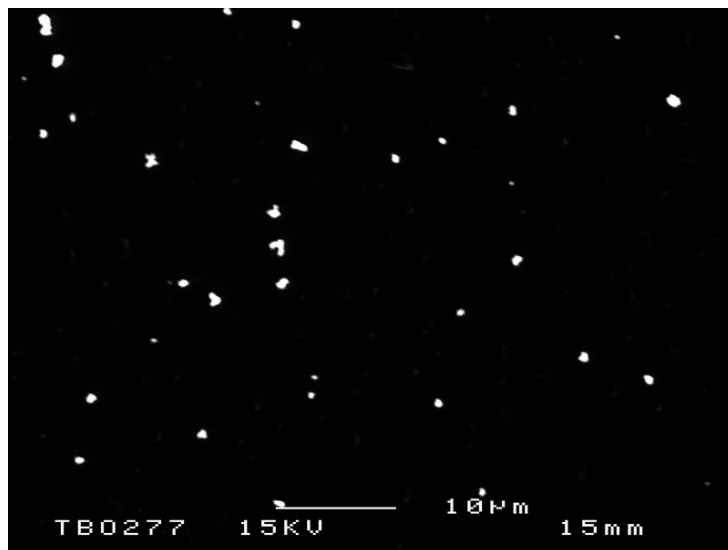


Figure 3.1.3 SEM image of the particle distribution in BT ink after Vibro-milling.

The results of BET specific surface area of various BaTiO₃ powders are shown in Table 3.1.1. The mean value of BET for as-received BaTiO₃ powder was 3.3 m²/g; for BaTiO₃ powders after Dyno-milling and Vibro-milling were 7.2 m²/g and 9.6 m²/g respectively. According to the BET results, the particle size of as-received BT powder was significantly reduced after milling; however, the effective particle size scale was still under the submicron level rather than the level of nanometres according to the BET values and SEM images (Figure 3.1.2-3). Further investigation on particle size distributions in dispersions was thus needed.

Table 3.1.1. The results of BET specific surface area.

Powder No.	Origin	BET Specific Surface Area /m ² g ⁻¹	Correlation Coefficient
1	As-received BaTiO ₃ powder	3.3±0.2	9.9980
2	After Dyno-milling	7.2±0.1	9.9992
3	After Vibro-milling	9.6±0.1	9.9994

The diluted suspensions using BaTiO₃ powders after Dyno-milling and Vibro-milling respectively were examined by the Zetasizer. The volume-distribution particle size results of BT powder after different milling processes are illustrated in Figure 3.1.4. Both particle size distributions were bimodal, indicating there were agglomerates in processed BT powders (also seen in SEM image in Figure 3.1.2-3). However, the powder after Vibro-milling showed smaller average size and narrower size distribution (also proved in SEM and BET results above). The particle size values corresponding to the main peaks in Figure 3.1.4 are around 380 nm for Vibro-milled BT powder and 600 nm for Dyno-milled powder. Whereas the values of the Z-average particle size of the BT powders after Dyno-milling and Vibro-milling were 707 nm and 510 nm respectively. The Z-average diameter is the mean diameter calculated from the Brownian motion of the particles as measured by the intensity of

scattered light. Those measurements are very sensitive to the presence of agglomerates, flocculates and large particles in suspension. Moreover, the values of the polydispersity index (PDI) for powders after Dyno-milling and Vibro-milling were 0.24 and 0.21 respectively. Low PDI value (<0.1) represents relatively narrow size distribution; however, large agglomerates or flocculates dominate the measurement when PDI exceeds 0.5. Both the PDI results of powders after different millings are close. The results above suggested that the Vibro mill is an effective milling processing to break the agglomerates and aggregates in the as-received powder. In conclusion, BaTiO₃ ceramic powder after Vibro-milling was chosen for further experiments due to their finer particle size characteristics.

Table 3.1.2. Particle size distribution of BT powders after various milling processing.

No.	Milling process	Z-average size	PDI index
1	Dyno-mill	707 nm	0.24
2	Vibro-mill	510 nm	0.21

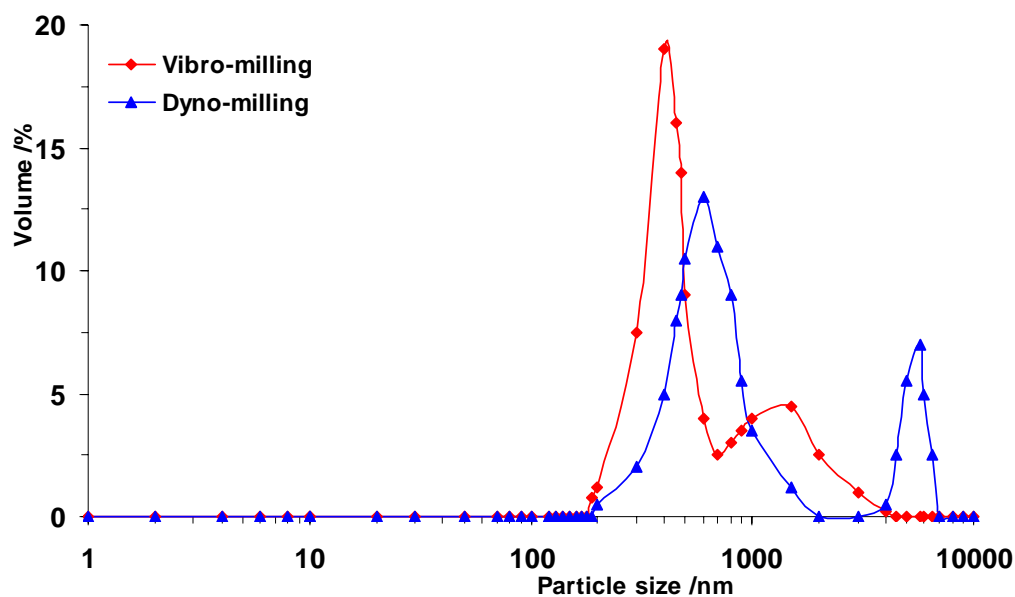


Figure 3.1.4 Particle size distribution by volume of BT powders after Dyno-milling and Vibro-milling respectively.

3.1.2 Assessment of Dispersion of BaTiO₃ Ceramic Powder

In this work, preparing relatively stabilized and long-standing ceramic ink is important because of the desire of high-throughput fabrication of the green sample by ink-jet printing method. In ceramic ink-jet printing, the nature of the ink especially its stabilization against sedimentation determines the quality of the products since the ink is left in a reservoir undisturbed for a relatively long time before being ejected. In a combinatorial printer, the importance of stabilized ink is much greater because inaccuracy in the composition of the mixtures may occur due to the concentration gradient in the ink caused by the different sedimentation speed of agglomerates. Badly dispersed ink also leads to loosely packed flocs after drying and low pre-fired density; thereafter, affecting the sintered quality. Moreover, it was observed that strongly flocculated suspensions resulted in inhomogeneous structure of the dried residue while colloidally stable and weakly flocculated suspensions can lead to relatively homogeneous green body microstructure.³⁹⁶ Hence to prepare well dispersed ink is an essential requirement here.

Barium titanate is a major electroceramic material for many applications. BaTiO₃ dispersion in either aqueous or non-aqueous systems has been investigated for many years.³⁹⁶⁻⁴⁰⁴ The dispersibility of BaTiO₃ particles is achieved by selecting fine grades of powder and compatible dispersant. Water as a liquid carrier was chosen as it is more environmentally acceptable and low residues are left during the burn-out stage which can impact the PTCR properties of the donor-doped BaTiO₃ samples.

EFKA and Solsperse series are the two most common series of dispersants in industrial applications. In the shortlist, EFKA 4540, EFKA 4580, EFKA 5071,

EFKA5010, EFKA 5207, EFKA 6220, EFKA6230, Solsperse 27000, Solsperse 44000, Solsperse 47000, Darvan 821A and Dispex A40 were chosen for the trial as they are all water based dispersants. The concentration of dispersant normally used is based on either the weight or specific surface area of the ceramic powder from the suppliers' recommendation.

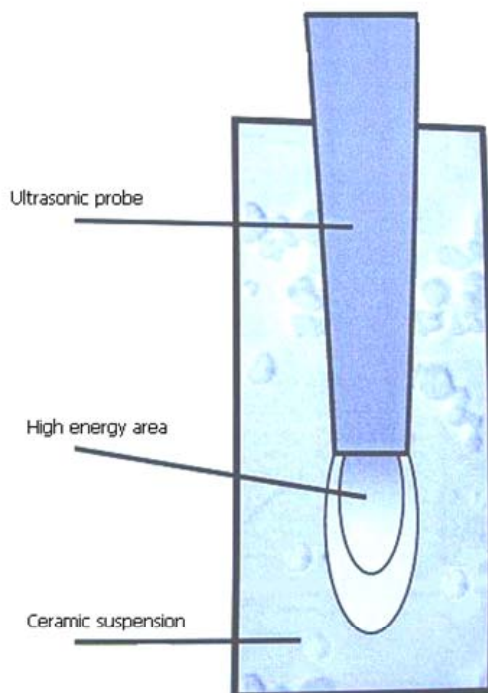


Figure 3.1.5 Schematic diagram shows the high energy zone at the tip of the ultrasonic probe during dispersion of ceramic powders.

All the inks were subjected to ultrasonic treatment which is a very efficient tool for preparation of ceramic dispersions particularly for ink-jet printing.⁴⁰⁵ The ultrasonic energy is able to not only break down the agglomerates but also stir the suspension. However, the particles are only effectively subjected to ultrasonic treatment when they are adjacent to the ultrasonic probe tip with a diameter of ~8 mm which in the

region of which the energy is propagating into the dispersion. A schematic diagram of the ultrasonic probe energy distribution in ceramic suspension is displayed in Figure 3.1.5. The ultrasonic energy has to be sufficient to overcome the bond strength of the agglomerates in order to break them. The working time must also be long enough to eliminate the chance of agglomerates escaping from the high ultrasonic energy field.

When the sedimentation of the powder in suspension started, an interface as a cloudy region between a clear water layer and sedimentation layer appeared. Thus, the criterion for selecting dispersants achieving the best stability is the combination of slow sedimentation and late appearance of supernatant fluid. Since the solid loading of barium titanate was very low (0.5 vol.%) and there is no substantial contrast of the colour between the sedimentation of BT with the cloudy region of its own suspension (both in light-gray colour), the sedimentation speed is very difficult to measure accurately. The height of the cloudy region is then defined as the distance between the dispersion/supernatant interface and the bottom of the tube, including the height of any sedimentation. The cloudy volume fractions of all dispersions during these sedimentation tests were recorded and are displayed in Figures 3.1.6 and 3.1.7. Furthermore, the BT powder reground by Vibro-milling with no addition of dispersant was also examined and the corresponding results are shown in Figure 3.1.6.

The concentration of all the testing dispersants was 3% based on the weight of BT ceramic powder. EFKA 5010, EFKA 6220, Solsperser 27000 were eliminated from the candidate list of dispersants because of rapid formation of supernatant in the ink.

The Vibro-milled ink without dispersant showed quite prolonged stabilization compared with those with dispersants. This proved that the ultrasonic treatment is effective for breaking the agglomerates which helps to stabilize the ink. Furthermore, because the zeta potential of BaTiO₃ powder in the pH \geq 7.0 region is high at 40 mV,⁴⁰⁶ there is already moderate electrostatic repulsion between particles. However, the repulsion may not be great enough to stabilize the dispersion without dispersant at increasing solid contents. EFKA 4580, EFKA 5071, Solsperse 44000, Solsperse 47000, Dispex A40 were not considered because they are not as good as EFKA 4540 and Darvan 821A and their performances are not even better than that of the ink with no dispersant addition. Based on this discussion, both Darvan 821A containing ammonium polyacrylate polymer and EFKA 4540 containing modified polyacrylate polymer showed the best capability to stabilize the suspension of barium titanate among all dispersant candidates.

Polyacrylate dispersant which is known to stabilize slurries by electrosteric means and polyelectrolyte-bridging flocculation⁴⁰⁷ shows high performance in applications involving BaTiO₃ aqueous suspension. However, for steric type stabilization, insufficient dispersant with only partial powder surface coverage cannot provide a full barrier to prevent flocculation; on the other hand, too much dispersant tends to entangle and increase viscosity. Seeking an optimum amount of dispersant was therefore the goal of the second test round. Various concentrations of EFKA 4540 and Darvan 821A were added to barium titanate suspension using the same procedure. Supernatants appeared after 4 hours for dispersions having 0.03 vol.% EFKA 4540 and 0.02 vol.% Darvan 821A dispersant (both equivalent to 1 wt.% of ceramic powder). However, when increasing the concentration of both the

dispersants in suspensions up to 4 wt.% of BT powder, there was no significant effect on the stabilization of inks as shown in Figures 3.1.8 and 3.1.9. Furthermore, the sedimentation rate slightly decreased as the concentration of dispersant increased and reached a minimum and then slightly increased again when the concentration of dispersant exceeded 3 wt.% of solid loading. This is presumably caused by complex flocculation mechanisms generated by high molecular weight polymer chains surrounding the particles. The optimum amount of dispersant in this case was chosen as 3 wt.% of BT powder which was also around 3 mg/m^2 related to the BT powder with a specific surface area of $9.6 \text{ m}^2/\text{g}$ based on the BET result. The dispersion with Darvan 821A showed more stabilization than that of EFKA 4540 from the results in Figures 3.1.8 and 3.1.9. The temperature of thermal decomposition by depolymerization of Darvan 821A is below $400 \text{ }^\circ\text{C}$ by performing a burnout test, which is allowing clean burnout with little residual carbon. Therefore, Darvan 821A at 0.06 vol.% (3 wt.% of ceramic powder) was selected as the best dispersant for use in subsequent barium titanate ink preparation.

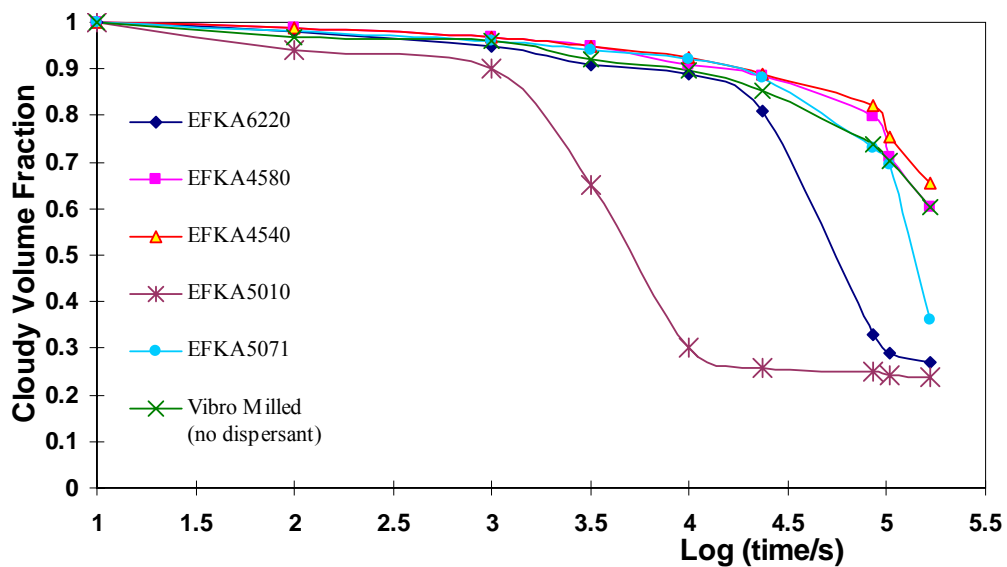


Figure 3.1.6 Cloudy volume fraction of test samples of BaTiO₃ powder dispersed using ultrasonication and using EFKA series dispersants. They are compared with a Vibro-milled suspension with no dispersant added.

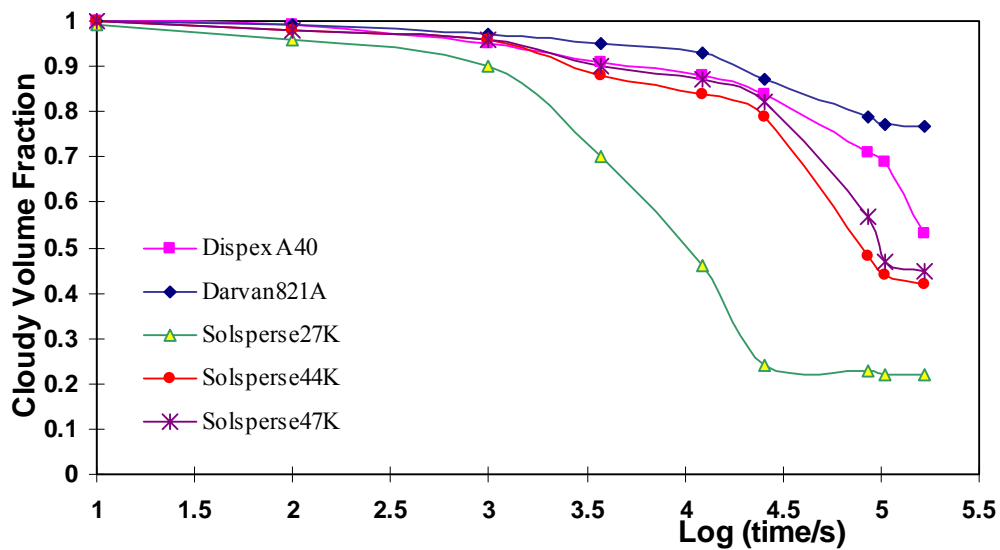


Figure 3.1.7 Cloudy volume fraction of test samples of BaTiO₃ powder dispersed using ultrasonication and using non EFKA type dispersants.

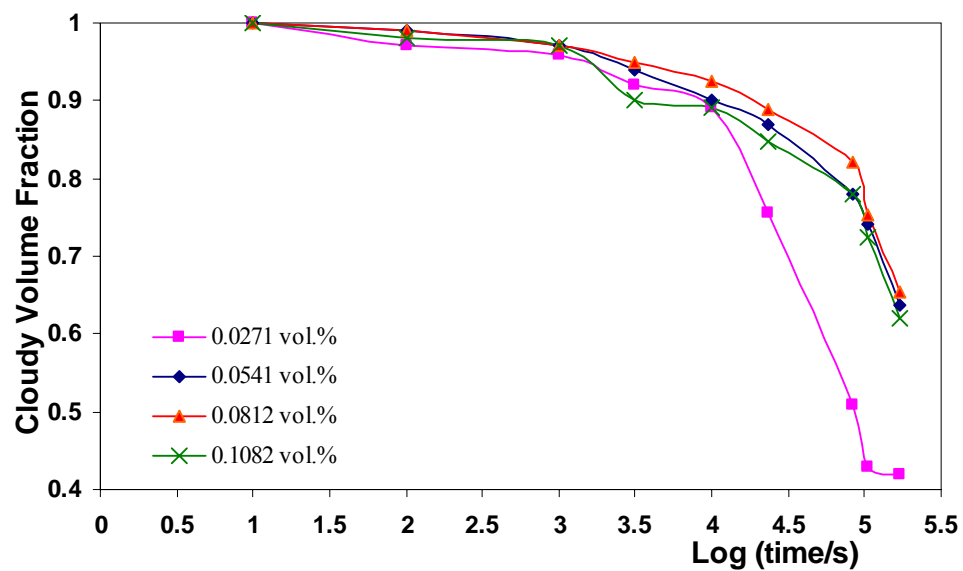


Figure 3.1.8 Stability of BaTiO₃ suspensions with different concentrations of EFKA 4540.

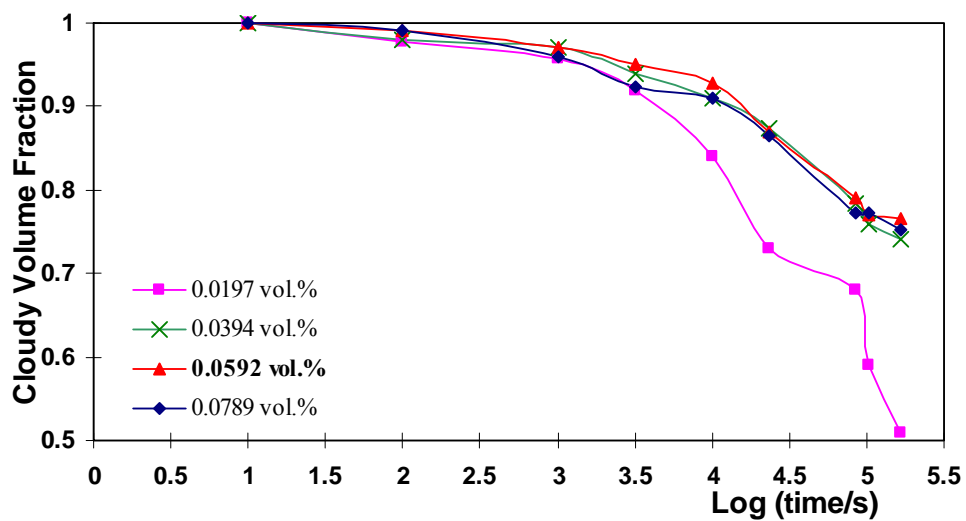


Figure 3.1.9 Stability of BaTiO₃ suspensions with different concentrations of Darvan 821A.

3.2 Control of Shape of Droplet Drying Pattern

Drying is a key step in colloidal processes that have been used to produce ceramic films and coatings. In the employment of ink-jet printing to fabricate the thick film ceramic combinatorial libraries, drying control is a more challenging topic because it not only can affect the induction of surface defects such as cracks, voids and pinholes etc⁹³; but also alter the figure of the drying residue in a printed sample. Various figures of drying pattern after drying the printed sessile droplet of ceramic ink have been reported. They form as doughnut shape,¹⁵⁸ well plate,⁴⁰⁸ arched pellet⁴⁰⁹ and dome-shape disc¹⁷⁶ etc. In this project, the distribution of dopant salt via subsequent infiltration doping is dependent upon the homogeneity of the structure of the green base; furthermore, the structure of the sample can also determine the accuracy of subsequent electrical characterization for the purpose of screening the PTCR effect of as-sintered samples. Therefore, disc-like or dome-shaped structures of the green body of ceramic samples with high green density are required.

3.2.1 Drying-induced Forming Agent Selection

Organic binder which is so-called a ‘film-forming’ additive is necessary for use with ceramic materials to assure sample integrity after drying and to attain adequate levels of handling strength. Polyvinyl alcohol (PVA) and methyl cellulose (MC) are widely used as the aqueous-based binder in ceramic casting processing. Hence they were tested to investigate the effect on drying residue of BT dispersion droplet by dip-pen printing.

It was reported that up to 10 wt.% of the binder based on ceramic powder is used in tape casting.⁴¹⁰ Various concentrations of binder were tested here to investigate the

effect on controlling the drying pattern. Figure 3.2.1 shows the morphology of an as-dried BT green disc from a printed droplet (ink 1) with a volume of 30 μL . This tablet was examined by a binocular microscope. There was a big crater in the centre of the sample and a peripheral ring. The configurations of the drying patterns with varying compositions are also described in Table 3.2.1.

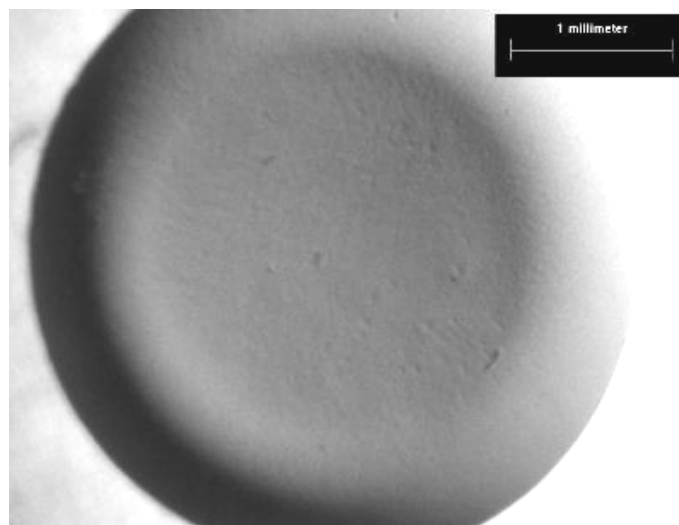


Figure 3.2.1 Binocular microscope image of the as-dried BaTiO₃ tablet sample.

The drying patterns of the printed droplets with different forming agents were various. Inks with PVA had generally smooth surface but a shallow sink in the centre. The depth of the sink was increased with the content of PVA in the ink. Inks with MC had macroscopic cracks on the top as-dried surface and deep crater in the middle; furthermore, when increasing the content of MC, a ‘well plate’ shape which having a through hole in the centre was formed. BT dispersions using Acrysol RM12W generally showed more homogeneous structure than those using other binders. There were relatively flat disc-like drying patterns formed by samples with Acrysol RM12W.

Table 3.2.1. The configurations of the drying residue of the ink with varying compositions.

Ink No.	Forming agent	Agent concentration ^a	Configuration of the as-dried sample
1	PVA	2 wt.%	Big and shallow sink
2	PVA	4 wt.%	Big and shallow sink
3	PVA	6 wt.%	Big and deep sink
4	PVA	8 wt.%	Big and deep sink
5	Methyl cellulose	2 wt.%	Deep crater and macroscopic cracks
6	Methyl cellulose	3 wt.%	Well plate shape
7	Acrysol RM12W	2 wt.%	Shallow crater
8	Acrysol RM12W	3 wt.%	Insignificant crater
9	Acrysol RM12W	4 wt.%	Insignificant crater

^a In the weight of BaTiO₃ powder

Inks using PVA (2 wt.% based on BaTiO₃ powder) and Acrysol RM12W (3 wt.% based on BaTiO₃ powder) were then printed in various volumes and the configurations of their drying residues are described in Table 3.2.2. The drying pattern of the BT ink with PVA was independent upon the printing volume based on the observation. However, for the ink contained Acrysol RM12W, there was a deteriorative effect on the surface quality after drying when increasing the printed volume of the ink. Macroscopic cracks were formed on the top surface of the dried ink with Acrysol RM12W from the printed volume larger than 100 μ L.

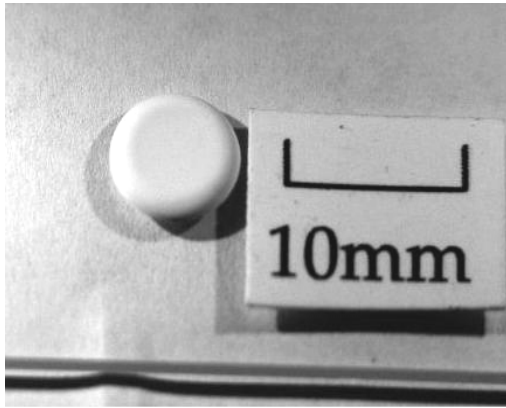
Table 3.2.2. The configurations of the drying residue of the ink with different volume.

Ink No.	Ink volume / μL	Forming agent	Configuration of the as-dried sample
10	50	PVA	Big crater
11	100	PVA	Big crater
12	200	PVA	Big crater
13	50	Acrysol RM12W	Little crater
14	100	Acrysol RM12W	Small crater and macroscopic cracks
15	200	Acrysol RM12W	Small crater and centre cracking

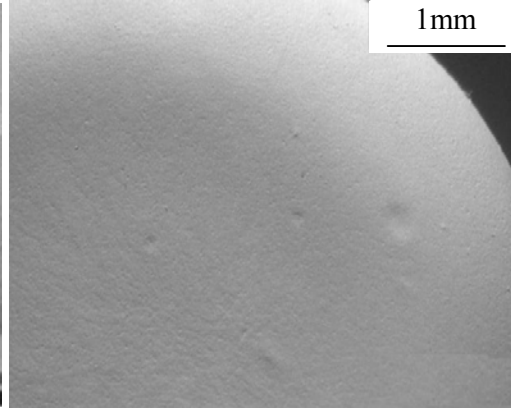
As the drying proceeds, in-plane tensile stresses develop within the printed droplet because of the constrained volume shrinkage. The solid network of the BaTiO_3 droplet is subjected to two forces: one is the compressive stress contributed by the capillary pressure induced from pore water evaporation to contract the body, while the other is the tensile stress generated by the substrate to resist the in-plane shrinkage due to the self pinning effect.¹⁶¹ Hence, the onset of cracking along with other surface defects such as curling and warping caused by the volume shrinkage during drying are dependent upon the magnitude of the misfit in-plane strain and the time at which it occurs. The possible solutions to cracking are reducing solvent content (thereby reducing volumetric shrinkage), increasing polymer binder content (thereby increasing matrix strength) and slowing the drying rate to allow more solvent to leave the matrix prior to gelation which can reduce the heterogeneous volumetric shrinkage during drying. Therefore, a covered container with saturated moisture was used to store the printed droplets contained Acrysol RM12W during drying. In addition, the crater-structure of drying residue is due to lateral particle motion while drying for which the details are discussed in the next section.

BaTiO_3 dispersions containing different solid contents using Acrysol RM12W as a

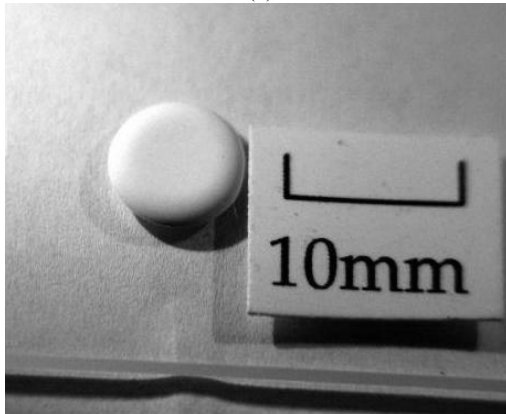
thixotropic agent were dip-pen printed in a volume of 100 μL on silicone release paper. The photographs of their corresponding drying residue are presented in Figure 3.2.2. The function of the thixotropic agent was to change the flow processes occurring during droplet drying to inhibit the radial flow to the periphery of the droplet which causes a bowl shape to result after drying.⁴¹¹ It was observed that the higher the solid content, the less sagging behaviour of the droplet drying pattern. The drying residue of ink with solid content of 40 wt.% had a crater in the centre compared with the wavelike drained surface of as-dried disc from the ink contained 45 wt.% of BaTiO_3 . A surface with minor wrinkling was observed for discs drying from the ink with solid content of 50 wt.%. The green sample having a top flat surface as a drying pattern was obtained when increasing the ink solid content above 50 wt.%. Ink contained 55 wt.% BT powder presented the best surface quality and homogeneous structure as seen in Figure 3.2.2(h). However, when the solid content was increased to 60 wt.% in dispersion, many pinholes and orange peel features appeared on the surface. Therefore, BT dispersion with solid content around 55 wt.% using Acrysol RM12W and Darvan 821A as polymer additive as ink 18 in Table 2.2.4 was used for the fabrication of porous BaTiO_3 base disc using the dip-pen printing method in subsequent experiments.



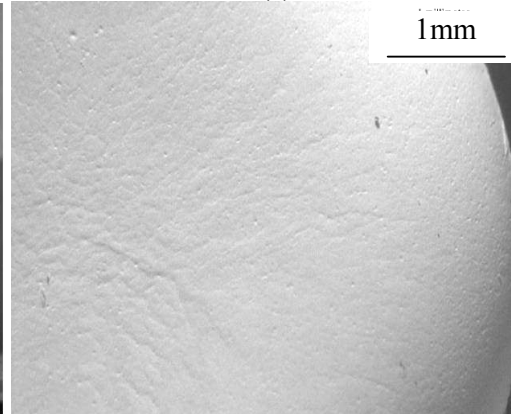
(a)



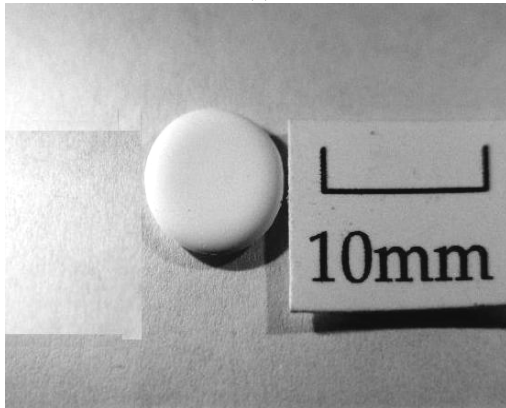
(b)



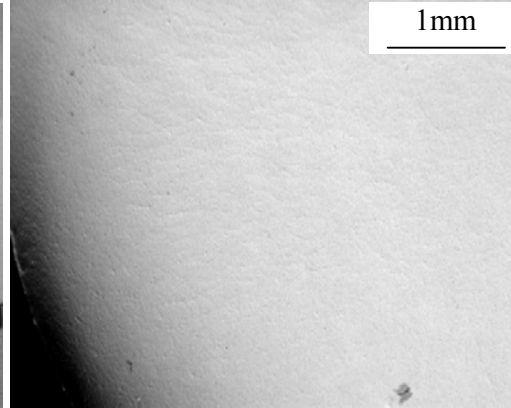
(c)



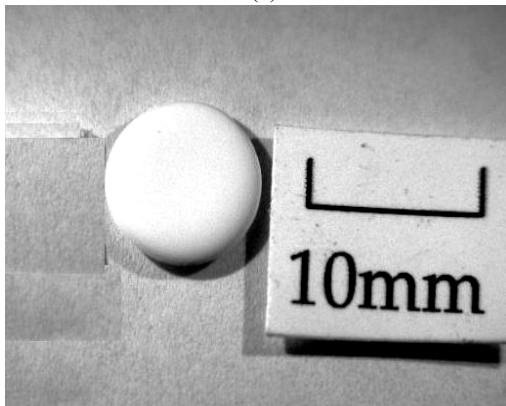
(d)



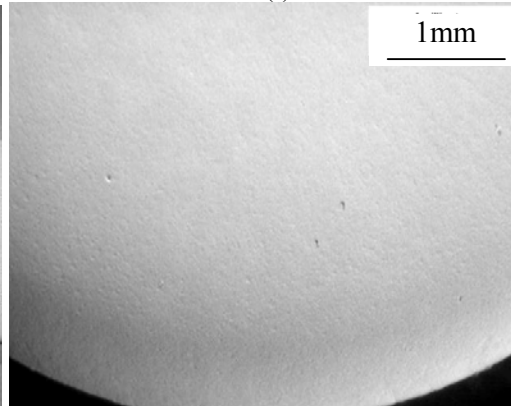
(e)



(f)



(g)



(h)

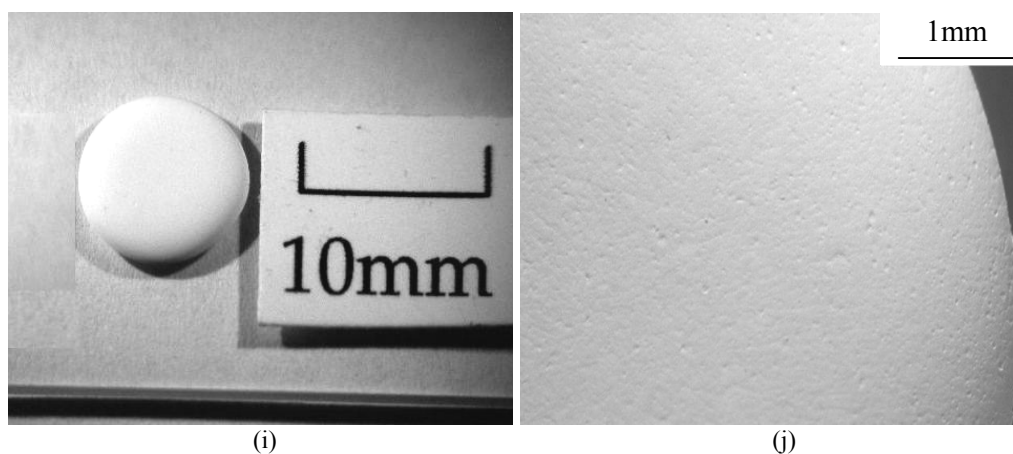


Figure 3.2.2 Photograph of as-dried BaTiO₃ droplet with different solid contents of (a) 40 wt.%, (c) 45 wt.%, (e) 50 wt.%, (g) 55 wt.% and (i) 60 wt.%. The details of their corresponding magnified top surfaces are displayed respectively in image (b), (d), (f), (h) and (j).

3.2.2 Discussion

Similar “doughnut” shapes of drying residue from colloidal ceramic film with PVA or MC as forming agent were reported in previously studies.^{153, 412, 413} Chiu⁴¹⁴ observed that three regions (supersaturated, saturated and semi-dry) can be identified during drying of ceramic dispersion, as illustrated schematically in Figure 3.2.3. The supersaturated region is defined as $\Phi < \Phi_{\text{sat}}$, where the volume fraction of solids (Φ) in the supersaturated region is lower than that at 100% saturation area. At this stage, the particles network has either not formed or yet been fully consolidated. The saturated region is defined as $\Phi = \Phi_{\text{sat}}$. In this case, consolidation of the particle network ceases and the remaining pore channels are filled with solvent. As drying proceeded, the semi-dry region (>100% saturation) emerged, which is accompanied by the retreat of the liquid/vapour meniscus into the body. In this case, the largest pores connected to the film surface drained preferentially as liquid is drawn to smaller pores of higher suction potential. For a printed sessile drop here, which

contains a circular-arc edge as displayed in Figure 3.2.3, the BT particles become semi-dry at the peripheral ring while the disc centre is still in a supersaturated state during drying because of the differential evaporation rate.⁴¹⁵ Lateral flow is then induced from the central region to the peripheral edge caused by the capillary force during evaporation; therefore, free particles entrained in the liquid phase migrate to and, ultimately, deposit at the edge leading to a non-uniformity in the spatial distribution of colloidal particles after drying.

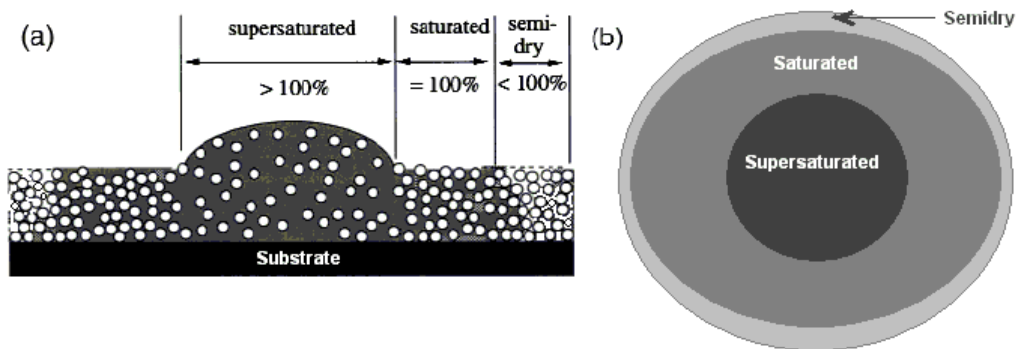


Figure 3.2.3. Schematic illustration of a drying disc outlining regions of varying saturation: (a) cross-section and (b) top view.⁴¹²

There are four types of particle motion in a colloidal droplet sample during drying. The first is sedimentation as particles aggregate on the bottom of the droplet due to the gravity effect. The second is Brownian motion which is a random movement of particles suspended in a colloidal fluid. It is caused by the bombardment of solvent molecules on particles and the effect of their own electromagnetic forces applied on each other. The third is lateral flow of liquid containing particles to the periphery of the droplet driven by capillary force to produce “doughnut” shape.^{158, 175, 408} The fourth is recirculation flow that takes place in the supersaturated region driven by Marangoni flow.^{168, 169}

According to the Stokes-Einstein equation,⁴¹⁶ the diffusion coefficient of Brownian motion of spherical particles, D , can be defined as

$$D = \frac{k_B T_a}{6\pi\eta a} \quad \text{Equation 3.2.1}$$

where k_B is the Boltzmann constant ($\text{J}\cdot\text{K}^{-1}$), T_a is the absolute temperature (K), η is the dynamic viscosity ($\text{Pa}\cdot\text{s}$) and a is the particle radius (m). Moreover, with the notification that the particle motion in x, y and z direction is independent, the mean square route of a particle migration by random Brownian diffusion during a time t can be defined as⁴¹⁷

$$r_x^2 = r_y^2 = r_z^2 = Dt \quad \text{Equation 3.2.2}$$

The slow sedimentation of suspensions of solid particles in a fluid is a complex phenomenon. The sedimentation velocity can be estimated by a simplified model which the gravitational potential energy gained as the particle moving up or down relative to the background suspension medium is equivalent to the energy lost to viscous dissipation caused by the particle motion due to shear.⁴¹⁸ Therefore, in a steady state system, the rate of energy gain, $dE_g/dt = \Delta\rho Vg\bar{v}$, equals with the rate of energy dissipation, $dE_\eta/dt = 6\pi\eta a\bar{v}^2$, where $\Delta\rho$ is the density difference between the particles and solvent, \bar{v} is the average velocity of particle, V is the particle volume and g is the gravitational acceleration. This leads to:

$$\bar{v} = \frac{\Delta\rho Vg}{6\pi\eta a} \quad \text{Equation 3.2.3}$$

Assuming the barium titanate particle is a sphere shape, hence the volume $V = 4\pi a^3/3$ and the velocity \bar{v} in Equation 3.2.3 can be rearranged:

$$\bar{v} = \frac{2\Delta\rho g a^2}{9\eta} \quad \text{Equation 3.2.4}$$

Given the radius of BT particle is 0.25 μm (from Z-average size value in Table 3.1.2), the density of BT powder is 6020 $\text{kg}\cdot\text{m}^{-3}$, T is around 300 K, dynamic viscosity of a dispersion containing 45 wt.% BT powder is 60 $\text{mPa}\cdot\text{s}$ ^{410, 419} and the height (r_z) of a 30 μL droplet is ≈ 2 mm; the value of diffusion coefficient D in this case is 1.46×10^{-12} m^2/s (calculated from Equation 3.2.1). Thus the time scale for a BT particle travelling from the top of the droplet to the bottom substrate by Brownian motion only is to take about 760 hours (calculated from Equation 3.2.2). However, the average velocity for particle sedimentation in this dispersion is around 1.2×10^{-8} m/s (Equation 3.2.4); hence it would allow 47 hours to let a particle travel from the top region of suspension to the bottom under the gravity effect. Therefore, it is confirmed that the thermally induced Brownian motion is negligible compared to gravitational settling in this case. Furthermore, noting that when the particle size in dispersion doubles (which is readily occurred due to the agglomerate reforming), the time scale related to Brownian motion would be double whereas the sedimentation settling would last only a quarter according to the equations above, which shows more insignificance of the Brownian effect of particle motion on the drying pattern.

The structure of the drying residue of ceramic suspensions results from the particle migration during drying which is driven by multiple forces such as gravity, capillary stresses and Marangoni stresses. The recirculating flow in a sessile droplet can be active when Marangoni stresses are created by establishing a surface tension gradient during drying. The magnitude of such Marangoni flow is determined by the Marangoni number:

$$M = \frac{\Delta\gamma L}{\eta D} \quad \text{Equation 3.2.5}$$

where $\Delta\gamma$ is the surface tension difference, L is the length scale involved (2 mm), η is the viscosity and D is the Stokes-Einstein diffusion coefficient. Using the values given above for L , η and D , M is of the order $10^{10}\Delta\gamma$. It shows that even a very small surface tension gradient will trigger a Marangoni flow. Surface tension gradient in an aqueous sessile droplet during drying is established caused by the temperature gradient throughout the droplet due to differential evaporation rate. According to Eötvös rule:⁴²⁰

$$\gamma V^{2/3} = k(T_c - T) \quad \text{Equation 3.2.6}$$

where γ is the surface tension, V is the molar volume of the liquid given by the molar mass M divided by the density ρ ($V = M/\rho$), k is the Eötvös constant with a value of $2.1 \times 10^{-7} \text{ (JK}^{-1}\text{ mol}^{-2/3}\text{)}$ for all liquid and T_c is the critical temperature. Hence,

$$\Delta\gamma = \frac{k}{V^{2/3}} \Delta T \quad \text{Equation 3.2.7}$$

where ΔT is the temperature gradient within an aqueous droplet during evaporative drying and depends on the contact angle and external environment.¹⁶⁸ Therefore, even a very tiny temperature difference such as 0.001K which is very likely to occur across the drying droplet surface can generate a significant Marangoni effect with very big Marangoni number ($M \approx 3 \times 10^3$) far beyond a critical value M_c which is typically less than 100 and recirculating flow can be propelled.⁴²¹

However, the Marangoni flow is readily suppressed by a very little amount of surfactant particularly in aqueous dispersion.¹⁶⁸ Thus lateral flow from centre to the periphery of droplet due to capillary forces is dominated during drying. This can well explain the phenomenon that nonuniform structures of drying residues particularly

from well-dispersed ceramic dispersion are formed.⁴⁰⁸

Various methods attempting to obtain dome-like patterns after drying from ceramic suspension have been tested by many workers. Wang and Evans⁴²² used a porous substrate, Fair and Lange⁴²³ added electrolyte salt, Wang and Evans⁴²⁴ used excess dispersant in order to enhance the speed of particle sedimentation by inducing extra flocculation leading to the similar outcome which had a spherical geometry and uniform structure after droplet drying. However its low green density does not sound ideal for the further doping and sintering processes. Park¹⁷⁶ and Schubert¹⁷⁵ used bi-solvent systems which have different surface tension values in different solvents and successfully obtained a dome-like structure pattern. However, this is not applicable to all ceramic powders, and besides, the carbon residues after polymer burn-out treatment generated from the non-aqueous solvent such as formamide among them may deteriorate the electrical properties of final ceramic products. Moreover, Haw¹⁷⁴ found that a homogeneous structure of the final drying residue can be achieved when the whole drying period stayed in the gelation region of the sessile droplet. The mobility of free particles in suspension is strongly restricted by a highly viscous gel network and hence impedes the capillary-driven structural rearrangement during drying. According to this theory, a ceramic dispersion which has high viscosity or promptly turns to gel state can be used to retain a homogeneous structure after drying without compromising the stability of ink by adding flocculation accelerators or manoeuvring the Marangoni flow by adding foreign solvent to purposely create surface tension gradients. However, the printability feature of the viscous ink must be taken into account. Hence, a polymer like Acrysol RM12W which also acts as a thixotropy agent is an ideal choice here.

3.2.3 Characterization of Green BaTiO₃ Disc after Polymer-burnout

The densities of the green BT discs drying from the printed droplet of ink 18 in different volumes were measured. The corresponding porosity results are presented in Table 3.2.3. It was found that the porosity of the green BT base slightly increased with the increase of the printed droplet's volume and it had an average value of 55%. The porosity results showed minor dependence on the printed ink volume whereas the standard deviation increased with the printed droplet's volumes. There is an important source of inaccuracy in performing this buoyancy method: the external water-resistant wax film. When there was wax infiltrated into some pores in the BT tablet body, the calculated density would be higher than the actual value leading to an underestimated porosity value. On the other hand, if the wax incompletely covered the entire outer surface of porous base, water may be sucked in to fill pores also leading to a higher-than-actual value of measured density; in other words, underestimating the porosity in the system. Noting that such buoyancy method is only ideal for measuring the density of solid dense sample, other technique such as helium pycnometry may be needed for further investigation.

Table 3.2.3. The porosity of green BT samples by buoyancy method

Sample ref.	Ink No.	Ink volume / μ L	Standard Deviation	P _{mean}
S1	18	50	2%	54%
S2	18	100	4%	55%
S3	18	200	4%	57%

The pore size distribution of green BT samples (S1 in Table 3.2.3) was determined by mercury intrusion porosimetry. The total open porosity of the sample was obtained from the cumulative porosity curve corresponds to the point of highest

pressure and the smallest equivalent pore size. The total Hg intrusion volume density (V_d) within green BT sample was 0.17 mL/g (as seen in Figure 3.2.4) which is approximately equivalent to the open pore volume density within the tested samples. The porosity can be calculated from the equation 3.2.8. Thus the average open pores volume ratio (V_{pores}) is 51%.

$$V_{pores} \% = \frac{mV_d}{mV_d + m / \rho_{th}} \times 100\% = \frac{V_d}{V_d + 1 / \rho_{th}} \times 100\% \quad \text{Equation 3.2.8}$$

where m is the weight of the tested samples. The value of the porosity examined by Hg porosimetry is close to the results from the buoyancy method. Hence the porosity of the BT base dried from ink 18 as 55% was accepted for further studies. Figure 3.2.4 also displays the pore size distribution of the green BT base examined by mercury intrusion porosimetry. The critical pores size corresponds to the steepest slope of the cumulative porosity curve(B) shown in Figure 3.2.4, in which the corresponding logarithm differential intrusion curve(A) versus the pore diameters was replotted in Figure 3.2.4. There is a bimodal distribution of pore sizes in the porous system. The first is at $\sim 0.12 \mu\text{m}$ determined by the main peak in curve A and corresponds to inter-cluster pore between small ($1 \mu\text{m}$) clusters of particles. A second very small peak can just be seen at $\sim 60 \mu\text{m}$, which from SEM observation can be attributed to near-spherical voids possibly originating from bubbles in the ink. Moreover, the pores with diameter around $0.12 \mu\text{m}$ contribute about 80% of the total pore volume.

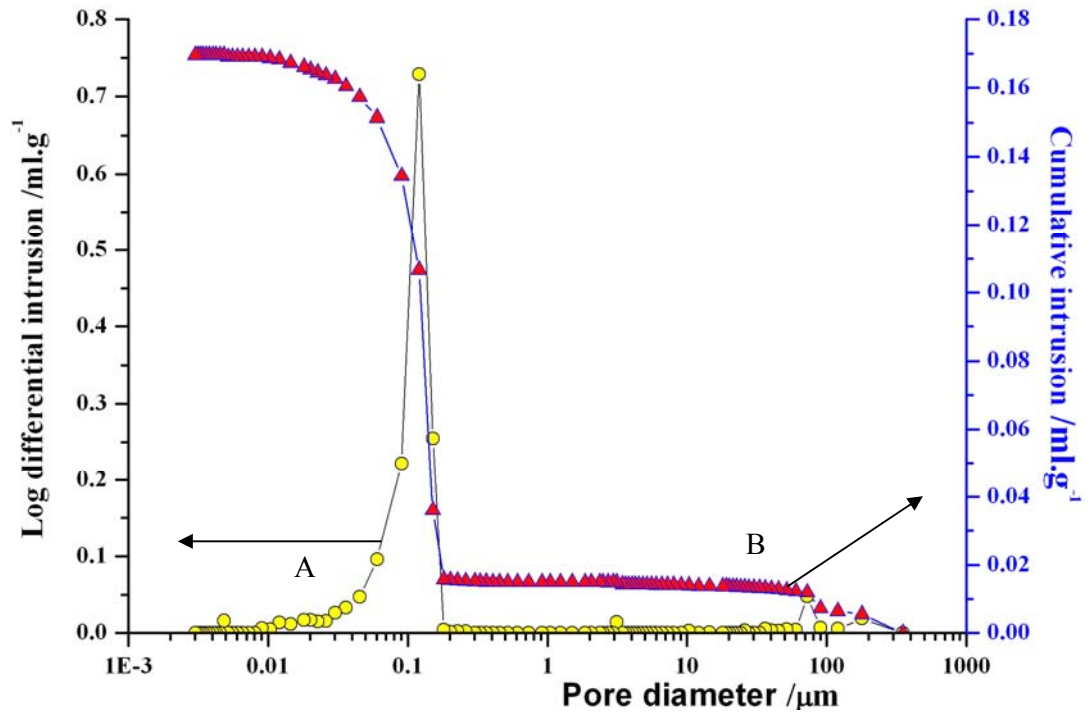


Figure 3.2.4. The pore size distribution of as-dried BaTiO₃ disc-shaped sample: log differential pore size distribution (A) and cumulative pore size distribution (B).

3.3 Investigation of Dopant Distribution in Porous BT Base via a Droplet-doping Method

The conventional doping techniques in fabrication of doped-BT PTCR ceramics include oxide mixing, sol-gel processing etc., which all need consistently strong external forces e.g. milling, stirring etc. during the preparation. Furthermore, such conventional methods have a common drawback that only one composition can be made at a time. In combinatorial donor-doped BT PTCR materials research, it is beneficial to be able to produce samples with a range of doping levels quickly and efficiently. The aim of this work is therefore to establish a high-throughput synthesis method suitable for low doping levels and directed to construction of libraries of donor-doped BaTiO₃ ceramics in order to discover new BaTiO₃-based PTCR materials. Infiltration doping which under the right circumstances can produce a range of different dopant levels in ceramics for various functions and properties were used. The nitrate salt of dopant cations was chosen here to prepare the liquid dopant precursor because it is well soluble in water and readily pyrolyzed to its oxide during subsequent heat treatment leaving minimum residues. Pure BaTiO₃ is an insulating material at room temperature, whereas it can turn to be a semiconducting material by doping with various donor dopants at relatively low doping levels and it can revert back to behaving as an insulator when the donor content exceeds the critical concentration which normally is only 0.5 mol.% for most of the donor candidates. Such low doping level makes it difficult to be characterized by common compositional characterization techniques such as SEM/EDS.

3.3.1 Droplet-doping Method

The uniformity of dopant salt distribution in the porous BT disc using droplet-doping

method is partly determined by the distribution of the infiltrating fluid into the base. In order to achieve a uniform distribution of dopant solution throughout the body of the porous base, the volume of the infiltrating solution must be equal to the total volume of the pores in the base which is determined by its porosity. If the dopant solution is less than this ideal volume, insufficient liquid is available to fully infiltrate the body of the porous disc and this adversely affects the homogeneity of distribution of dopant. If the volume of dopant solution exceeds this level, excess liquid remains on the outer surface of the disc. This dries and leaves a thin film of solute on the surface which reduces the effective dopant concentration compared with the planned concentration and places an excess in the surface region. A preliminary infiltration experiment was conducted using an aqueous red ink by dissolving red food colouring in distilled water. Different amounts of the ink were printed on the green BT porous disc. This provided a distinct colour contrast such that saturated and unfilled regions could be visually distinguished. Observations of the outside surface and fracture surface revealed that the saturated red ink quickly percolates into the body to form a uniform colour. If less than the total pore volume was added, there was a darker colour at the bottom and lighter colour at the top which witnesses non-uniform distribution of 'dopant' in the case of insufficient doping as shown schematically in Figure 3.3.1(c). Over-doping resulted in a large amount of coloured dye on the upper surface displayed as a darker colour (Figure 3.3.1(d)). Moreover, the ideal volume of dopant solution can be dispensed onto the disc in one drop at the centre (Figure 3.3.1(b)), or by printing multiple small drops at various locations (Figure 3.3.1(a)) on the surface. In the latter method, the coverage of ink over the surface of the porous base provides more uniform distribution than that of the single droplet due to the spreading effect as discussed in a subsequent section.

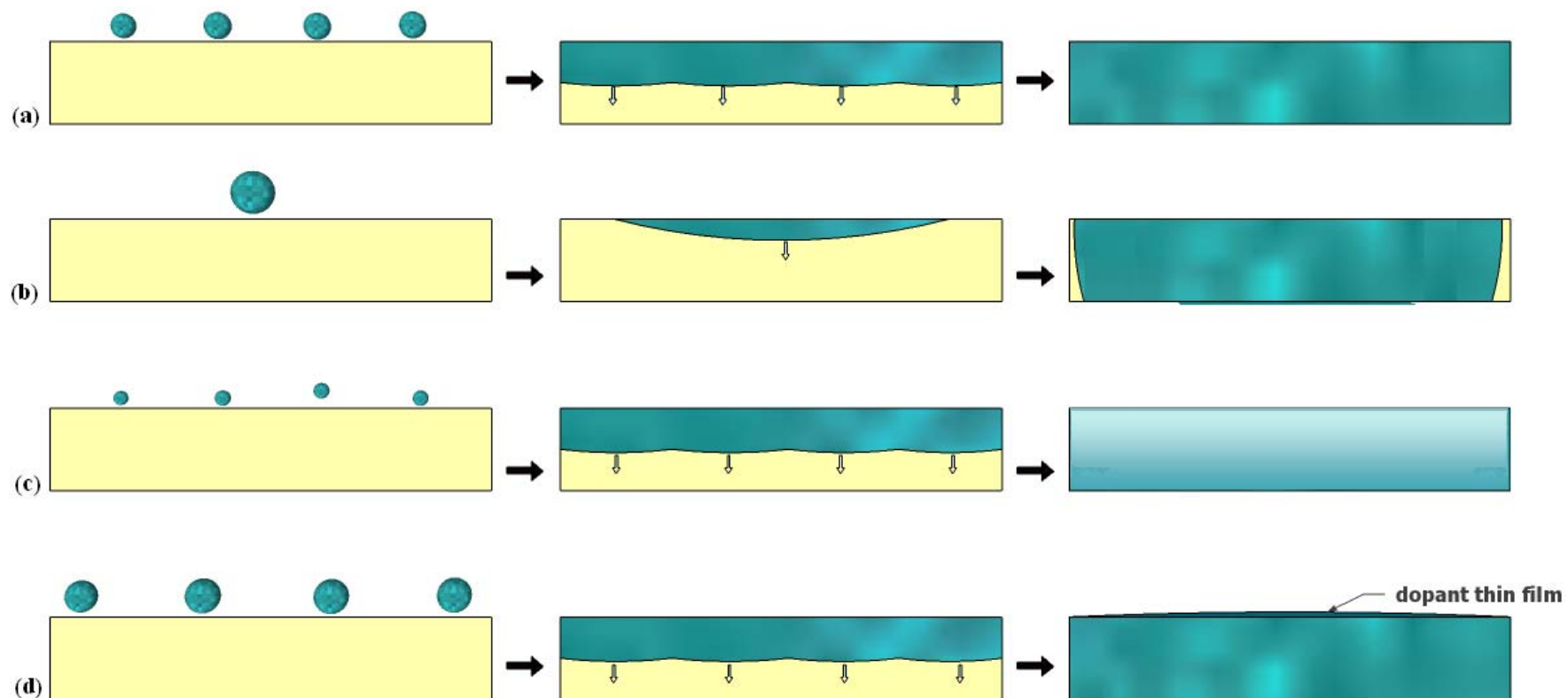


Figure 3.3.1 Schematic diagram of the BT porous base infiltration with saturated ink of dopant liquid precursor: (a) ideal condition; (b) single drop printing; (c) insufficient ink printing; (d) over saturated ink printing.

3.3.2 Characterization of Erbium-doped BaTiO₃ Ceramics

3.3.2.1 STA Measurements

Figures 3.3.2-4 present the differential thermal analysis (DTA) and thermogravimetric analysis (TGA) data as a function of temperature for samples with various erbium concentrations. Both DTA and TGA curves for each sample were recorded simultaneously. Several stages in the decomposition can be seen. The hydrated Er(NO₃)₃ is very hygroscopic, thus as-dried doped-BT porous sample readily adsorbed moisture from atmosphere which can explain the initial weight loss occurring below 100 °C in Figures 3.3.2-4. The erbium nitrate pentahydrate is gradually losing the hydrates during heating and the whole thermal decomposition procedure ends at around 550 °C confirmed by both the DTA and TGA results shown in Figures 3.3.2-4 and this is also in line with the values in literature.⁴²⁵ There were exothermic peaks at around 1100 °C detected by DTA on samples regardless the doping level which might be due to the occurrence of the diffusion of dopant ion into the BT lattice.⁴²⁶ Thus it indicated the onset of calcination of Er-doped BT which is analogous with the results in literature.²⁶⁵ Note that XRD method may be needed to confirm the validity of such calcination temperature by examining the purity of phase of the powders after being fired at 1100 °C. There was a slight difference in temperature according to the exothermic peaks between the samples of 0.1 and 8 mol.% Er-doped BT (1060 °C) and the BT sample doped with 1 mol.% Er (1110 °C). This might be due to the differences in experiment settings. The heating rate of DTA test for BT discs doped with 0.1 and 8 mol.% Er was 10 °C/min compared with 5 °C/min for which the samples contained 1 mol.% Er.

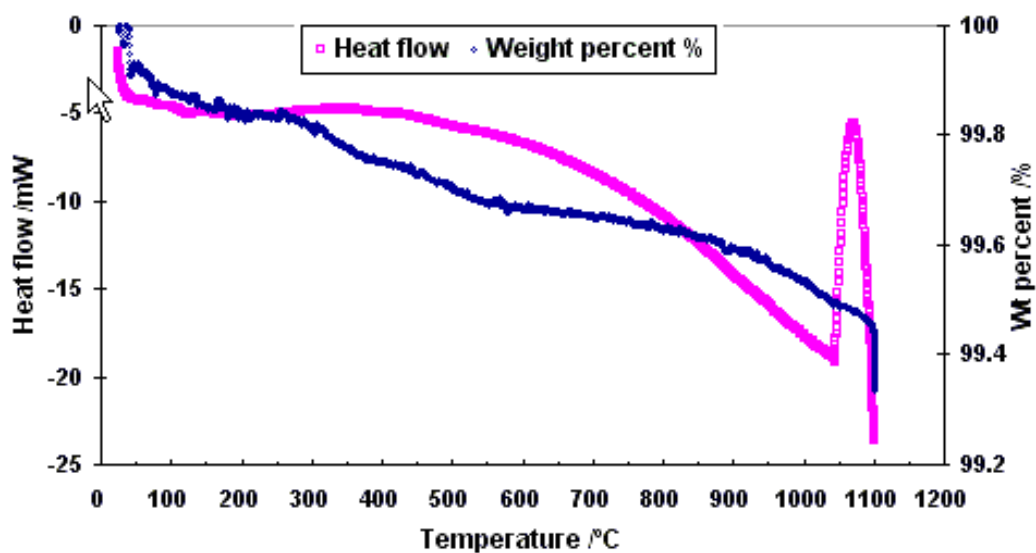


Figure 3.3.2 The DTA curve and thermogravimetry for 0.1 mol.% Er-doped BT via droplet doping method.

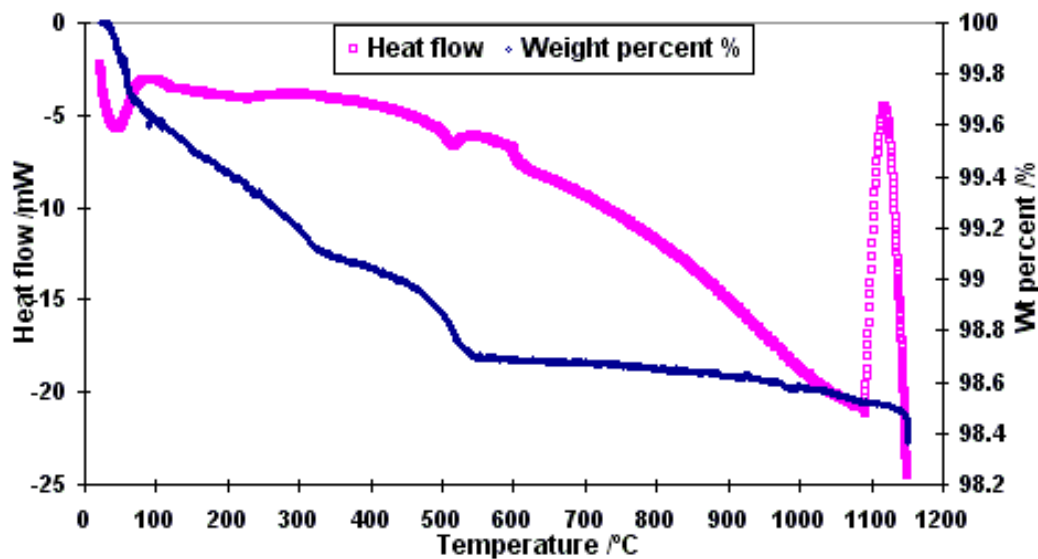


Figure 3.3.3 The DTA curve and thermogravimetry for 1 mol.% Er-doped BT via droplet doping method.

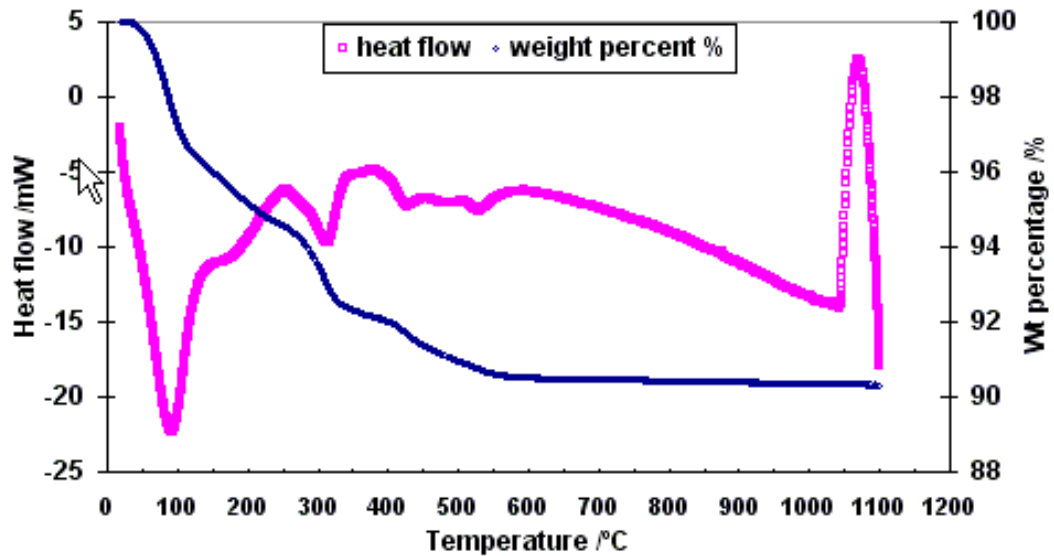


Figure 3.3.4 The DTA curve and thermogravimetry for 8 mol.% Er-doped BT via droplet doping method.

3.3.2.2 Structures and Microstructures

Er-doped BT samples under both light doping and high doping levels can maintain a disc structure after sintering, whereas samples with intermediate dopant concentration (1-2 mol.%) were deformed substantially as seen in Figure 3.3.5. Figure 3.3.5(a) shows the morphologies of Er-doped BT with erbium content of 0, 1, 2 and 5 mol.% respectively sintered at 1350 °C for 2 hours. Highly-doped BT (5 mol.%) was not fully sintered at this temperature as it still maintained a loose structure after firing. However, samples with lower Er^{3+} concentration can be well sintered at 1350 °C. According to the appearance, there was little difference for samples with low doping level (≤ 2 mol.%) sintered at various temperatures. Furthermore, the BT disc with 5 mol.% Er^{3+} content can reach dense structure when increasing the sintering temperature to above 1450 °C. The warping effect of erbium-doped BT with intermediate erbium content was caused by the inhomogeneous volume shrinkage over the curved surface of the specimen during densification. The

span ratio (diameter over thickness) of these erbium-doped BT samples produced by dip-pen printing was around 13 (diameter ~8mm and thickness ~0.6mm). The discs with such a large span ratio may deteriorate the strength against the geometric distortion caused by the strains generated during sintering. Reducing the size of BT disc by printing less ink can significantly reduce the span ratio thereafter and this may improve the heterogeneous deformation during sintering. The heterogeneous volume shrinkage across the body of doped-BT disc during sintering may be caused by non-uniform compositional distribution throughout the body in the droplet-doping method; however, this assumption can hardly explain the sustainable flat structure of samples containing even heavier doping levels (5 mol.% Er-doped BT sample in Figure 3.3.5).

Figure 3.3.6 displays the microstructures on the fracture surface of erbium-doped BT samples with various doping concentrations sintered at 1350 °C for 2 hours. A high density of pores was observed on the fracture surface of BT samples with a variety of erbium contents. The pore size generally increased with the erbium concentration. Figure 3.3.7 shows the morphologies of fracture surfaces of undoped BT samples sintered at various temperatures. It was observed that the pore size and pore density were significantly reduced when increasing the sintering temperature and dwell time. The highly doped BT sample (5 mol.% Er³⁺) which was not fully sintered at 1350 °C was then sintered at 1450 and 1500 °C respectively. It finally reached a dense structure when sintered at 1500 °C for 4 hours and the corresponding microstructures are displayed in Figure 3.3.8.

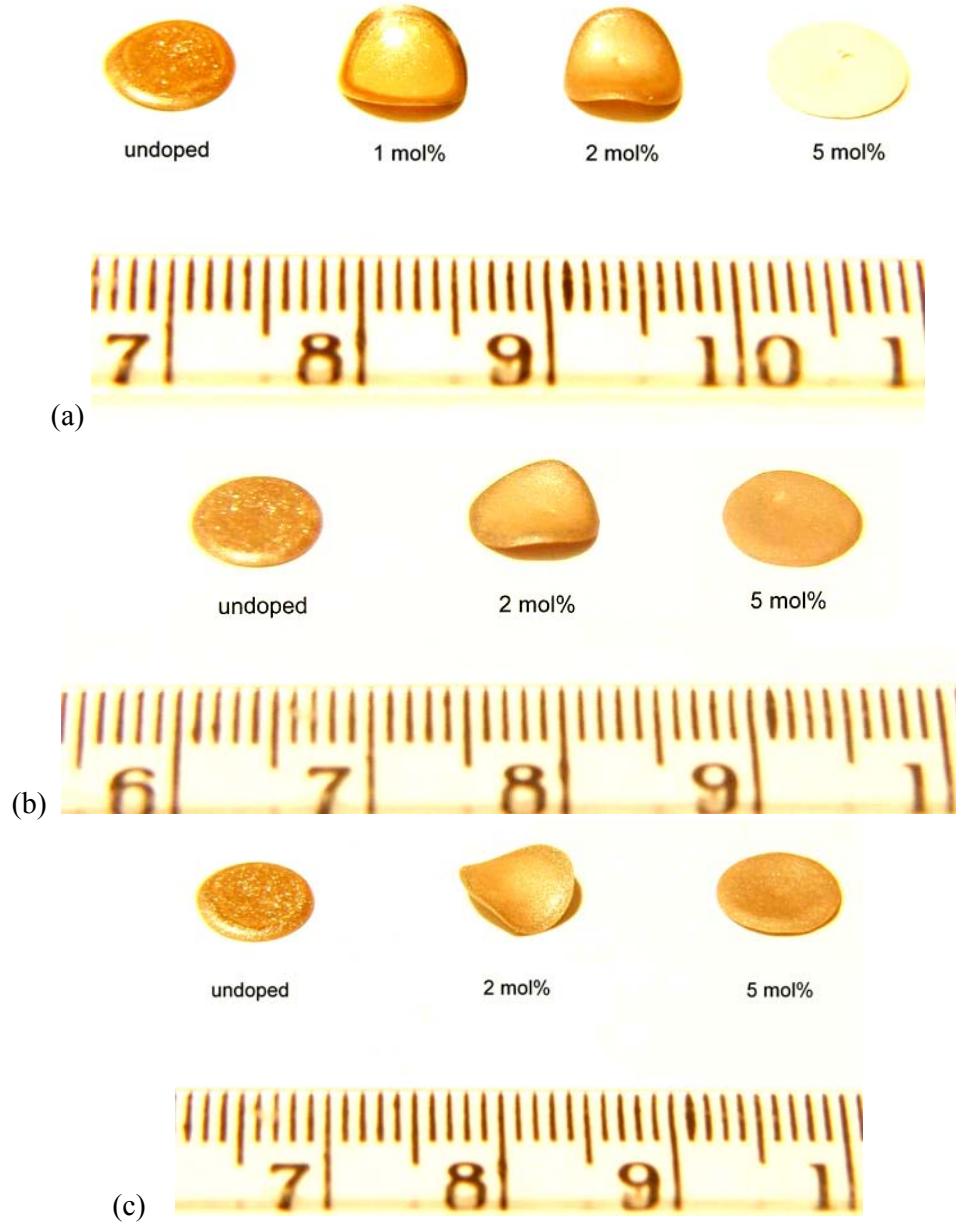


Fig 3.3.5 The shape of as-sintered Er-doped BT with various concentrations: (a) sintered at 1350 °C for 2h, (b) sintered at 1450 °C for 4h, (c) sintered at 1500 °C for 4h.

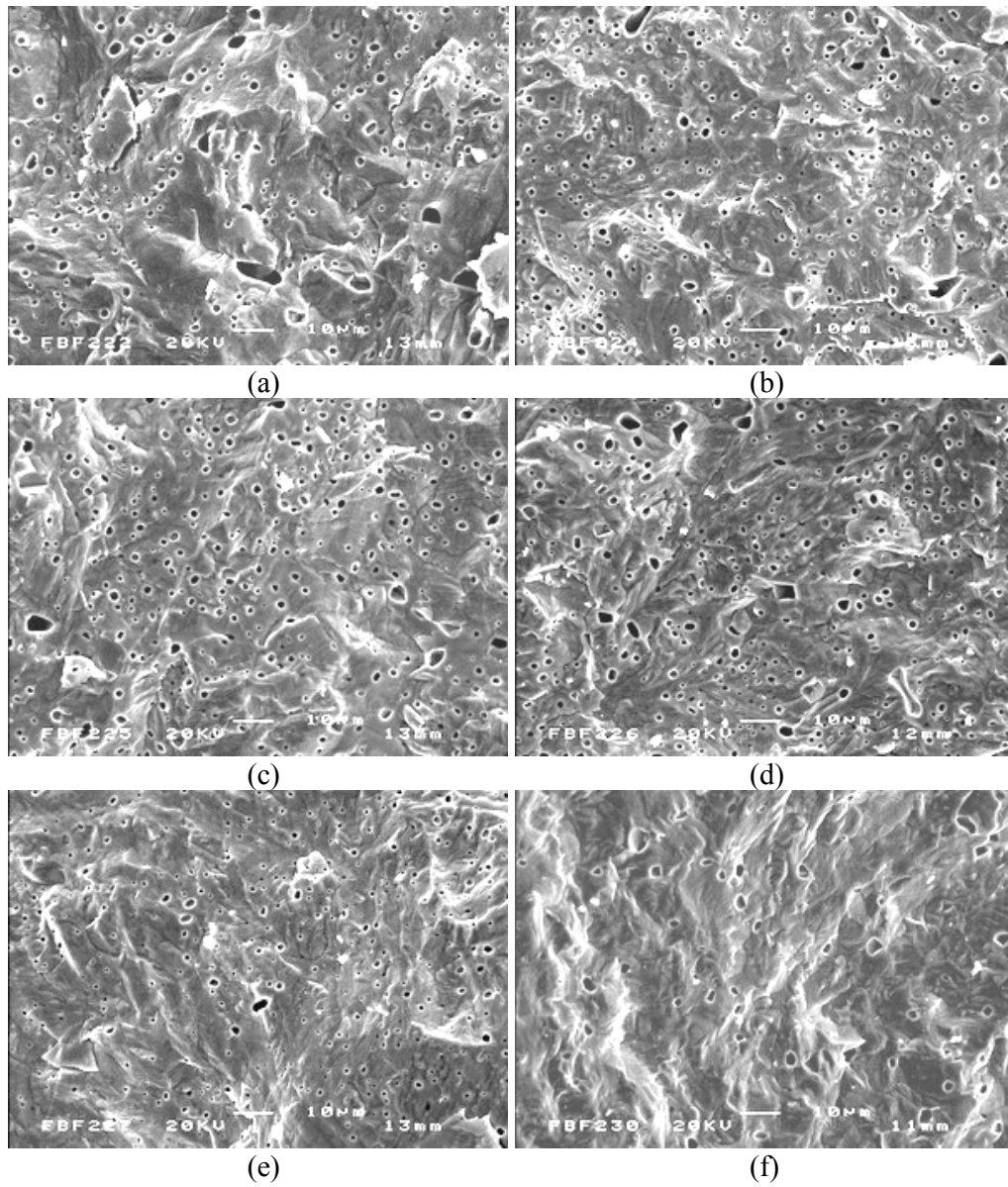


Figure 3.3.6 The microstructure of fracture surfaces of erbium-doped BT sintered at 1350 °C for 2h with dopant concentrations of: (a) undoped (A0), (b) 0.1 mol% (A1), (c) 0.25 mol% (A2), (d) 0.5 mol% (A3), (e) 1 mol% (A4), (f) 2 mol% (A5).

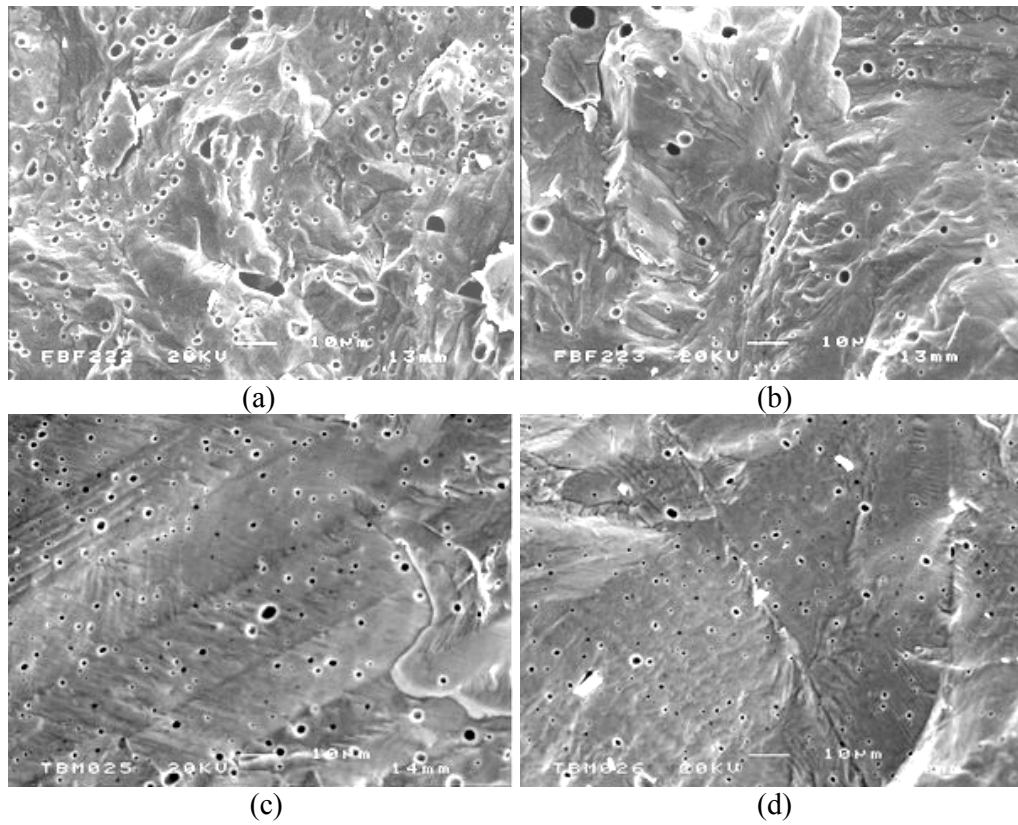


Figure 3.3.7 The SEM images of fracture surfaces of undoped BT sintered at (a) 1350 °C for 2h (A0), (b) 1350 °C for 4h (B0), (c) 1450 °C for 4h (C0), (d) 1500 °C for 4h (D0).

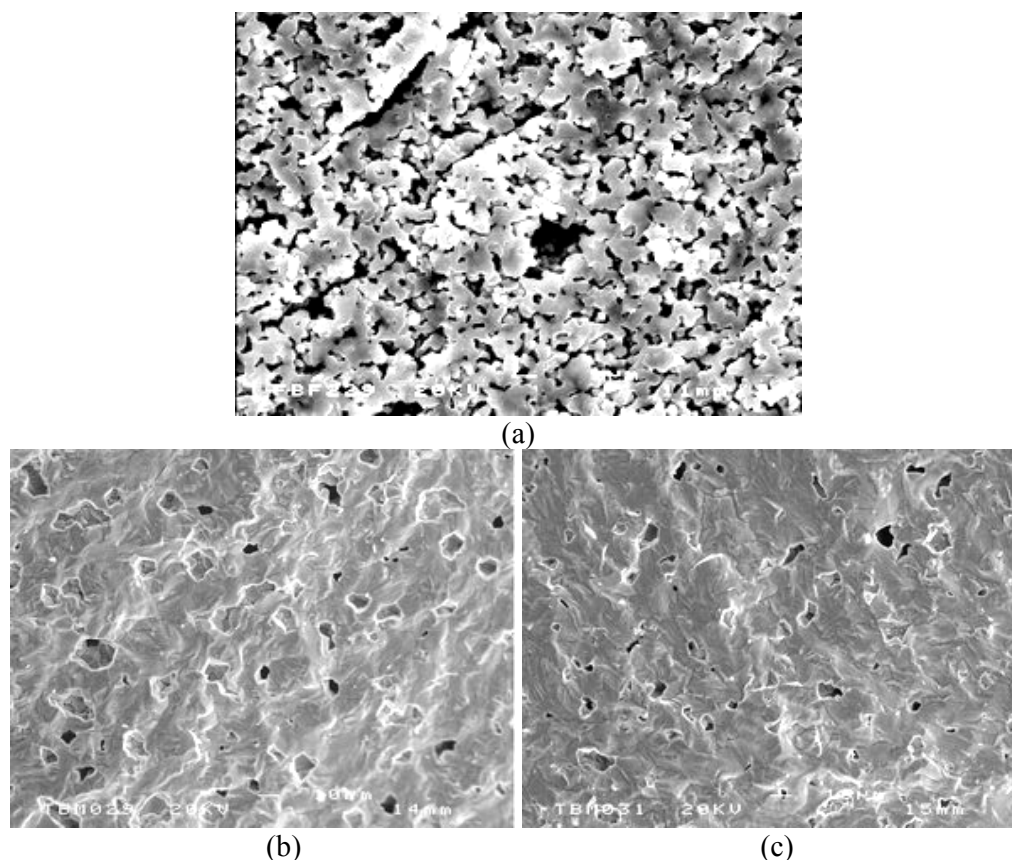


Figure 3.3.8 5 mol% Er^{3+} doped BT samples sintered at (a) 1350°C for 4h (B1), (b) 1450°C for 4h (C1) and (c) 1500°C for 4h (D1).

3.3.3 Investigation of Erbium Distribution in BT Disc Sample

The cross section, upper and lower surfaces of Er-doped BT with various erbium concentrations were examined by EDS analysis as illustrated in Figure 2.4.2. The corresponding results are presented in Table 3.3.1. It was observed that the EDS values for erbium concentration on the cross sections were generally smaller than those on either upper or lower surfaces of the disc, and they all were lower than the planned concentration. This phenomenon may be due to the existence of pores in the EDS scanning area and the unpolished surface for EDS used for measurement. Furthermore, throughout the cross-sectional surface, the EDS scanning results

showed that there was higher erbium content in the top centre area (Point 10) than in the top periphery (Point 6); whereas the erbium content in the bottom centre (Point 13) was less than that at the bottom periphery (Point 7). The erbium concentration was relatively consistent in the central body area of the disc regardless of position (Point 8, 9, 11 and 12). Moreover, it was found that the erbium content on the upper surface centre (Point 3) is higher than that at the periphery (Point 1 and 5); whereas the erbium on the lower surface centre is lower than that at the periphery. Such differences in erbium distribution along surfaces may result from the geometric effect of the disc sample. Since the dopant salt solution was printed on the centre of the upper surface where there was often a crater formed after drying, unsaturated ink spreaded to the periphery area. Therefore, to print the dopant precursor solution on the flat bottom surface by turning the green porous BT base upside-down prior to droplet-doping might eliminate such geometric distribution differences. Furthermore, multi-drops should be printed at various locations rather than a single drop printed in the centre of the surface in order to distribute the infiltrating liquid more homogeneously.

EDS line-scan investigation on cross sections of sintered BT doped with 5 mol.% erbium content was employed and the corresponding semi-quantitative compositional analysis results are shown in Figure 3.3.9. The sample was scanned across its fracture surface as illustrated by the bottom yellow line in Figure 3.3.9. The amplitude of the scanning curves represents the detected amount of the corresponding elements. There was no significant heterogeneous erbium distribution observed along the scanning line across the sample body as seen in Figure 3.3.9. Furthermore, the barium distribution behaves synchronously as that of titanium. Area

mapping study was thus needed because an image of the compositional distribution in 2-D scale is better than that in 1-D.

Table 3.3.1 EDS analyses for the as-sintered erbium doped BT samples

Planned doping concentration /mol.% (Sample No.)	0.5	2.0	5.0
	(A3)	(A5)	(D1)
Scanning position /mol.%			
Point 1 upper/lower (mol.%)	0.4/0.5	1.5 /2.0	4.0/4.9
Point 2 upper/lower (mol.%)	0.4/0.4	1.7/1.7	4.9/4.1
Point 3 upper/lower (mol.%)	0.7/0.3	2.6/1.4	5.7/4.4
Point 4 upper/lower (mol.%)	0.5/0.4	1.9/1.7	5.1/4.6
Point 5 upper/lower (mol.%)	0.3/0.6	1.4/2.3	4.4/5.3
Point 6 (mol.%)	0.4	1.0	3.6
Point 7 (mol.%)	0.6	2.0	5.4
Point 8 (mol.%)	0.4	1.7	4.5
Point 9 (mol.%)	0.5	1.6	4.4
Point 10 (mol.%)	0.6	2.2	5.5
Point 11 (mol.%)	0.5	1.6	4.4
Point 12 (mol.%)	0.4	1.8	3.7
Point 13 (mol.%)	0.2	1.2	3.8

The cross sections of samples as listed in Table 3.3.1 were polished prior to performing EDS area mapping. In the mapping image for a specific scanned element, the magnitude of contrast across the scanning area is determined by the amount of the scanned element at the corresponding place in the area of the image. Figure 3.3.10 shows the microstructure and corresponding compositional (barium, titanium, erbium and oxygen) distribution results for BT sample with 0.5 mol.% erbium content. There was no sign of erbium enrichment spotted by EDS mapping under

such low doping level which might be indicated that the erbium ion distribution is homogeneous in the body of BT disc. Considering the limitation on the accuracy of EDS for the trace dopant concentration, further investigation on ion distribution in doped-BT sample may be needed. Furthermore, the elemental distributions of oxygen, barium and titanium were coincident with each other and they were independent on the dopant concentration (as shown in Figure 3.3.10-13). However, erbium enrichment was clearly detected in doped-BT discs when the Er^{3+} concentration exceeded 2 mol.% as seen in Figure 3.3.11(e), 12(e). The erbium enrichment in both images were then emphasized in green colour in order to increase the contrast against the background; furthermore, the Erbium mapping results were lapped over the corresponding titanium mapping image in order to assess the erbium enrichment spatial distribution. It was found that most of the erbium enrichment was located closed to the pores as seen in Figure 3.3.11(c) and 12(c). Nevertheless, no evidence of erbium enrichment was detected by EDS area mapping for as-dried ultra-highly doped BT sample (20 mol.%) before firing as displayed in Figure 3.3.13(e), which implied that the appearance of erbium enrichment might occur during the heat treatment rather than the infiltration stage. According to the X-ray spectrum (in Figure 3.3.14) and composition (in Table 3.3.2) results by EDS, the concentration of erbium in enriched areas can reach up to 12 times the planned concentration. This heterogeneous erbium distribution throughout the body of highly doped BT disc may be due to the melting effect of erbium nitrate hydrate salt before decomposition to oxide during the early stage of heating. Normally the dopant nitrate hydrate salts have low melting temperature (40-130 °C) compared with the pyrolysis temperature (550-750 °C). Moreover, not only could the low viscosity molten erbium nitrate hydrate trigger re-infiltration within the porous framework of the green BT base, but

also the likely explosive boiling of water of crystallization can lead to the redistribution of erbium ion during firing. In addition, the appearance of erbium enrichment in BT samples with high erbium content (≥ 2 mol.%) also probably contributed to the presence of second phase by the formation of $\text{Er}_2\text{Ti}_2\text{O}_7$.²⁶⁶

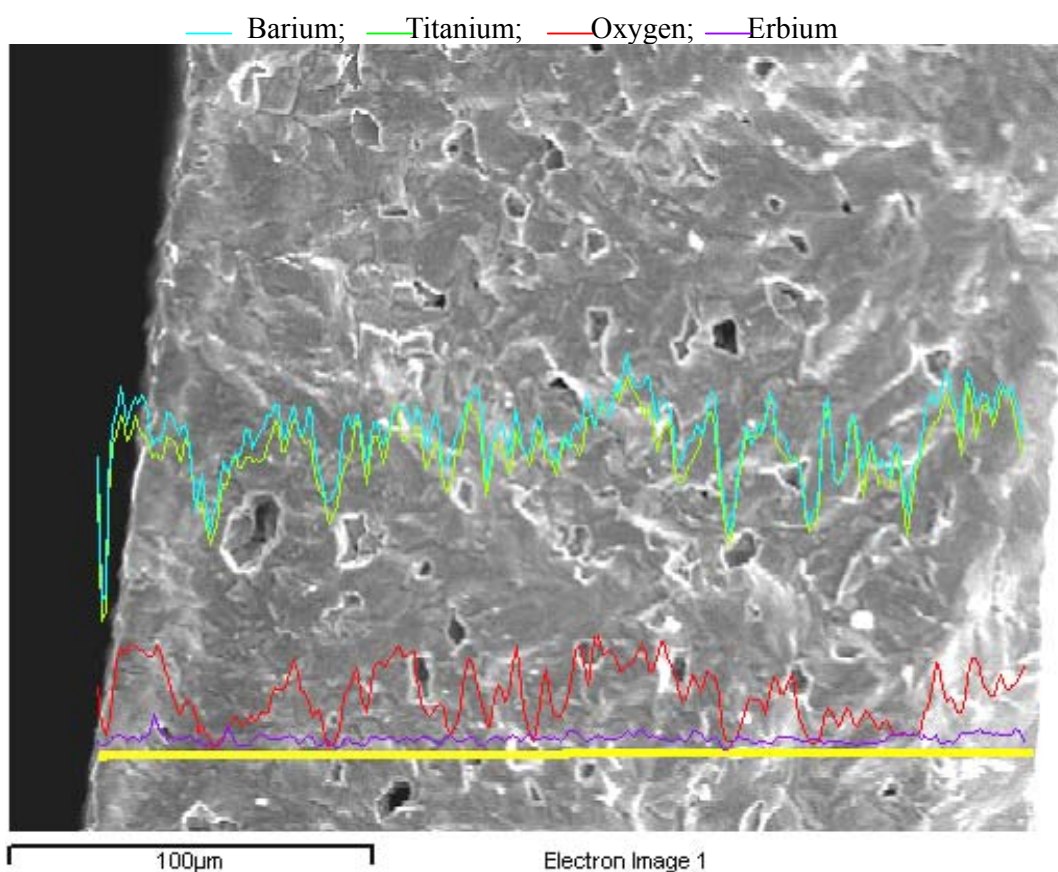


Figure 3.3.9 EDS line-scan image of fracture surface of sample D1. The yellow line at the bottom is scanning path.

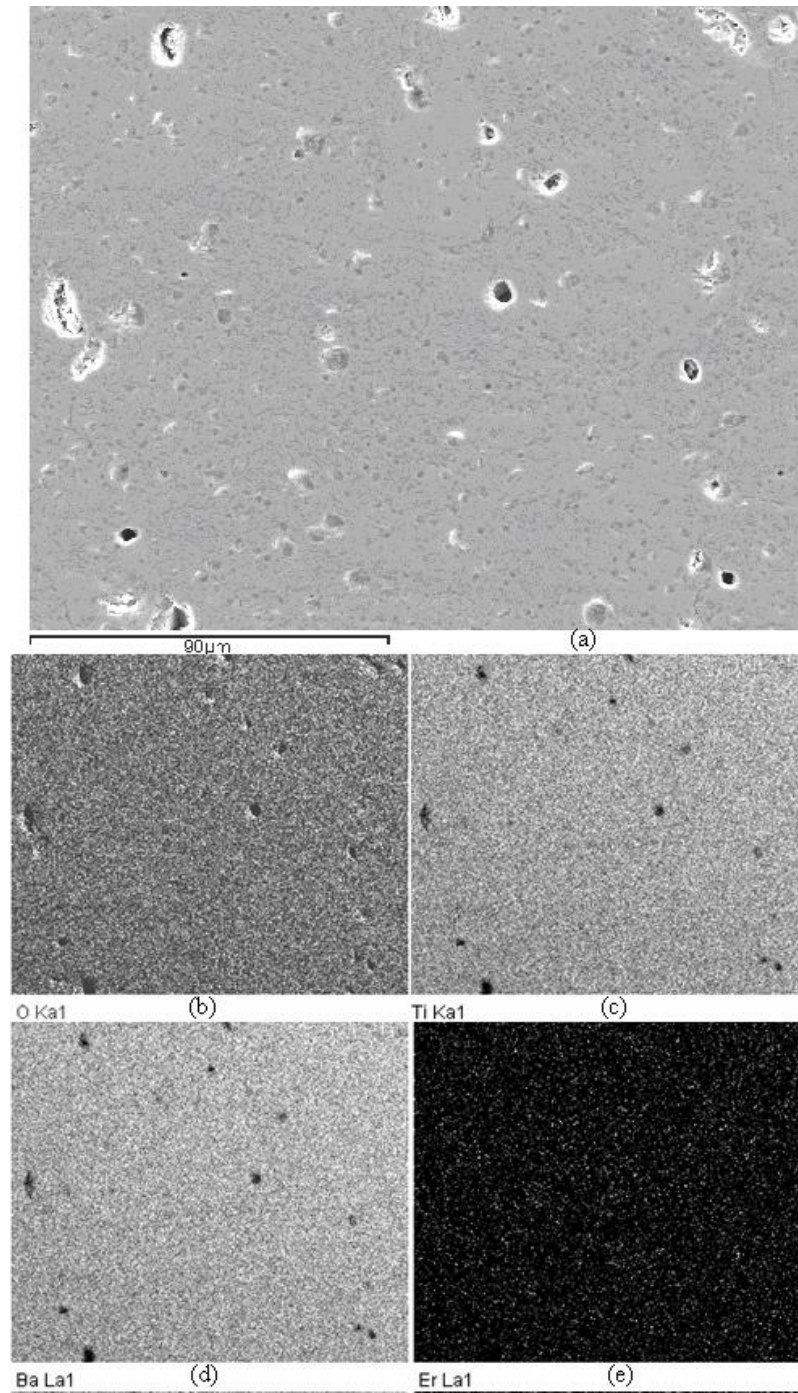


Figure 3.3.10 SEM/EDS mapping results for specimen A3: (a) microstructure of cross section, the corresponding element mapping image of O (b), Ti (c), Ba (d) and Er (e).

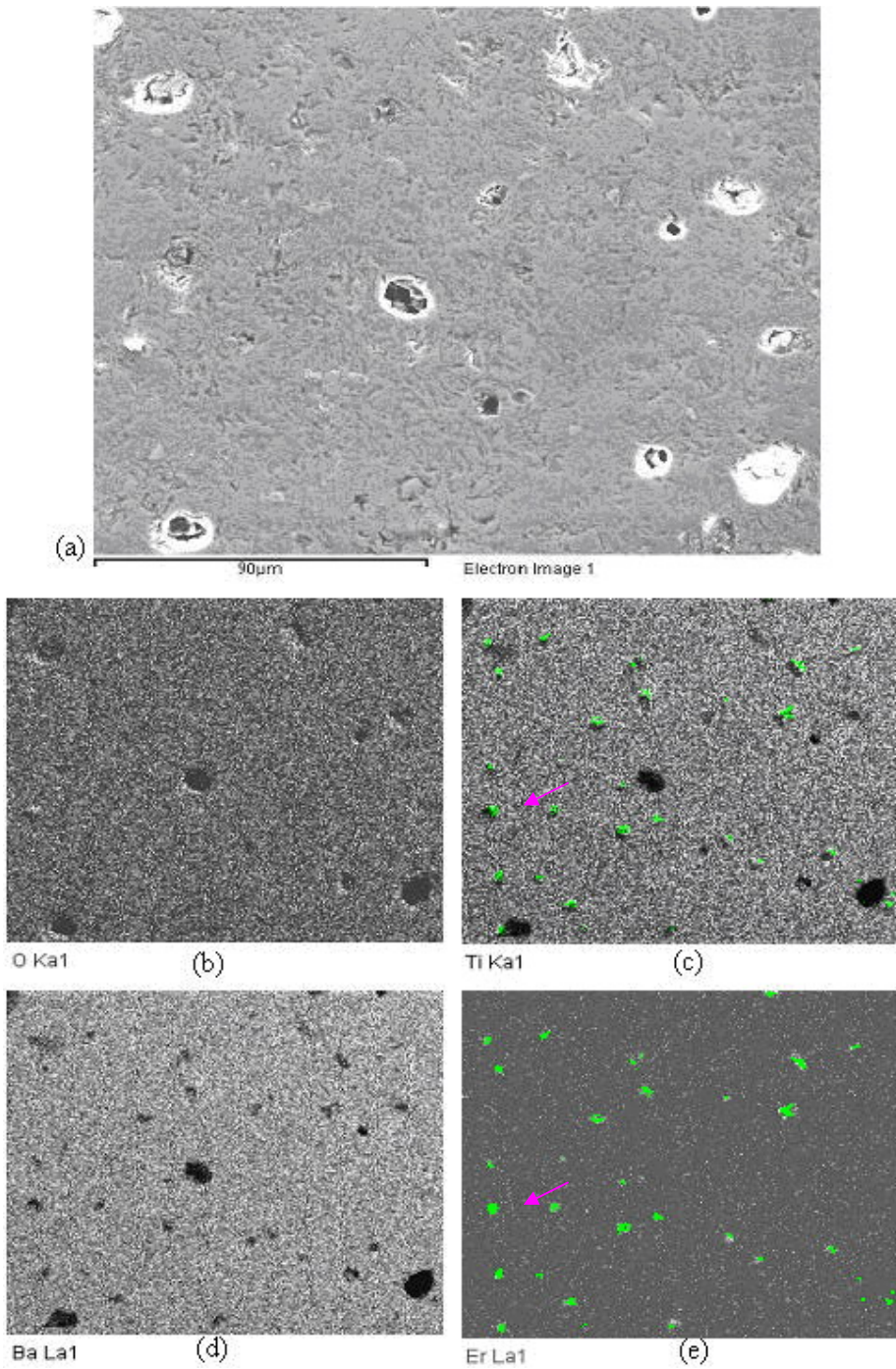


Figure 3.3.11 SEM/EDS mapping results for specimen A5: (a) microstructure of cross section, the corresponding element mapping image of O (b), Ti (c), Ba (d) and Er (e).

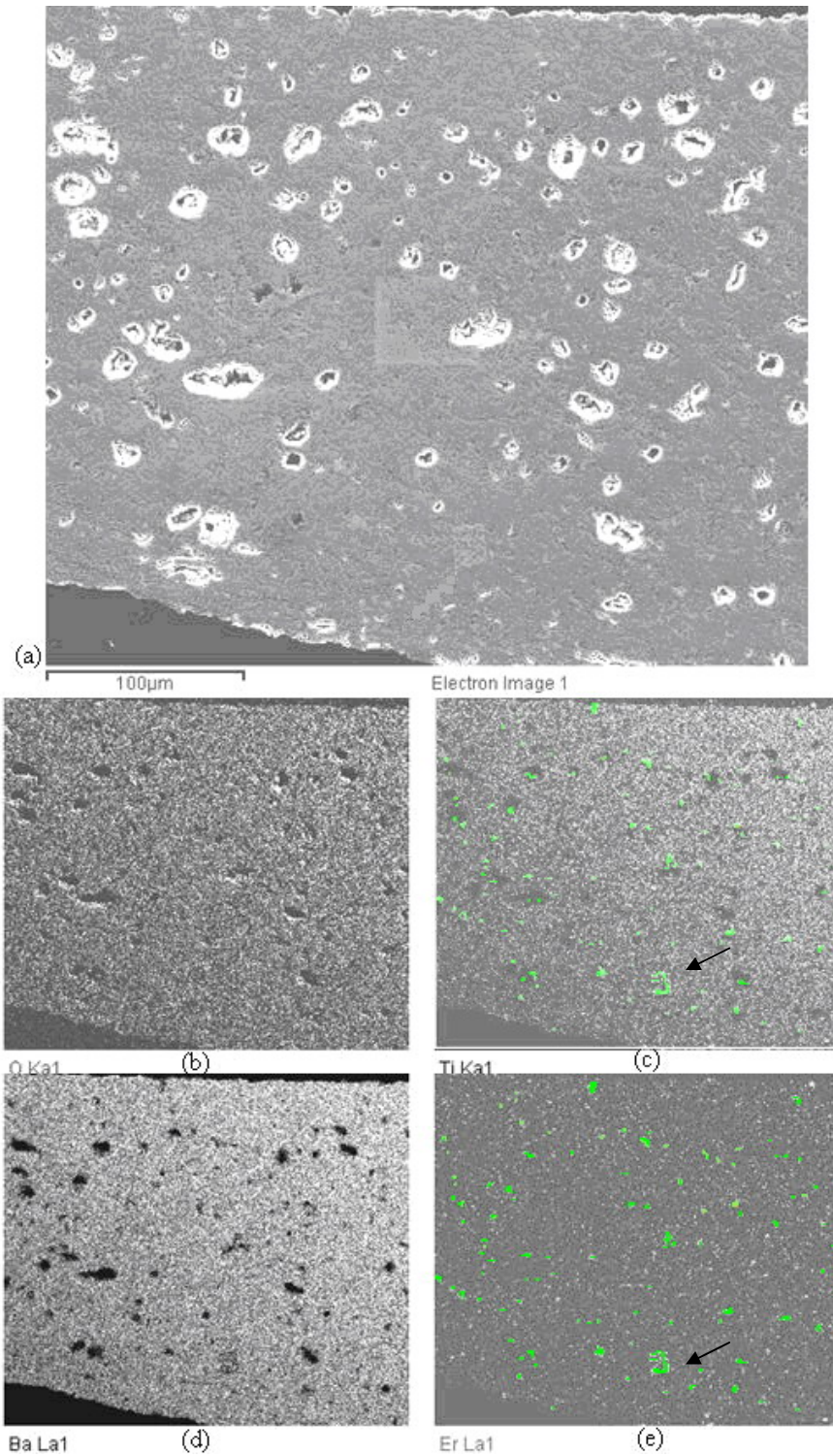


Figure 3.3.12 SEM/EDS mapping results for specimen D1: (a) microstructure of cross section, the corresponding element mapping image of O (b), Ti (c), Ba (d) and Er (e).

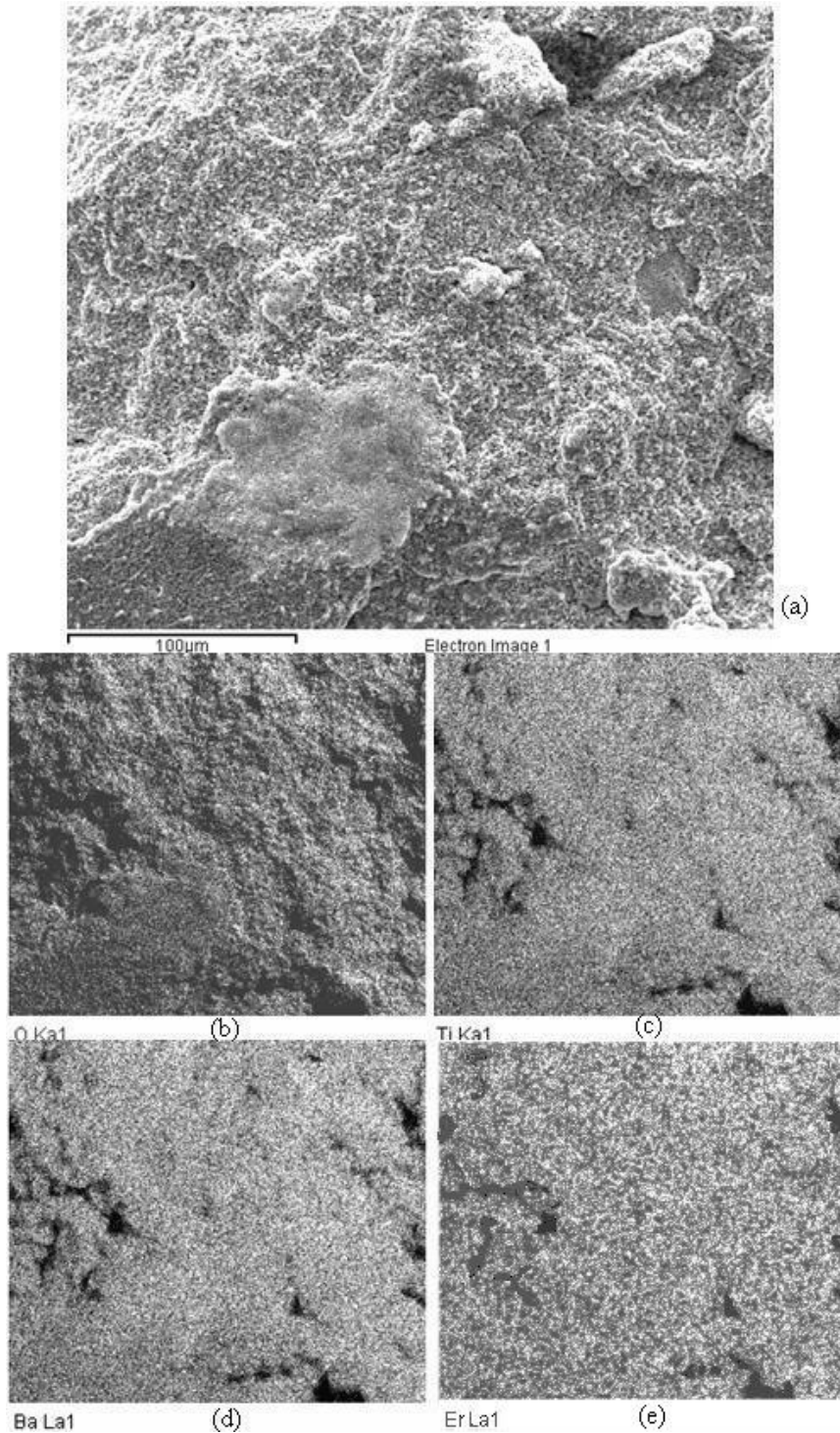


Figure 3.3.13 SEM/EDS mapping results for as-dried BT sample with Er content of 20 mol.%: (a) microstructure, the corresponding element mapping image of O (b), Ti (c), Ba (d) and Er (e).

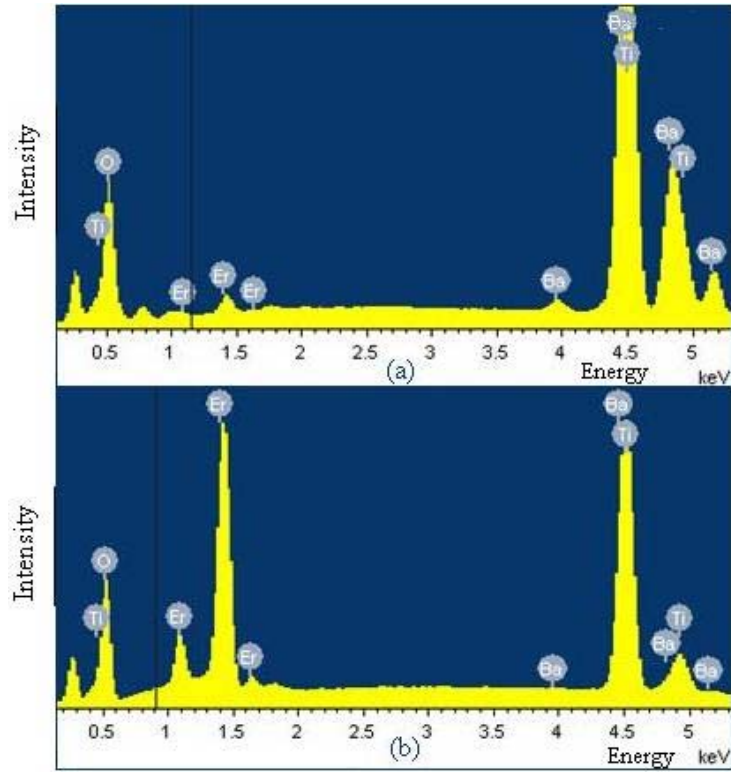


Figure 3.3.14 EDS spectrum results for sample D1 under the scanning the plain area (a) and the Er-enrichment (b).

Table 3.3.2 EDS analysis for erbium doped BT.

Sample I.D.	Element	Planned composition /at.%	EDS analysis ^a /mol.%	
			Er-enrichment area	Plain area
A5	Ba	19.6	10.3±4.3	19.9±0.1
	Ti	20.0	17.7±1.1	19.7±0.1
	Er	0.4	3.4±2.4	0.37±0.2
D1	Ba	19.0	4.1±3.4	17.8±0.5
	Ti	20.0	16.2±1.8	18.3±0.5
	Er	1.0	12.9±2.6	0.78±0.2
T1	Ba	16.0	Null	15.6±3.4
	Ti	20.0		16.2±3.2
	Er	4.0		2.7±1.2

^a Average for five analysis at different positions with 95% confidence limit.

3.3.4 Investigation of Yttrium Distribution

The upper limit on doping is set by the maximum concentration of nitrate salt solution and hence by the aqueous solubility of dopant nitrates which are 58.75 wt.% for $\text{Y}(\text{NO}_3)_3$ at 20 °C.⁴²⁷ For example, to print 3.6 μL of saturated concentrated $\text{Y}(\text{NO}_3)_3$ solution (58.75 wt.% of $\text{Y}(\text{NO}_3)_3$) into a green BT disc with a volume of $\approx 6.5 \text{ mm}^3$ with 55% porosity, the upper limit of the incorporated concentration of yttrium dopant can be up to 16 mol.%, which is far larger than the critical concentration of donor content in BT based PTCR materials. For lower levels of doping, the salt solution was diluted accordingly.

After infiltration of dopant precursor solution into porous BT base, the solute ions are attached to BT particle surfaces because a liquid film is formed along the surface of the particle caused by the fluid fluxes during both the stages of the liquid imbibition and subsequent evaporation.³⁶⁵ Hence the morphology of particle structures after doping can be examined to assess the extent of the dopant distribution. Figure 3.3.15 shows the morphology of BT particles before doping: particles had sharp and clear surfaces. Figure 3.3.16 shows the morphology of particles in the cross section of as-dried BT disc doped with 1 mol.% Y^{3+} content examined by SEM. The observation under SEM by browsing the entire cross section of as-doped BT disc showed similar images: all particles throughout the base were coated by a thin film with a thickness of around 30 nm which is displayed as a ‘halo’ surrounding the BT particle seen in Figure 3.3.16. This indicated that the droplet-doping method was able to effectively deposit the dopant salt on to the BT particle surface and thoroughly distribute them throughout the porous base.

Although the preliminary check of as-doped particle morphology after drying did not show significant heterogeneous dopant salt distribution in terms of the presence of particles coating, another factor potentially affecting uniformity is the remelting and flow of the hydrated nitrate salt before pyrolysis. In conducting the slow pyrolysis, the samples were put into the furnace at room temperature. In fast pyrolysis, the samples were put into a furnace preheated to 650 °C. A microstructural survey across the sections of 1 mol.% Y-doped discs subjected to slow and fast decomposition prior to sintering was performed by SEM. Examples of the particle morphologies are shown in Figure 3.3.17 (slow rate) and 3.3.18 (fast rate) which are representative of the many areas viewed. The particle arrangement is similar for both samples after heat-treatment on these different pyrolysis schedules but the structure of the dopant film is not. Smooth uniform particle coating results from fast decomposition whereas irregular structures such as bridges of pyrolysis product were found between BT particles in the sample subjected to slow decomposition. No such non-uniformity was observed in samples subjected to fast decomposition. This is likely to be due to the melting and movement of yttrium nitrate hydrated salt before pyrolysis during the thermal processing. Therefore, the fast pyrolysis path before sintering was then adopted.

Figure 3.3.19 shows the optical image of the 0.5 mol.% Y-doped BT disc sintered in N₂ at 1380 °C. It was observed that the sample presented a uniform blue colour across the outer surface. Quantitative analyses of the spatial distribution of yttrium on the cross section of the samples doped with 0.5 mol.% yttrium content were then performed by EDS and WDS. Neither spatial non-uniformity nor enrichment of yttrium was detected by EDS line-scan and mapping mode throughout the cross

section of the sample. It could well be argued that the resolution of EDS may not detect the variation of dopant element in such low level of doping. So WDS was used to further analyse the uniformity.

Dopant distributions on the cross sections of BT discs with 0.5 mol.% yttrium content by printing different volumes of yttrium nitrate solutions during droplet-doping were investigated and compared using WDS. The as-sintered sample obtained by printing an unsaturated volume of dopant salt solution (60% of the total pore volume) displayed a central bright region with dark blue periphery pattern on the cross section as seen in Figure 3.3.20 (photo was taken by a digital CCD camera); however, the samples that were subjected to saturated dopant salt liquid volume doping showed homogeneous blue colour on the cross section (in Figure 3.3.21, picture was taken using a DELL scanner). Nevertheless, both types of samples presented the same uniform dark blue colour on their outer surfaces. The WDS results (in both Figures 3.3.20 and 21) also confirmed that heterogeneous yttrium distribution occurred in samples subjected to unsaturated volume doping by examining the polished cross section vertically (from top down bottom) and horizontally (from edge to centre). Samples subjected to saturated volume doping presented relatively even distribution of yttrium throughout the BT base according to the WDS results. These results also supported the observation in Figure 3.3.1 (a) and (c) noting that the yttrium nitrate solution was printed on the bottom flat surface of the BT base. Furthermore, it was found that overall; the outer surface of the sintered pellet contained slightly more yttrium content than the body.

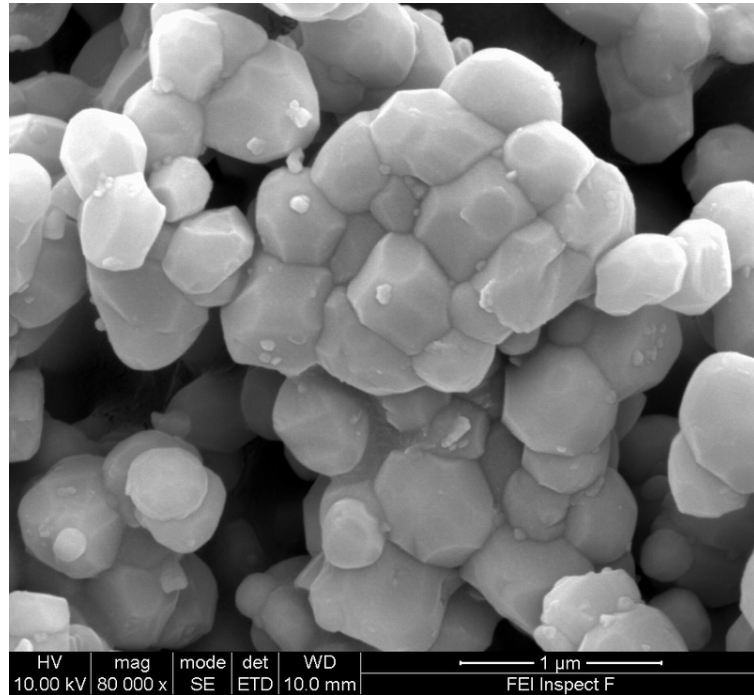


Figure 3.3.15 SEM picture of fracture surface of undoped BT base disk.

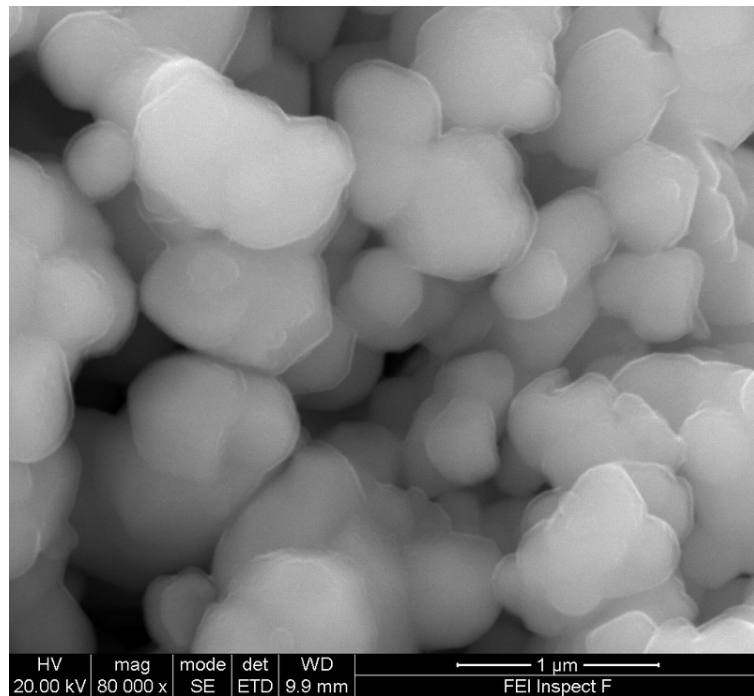


Figure 3.3.16 As-dried 1 mol.% Y-doped BT.

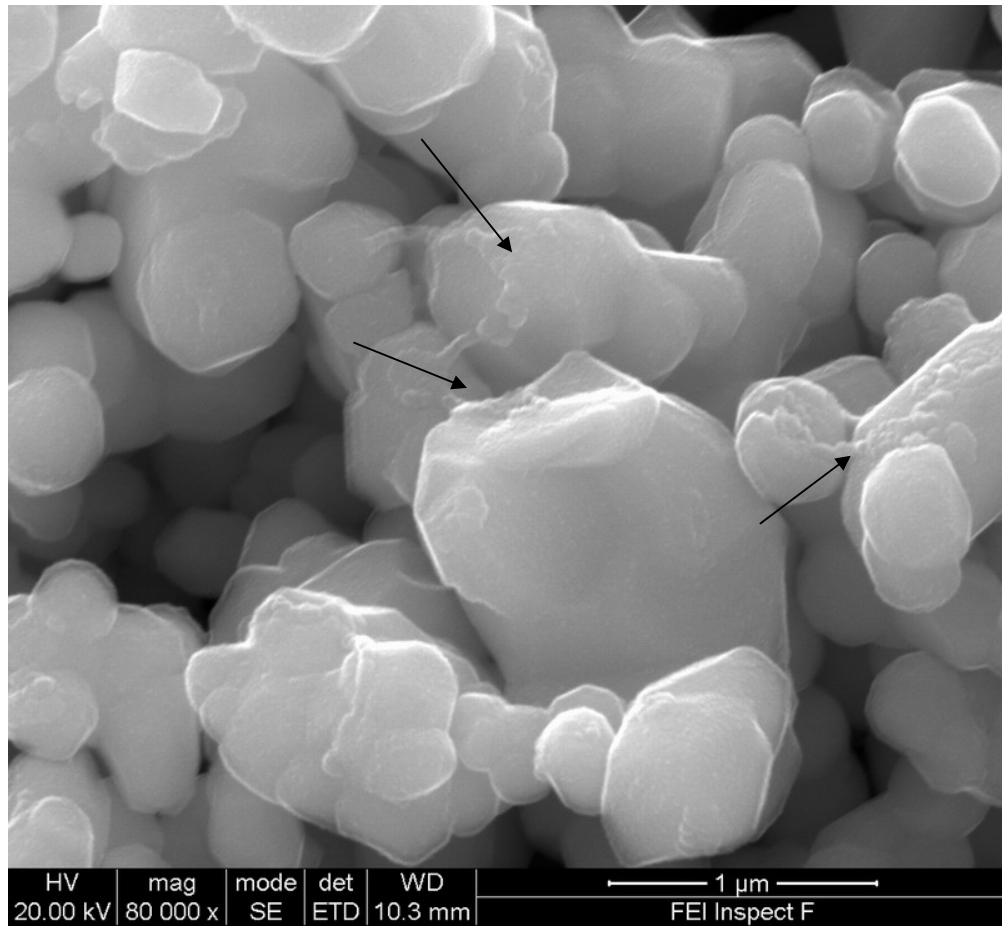


Figure 3.3.17 BT doped with 1 mol.% yttrium subjected to slow decomposition ($5^{\circ}\text{C}/\text{min}$, from room-temperature to 650°C). Arrows show the decomposed yttrium oxide from the molten nitrate salt during thermal treatment.

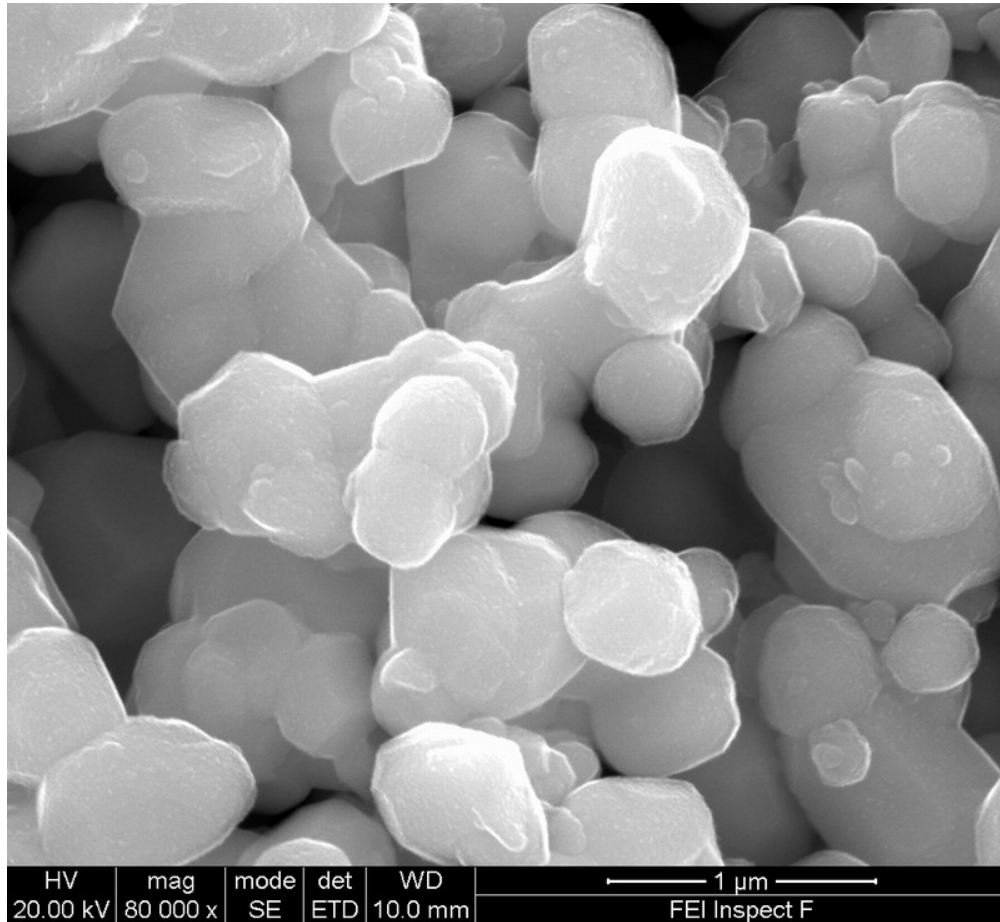


Figure 3.3.18 BT doped with 1 mol.% yttrium subjected to fast decomposition (placed in furnace preheated at 650 °C).



Figure 3.3.19 Optical image of the top surface of the 0.5 mol.% Y-doped BT sample via droplet-doping method sintered at 1380 °C in N₂ flow.

Results and Discussion

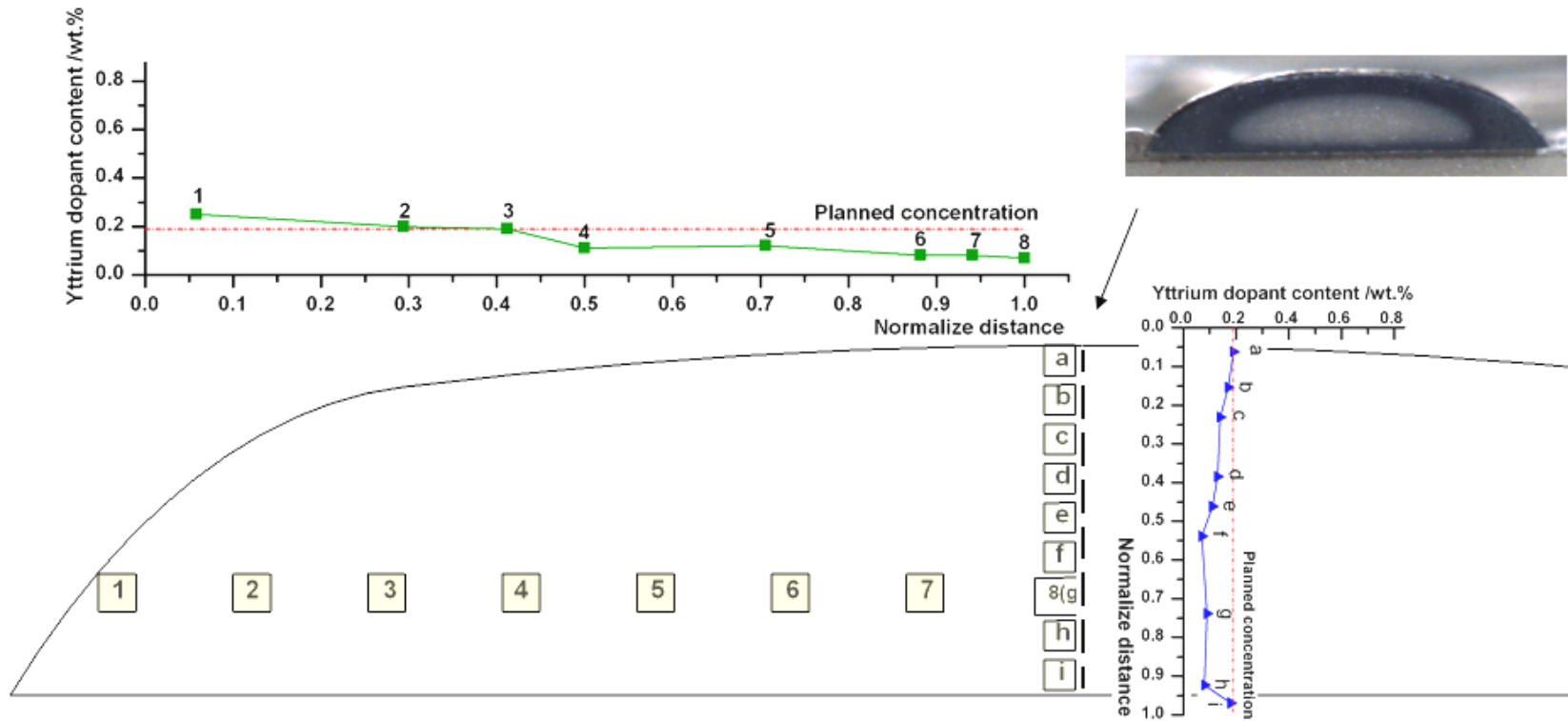


Figure 3.3.20 Distribution of yttrium for sample printed with unsaturated volume of yttrium nitrate solution measured by WDS vertically and horizontally across the cross-section of Y-doped BT via drop doping, broken lines in both Cartesian coordinates indicate the expected dopant level.

Results and Discussion

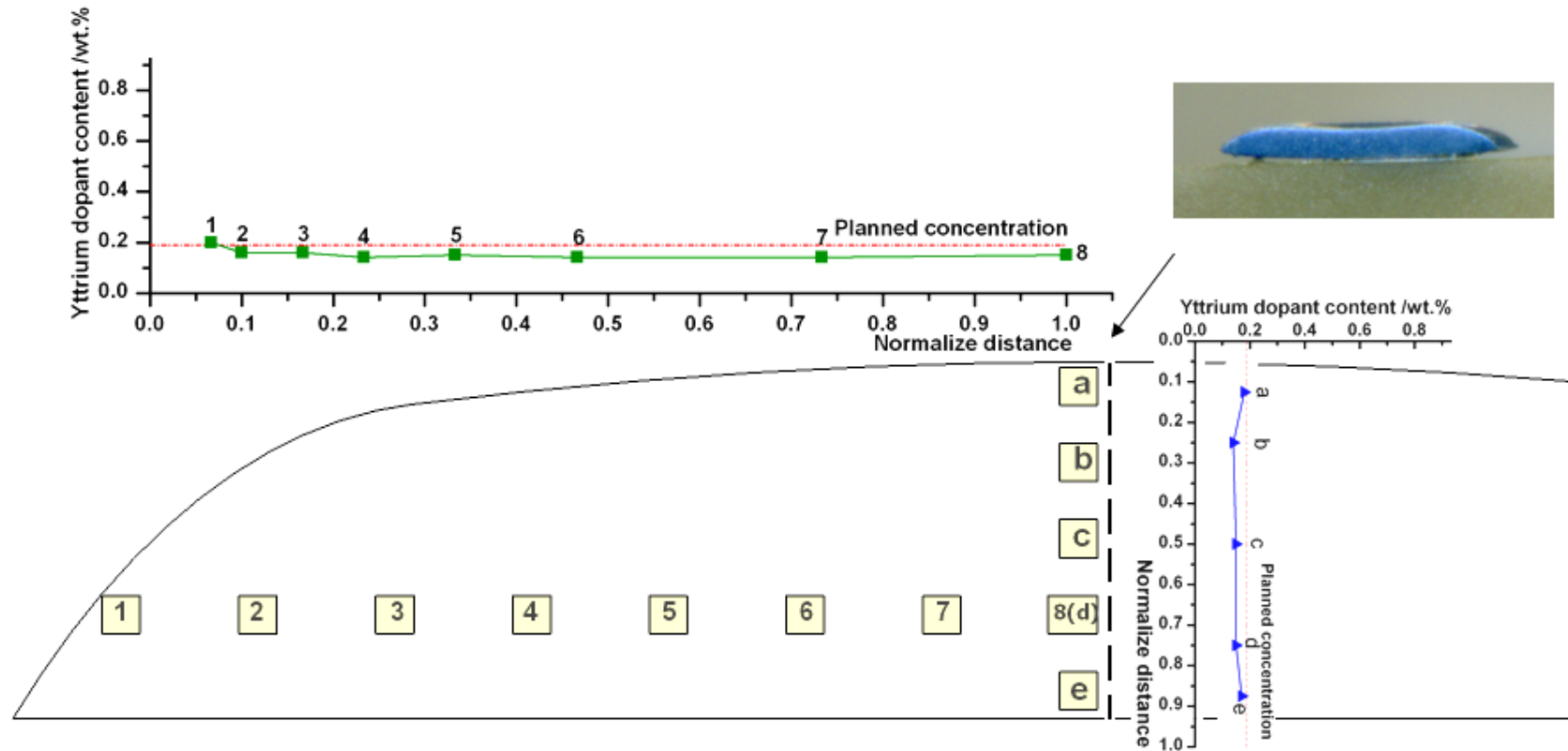


Figure 3.3.21 Distribution of yttrium dopant measured by WDS vertically and horizontally across the cross-section of Y-doped BT via droplet-doping, broken line indicates expected dopant level.

3.3.5 Discussion

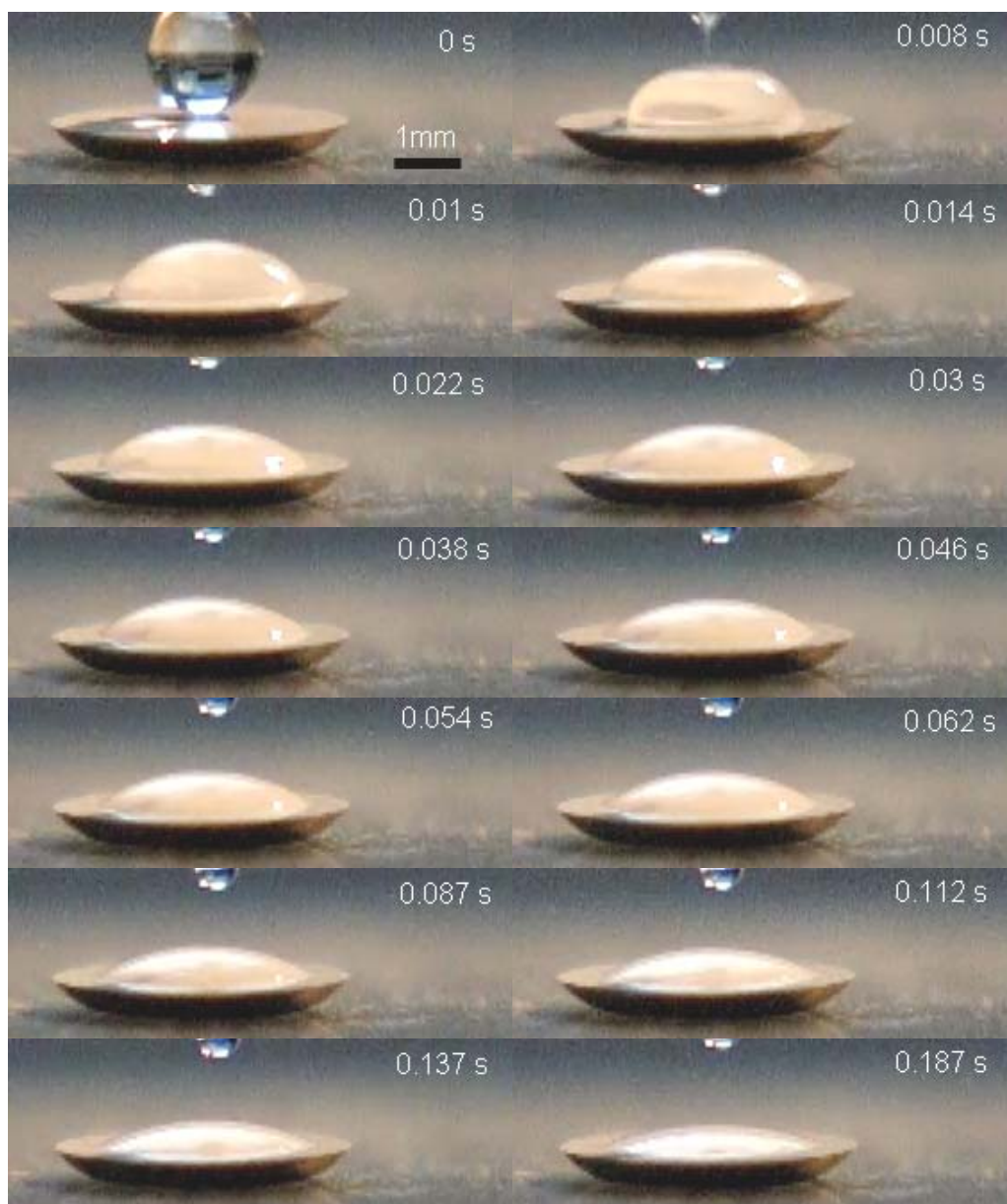
The important criterion to be met here is the uniformity of donor distribution inside the BT base disk. At any stage of sample preparation, the factors that could affect the uniformity of dopant in the final samples are:

- a) The infiltrating flow profile of the dopant salt solution from the surface into the body of the base disc during droplet deposition.
- b) The redistribution of the dopant salt inside the base disc during the evaporation of solvent due to capillary flow.
- c) The melting and flow of molten nitrate salt before decomposition to oxide during early stages of heating. The nitrate hydrated salts used here have low melting temperatures (<130 °C) compared with the pyrolysis temperature (550-750 °C). To restrict the flow of molten salt inside the porous disk, the furnace was preheated to 650 °C before the samples were loaded.
- d) Diffusion during sintering which is expected to redistribute the additive but only over small diffusion distances.
- e) The evaporation of volatile dopants during sintering.

The dopant distribution within porous BT is discussed below in terms of the different time scales associated with the infiltration process. All theoretical calculations are based on a simplified model of porous BT with a uniform cylindrical pore structure. The contact angle of water on dense BT disc was measured as 40°. Considering the dopant precursor solution used here for producing lightly doped BT PTCR samples has closed physical properties such as density, viscosity and surface tension etc. to water, thus the corresponding water values were used for the calculations below.

3.3.5.1. Effect of Drop Spreading and Imbibition

As soon as a drop is printed on the surface of the porous base, there are two different motions of liquid: droplet spreading across the surface and infiltration into the underlying substrate. The dynamics of the spreading and imbibition of a liquid drop on the flat surface of a green BT porous base was recorded and is shown in Figure 3.3.22. The term imbibition here is defined as the absorption of one fluid by a solid or gel.



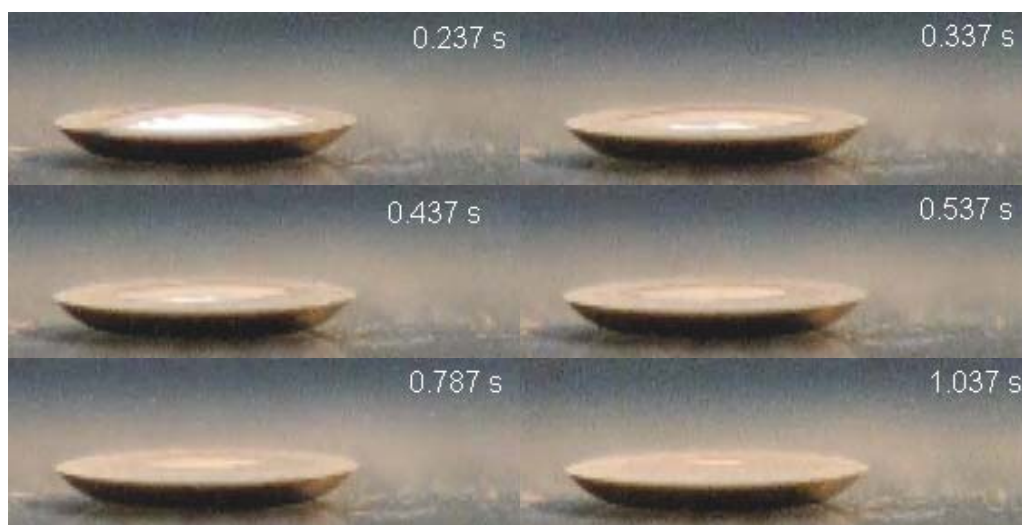


Figure 3.3.22 Sequence of water spreading and imbibition into green BT porous base. Pictures were captured using high speed camera at 1200 frames per second.

Figure 3.3.23 displays the dependence of the diameter of the drop base on the time by measuring from the images in Figure 3.3.22 using line intercept method. It was observed that the drop spread quickly and reached a maximum value in less than 0.03 second after placing on the porous surface. After that the drop base started to shrink slowly due to the imbibition proceeding. The time evolution of the diameter of drop base is in line with the results in literature³⁸⁷ and well supporting the theory that the spreading flow generally ceases before significant infiltration occurs.⁴²⁸ In order to effectively wet the whole surface of the BT porous base disc with precursor solution, 3 or 4 multiple drops were dispensed over the surface, each being an equi-fraction of the calculated volume of dopant solution.

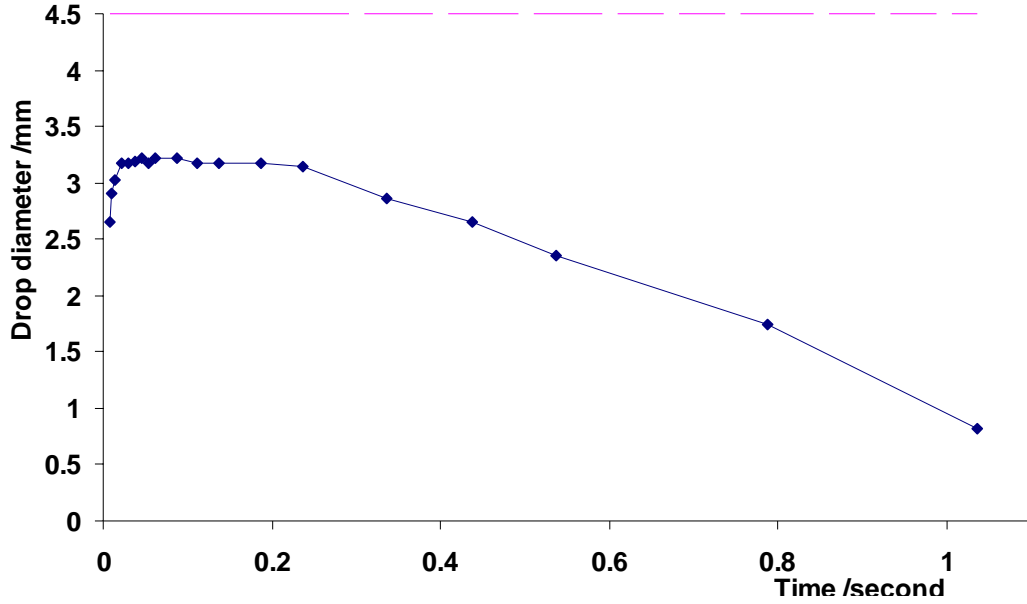


Figure 3.3.23 The spreading diameter as a function of time for a water drop on the BT base as in Figure 3.3.22. The pink dash line represents for the diameter of the BT base.

If V is the volume of the droplet placed on the surface and θ is the contact angle just before intrusion has started, then a_w , the radius of the wetting footprint is given by equation 3.3.1.³⁷²

$$a_w = \left(\frac{3 \cdot V \cdot \sin^3 \theta}{\pi(1 - \cos \theta)^2 (2 + \cos \theta)} \right)^{1/3} \quad \text{Equation 3.3.1}$$

Given the total pore volume of this porous substrate as $3.6 \mu\text{L}$ and the volume of a single printed droplet as $0.9 \mu\text{L}$ and contact angle 38° (as measured by high-speed camera), the spreading radius can reach 1.15 mm , which means four separated droplets are able to cover the whole surface which has a diameter of 4.3 mm . Alternatively, if a single droplet with a volume of $3.6 \mu\text{L}$ is printed, the maximum diameter of the spreading drop is only 3.6 mm , which is less than that of the base disc. This may increase the chances that a small amount of the infiltrating dopant

precursor solution will migrate to the open space between the central base of the porous disc and the impermeable silicone release paper used as a substrate (Figure 3.3.1(b)).

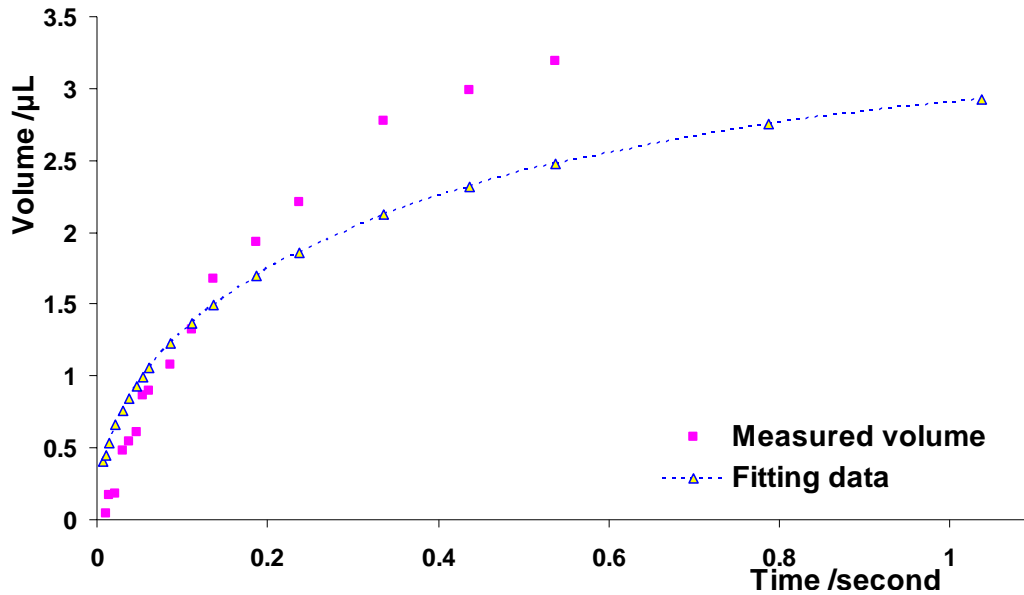


Figure 3.3.24 Comparison between modelled and experimentally obtained $V(t)$, the imbibition volume of water as a function of time into the green BT porous base.

Figure 3.3.24 presents the imbibition volume of a liquid drop on the porous BT base as in Figure 3.3.22 as a function of time. The imbibition drop volume was calculated by the subtraction of the remaining volume of drop on the surface from the initial printed drop volume (3.6 μL). Since the shape of the remaining drop on the porous surface can be approximated a spherical cap,^{385, 386} thus its volume can be estimated using equation: $V = \pi h(3a^2 + h^2)/6$ where a is the droplet base radius and h is the droplet height. A model was developed using the Washburn equation to determine the volume of the wetted region inside the porous material which was assumed in the form of a truncated paraboloid.³⁷³

$$V'(t) = \frac{\pi a_p}{2} \left(2d(t) - \frac{d(t)}{d_{\max}} \right) \quad \text{Equation 3.3.2}$$

where a_p is the initial drop base radius, d_{\max} is the maximum wet spot depth in the porous base equal to the initial droplet height (h) divided by the porosity (P) and the depth of the liquid infiltrating $d(t)$ is a function as a square root of time:

$$d(t) = \sqrt{\frac{a\gamma \cos \theta}{2\eta} t} \quad \text{Equation 3.3.3}$$

where η is the liquid viscosity, γ is the surface tension, a is the average pore radius. Hence, the absorbed liquid volume $V(t) = V'(t) * P$. The dotted line in Figure 3.3.24 is the fitting data derived from $V(t)$ by using the typical values $\eta \approx 10^{-3}$ Pa·s and $\gamma \approx 72.75$ mN/m,⁴²⁹ $\theta = 38^\circ$, $a = 0.06$ μm , $h = 0.93$ mm and $a_p = 1.45$ mm (measured from image results in Figure 3.3.22 using line intercept method).

It was observed that the experimental measurement of volume is well fitted to the modelled curve in the beginning short period of time as seen in Figure 3.3.24. However, the deviation between them became significant when the droplet began to retract after placing on the surface for 0.2 second (in Figure 3.3.23). The probable reasons that caused such deviation between the measured and modelled volumes are:

1. During drop imbibition, the shape of the remaining drop on the porous surface may not be in the form of a perfect spherical cap. Thus the corresponding *in-situ* volume measurement calculated from the related drop height and drop contact radius may not be accurate any more.
2. The errors generated from the droplet geometry measurement using line intercept method may significantly increase due to poor contrast of the boundary in images where only a small amount of droplet remained on surface.

3. The modelled equation was based on the assumption that the wet spot inside the porous base has the shape of a truncated paraboloid, which might not exactly fit the geometry here.
4. The thickness effect of porous substrate needs to be considered here. The equation 3.3.2 was based on a thick porous system which the thickness is much larger than the droplet height. However, the BT porous base used here was as thin as 0.45 mm, in comparison with the initial droplet height with 0.93 mm. According to Daniel's theory,⁴³⁰ the droplet imbibition in a thin porous substrate (the thickness of substrate far less than the droplet height) can be described as unidirectional radial wicking during the spreading event rather than a soft rounded edges of wicking profile for thicker porous systems. Because it only takes 0.12 second for water infiltrating through the entire BT base with a thickness of 0.45 mm according to equation 3.3.3, this may explain the phenomenon that the deviation between the measured and modelled volume results occurred at the time of ≈ 0.12 second in Figure 3.3.24, after which unidirectional radial wicking began rather than permeating in both normal and tangential directions³⁸⁷.

In soil science, it is believed that the degree of homogeneity of fluid infiltration of a porous medium is determined by the degree of stabilization of the fluid displacement front, which is dependent on the combined effect of gravity, viscous and capillary forces if the pore geometry effect is ignored.³⁶⁴ The capillary number (C_a) is a dimensionless parameter defined below that can be introduced to measure the features of infiltrating fluid distribution.³⁶⁴

Capillary number is the ratio of viscous forces to capillary forces at pore level:

$$C_a = \frac{4\eta\nu a^2}{\gamma\kappa} \quad \text{Equation 3.3.4}$$

where ν is the filtering flux or Darcy velocity in the medium, κ is the permeability of the porous medium. Furthermore, according to Darcy's Law and the Young-Laplace equation:

$$\nu = \frac{\kappa\Delta P}{\eta L} \quad \text{Equation 3.3.5}$$

and $\Delta P = \frac{2\gamma \cos \theta}{a}$ Equation 3.3.6

where ΔP is the capillary pressure and L is the thickness of the medium. Rearranging equations 3.3.4-6, $C_a = \frac{8a \cos \theta}{L}$. Given the thickness of porous BT samples of 0.45 mm, the dominant pore radius of 0.06 μm , the density of water 1000 kg m^{-3} and the contact angle of water on BT 38°, the capillary number (C_a) can be estimated about 8×10^{-4} .

What is required here is to achieve a near-uniform flow front to prevent finger-like flow which can cause air pockets. In liquid imbibition, a porous system with a large capillary number ($>10^{-4}$) performs in a more stable way in terms of the liquid displacement pattern than one with a small value of C_a ($<10^{-6}$) because capillary-driven finger-like flow is less likely to occur.^{380, 381} Furthermore, gravity contributes a stabilizing force by reducing the height differences induced by viscous instability or capillary fluctuations hence flattening the wetting front.³⁸³ These analyses support the rationality of this droplet-doping method especially on the uniform distribution of the precursor liquid during infiltration. From the equations given above, it can be seen that a large pore radius (a), a small contact angle (θ) and small sample thickness

(L) favour a large value of C_a and hence stable infiltration. In this high throughput method, sample discs have low thickness which also favours uniform infiltration. Furthermore, observation under SEM by surveying the cross section of the whole disc after infiltration doping demonstrates that the donor precursor has the capability of infiltrating throughout the porous body (as seen in Figure 3.3.16).

Taking the effect of pore geometry into account, the pore network structure can be simplified as an array of wide granular pores interconnected by narrower regions which are so-called throats as displayed in Figure 3.3.25.³⁸⁴ According to the research by Blunt,³⁸⁴ there are two different kinds of water advances in infiltration into a porous system. The first is piston-like, where the fluid advances in a connected front occupying the pore spaces. Different modes of this piston-like advance are schematically displayed in Figure 3.3.26. The second type is the wetting fluid flowing along crevices in the pore space, filling pores in advance of the connected wetting front. This filling mechanism is also called a snap-off event in which the water film that covers the surface of the throat may swell and eventually choke off the throat and hence may separate connected empty pores into two regions or clusters that are no longer connected.⁴³¹ Therefore, the water displacement pattern in porous media is determined by the competition between the fluid piston-like advance and the snap-off event in throats. According to the Young-Laplace equation (equation 3.3.6), capillary pressure is higher at the pore having smaller radius. Hence the invading solution tempts to get into the small pores before entering the large pores or into throats of a pore with a large aspect ratio rather than into the pore. The uniform water frontal advance in porous media only occurs when assuming there is no flow in crevices, pore size distribution is narrow and pores are only slightly larger than their

throats.³⁸⁰ Furthermore, for pore-network systems with a large aspect ratio, ramified structure of the water displacement front was observed because of the invasion percolation effect.^{432, 433}

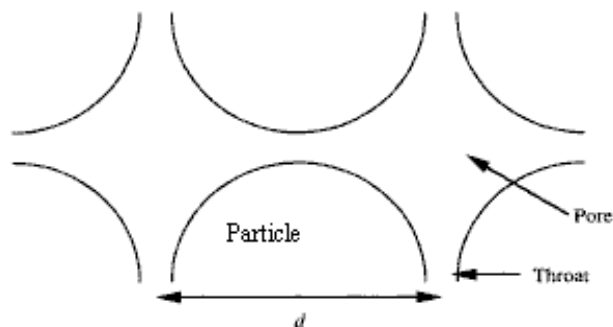


Figure 3.3.25 Schematic diagram of a porous system.

The green BT disc which was used here as a porous base for doping had a generally narrow pore size distribution according to the porosimetry results (in Figure 3.2.4). The dominant pore size was $\approx 0.12 \mu\text{m}$ which contributed around 83% of the total pore volume. Although there were about 3 vol.% of the pores with the size as $60 \mu\text{m}$ and the rest of 14 vol.% of pores' sizes were varied, a flat frontal advance of infiltrating liquid in the BT porous base is still expected. Nuclear magnetic resonance (NMR) imaging^{434, 435} can be used to examine the water front for investigating the possible existence of discrete flow and fragmentations. Moreover, in order to avoid any potential trapped air pockets in the porous system during infiltration doping, vacuum condition might need to be deployed.

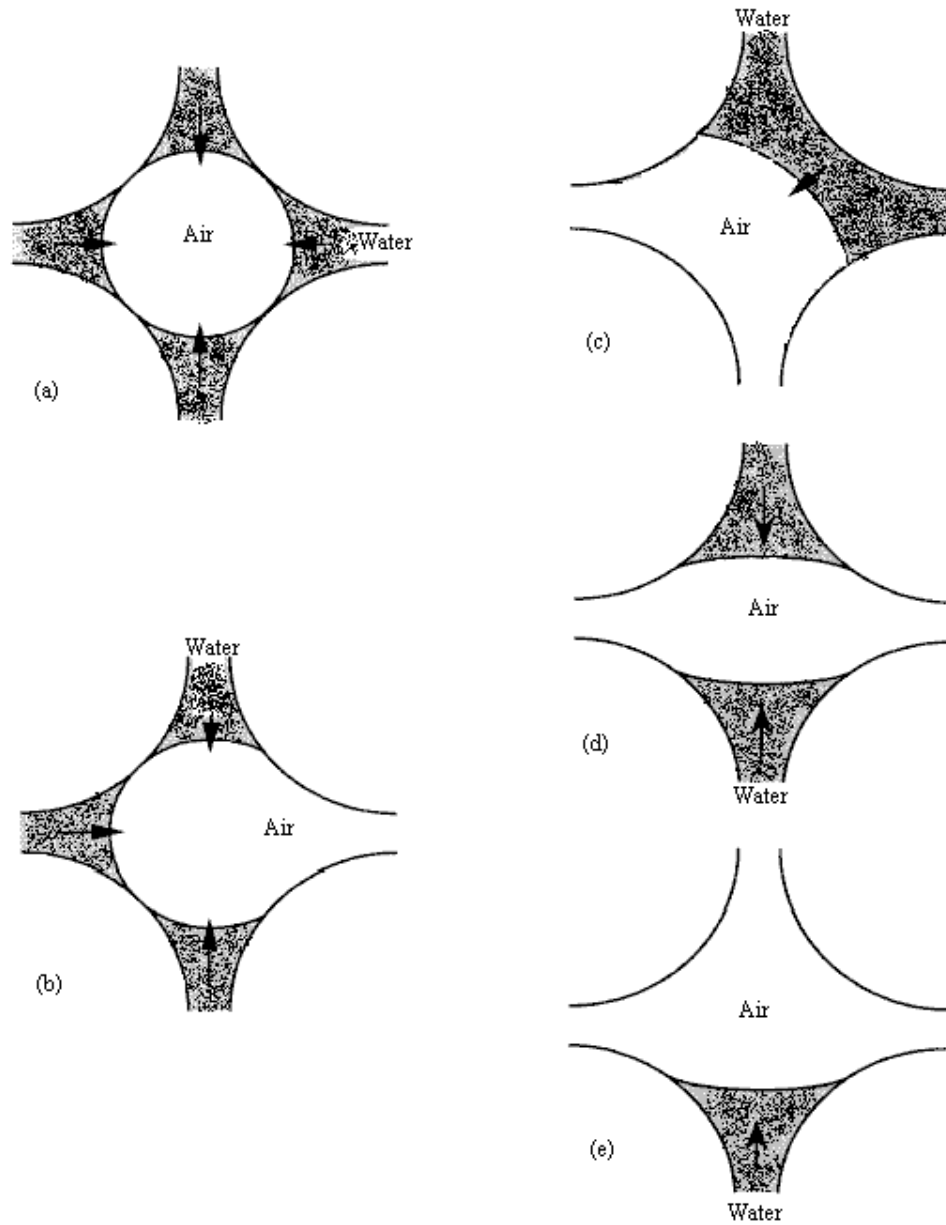


Figure 3.3.26 Different types of piston-like advance. (a) I_0 , all neighbouring throats are filled with water. This did not occur here since the air is not trapped. (b) I_1 , one neighbouring throat is empty. (c) I_{2a} , two adjacent throats are filled with water. (d) I_{2o} , two filled throats are opposite each other. (e) I_3 , only one throat is filled with water. The capillary pressures for each mode are ranked: $P(I_0) > P(I_1) > P(I_{2a}) = P(I_{2o}) > P(I_3)$.³⁸⁴

Zevi³⁶⁵ observed that the flow of water in a porous media not only fills the cavities and crevices in the bulk of the body but also forms films along the surface of the particles especially for liquid with strong wettability and with very low flow rate. Considering the diameter of Er^{3+} ion is $89 \times 10^{-3} \text{ nm}$ ⁴³⁶ which is far less than the water film thickness (20-40 nm calculated by Wan⁴³⁷ or 5-25 μm measured by Zevi³⁶⁵), thus the transport of erbium ion participating in the water films covering the BT particles and agglomerates is efficient. It was observed that the area adjacent to the back of the wetting front contains more liquid content during imbibition than the inlet area when the gravity effect is accounted for.^{438, 439} Moreover, the saline front in a porous media was found tailing the water front and exhibiting more heterogeneous displacement than the water front because of the binding of the ions to the particle surface.^{366, 440} Nevertheless, given printing saturated volume of dopant precursor solution and allowing sufficient time to settle, as well as considering the thickness of the porous BT base is less than 1mm used here, the concerns of the uniformity of dopant salt distribution in the BT disc body during imbibition can be eliminated.

3.3.5.2 Effect of Evaporative Drying

The distribution of dopant salt in the as-dried BT disc after droplet-doping is dependant not only upon the liquid infiltration into the porous material but also the subsequent motion of solute during evaporative drying which is closely related to the transport behaviour during 'wick action'.⁴⁴¹ In saturated porous systems, there are liquid flows in the direction of the evaporating surface, which also involve solute ions in the liquid. Hence the salt transport during drying is influenced by the mixed effects of convection-diffusion of liquid fluxes induced by evaporation. The evaporative drying rate of a BT disc subjected to over-saturated liquid infiltration

was measured by a microbalance and the corresponding results are displayed in Figure 3.3.27.

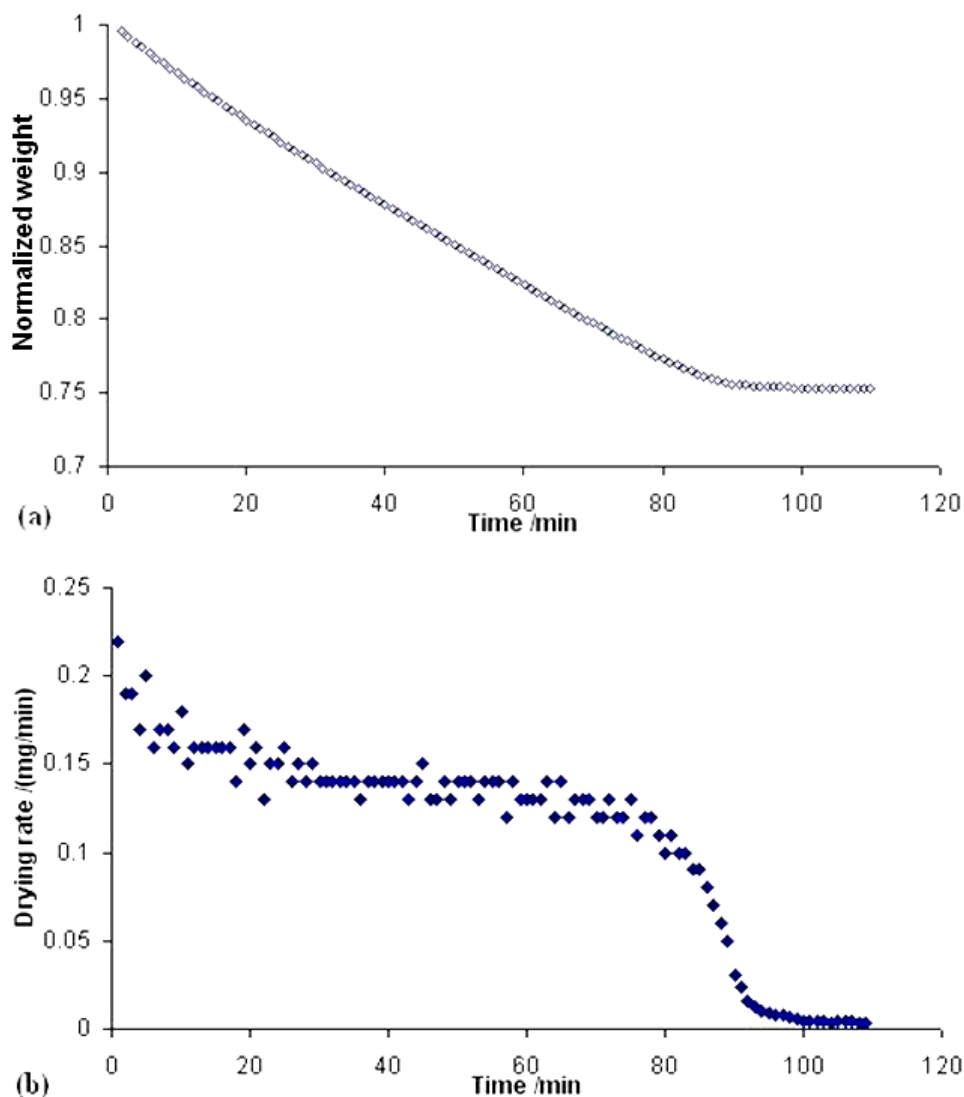


Figure 3.3.27 (a) the normalized weight compared with the initial value of an over-saturated disc as a function of time measured by a microbalance with sensitivity as 0.1 μg ; (b) the calculated drying rate as a function of time based on (a).

It was observed that there were approximately four regimes during the drying of the porous disc which is analogous to previous studies.⁴⁴² After the initial surface evaporation regime, the drying rate became almost constant. During this constant rate

period, capillarity controls the liquid flow from inside the pore space to the product surface, where the liquid evaporates. This is followed by a falling rate period, during which the recovery rate decreases rapidly. During this period, drying is controlled by mass transfer through the dry pore space due to disconnected liquid clusters formed near the surface. The last drying regime is the so-called ‘receding front’ regime in which the liquid phase in the porous medium completely disconnects from the surface and a fully dry zone with increasing thickness develops.⁴⁴² The Peclet number (Pe), the transport parameter which shows the balance between convection and diffusion, can be used to assess the ion re-distribution during drying.⁴⁴³ Equation 3.3.7 defines the Peclet number:

$$Pe = \frac{hL}{DP} \quad \text{Equation 3.3.7}$$

where h is the evaporation rate, L the thickness of pellet, D the diffusion constant and P the porosity. Typical values are $D \approx 10^{-9} \text{ m}^2/\text{s}$,⁴⁴³ $P \approx 0.55$, $L \approx 0.45 \text{ mm}$ and h as measured from the weight loss results in Figure 3.3.27, which is around 0.15 mg/min . Given the diameter of the pellet as 4.3 mm , the rate of evaporation is $1.72 \times 10^{-4} \text{ mm/s}$ and hence Pe in this system is estimated to be 0.14 ($Pe < 1$). This implies that donor ions can remain uniformly distributed in the porous medium due to the dominance of diffusive transport according to Huinink’s theory.⁴⁴³

3.4 Furnace Calibration

Both K-type thermocouples plus different voltage-to-temperature converters were cross-examined (as listed in Table 3.4.1) respectively by comparing the temperature measurements in a water bath with the reference temperatures measured simultaneously from a mercury thermometer. Several readings in the range of 15 °C to 100 °C are presented in Figure 3.4.1. All results, regardless of the sensor type were close to the reference values which were determined by the mercury thermometer. The difference of temperature readings from different thermocouples when connected to the same converter was less than 0.2 °C over the whole testing range. The temperature measurements using Eurotherm were close to the reference value; however, there were discernable gradients for the readings from Fluke as seen in Figure 3.4.1. Considering there is 1-2% in error for the temperature readings from the Fluke indicator, such difference in reading is within the expected accuracy range of the equipment.

Table 3.4.1. A combination of components of thermocouple and V/T converter

Thermocouple	V/T converter	Temperature controller (Eurotherm)	Voltage-to-temp converter plus an indicator (Fluke)
K-type thermocouple with ceramic sheath (A)		Eurotherm + thermocouple A	Fluke + thermocouple A
K-type thermocouple with glass-fibre insulation (B)		Eurotherm + thermocouple B	Fluke + thermocouple B

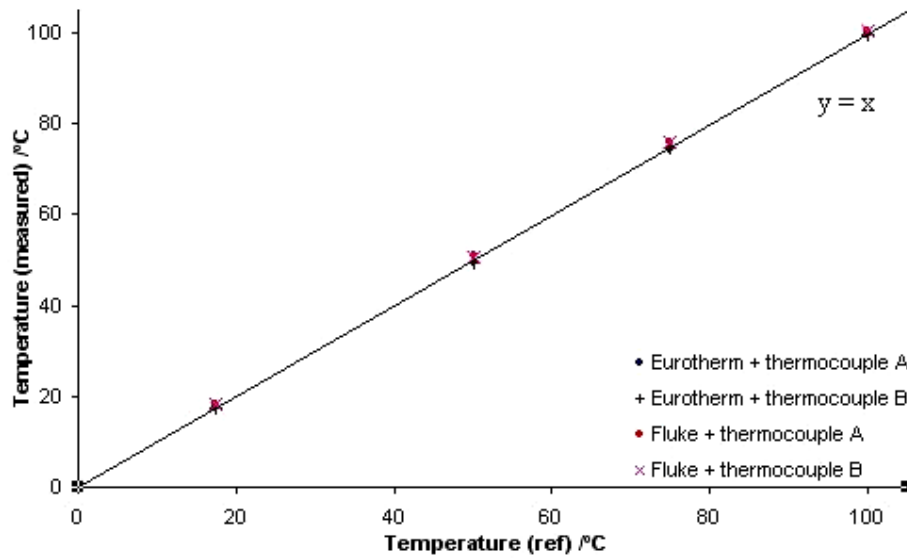


Figure 3.4.1 Cross-calibration the combination of thermocouples and voltage-to-temperature converters.

The heating profile of the modified pre-tuned furnace was examined under a pre-loaded programme in which the targeted setpoints were increased 5 °C every 10 minutes with no presetting ramp rate over a range of 20 to 300 °C (seen as a reference signal curve in Figure 3.4.2). The whole heating process lasted about 10 hours and the temperatures in the furnace measured as a function of time are presented in Figure 3.4.2. There were significant overshoots at each heating segment in this pre-tuning furnace. It was observed that the temperature in the furnace could not attain stabilization at the setpoint within a short scale of time.

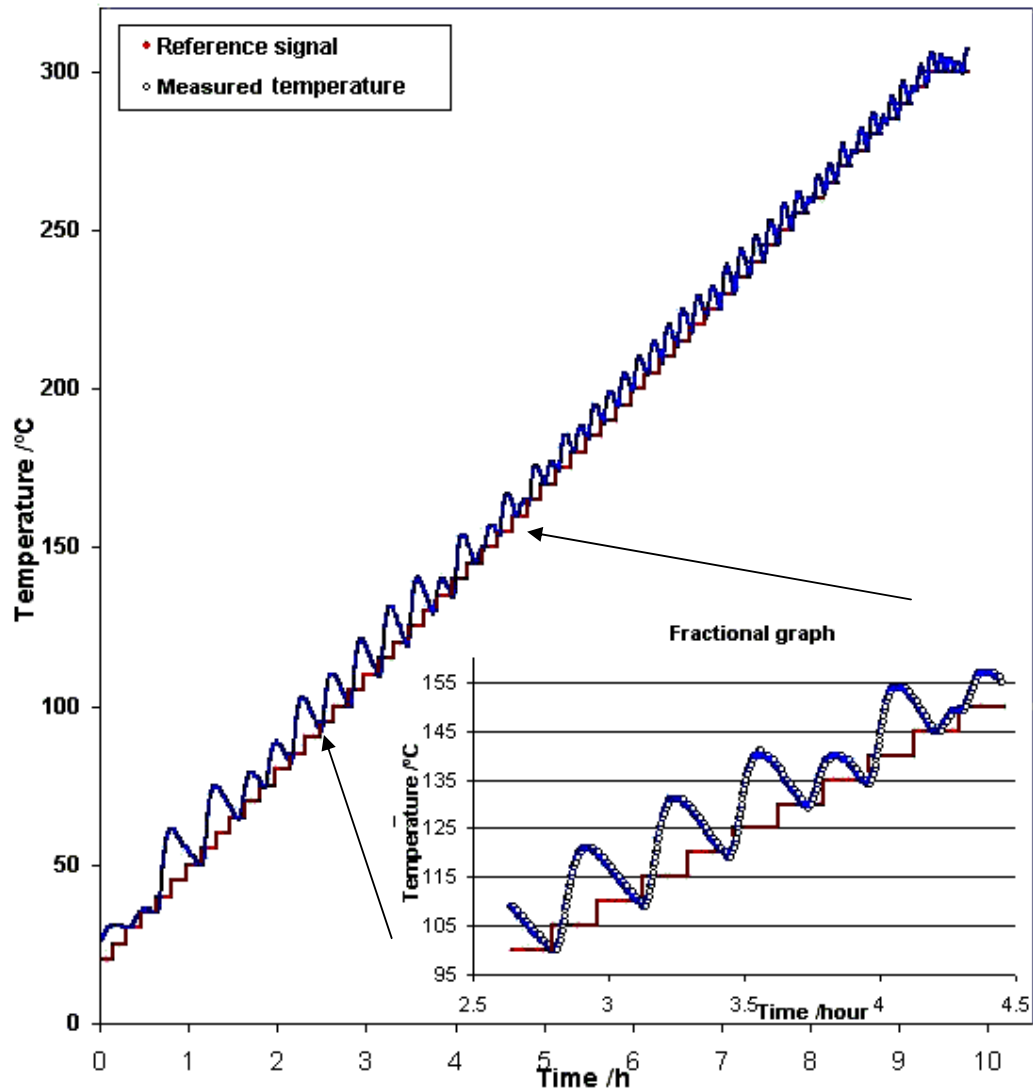


Figure 3.4.2 Heating profile of the modified pre-tuning furnace as a function of time.

The ideal heating curve should have a stable, 'straight line' of temperature rise to the setpoint without fluctuation and quick response to deviations from the setpoint caused by external disturbances, thereby rapidly restoring the temperature to the setpoint value. The heating control for the furnace is PID (proportional-integral-derivative) conducted by the Eurotherm temperature controller. The furnace was first tuned using the "I-Tools" software provided by the manufacturer and PID constants were adjusted accordingly in order to restrict the amount of overshoot or undershoot

while heating up to the setpoint.

Because the furnace is required to deliver accurate temperature rises to various setpoints in the range 20 to 300 °C, the results of tuning at different temperatures such as 100 and 200 °C were investigated. The heating profiles of the tuned furnace operating on the same heating program as in Figure 3.4.2, apart from using a ramp rate of 1 °C/min were monitored and the corresponding partial heating curves are presented in Figure 3.4.3. The heating program is displayed as the reference signal in Figure 3.4.3. For the furnace tuned at 100 °C, the heating temperature offsets at each setpoint after 10 minutes of heating were 0.2 °C which was smaller than that in the furnace tuned at 200 °C. Therefore, the modified furnace tuned at 100 °C was used for the further electrical tests.

The effect of applying different ramp rates during heating on the temperature profile was also investigated. The furnace was heated from 145 to 150 °C by a ramp rate of 1 °C/min and no preset ramp rate with sufficient dwell time (50 minutes). The corresponding heating profiles as a function of time are shown in Figure 3.4.4. The curve in blue (as seen in Figure 3.4.4) displays a heating profile using a ramp rate of 1 °C/min and the red curve represents the heating profile with no preset ramp rate. Both heating paths can reach thermal equilibrium in a period of 40 minutes during heating. It was observed that the maximum temperature offset during a setpoint increase of 5 °C was 0.2 °C and independent of the ramp rate. Furthermore, the furnace with a ramp rate of 1 °C/min during heating showed more steady increase of temperature and a less volatile state as a function of time than that with heating under no preset rate. Hence, the ramp rate of 1 °C/min was chosen for subsequent electrical

measurements. Moreover, 10 minutes as the period for each heating segment was adopted because it offers the best compromise between reaching thermal equilibrium and satisfying the efficiency of the test.

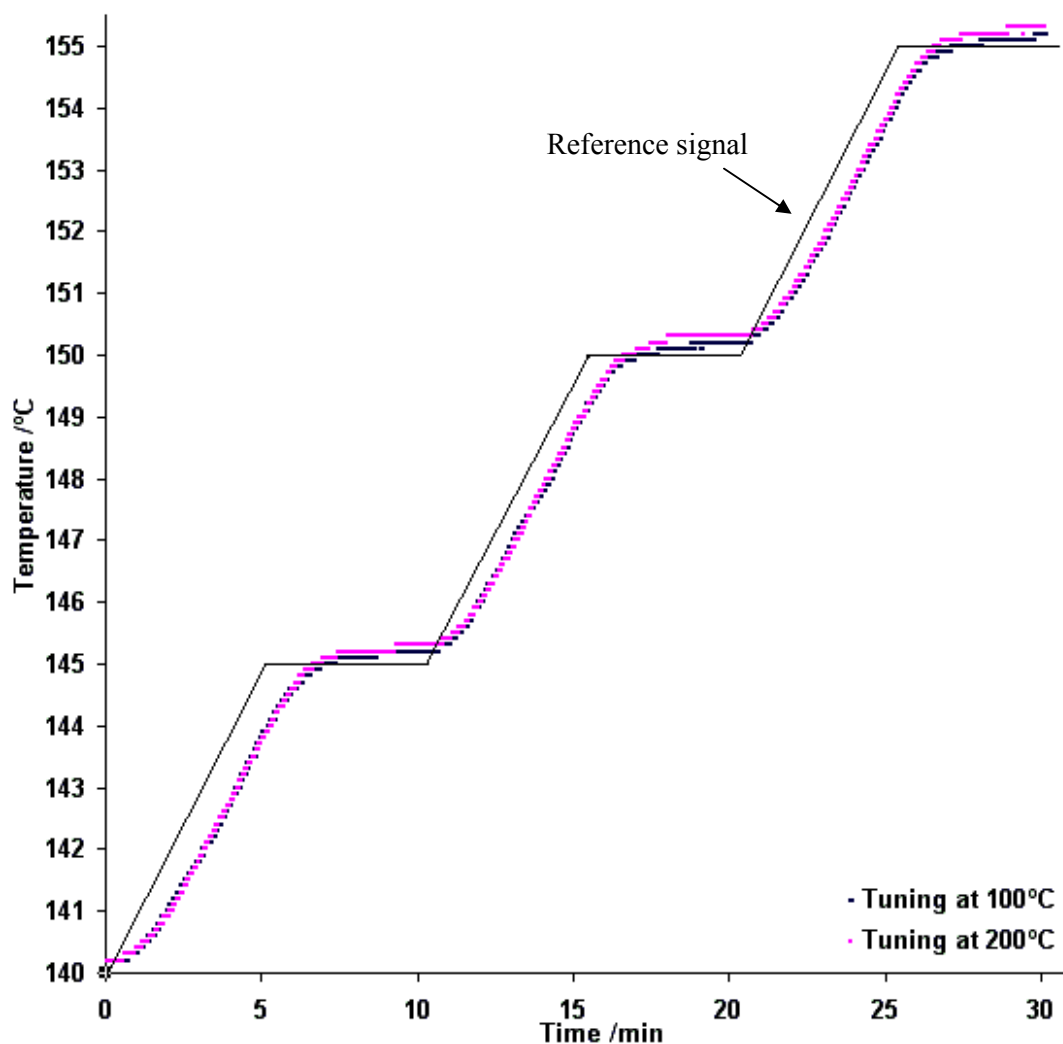


Figure 3.4.3 Heating profiles of the modified furnace after tuning at 100 °C and 200 °C respectively at a ramp rate of 1 °C/min.

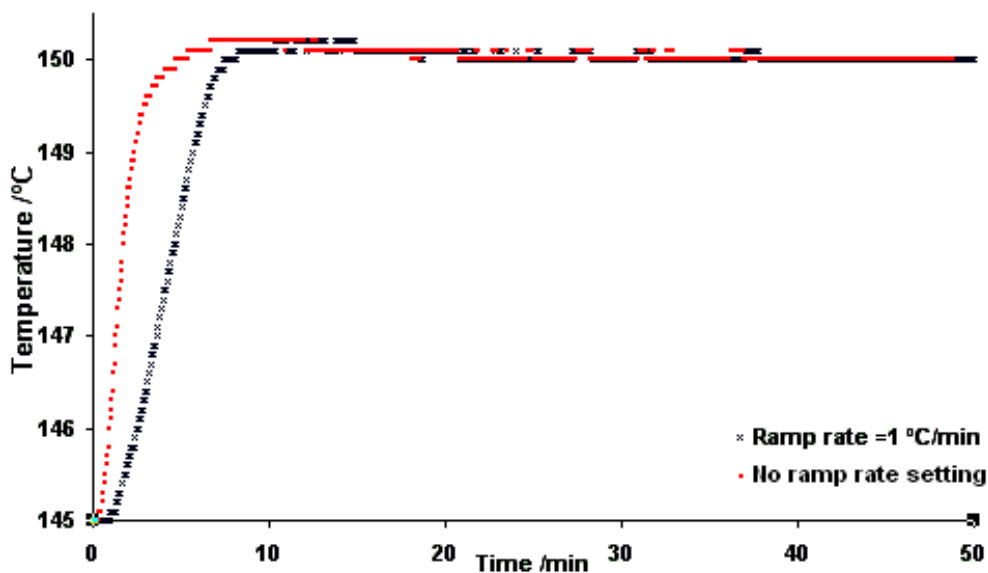


Figure 3.4.4 Temperature profiles of furnace heating at different ramp rates.

The surface temperatures of BT discs in the furnace were measured synchronously with the furnace temperature obtained from the controlled thermocouple located in the centre of the furnace. The heating profiles of the sample surfaces were compared with that in the furnace under different ramp rates. Figure 3.4.5(a) shows the measured temperature as a function of time on the sample surface and in the furnace during an increase of furnace temperature from 145 to 150 °C under no preset ramp rate and a dwell of 50 minutes. There was a significant difference in temperature between on the sample surface and the furnace during heating at around 150 °C: the temperature on the sample surface were around 3 °C lower and more volatile than the external environment (furnace) during heating at around 150 °C. A similar phenomenon was also observed for the BT sample in the furnace when heated at a ramp rate of 1 °C /min (in Figure 3.4.5(b)). However, temperature profile on the sample surface during heating showed quicker stabilization and less fluctuation when subjected a ramp rate of 1 °C /min.

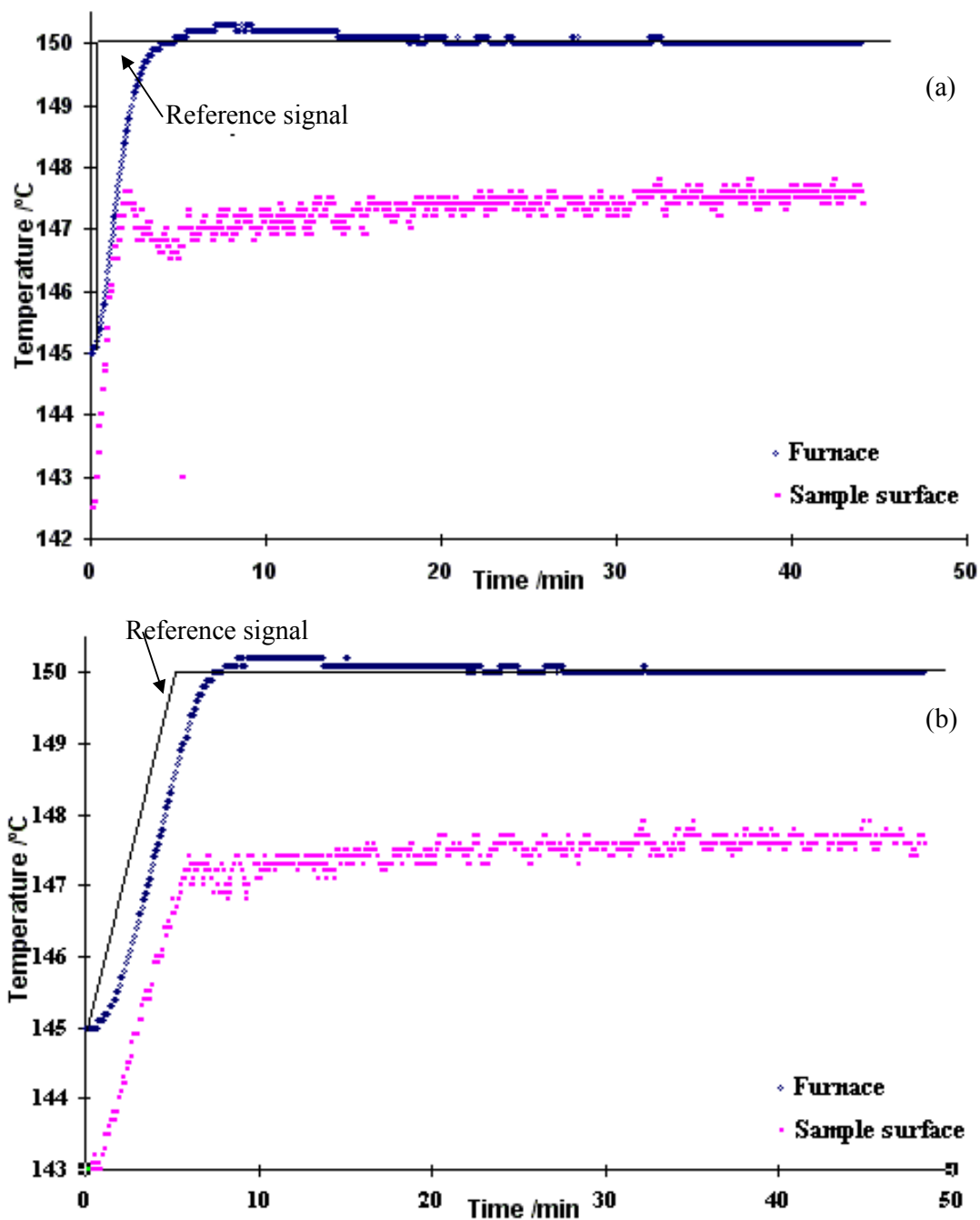


Figure 3.4.5 Furnace temperature and sample surface temperature respectively as a function of time during heating by a ramp rate as: (a) no preset ramp rate, (b) 1 °C/min.

The temperature gradients between furnace and sample surface during heating across

the range of 20 to 250 °C were measured in order to gain better understanding of the temperature uncertainty when undertaking subsequent electrical tests. The temperature gradients increased with the setpoint as displayed in Figure 3.4.6. These gradients in temperature are attributed to heat abstracted by the thermocouple due to thermal conduction.⁴⁴⁴ This effect can be significant if the sample is small enough. The temperature gradients along the furnace chamber are complex and affected by many factors including the size and the shape of the heating chamber, the type and location of the heating elements, conditions of insulation and circulation of the furnace, the power input and the furnace material, etc. Temperature variation between the distances of a few centimetres away at the corner of the furnace can be as much as 10% at very high temperature.^{445, 446} It is also reported that in a horizontal electric furnace, the radial temperature gradient is much smaller than the longitudinal temperature gradient⁴⁴⁷ because of the non-uniformly heat lost within the furnace chamber.⁴⁴⁸ For the range of test temperatures below 300 °C with all the sample tablets arrayed closely in a small area in the centre of the furnace, the temperature gradient between testing samples can be neglected.

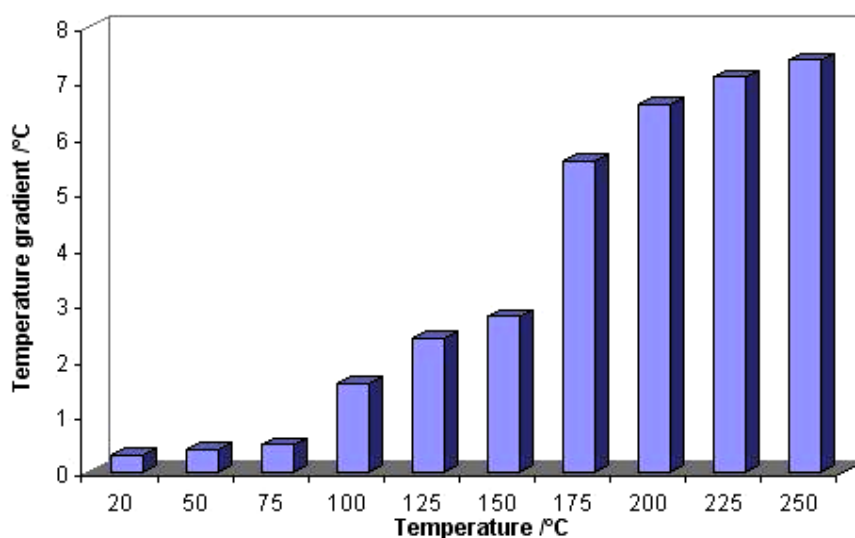


Figure 3.4.6 The temperature gradients between furnace and sample surface while heating the furnace from 20 to 250 °C.

3.5 Parallel R-T Screening System

A commercially produced PTC thermistor was loaded on the testing platform and its PTC characteristics were examined by the in-house testing programme. The reference R/T characteristic of this PTC thermistor as provided by the supplier was replotted (curve B in Figure 3.5.1) and compared with the values measured by the in-house testing system (curve A in Figure 3.5.1).

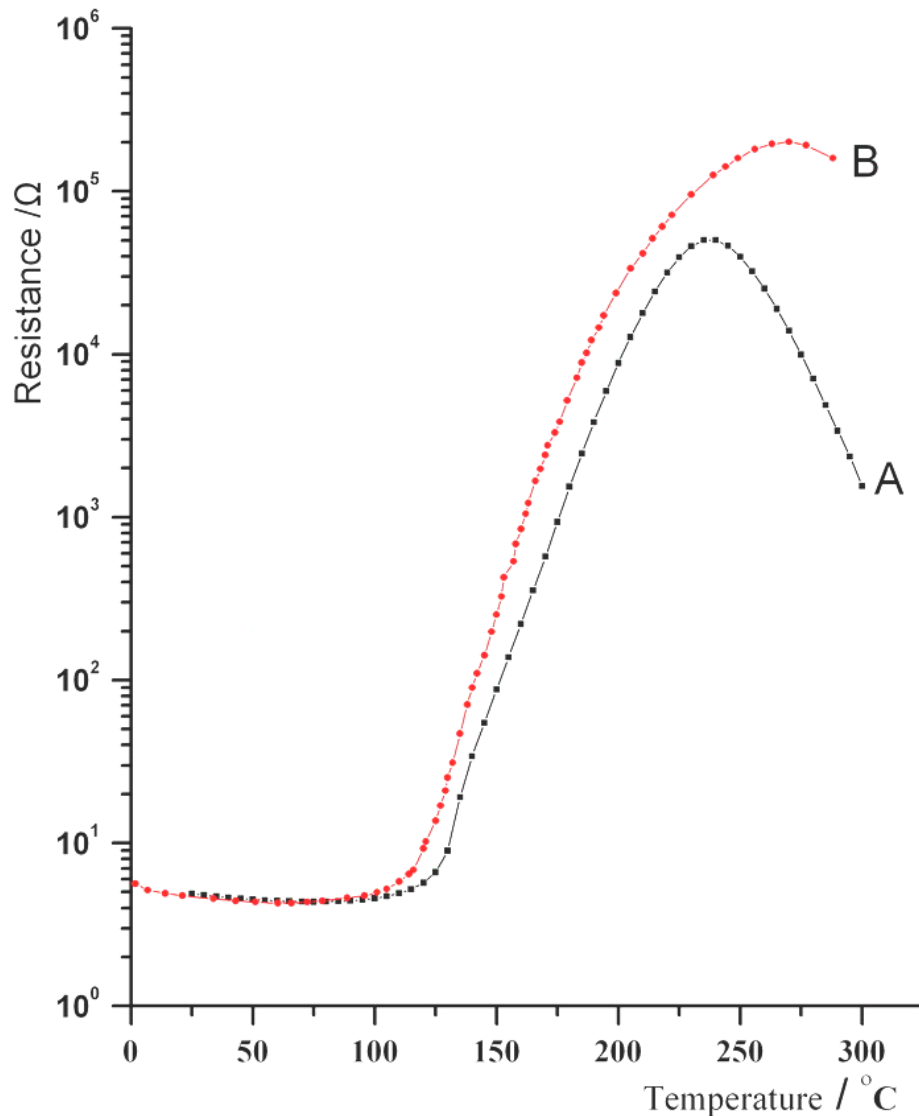


Figure 3.5.1 R/T characteristics of a commercial PTC thermistor: experimental results using in-house system (curve A) and reference values from the supplier (curve B).

The measured curve A was well fitted with the reference values in curve B below the Curie temperature (T_c); however, there was deviation occurring above T_c . Some key parameters of the PTC thermistor from the reference and the measured curves respectively are listed in Table 3.5.1. The temperature at which the start of the steep rise in resistance, also defined as the temperature at which the resistance is equal to the value $R = 2 \cdot R_{\min}$, corresponds approximately to the ferroelectric Curie point according to the handbook from EPCOS.⁴⁴⁹ Hence its corresponding value is estimated as the value of T_c here. Note that the more accurate methods to determine the T_c of doped BT materials are the differential thermal analysis³²⁶ and permittivity measurement etc. which they can more accurately measure the process of the tetragonal to cubic phase change of the BT during the heat treatment. The room-temperature resistance of this PTC thermistor was measured as 4.8Ω which was very close to the reference value of 4.6Ω . Moreover, because the blank resistance of the parallel conducting jig was very small ($\approx 0.1 \Omega$) compared with the measured value of R_{\min} , the correction for the jig effect was unnecessary and similarly, the effect on resistance from the measuring leads and multimeter could also be neglected. The temperature coefficient α is defined as the relative change in resistance referred to the change in temperature and can be calculated for each point on the R/T curve by:⁴⁴⁹

$$\alpha = \frac{1}{R} \cdot \frac{dR}{dT} = \frac{d \ln R}{dT} \quad \text{Equation 3.5.1}$$

In the range of the steep rise in resistance above T_c , α can be regarded as being approximately constant. Therefore,

$$\alpha = \frac{\ln\left(\frac{R_2}{R_1}\right)}{T_2 - T_1} \quad \text{Equation 3.5.2}$$

In the temperature range of 130-180 °C, the measured value of α for this PTC thermistor was 0.103 K^{-1} which is close to the reference value of 0.105 K^{-1} .

Considering the associated tolerance of the resistance value of the thermistor is 25% provided by the supplier, this in-house testing system is proved to be reliable for subsequent R/T measurements for the libraries of donor-doped BT samples produced by HT method. Note that the values of the maximum resistance, R_{max} , and the temperature at which R_{max} occurs, T_{max} , were substantially different between that in the curve A and B. The mechanism of such difference is unclear.

Table 3.5.1 Parameters of the PTC thermistor.

	T_c / °C	R_{RT} /Ω	R_{min} /Ω	R_{max} /Ω	T_{max} / °C	α / K ⁻¹
Reference value	120	4.6	4.1	2×10^5	270	0.105
Measured value	130	4.8	4.3	5×10^4	235	0.103

3.6 Fabrication and Characterization of La-doped BT Ceramics with PTCR Effect

All Er-doped BT thick film samples regardless the doping levels in chapter 2.4.1 made by the combinatorial method using the dip-pen printing and droplet-doping and sintered in air were electrically insulating materials at room temperature ($R_{25} > 1 \times 10^7 \Omega$). It was reported that erbium can behave as an amphoteric dopant in BaTiO_3 in which its character is highly dependent on the cation stoichiometry in BT along with other factors.²⁰⁶ Thus, it was found that Er-doped BaTiO_3 is weakly semi-conducting at room temperature when $\text{Ba/Ti} = 1$; erbium dopant even behaves as an acceptor (preferential substitution at Ti^{4+} sites) when $\text{Ba/Ti} > 1$ but as a donor (preferential substitution at Ba^{2+} sites) when $\text{Ba/Ti} < 1$.²⁰⁶ Although the Ba:Ti molar ratio is equal to 1 as provided by the supplier for the as-received BaTiO_3 powder (Inframat Advanced Materials), the EDS result showed molar ratio $\text{Ba:Ti} \approx 1.2$ by scanning the powder particles. Noting that there is significant overlapping of characteristic EDS energies between the elements barium and titanium, as well as errors generated from the quantitative EDS analysis by scanning the unpolished particle surface, the true molar ratio of Ba and Ti of the as-received BT powder is still uncertain. Lanthanum, as a donor dopant candidate for BT-based PTCR materials which has been extensively claimed, involves less sensitivity of electrical conductivity to the cation stoichiometry of BT in comparison with the amphoteric dopant like erbium.^{235, 237, 253} It was therefore selected for initial investigation for preparing donor-doped BT material exhibiting PTCR behaviour. It was necessary to fabricate reference La-doped BT PTCR samples by a conventional solid-state reaction route first in order to compare the PTCR performance with that produced by HT method. Moreover, TiO_2 -

excess BT and additional SiO₂ were both employed here to enhance grain growth during sintering by providing extra liquid phase.

3.6.1 Preparation of La-doped BT PTCR Ceramics by Solid-state Reaction (SSR)

Method

The critical concentration of La³⁺ for doped BT sintered in air was found to be 0.6 mol.%, above which the sample would revert back to behaving as an insulator.²³⁵ Thus samples of BT doped with 0.3 and 0.5 mol.% La³⁺ as donor dopant were prepared in order to investigate the PTCR profiles. BT powders from different sources were used and compared as a starting material and the details of different batches of samples in terms of composition and firing parameters are listed in Table 2.6.1.

Figure 3.6.1 shows the morphologies of the powders used as the starting materials in Table 2.6.1. The particle sizes of as-received (from PI-KEM) and synthesized BT powders are similar and are all in the submicron scale ($d_{\text{BT(PI)}} \approx 0.5 \mu\text{m}$, $d_{\text{BT(syn)}} \approx 0.3 \mu\text{m}$) measured by a line intercept method. The size of TiO₂ particle is very fine at around 0.1 μm , whereas the size of La₂O₃ particle is around 1 μm .

The room-temperature resistance of samples in batches A3, 5 and B3, 5 were all >20 M Ω ($2 \times 10^7 \Omega$) which indicated that they were electrically insulating materials. The microstructures of 0.3 mol.% La³⁺-doped BT in batches A3 and B3 were examined by SEM and the low magnification images of fracture surfaces are presented in Figures 3.6.2a and c. The details of their grain structure are shown in Figures 3.6.3a and c respectively. Sample A3 had high porosity and contained heterogeneous large

grains after sintering, whereas a homogeneous fine-grained (1-2 μm) and denser microstructure was observed in sample B3.

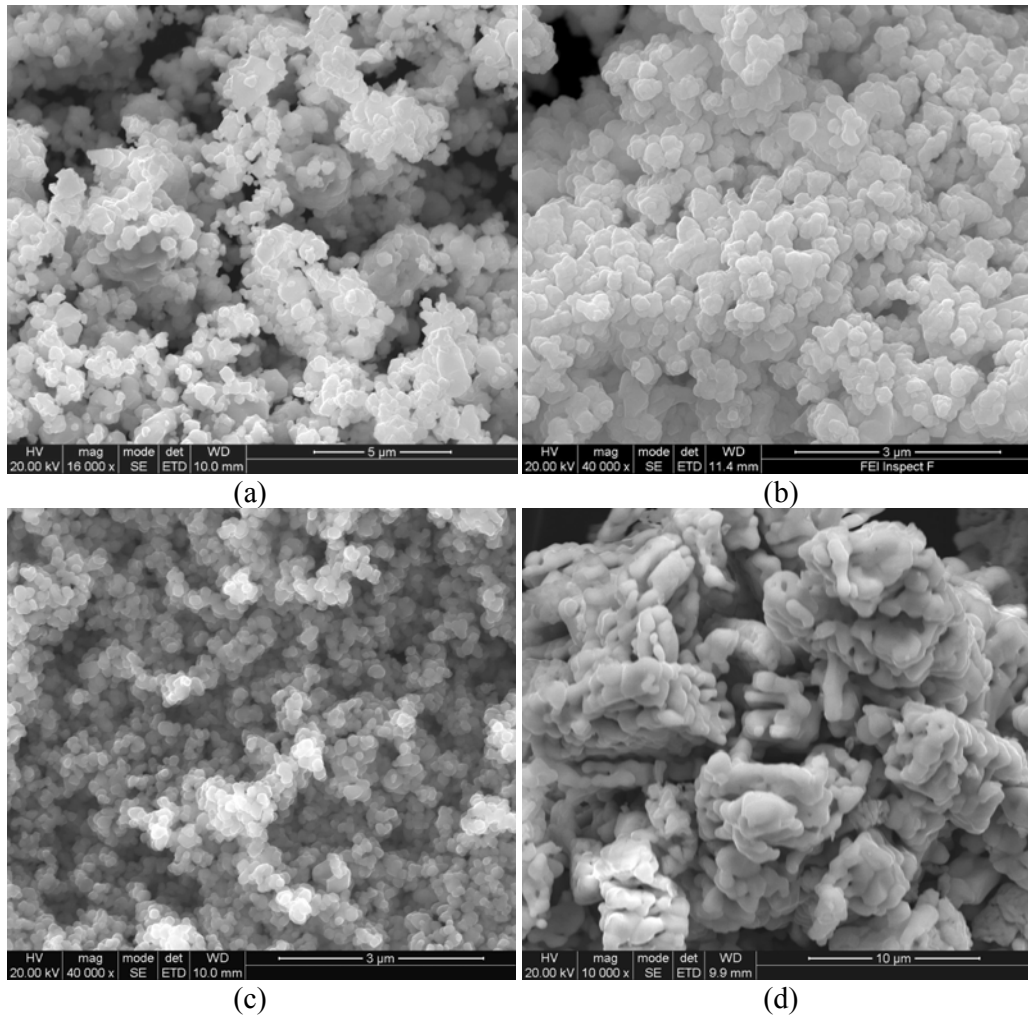


Figure 3.6.1 SEM images of the starting materials: (a) as-received BaTiO_3 powder from PI-KEM, (b) synthesized BT (Ti:Ba=1.01), (c) as-received TiO_2 powder and (d) as-received La_2O_3 powder.

It has been generally observed that the room-temperature resistivity (r_{RT}) is low for donor-doped BaTiO_3 having large grains and the r_{RT} of a doped- BaTiO_3 sample with fine grains is large ($>10^5 \Omega \cdot \text{cm}$).³³⁴ Under the same composition of doped- BaTiO_3 , the fine grain structure that reduces the electrical conductivity may be due to a strain

effect which increases the potential barrier and hence the resistivity at the grain boundaries.²⁸⁷ Furthermore, the small grain system contains a larger fraction of insulating grain boundaries compared with the sample having large grains and thus presents higher resistivity.^{335, 336} Therefore, higher sintering temperature which is up to 1450 °C,²⁶⁵ longer dwelling time (9 hours)²³⁴ and adding a sintering aid (SiO₂)³⁴⁸ were used in order to enhance grain growth during sintering. There were no signs of over-sintering phenomena on samples in batches C-E. The fracture surfaces and microstructures of sample C3, D3 and E3 were also examined by SEM and the corresponding images are displayed in Figures 3.6.2(b),(d),(e) and 3.6.3(b),(d),(e). The grain size increased with increasing sintering temperature and dwell time. However, sample E3 has significant bimodal grain size distribution (Figure 3.6.3(d)). The large grain ($\approx 20 \mu\text{m}$) was found embedded in a fine-grained ($\approx 2 \mu\text{m}$) matrix of BT. Sample C3 (Figure 3.6.3(e)) contained larger grains ($\approx 4 \mu\text{m}$) in comparison with sample B3 (Figure 3.6.3(c)) attributed to the SiO₂ additive which facilitates grain growth by creating a liquid phase during firing. Samples in batches C-E were all electrically insulating materials at room temperature apart from C3 for which resistance at room temperature was around $8 \times 10^5 \Omega$. The as-sintered samples using BT (I) contained relatively large grains (Figure 3.6.3(a,b)) in comparison with samples using BT (II); however, they both exhibited no PTCR effect. The probable reason for this insulating behaviour of samples using BT (I) is explained as follows.

The PTCR donor-doped BT is a composition-sensitive material especially to some *3d*-elements as acceptor dopants,²⁴⁵ and the solubility range for semiconductivity of acceptors such as Fe and Cu in BT can be as little as 0.04 mol.%.⁴⁵⁰ The BT powder (I) used as a starting material might be already contaminated by the Vibro milling

processing because incomplete cleaning of the mill chamber and the grinding media which had been used for grinding many inorganic compounds previously is unavoidable. In addition, Vibro milling has the risk of contamination from the lining. Although the SEM/EDS examination had been performed for the powder after Vibro milling, no detectable impurities were found in the powder because it may be below the detection limit of the equipment. Hence impurities may result in electrical insulation using BT (I) regardless of whereas the system contained a large grained microstructure. The high resistivity and fine grain structure of samples using BT powder from PI-KEM may be due to the high crystallinity of the original BT powder. It has been observed that an increase of crystallinity of the starting BT powder suppresses recrystallization leading to fine-grained microstructure and growth in resistivity.³⁰⁶ The SEM images of samples in batches B, C&E support this view. Again, the fine grain structures in those batches of samples might be also caused by a Ba/Ti ratio of larger than 1 for as-received BT powder (II).³³⁴

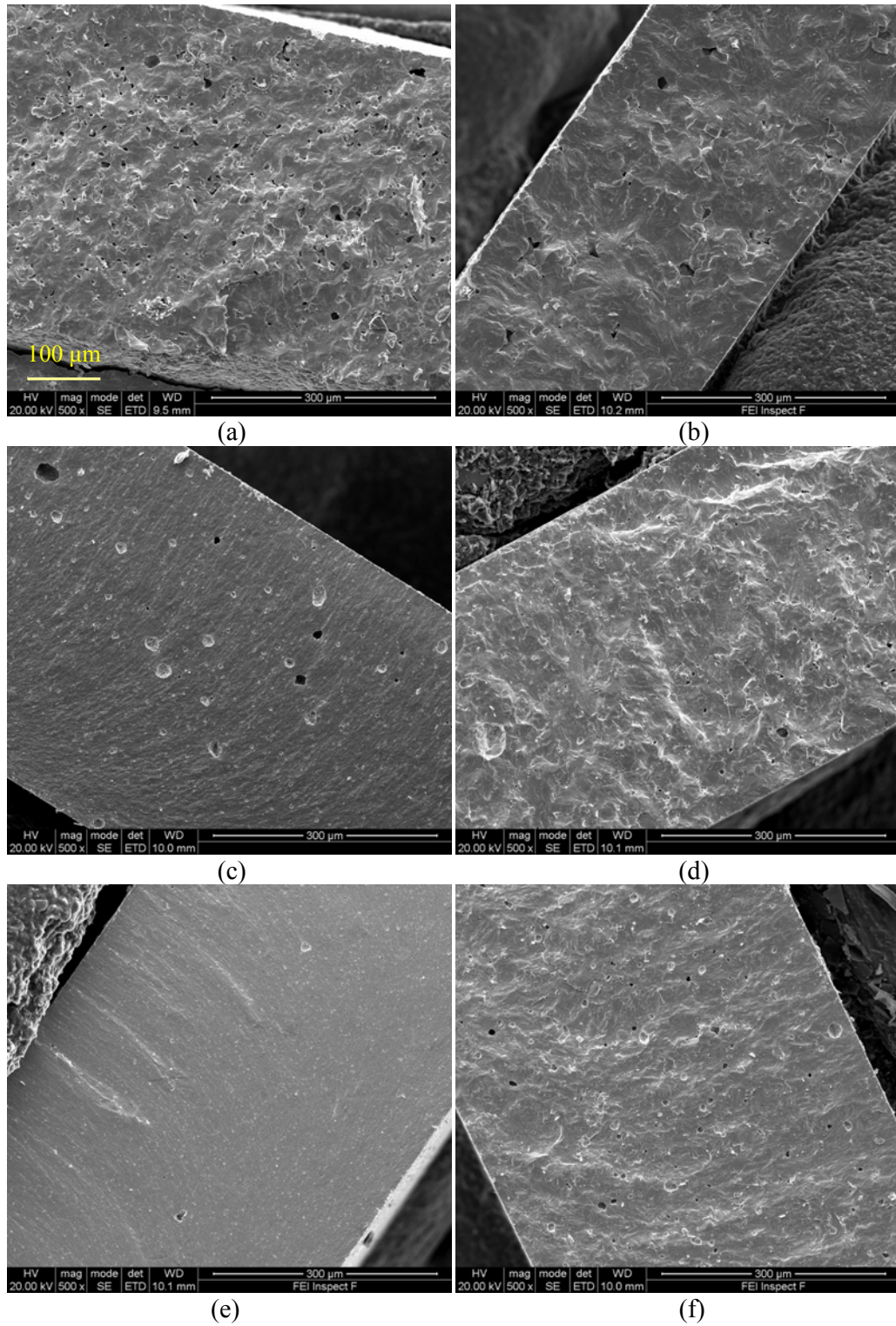


Figure 3.6.2 Microstructures of the fracture surface of (a) A3, (b) D3 (c) B3, (d) E3, (e) C3 and (f) F3 samples under 500x magnification.

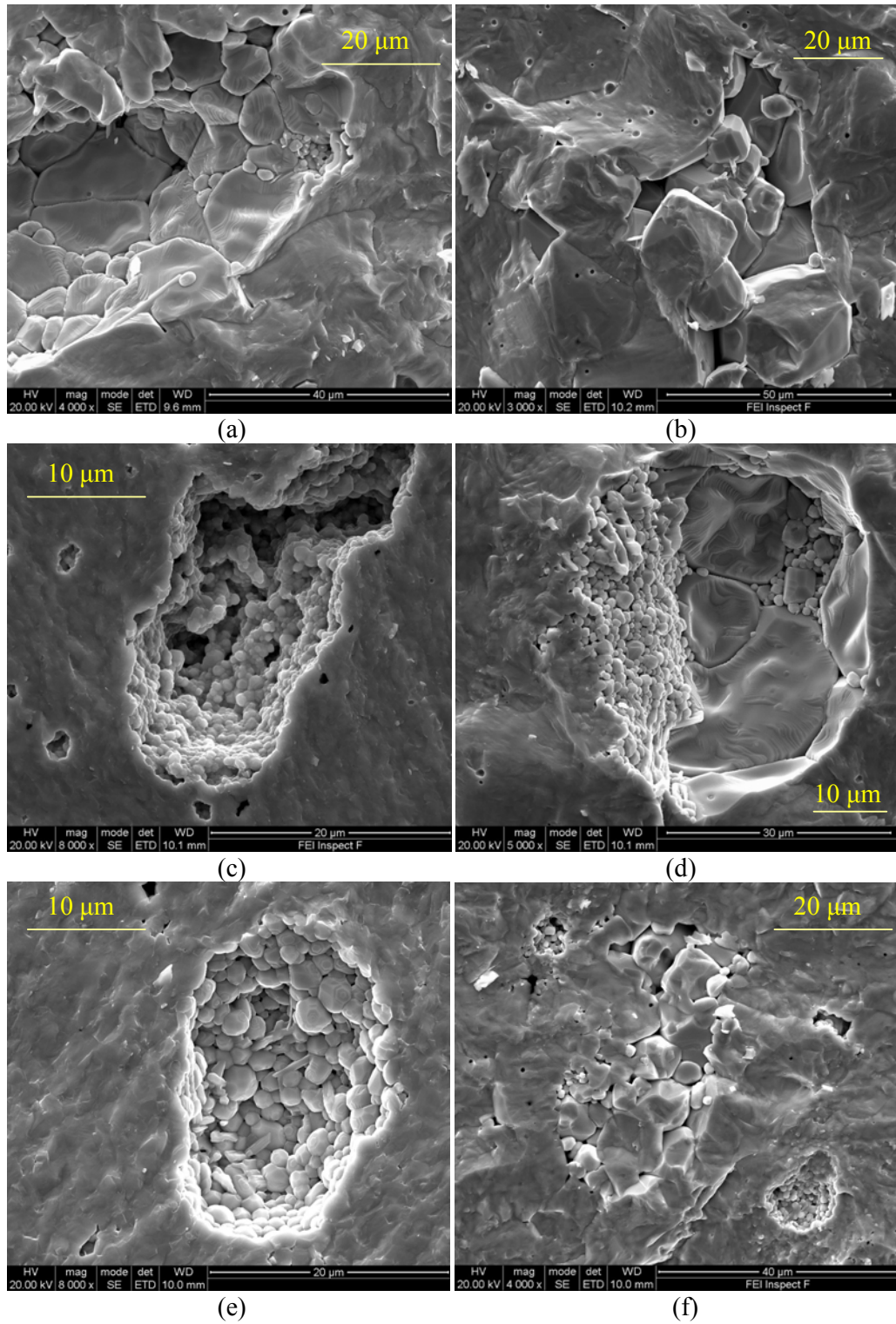


Figure 3.6.3 Microstructures of La-doped BT specimens synthesized by SSR route sintered in air under conditions: (a) A3, (b) D3 (c) B3, (d) E3, (e) C3 and (f) F3.

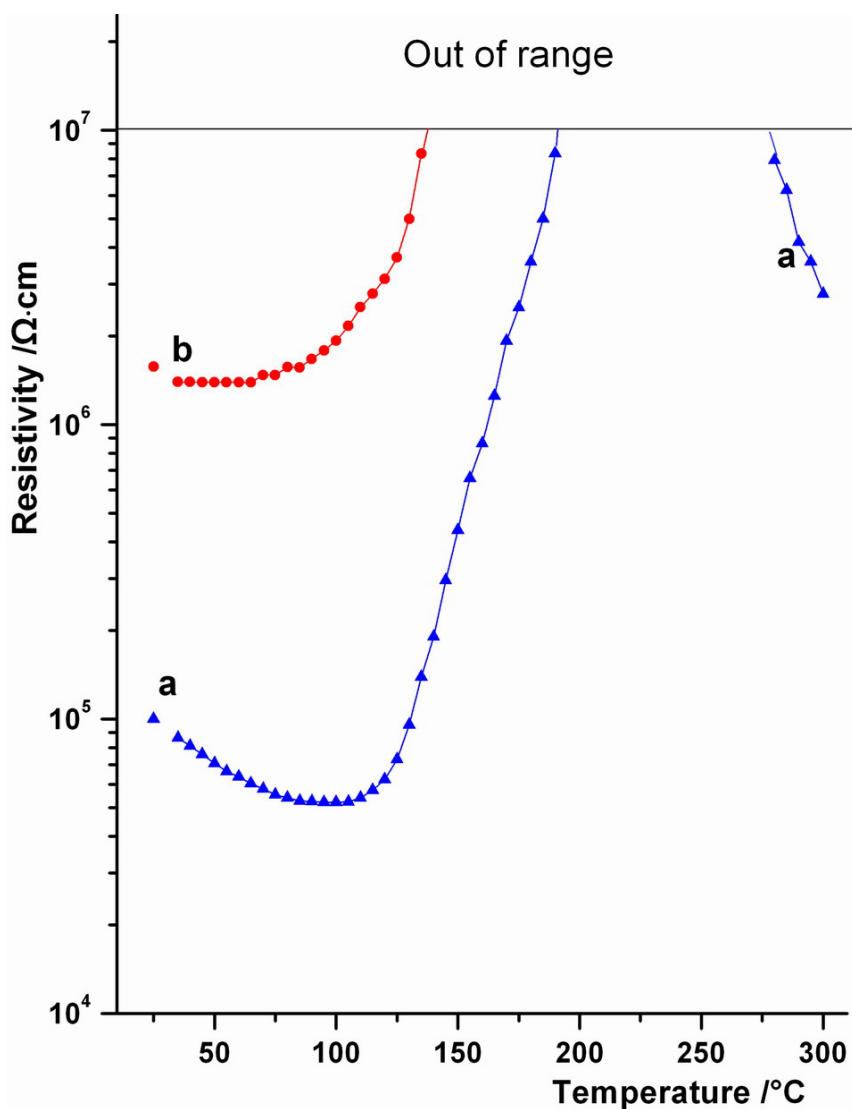


Figure 3.6.4 Temperature dependence of the electrical resistivity for (a) F3 and (b) F5 sintered at 1380 °C in air.

Therefore, BaCO_3 and TiO_2 were used as the starting powders to synthesize BaTiO_3 for which the Ti/Ba molar ratio can be precisely managed and lanthanum ions as donor dopant can be incorporated into the BT lattice during the reaction-calcination process. Furthermore, because the observation that the room-temperature resistivity of donor-doped BaTiO_3 can increase with sintering temperature and dwell time which is attributed to an increase in the amount of acceptor-states along the grain boundaries,^{322, 326, 327} the samples in batch F were sintered at 1380 °C for 1 hour.²³⁷

The resistance at room temperature of sample F3 and F5 were about 30 and 500 k Ω respectively. The grains of sample F3 were of intermediate size as seen in Figure 3.6.3(f).

A 2-probe measurement was applied to measure the voltage (U) and current (I). The resistance is thus calculated as $R = U/I$ and the corresponding resistivity (r) is obtained from the equation:

$$r = \frac{RS}{L} = R \cdot \frac{\pi a^2}{L} \quad \text{Equation 3.6.1}$$

where a is the disc radius and L is the thickness. The r - T curves of batch F samples sintered in air are shown in Figure 3.6.4. The samples using synthesized BT exhibited obvious PTCR profiles. The room-temperature resistivity of sample F3 was around $10^5 \Omega \cdot \text{cm}$ and increased abruptly when the temperature passed the Curie point ($\approx 131 \text{ }^\circ\text{C}$) as curve a in Figure 3.6.4. The sample also presented a strong negative temperature coefficient resistivity (NTCR) effect at both temperatures below T_c and in the high temperature range ($T > T_c$). The initial drop of resistivity with temperature below T_c is due to the increase of spontaneously polarization in ferroelectric BT according to Jonker's model.²¹² The NTCR effect of sample F3 when passing the point of maximum resistivity (r_{max} , not shown here because the current was below the minimum measurement limit of the multimeter) results from the increase of energy of trapped electrons surpassing the increased potential barrier in the grain boundary.²¹⁰ For a sample containing 0.5 mol.% of La^{3+} content (F5), the room-temperature resistivity was much higher than that with lower donor concentration (F3). This is due to the shift of electronic compensation at low donor concentration level to ionic compensation when increasing the donor concentration. As a

consequence, the potential barrier in the grain-boundary region was increased significantly because of the dopant segregation effect leading to the increase of resistivity.^{256, 286, 287} The r - T curve of F5 in the high temperature range and part of F3 was not obtained because of the measuring limit of the multimeter.

There is general agreement that the PTCR feature of doped-BT is defect sensitive. The low temperature ($T < T_c$) conductivity of donor-doped BT is influenced by a broad variety of factors including impurities in the starting powders, stoichiometric difference, attributes of dopant additives, firing parameters and nature of the external/internal defects etc. The origin of the room-temperature conductivity of doped-BT is very complex and still under dispute.²³⁵ Although it is reported that the room-temperature resistivity of La-doped BT with similar composition of sample F3 sintered in air can be as low as $300 \Omega \cdot \text{cm}$ ^{334, 394} in comparison with $10^5 \Omega \cdot \text{cm}$ of the sample made by the SSR route here, to explore the reasons what makes a La-doped BT PTCR sample sintered in air exhibited such low resistivity at the same doping level is beyond the scope of this project. Nevertheless the ultra high resistivity of the air-sintered samples can reduce the accuracy of subsequent PTCR property screening because of the limitation of the measurement scale of the multimeter. It was believed that electron compensation is preferred in reducing conditions during sintering resulting from the tendency for oxygen loss, while ionic compensation by generated Ti vacancies is favoured by an oxidative environment.²²⁸ Furthermore, the quantitative analysis of the oxygen deficiency of donor-doped BT has proved that the carrier concentration is still dependent on the donor concentration.²²⁹ Hence, consistent nitrogen flow was employed during sintering in order to increase the room-temperature conductivity of donor-doped BaTiO₃, as well as increase the

critical donor concentration.^{324,325}

Figure 3.6.5 shows resistivity vs. temperature behaviour in La-doped BaTiO₃ fabricated by the SSR route in various batches as listed in Table 2.6.2 sintered in nitrogen gas flow at 1380 °C. Unlike those samples sintered in air which had high r_{RT} , they presented good electrical semiconduction at room temperature with strong PTCR profiles. Samples in the batch NC showed the lowest r_{RT} (100-300 Ω·cm) with significant magnitude of PTCR rise among all batches in Table 2.6.2 because they contained a larger total amount of TiO₂ and SiO₂ as a sintering aid, which can facilitate grain growth by providing more liquid phase during sintering compared with that in other batches. Furthermore, the temperature at the maximum resistivity of the sample was increased from ≈270 °C (batch NA with no SiO₂ content) to 300 °C (both batches NC&NF with SiO₂ content). This phenomenon agrees with the findings that SiO₂ addition has some effect on electrical performance such as decreasing the room-temperature resistivity and increasing the temperature of maximum resistivity.³³⁰ Batch NF showed moderate PTCR jump (1.4-2.1 order of magnitude), indicating that the samples prepared from mixing BaCO₃, TiO₂ and La₂O₃ by a one-step calcination contained less density of surface acceptor-state than that of using commercial crystalline BT powder as starting materials. Sample NA3 exhibited the highest PTCR effect with 2.8 order of the magnitude.

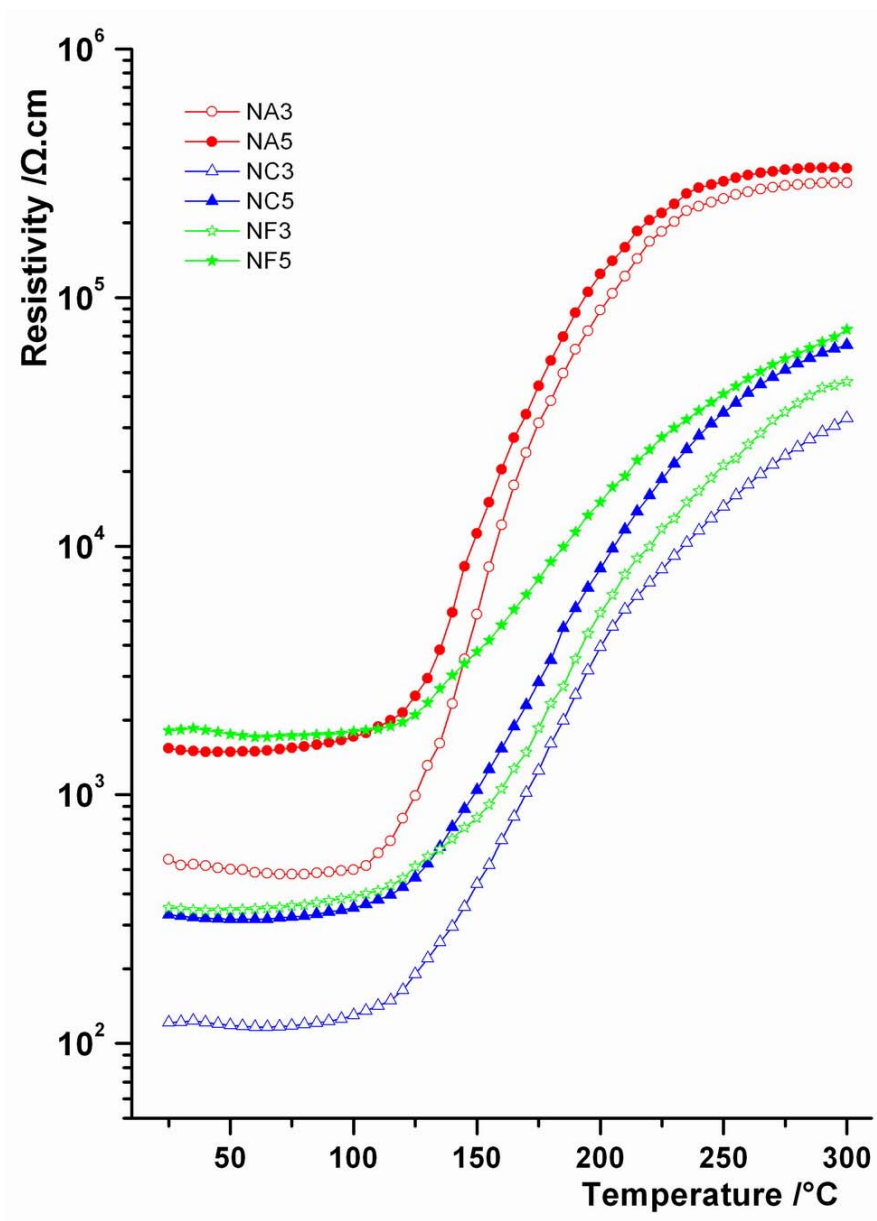


Figure 3.6.5 r - T characteristics of La-doped BT in Table 2.7.2 using SSR method sintered at 1380 $^{\circ}\text{C}$ for 1 hour in N_2 .

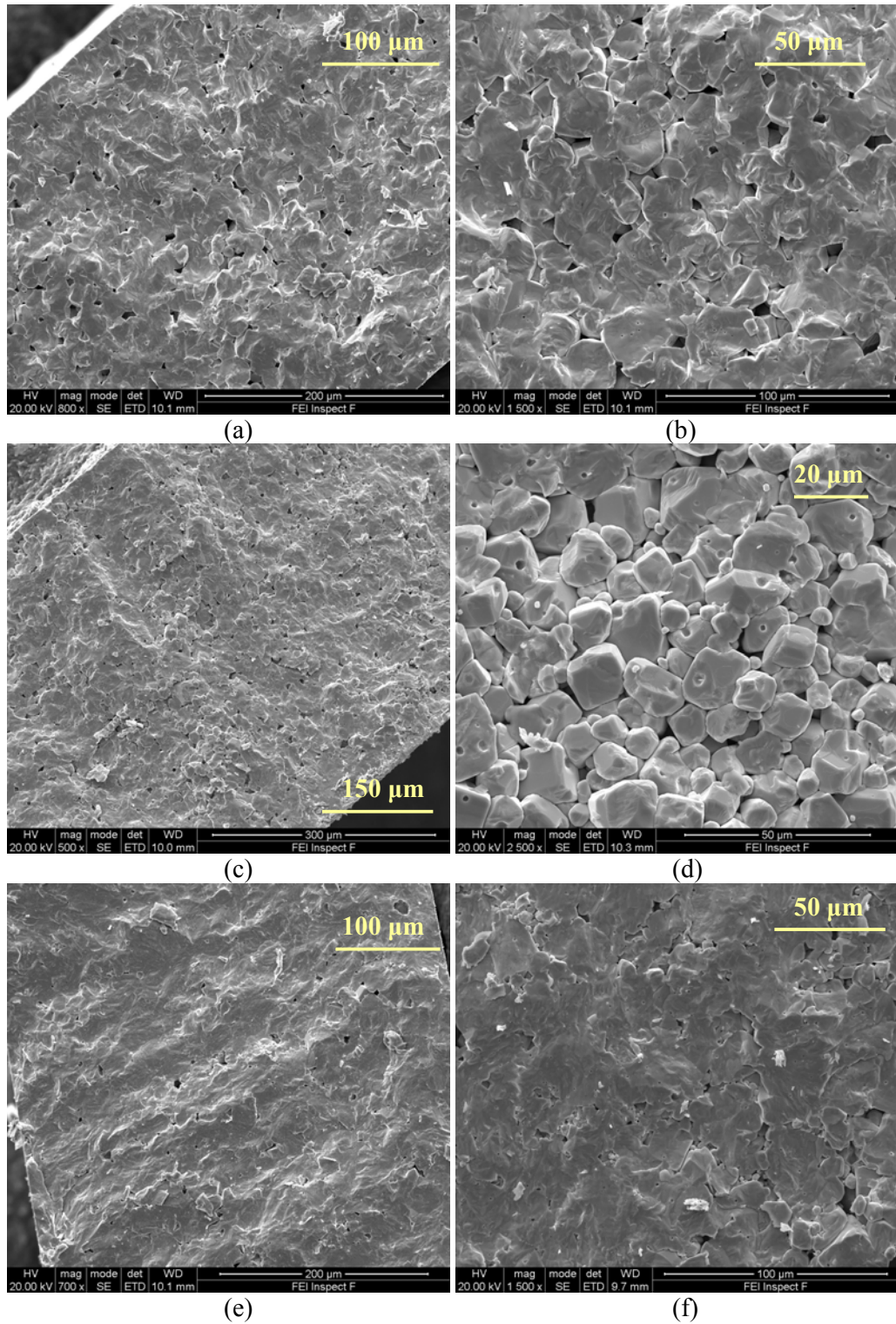


Figure 3.6.6 Microstructures of La-doped BT specimens synthesized by SSR route sintered in N_2 : (a),(b) NA3; (c),(d) NC3; (e),(f) NF3.

There was obviously abnormal grain growth observed for samples sintered in N_2 (Figure 3.6.6) in comparison with those sintered in air (Figure 3.6.3). Particularly, grains as large as $30\ \mu\text{m}$ were found in sample NC3 (Figure 3.6.6(d)) which was $1\text{-}2\ \mu\text{m}$ in sample C3 (Figure 3.6.3(e)). The increase of the grain size when sintering under low oxygen partial pressure is in good agreement with observations in the literature.²⁶³ According to the thermodynamic model for donor-doped BT,⁴⁵¹ the solid-state grain growth is strongly limited by the suppression of the oxygen-ion diffusion. Consequently, the lower the oxygen partial pressure in the sintering atmosphere, the greater is the driving force for exaggerated grain growth.

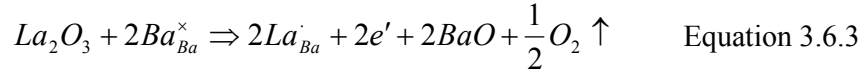
Figure 3.6.7 displays the r-T characteristics of samples NA3, NC3 and NF3 annealed in air at $1000\ ^\circ\text{C}$ for 0.5 h and $1100\ ^\circ\text{C}$ for 4 h respectively. r_{RT} of all the annealed samples were dramatically increased compared with the results for those without post-sintering reoxidation (Figure 3.6.5). It was observed that samples NA3 and NC3 after annealing $1100\ ^\circ\text{C}$ for 4 h exhibited no more PTCR characters; alternatively, they behaved like NTCR materials. However, sample NF3 which was a semiconducting material when sintered in air with the same composition still retained a PTCR profile after heavily reoxidized at $1100\ ^\circ\text{C}$ as seen in Figure 3.6.7. It was also noted that with lower annealing temperature ($1000\ ^\circ\text{C}$) and shorter time (0.5 h), the PTCR behaviour of samples using commercial crystalline BT as a starting material e.g. sample NA3 was sustained.

It is believed that the semiconductivity observed in donor-doped BaTiO_3 ceramics is generally attributed to an electronic compensation mechanism that induces n-type semiconductor characteristics.²²⁴ Using lanthanum ion (La^{3+}) as a donor dopant, free

electrons in the BaTiO₃ lattice can be generated according to equations (written in Kröger-Vink notation):



and/or



Based on equation 3.6.2, the free electrons are generated by oxygen deficiency as occurs when sintering at high temperature and/or in reducing atmospheres.²²¹ Based on equation 3.6.3, the electrons are associated with the replacement of barium ion by La³⁺. This model can explain the semiconductivity profiles observed for batches NA & NC by the occurrence of oxygen loss in the reducing sintering atmosphere. On reheating in air at lower temperatures than the sintering temperature, the samples absorb oxygen at surfaces and grain boundaries. The O₂ molecules dissociate and capture electrons from adjacent regions of the sample (equation 3.6.3), thereby create depletion layers leading to increasing resistivity.⁴⁵²



Considering the ink prepared for dip-pen printing should ideally be a single-component ceramic suspension,⁴²⁴ a synthesized TiO₂-excess non-stoichiometric BaTiO₃ powder as described in section 2.7.3 was needed as a starting material. The reducing atmosphere in sintering was also needed for further HT production.

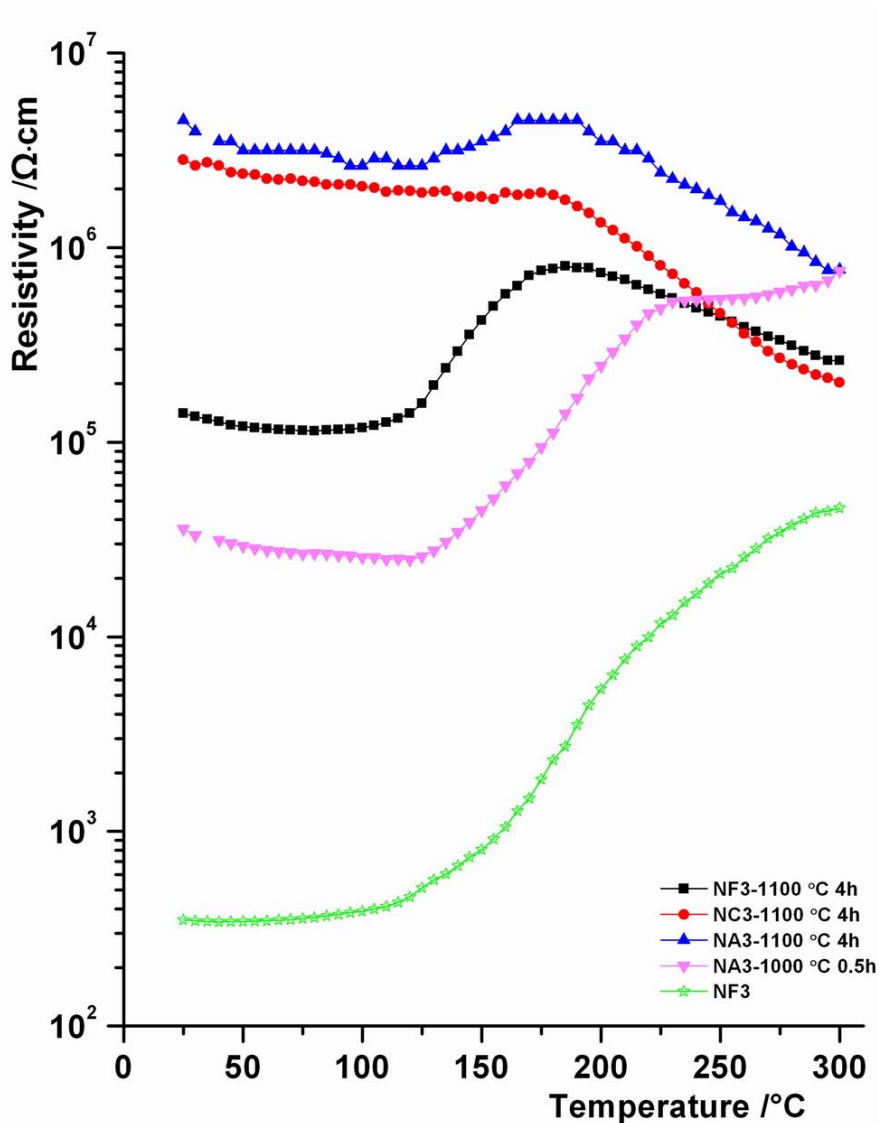


Figure 3.6.7 r - T characteristics of La-doped BT using SSR method subjected to different annealing processing after sintering in N_2 . The NF3 curve (no annealing) was plotted here for comparison.

3.6.2 Selection of Electrode Materials

Electrode contacts to semiconducting BT-based PTCR materials are required to have a high conductivity and to form an Ohmic contact to the semiconductor.⁴⁵³ A vast number of metal materials such as Ni,³⁴⁵ Ag,³³¹ Al,³⁰⁷ Pt,²³⁶ Au³⁶¹ and In-Ga⁴⁵⁴ have

been used for making electrodes of semiconducting BT-based PTCR ceramics. Among them, the electrode effects vary widely depending on surface and processing conditions.

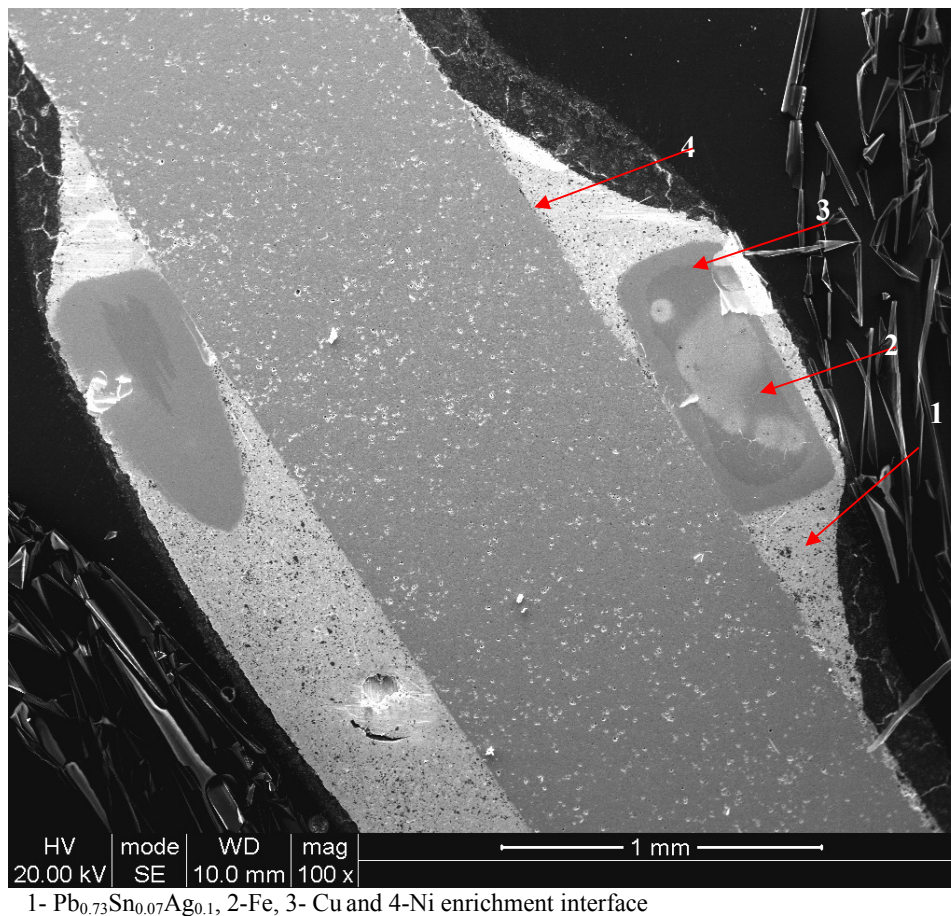


Figure 3.6.8 Commercial PTC product with its original electrode. The compositional label above was determined by the EDS results.

The original electrode on a commercial PTC thermistor was examined by SEM/EDS on the polished cross-sectional surface in Figure 3.6.8. A thin nickel-rich layer as an interface between the opposite sides of thermistor body and the outer solder layer was detected by EDS analysis. In addition, the copper-steel wires were attached on both sides by soldering.

The room-temperature resistance of PTC thermistors with different electrodes are listed in Table 3.6.1. All measured results were corrected to their equivalent values in terms of unifying the geometry. The electrode effects on R/T characteristics of the commercial PTC thermistor were investigated and shown in Figure 3.6.9. The R/T curves of the samples using In-Ga and Al electrodes (respectively curves C&D) were analogous to the reference values (curve B) except that they had higher room-temperature resistivities. There was no NTCR effect in the high temperature region ($T > T_c$) observed for using either In-Ga or Al electrodes (curve C&D) in comparison with the strong NTCR feature measured from the sample with original electrodes (curve A). This might be due to the absence of the oxidized outer layer of the thermistor caused by the electrode recoating process after grinding away the preceding one. This is also likely to cause a decrease of temperature coefficient (in Table 3.6.2). The values of T_c in Table 3.6.2 were determined by the way as described in section 3.5. Since In-Ga alloy presented lower contact resistance than Al for making electrodes, it was selected as an electrode material for subsequent testing of the doped-BT disc via the high-throughput method.

Table 3.6.1 Room-temperature resistance of the PTC thermistor with different electrodes

No.	Electrodes	R / Ω
1	Original electrodes	4.8 (measured)
2	Silver paste	20000
3	Aluminium	53
4	Ni-Fe(30:70 wt.%)	20000
5	Cr/Au	5000
6	In-Ga amalgam	25

Table 3.6.2 Measured properties of PTC product with different electrodes

Electrodes	T_c / °C	$R_{25^\circ\text{C}}$ / Ω	R_{min} / Ω	R_{max} / Ω	T_{max} / °C	α / K^{-1}
Original electrodes (ref.)	120	4.6	4.2	2×10^5	270	0.105
Original electrodes (meas.)	130	4.8	4.4	5×10^4	235	0.103
Aluminium	145	53	43	1.6×10^5	300	0.075
In-Ga amalgam	137	25	25	1.6×10^5	300	0.073

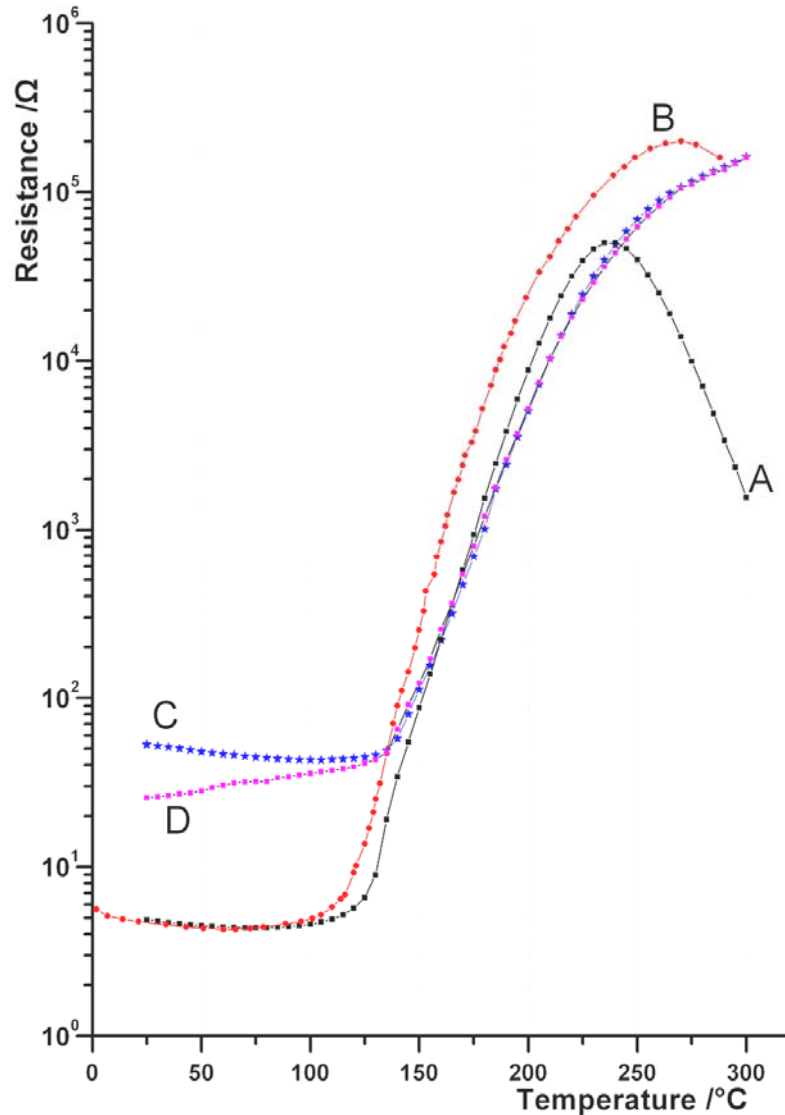


Figure 3.6.9 Electrode effects on R/T characteristics of a commercial PTC thermistor: retested results using original electrode (curve A), aluminium electrode by evaporative coating (curve C) and In-Ga alloy electrode (curve D); curve B was replotted from the reference values provided by the supplier.

3.6.3 Investigation of La-doped BT PTCR Materials Fabricated by the High-throughput (HT) Method

Figure 3.6.10 shows the shapes of drops containing synthesized BT powder produced with and without the thixotropic agent. A flat, slightly dome-like shape developed in the drying residue from the BT suspension containing the thixotropic agent. On the other hand, a concave shape was produced from a BT dispersion with organic dispersant only. The inks with synthesized BT powder here showed similar characters in the drying residue to that of commercial BT powder studied in section 3.2.1.

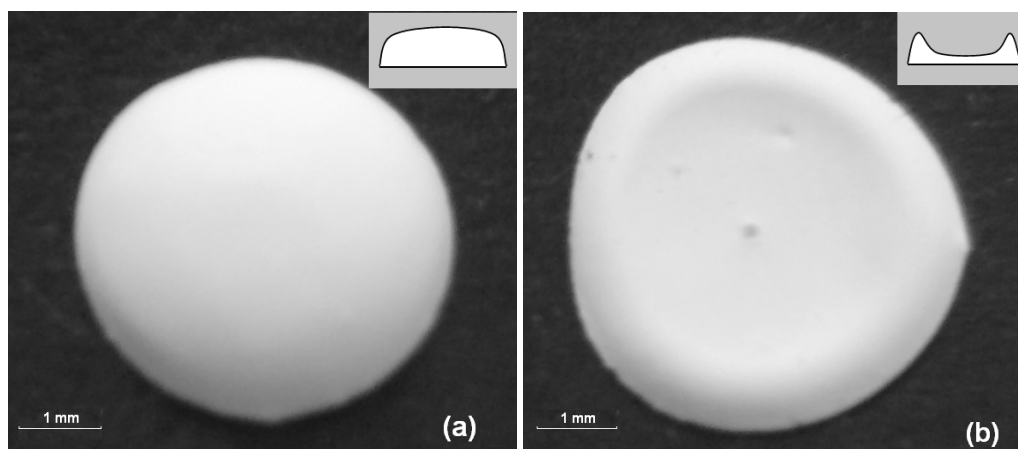


Figure 3.6.10 The drying of droplets of BT suspension containing: (a) Acrysol 12W; (b) dispersant only. It is thought the thixotropic agent restricts the radial flow of powder during drying. In the insert, schematic drawings were shown for the morphologies of the cross section of as-dried discs.

An array of BT tablets prepared by manual printing using a digital transfer pipette is shown in Figure 3.6.11. The discs that result from drying of a 20 μL BT ink droplet have diameter ~ 4.3 mm and thickness ~ 0.45 mm. The disc in the array has an average weight of 17.5 mg with a standard deviation of 1.1 mg. This error is due to

the pendant liquid residue on the pipette tip and can be significantly reduced by using LUSI printer for automatic production.¹⁰²

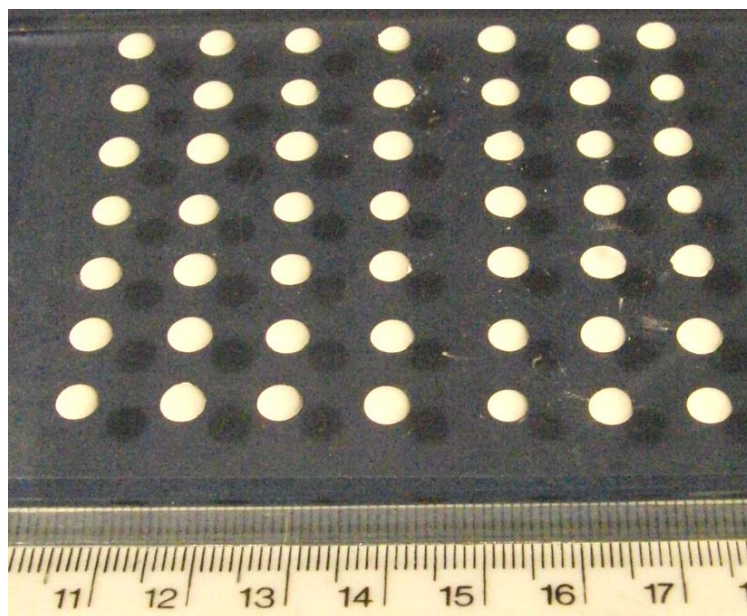


Figure 3.6.11. An array of unfired as-dried BaTiO₃ discs.

Abnormal grain growth was found for the doped-BT ceramics with 0.1-0.7 mol.% of La³⁺ content made by the HT method and sintered in N₂ at 1380 °C as seen in Figure 3.6.12(b-e). There were more intergranular pores observed in HT-made samples than in those fabricated by the SSR route sintered in N₂ (comparing Figure 3.6.12 with Figure 3.6.6, respectively). Figure 3.6.12(a) shows the surface of an undoped BT disc via HT method, grains as large as 50 μm were observed. At a La donor level above 0.7 mol.%, the exaggerated grain growth was blocked (Figure 3.6.12(f)); the microstructure consists of equi-sized uniform grains with grain sizes between 1 to 2 μm.

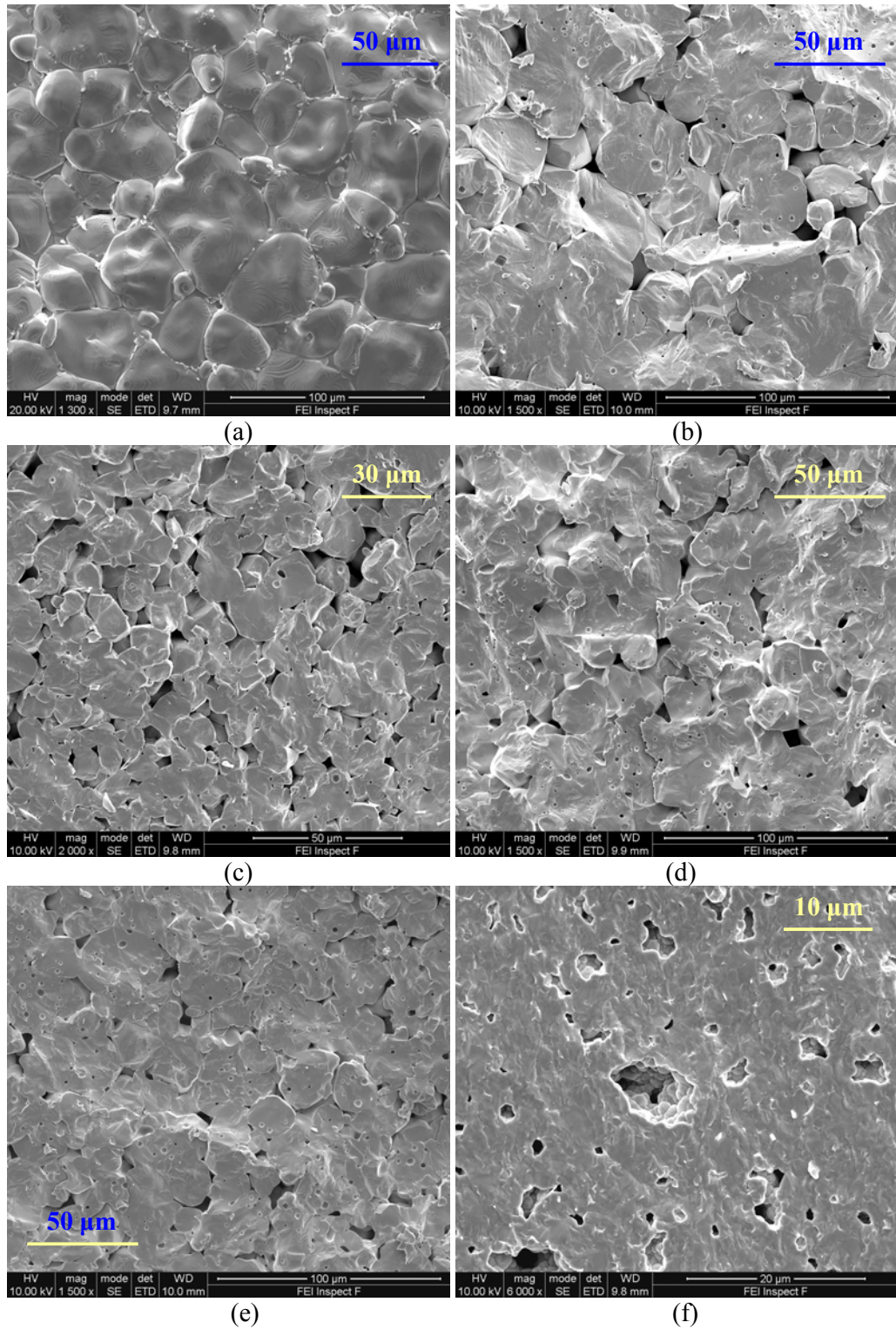


Figure 3.6.12 Microstructures of La-doped BT specimens synthesized by HT method sintered at 1380 °C in N₂: (a) undoped, (b) 0.2 mol.%, (c) 0.3 mol.%, (d) 0.4 mol.%, (e) 0.6 mol.% and (f) 0.8 mol.% La³⁺.

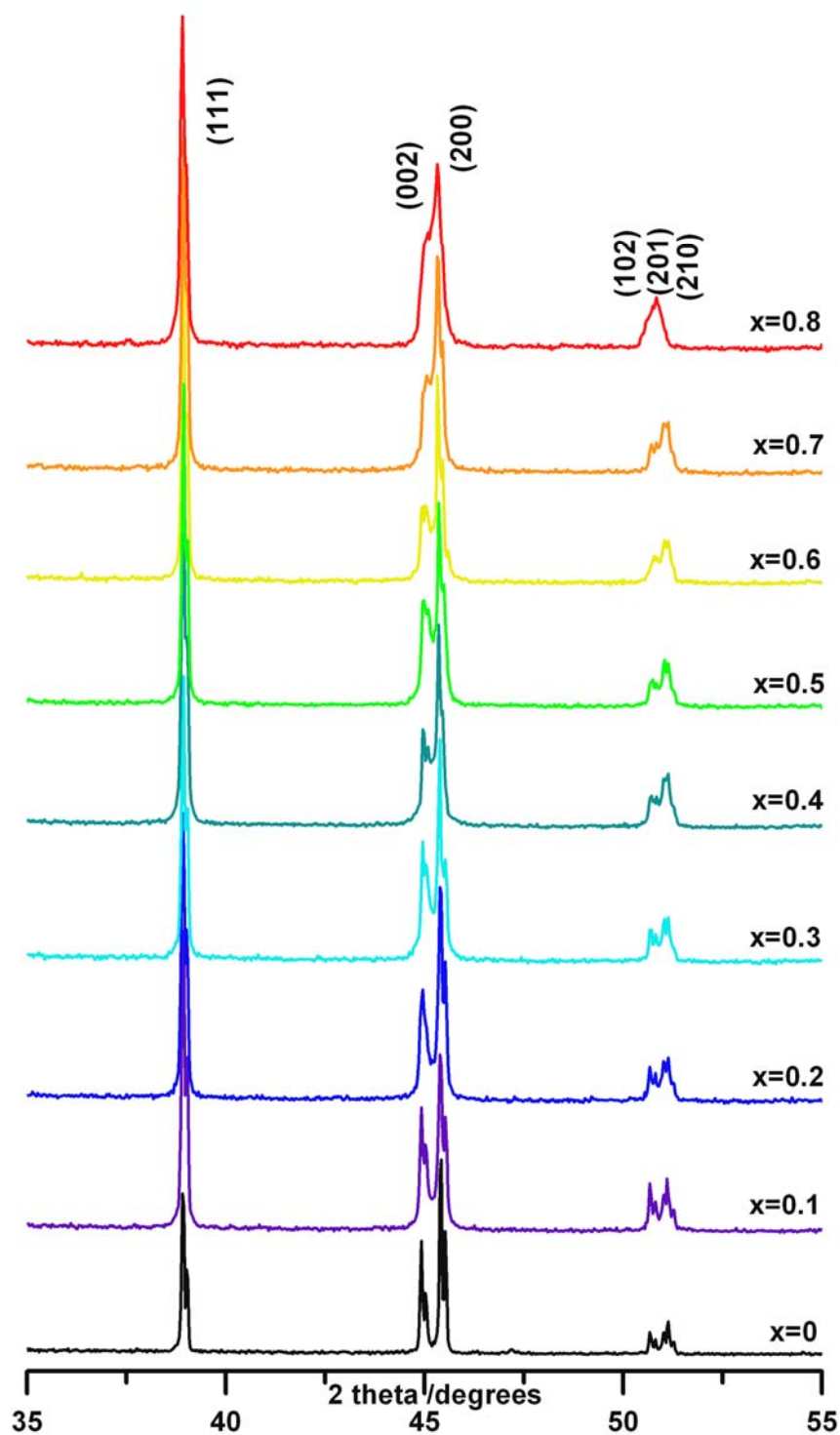


Figure 3.6.13 XRD peaks between $2\theta = 35$ and 55° for La-doped BaTiO₃ library under the doping concentration of x mol.% sintered at 1380°C in nitrogen flow.

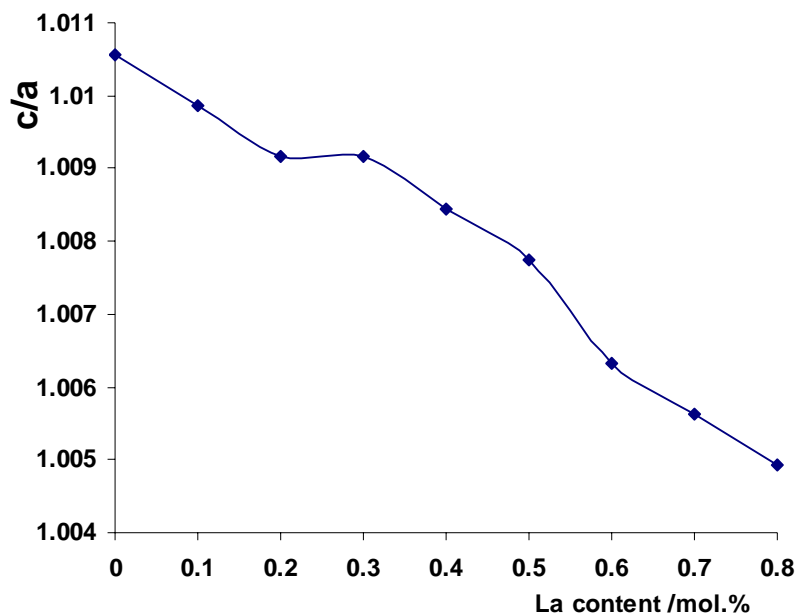


Figure 3.6.14 Tetragonality parameter (c/a) vs. La donor concentration produced by HT method and sintered in N_2 at 1380°C for 1 hour.

XRD measurements showed no secondary phase in La-doped BT via HT method. Figure 3.6.13 shows the (002) and (200) diffraction lines in the XRD patterns of La-doped BT with various donor concentrations in the range of 0.1-0.8 mol.% in steps of 0.1 mol.%. The evolution of the peak from a tetragonal structure split into two peaks in undoped material to a pseudo-cubic structure with a single peak merging at around $2\theta=45.5^\circ$ for the highest donor concentration (0.8 mol.%) can be seen. This is due to the effect of tetragonal distortion caused by the dopant incorporation into the perovskite lattice.²⁵⁰ The lattice parameters (c/a) as a function of La concentration were plotted in Figure 3.6.14, which shows a continuous decrease in c/a on donor addition. This is consistent with the results in the literature,²⁵³ which indicated that the way of infiltrating the dopant salt solution into porous BT base as a doping method used here was effective.

Considering the shape of as-sintered La-doped BT disc via HT method approximated

to a solid frustum, hence the equation 3.6.1 which is used for uniform structure sample may not be suitable here for resistivity calculation. Figure 3.6.15 shows the side view of cross section of disc. Because the opposite sides have different size, the whole chunk of disc could be equivalent to a series of an infinite number of circular discs of infinitesimal thickness stacked centred side by side along the x axis from $x=0$ where the disc has radius a_1 to $x=L$ where the disc has radius a_2 . Therefore, assuming the r is a uniform value throughout the sample disc, the resistance between the opposite sides of the whole BT disc is equal to the resistance integration to sum all the incremental discs which are in shapes of uniform cylinders.

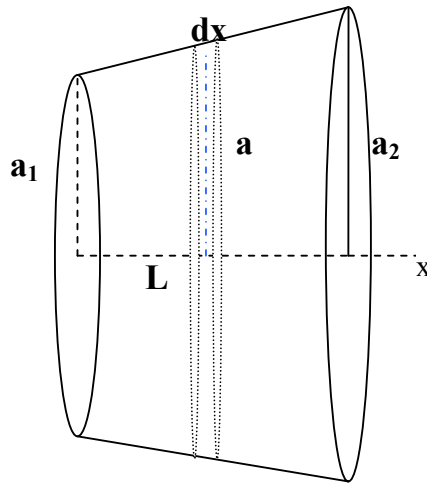


Figure 3.6.15 The side view of cross section of a BT disc.

At any given x , the incremental disc resistance (dR) is given by the equation:

$$dR = \frac{rdx}{\pi a^2} \quad \text{Equation 3.6.5}$$

And the length of a is associated with the size effect which is dependent on a_1 , a_2 and L :

$$a = \frac{a_1 L + (a_2 - a_1)x}{L} \quad \text{Equation 3.6.6}$$

Thus, substituting a with a function of x in Figure 3.6.5 and integration gives:

$$R = \int_0^L \frac{r dx}{\pi \left[\frac{a_1 L + (a_2 - a_1)x}{L} \right]^2} \quad \text{Equation 3.6.7}$$

This can be evaluated:

$$R = \frac{rL^2}{\pi(a_1 - a_2)} \left[\frac{1}{a_1 L + (a_2 - a_1)x} \right]_{x=0}^{x=L} = \frac{rL}{\pi a_1 a_2} \quad \text{Equation 3.6.8}$$

Therefore, $r = R\pi a_1 a_2 / L$ is the equation for estimating the resistivity of disc sample made by HT method.

Reoxidation for 0.3 mol.%-La-doped BT discs by the HT method after sintering in N_2 was carried out at 1100 °C in air. The changes of the PTCR properties corresponding to the duration (0.5, 4 and 24 hours) of the reoxidation which was varied to change the surface acceptor state density³⁹⁴ were investigated. Their temperature dependence of electrical resistivity is presented in Figure 3.6.16. The resistivity profile change after reoxidation for samples made by the HT method was not as drastic as for the samples made by the SSR method when compared the results in Figure 3.6.7 with Figure 3.6.16. There were two types of dependence of resistivity profile found here. At short periods, the magnitude of the PTCR jump decreased; at long times, the magnitude of the PTCR jump increased and T_{max} shifted to lower temperature. These findings are similar to those in the literature.⁴⁵² However, drastic changes of r_{RT} were noted for highly doped samples e.g. 0.8 mol.% after annealing in air for more than 4 hours where it turned to a insulating material. This may be because the highly doped samples in which the anomalous grain growth was not developed during sintering are prone to reoxidation leading to the dramatically increasing resistivity.⁴⁵⁵ Therefore, annealing at 1100 °C for 0.5 hour was used for subsequent sample preparation.

As shown in Figure 3.6.17, the resistivity of the La-doped BT ceramics made by this high-throughput fabrication method was measured as a function of temperature. All samples in the doping range 0.1-0.8 mol.% exhibited the expected PTCR performance with an increase in resistivity up to several orders of magnitude occurring at a Curie temperature of around 120 °C. The room-temperature resistivity of La-doped BT samples initially reduced with increasing La doping level from 0.1 to 0.4 mol.% and then increased with the donor concentration; furthermore, the PTCR jump generally decreased with the increase of donor contents as displayed in Figure 3.6.18, which is in good agreement on the previous studies.¹⁹¹ It was observed that the T_c generally decreased with an increase of La content by around 20°C per mole percent due to the incorporation of La into BaTiO₃ lattice at the Ba sites which is also in line with the results from previous studies.^{237, 456, 457}

As can be seen in Figure 3.6.19, these results showed good agreement with previously published r - T curves for the BT samples contained around 0.2 mol.% La donor dopant via conventional oxide-mixing routes.^{319, 322, 361} Analogous PTCR characteristics are displaying between the tested sample and literature values in Figure 3.6.19. The r_{RT} (620 Ω·cm) of the sample (0.2 mol.%) produced by the HT method is at the mid-range of the literature results. Furthermore, it contains a moderate PTCR jump compared with the published values in Figure 3.6.19. Hence, the results above confirm that the BT-based PTCR samples made by this HT method have similar PTCR properties compared with those made by the conventional fabrication methods.

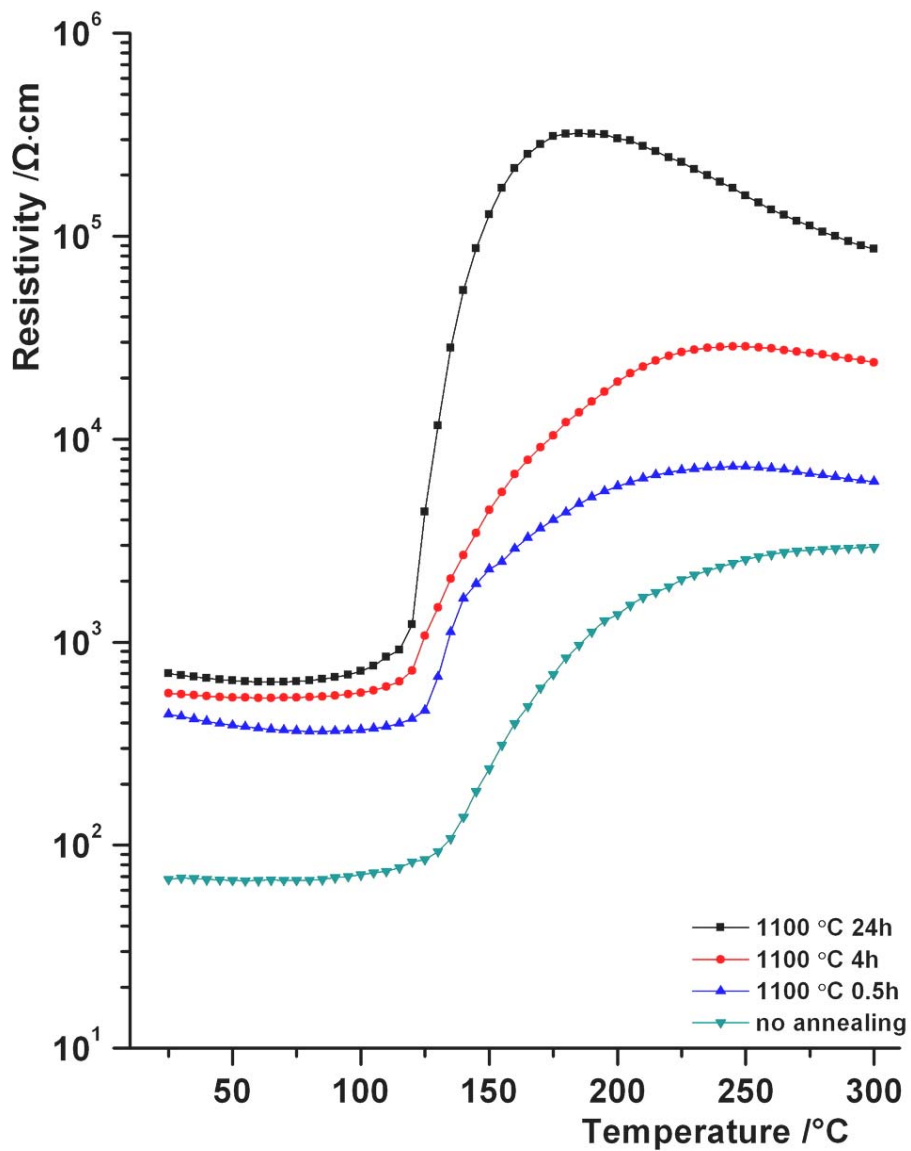


Figure 3.6.16 r - T characteristics of 0.3 mol.% La-doped BT using HT method annealed at 1100°C for various periods after sintering at 1380°C in N_2 .

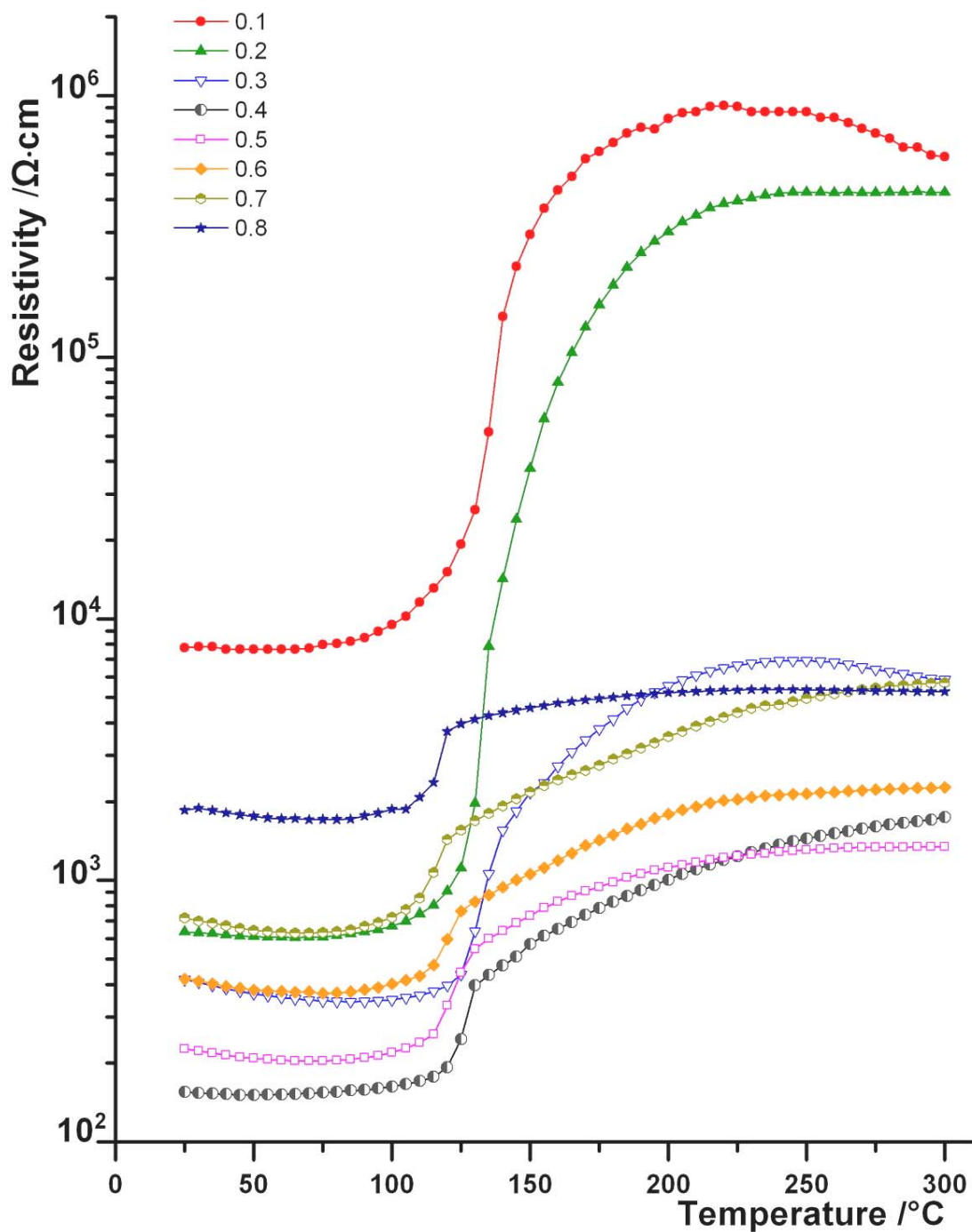


Figure 3.6.17 r - T characteristics of La-doped BT via HT method reoxidized at 1100 $^{\circ}\text{C}$ for 0.5 hour after sintering at 1380 $^{\circ}\text{C}$ in N_2 .

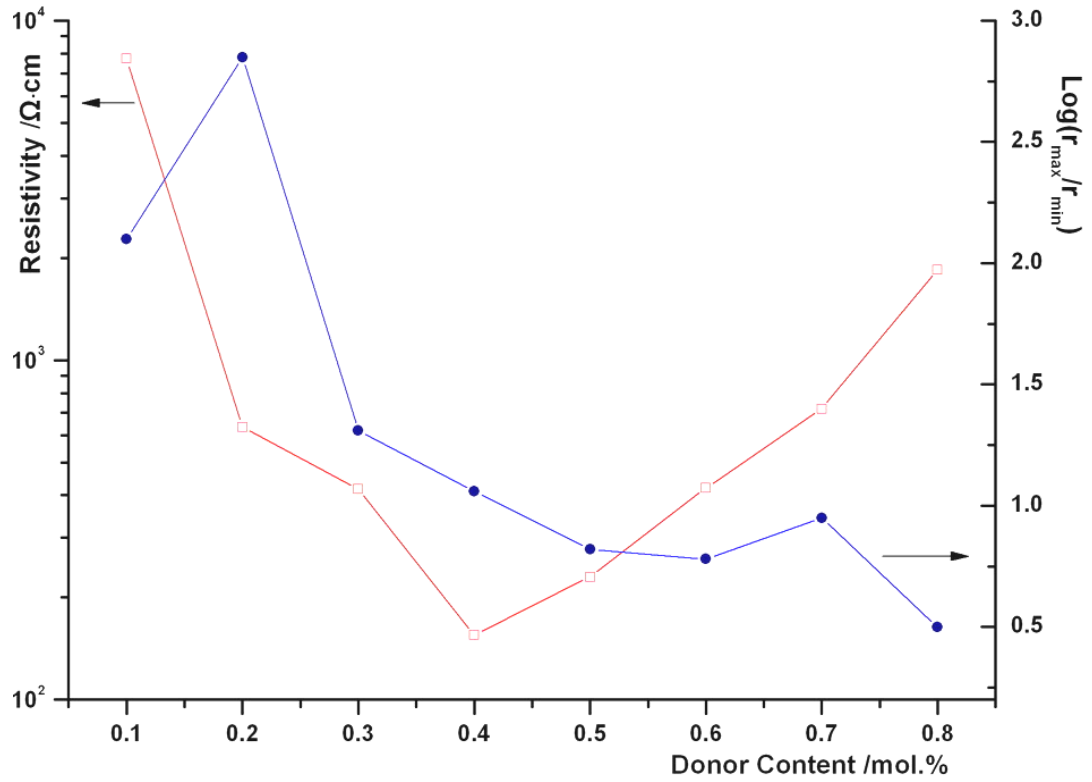


Figure 3.6.18 Relationship between room-temperature resistivity and PTCR jump of La-doped BT with various donor concentrations via HT method sintered at 1380 °C in N₂.

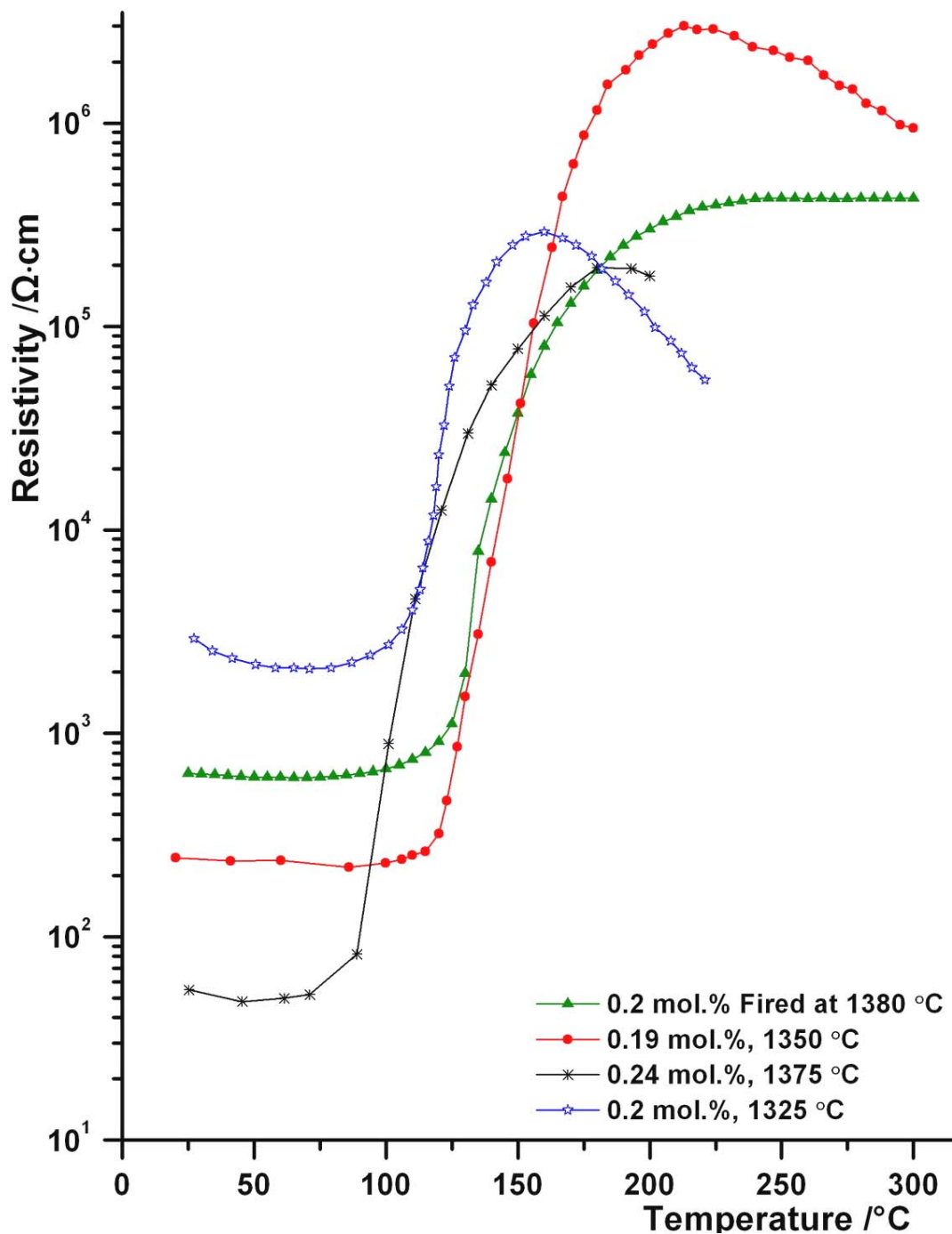


Figure 3.6.19 Comparison of resistivity-temperature curve for combinatorial 0.2 mol.% La-doped BT (fired at 1380°C) to previously published r - T curve for similar composition. Curves are from ref.: \bullet ³⁶¹, \ast ³¹⁹, \star ³²².

3.7 Investigation of Er-Mn and Y-Mn Donor-acceptor co-doped BT PTCR Ceramics via HT method

Yttrium ion as a donor dopant has been widely used to tailor the positive temperature coefficient resistivity effect in semiconducting BaTiO_3 .^{458, 459} Er^{3+} is also a very important dopant for fabrication of doped-BT PTCR ceramics. The incorporation of *3d* transition metals such as V, Cr, Mg or Mn allows surface traps to form within the grain boundary regions, leading to an increase in the magnitude of the PTCR jump. Among them, doping with Mn forms the deepest traps and has the greatest effect.⁴⁶⁰ Furthermore, all those elements (Er, Y and Mn) have easy-access via soluble nitrate salts. This makes the materials ideal for proof-of-concept investigation using the HT method.

The incorporation of Er^{3+} into BT perovskite lattice has a solubility at the Ba site that does not exceed 1 mol.%, whereas solubility at the Ti site is above 10 mol%.²⁶⁶ Similar results were also observed for Y^{3+} , with a slight solubility (~1.5 mol.%) of Y content at the Ba sites but a high solubility (~12.2 mol.%) of Y at the Ti sites.²⁶⁹ The samples fabricated here via the HT method were all less than the corresponding level of solubility of dopant substitution for the Ba sublattice.

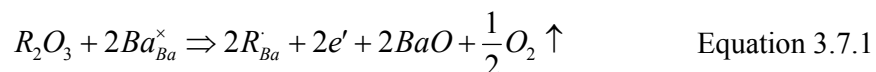
Figure 3.7.1 presents the resistivity-temperature curves of BT discs co-doped with a fixed 0.02 mol.% Mn^{2+} as an acceptor dopant and different Er^{3+} donor concentrations in the range of 0.1-0.8 mol.% in a step of 0.1. All samples exhibited PTCR behaviour above the Curie temperature. The room-temperature resistivity decreased with the erbium content and reached a lowest value of 450 $\Omega\cdot\text{cm}$ and two orders of magnitude

of resistivity jump passing T_c at 0.3 mol.% Er^{3+} doping level (seen in Figure 3.7.3) and reverted to high electrical resistivity material when doping with higher content, which is similar to values observed for erbium-doped BT prepared by the conventional SSR route.²⁶⁵ The results in Figure 3.7.3 also show a clear trend of decrease in r_{max}/r_{min} ratio with increasing erbium donor concentration.

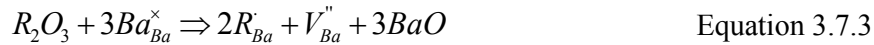
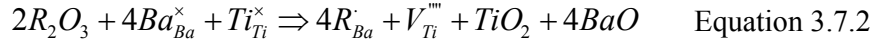
In comparison with yttrium-manganese co-doped BT library, the corresponding electrical resistivity as a function of temperature was measured and displayed in Figure 3.7.2. The minimum resistivity at room temperature of around $40 \text{ } \Omega \cdot \text{cm}$ can be achieved when the yttrium concentration is 0.6 mol.%, which is in line with the value (the minimum value of r_{RT} equals to $16 \text{ } \Omega \cdot \text{cm}$ at 0.7 mol.% of Y^{3+} content) in the literature.⁴⁵⁸ Furthermore, similar with BT samples doped with other donor ions such as La^{3+} and Er^{3+} previously, the room-temperature resistivity of BT disc containing Y^{3+} changes as a V-type curve with the increase of yttrium content (Figure 3.7.4). According to the data from r/T curves in Figure 3.7.1-2, the relationships between the room-temperature resistivity, PTCR jump and the donor content are illustrated in Figure 3.7.3-4. BT discs co-doped with Y^{3+} and Mn^{2+} generally showed higher PTCR jumps than those of BT samples co-doped with Er^{3+} and Mn^{2+} ; however, the latter one presented relatively stronger NTC effects (particularly at $T < T_c$) than that of BT disc containing with Y^{3+} . Figure 3.7.5 displays the microstructure of a polished cross section of 0.5 mol.% Y and 0.02 mol.% Mn co-doped BT disc after thermal etching. Coarse grains with some intragranular porosity and voids were observed; in addition, the acicular crystals in the image probably were accounted for a Ti rich-phase ($\text{Ba}_6\text{Ti}_{17}\text{O}_{40}$).⁴⁶¹ The average grain size is around $30 \text{ } \mu\text{m}$ which is similar with the La-doped BT samples as displayed in Figure 3.6.12.

Mn^{2+} that used here is an acceptor dopant in comparison with donor dopants such as Er^{3+} , Y^{3+} and La^{3+} . The addition of the acceptor Mn in co-doped BT PTCR materials is known to improve the both steepness and jump order of the resistivity-temperature curve.⁴⁵⁸ The co-doped BT systems (in Figure 3.7.1 and 2) exhibited similar PTCR features compared with the single doped BT materials (in Figure 3.6.17). The room-temperature resistivity changes as a V-type curve with the increase of the donor content. However, there are significant differences in the patterns in terms of the relationship between the PTCR jump and the donor concentration in single donor system compared with donor-acceptor co-doped system. For La-doped BT materials, the PTCR jump begins to reduce abruptly at low doping level at which the minimum value of r_{RT} does not occur as seen in Figure 3.6.18. For Er-Mn co-doped BT system, the PTCR jump ratio stays relatively consistence at low doping concentration and it decreases significantly after passing the minimum r_{RT} level (in Figure 3.7.3). There is even an inverse-V-shape of the PTCR jump pattern corresponding to the donor content for Y-Mn co-doped BT materials (in Figure 3.7.4).

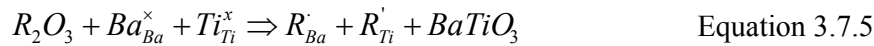
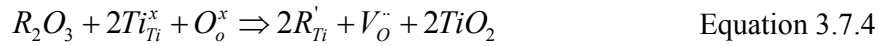
Erbium and yttrium, as aliovalent dopant elements for BT-based PTCR ceramics, have similar attributes in terms of incorporation in the BT lattice because both of their ions have the same valence charge and close ionic radius (Er^{3+} , 0.96 Å; Y^{3+} , 0.93 Å). The analogous amphoteric behaviour of Er^{3+} and Y^{3+} has been investigated and confirmed by the room-temperature electrical conductivity measurements and microstructure observations.^{206, 246, 269} It has long been known that the semiconducting at T ($T < T_c$) of BT doped with a small amount of donor dopant is due to the electronic compensation scheme according to²²⁶



where R represents Er and Y. The R^{3+} acted as donor on replacing Ba^{2+} ions. Maximum conductivity of Er-doped and Y-doped BT is due to more effective incorporation of dopant through equation 3.7.1 with the free electrons increasing. When the donor concentration further increases, the charge compensation takes place by formation of barium (V_{Ba}'') or titanium (V_{Ti}'''') vacancies, according to²²⁵



Barium vacancies and/or titanium vacancies can be produced at the grain boundaries and diffuse from the grain boundaries into the grains during sintering. The cation vacancies act as electron traps and there is an increase in the potential barrier at the grain boundaries therefore increasing the resistivity. Although it was observed that R^{3+} (Er^{3+} and Y^{3+}) substitutes for Ba site when Ba/Ti molar ratio smaller than 1, the possibility of these dopant ion substituting for Ti site cannot be ruled out. This phenomenon yields to a formation of double-ionised oxygen vacancies or/and self-compensation as follows:²⁶⁶



where the oxygen vacancies can trap electrons according to



Furthermore, the transition series ion such as Mn^{2+} (0.8 Å) gives exclusive substitution on the Ti site because of their small size. It was observed that the positive excess charge of the Mn^{2+} as an acceptor ion at the Ti site is mainly

compensated by creation of oxygen vacancies as in equation 3.7.4.⁴⁶² Equations 3.7.4-7 all lead to high-resistivity behaviour. The underlying mechanism that caused the differences in PTCR properties associated with the change of donor species and with/without acceptor is however beyond the scope of this project.

The biggest single resource for error in sample preparation and measurements here is the green porous BT base disc via dip-pen printing method. The dopant precursor solution was prepared based on the assumption that all as-dried green BT discs within the same batch are identical. However, because there was 6% in standard deviation of the average value of weight from measuring more than 50 discs, equivalent error would be generated in terms of doping concentration. This may have a substantial impact when compares the PTCR performance for samples doped with insignificantly different donor concentrations (e.g. samples doping with 0.7 and 0.8 mol.% respectively). However, using robotic LUSI system, such error in the weight of printed disc can be reduced effectively.¹⁰² The possibly difference in pore density and structure of individual green disc may also affect the dopant distribution during the droplet-doping processing; however, this would have relatively little influence on the actual dopant composition. Based on error propagation from resistance and dimension measurements, the estimated errors in resistivity are 13%. The measurement error in a combinatorial process that uses very small samples is clearly expected to be higher than that from measurements on conventional samples, a compromise associated with high throughput methods in general but interestingly one that does not impinge on the intensive property of Curie temperature, relevant in this case.

It must be stressed that the principle of combinatorial searching is to identify novel compounds which can then be optimized and characterized with more precision, and as such it is a tool to discover trends, rather than a technique intended for precise fabrication and characterization.

The HT procedures used to produce dopant-doped BT PTCR disc has been validated by testing the single donor doped and co-doped BT materials and compared with the literature values from samples that made by conventional methods. This HT method eliminates the multiple steps in traditional sample preparation: mixing, drying, calcination, regrinding, drying, pressing and sintering but as with all high-throughput operations there is a compromise between compositional exactitude and sample processing speed. It has the potential to deliver dopant-doped BT-based PTCR libraries rapidly with a very wide range of dopant mixtures and concentrations for electrical property measurement and deserves to be applied to other low level dopant ceramic systems. It also promises the great potential of realizing full robotic control on the production of libraries of lightly doped functional ceramics.

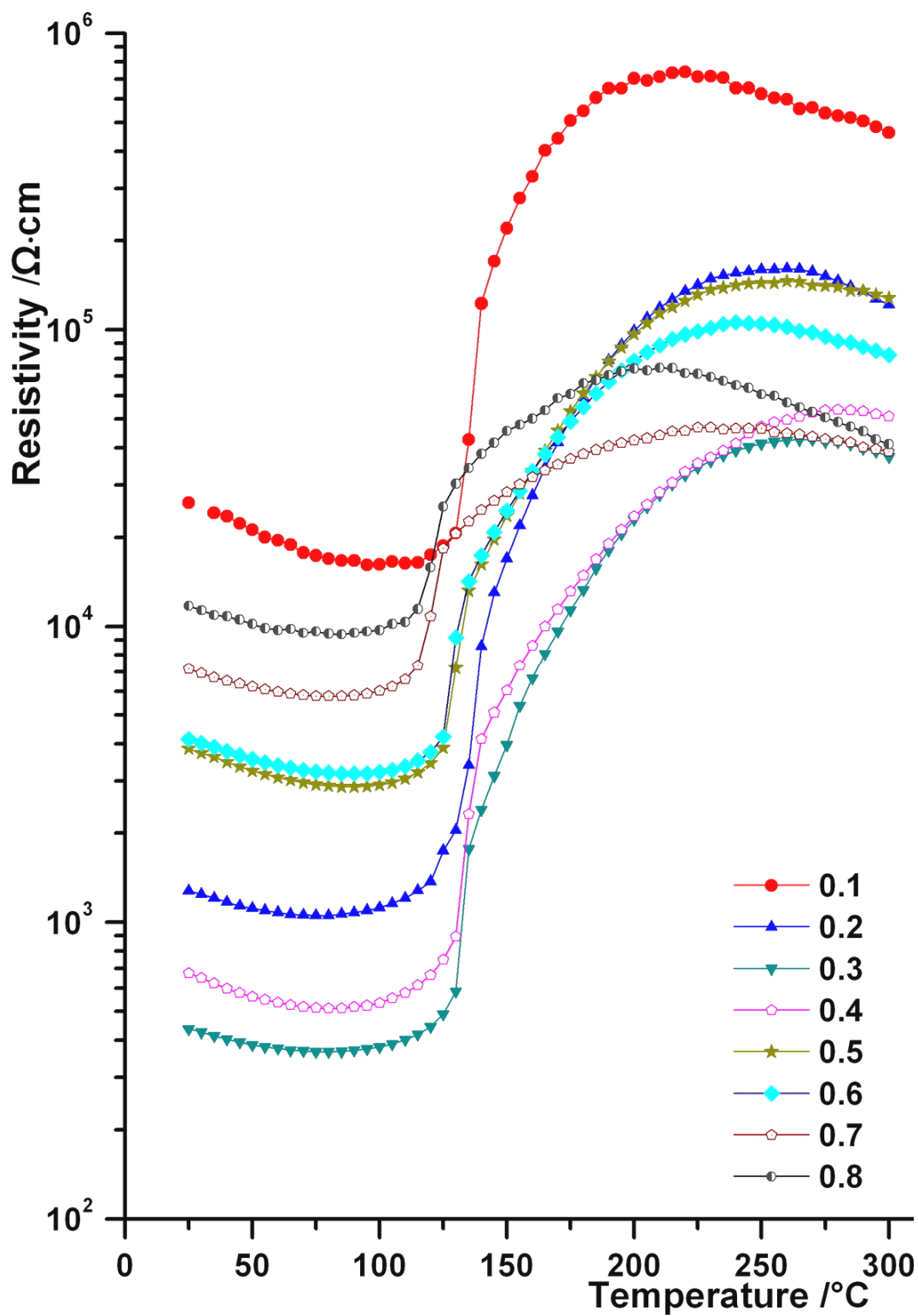


Figure 3.7.1 r - T characteristics of Er-Mn co-doped BT sintered at 1380°C in N_2

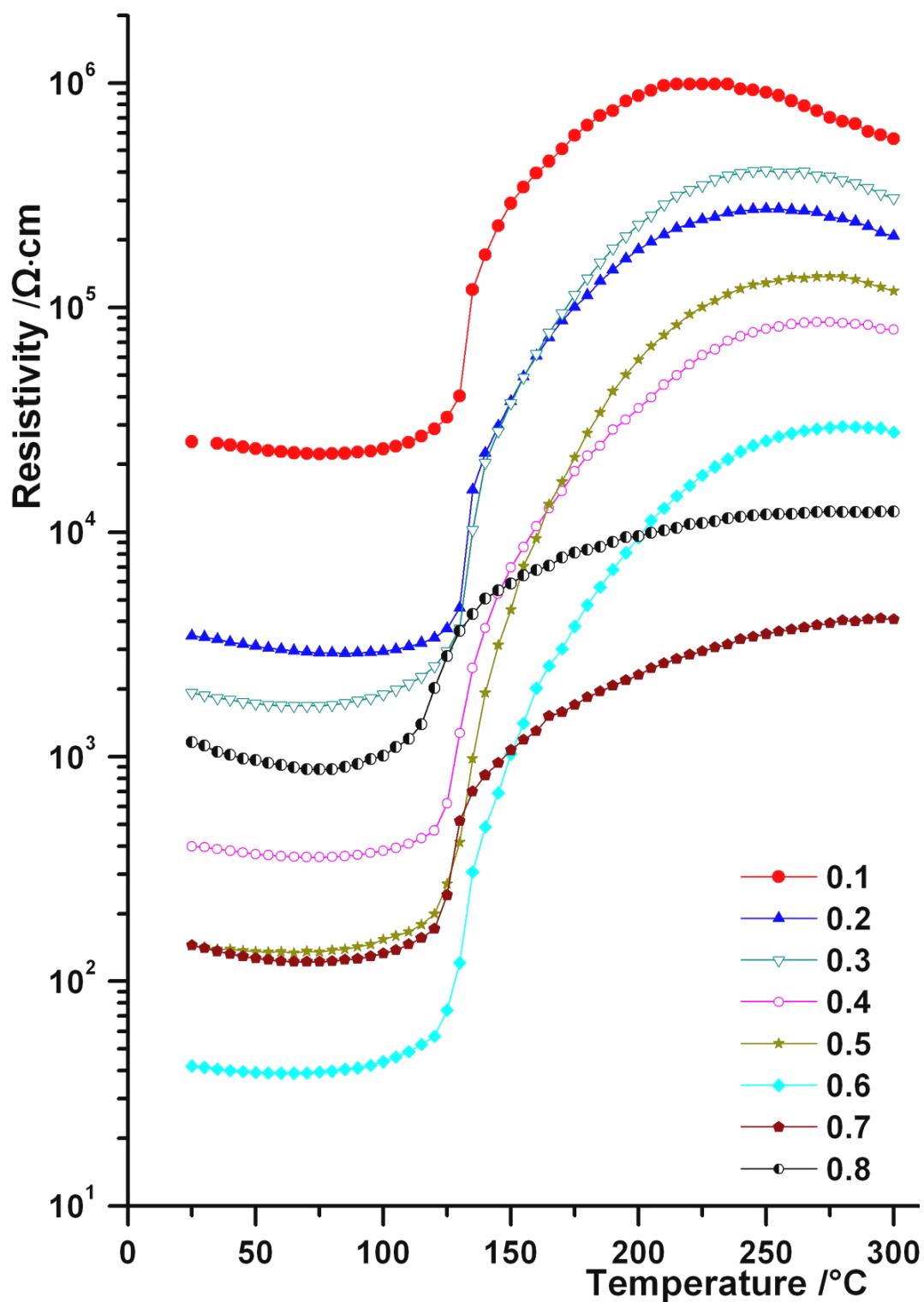


Figure 3.7.2 r - T characteristics of Y-Mn co-doped BT sintered at $1380\text{ }^{\circ}\text{C}$ in N_2 .

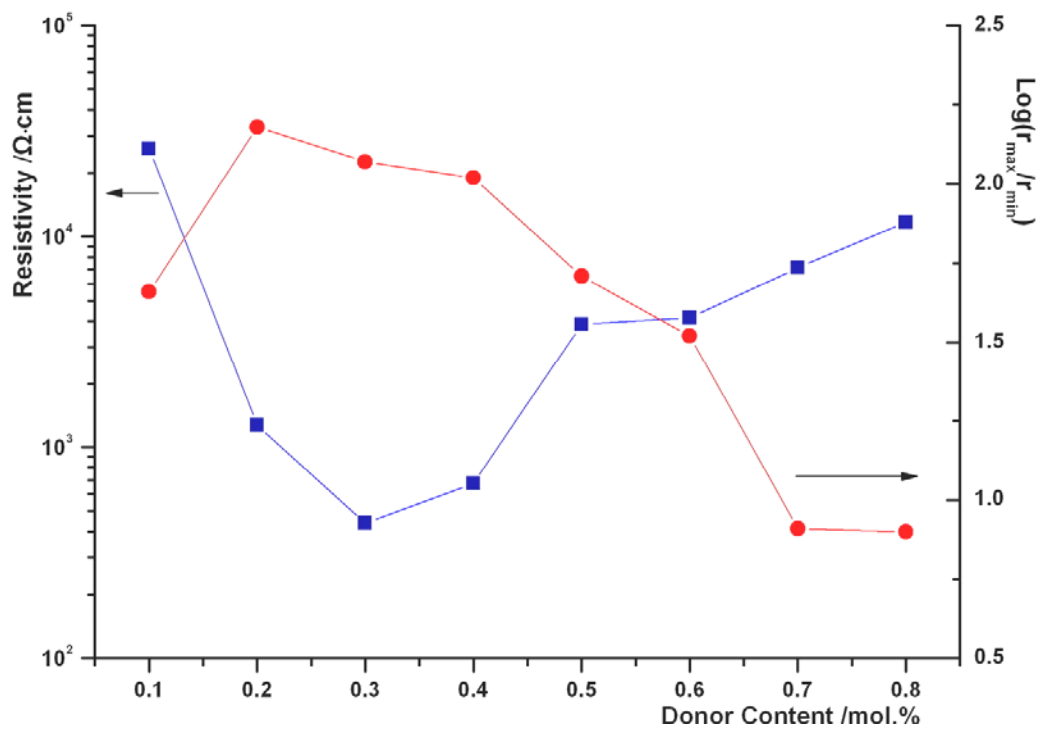


Figure 3.7.3 Relationship between room-temperature resistivity and PTCR jump of Er, Mn co-doped BT with various donor concentrations via HT method sintered at 1380°C in N_2 .

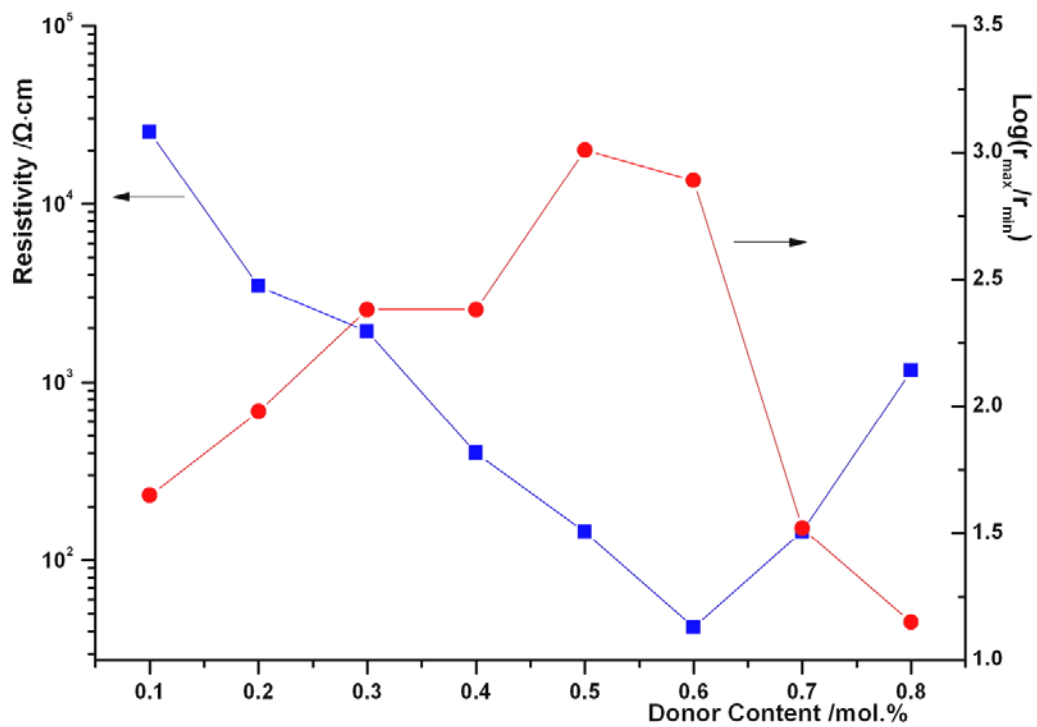


Figure 3.7.4 Relationship between room-temperature resistivity and PTCR jump of Y, Mn co-doped BT with various donor concentrations via HT method sintered at 1380°C in N₂.

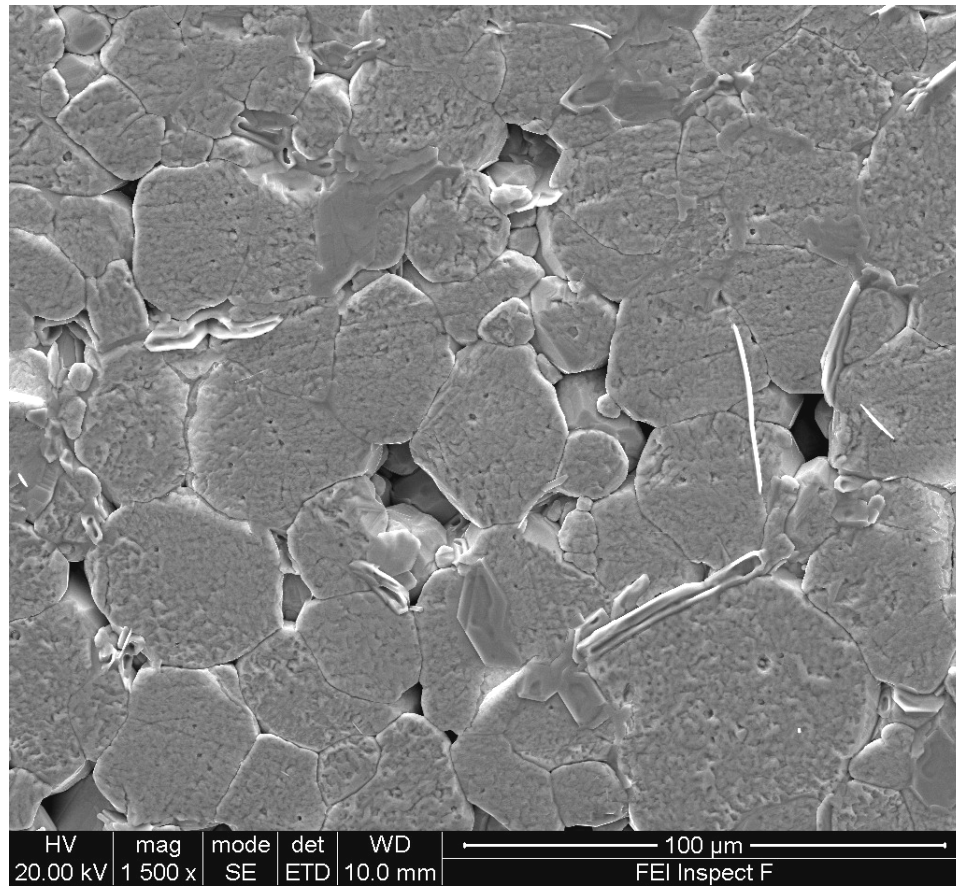


Figure 3.7.5 Microstructure of doped BT sample containing 0.5 mol.% Y^{3+} and 0.02 mol.% Mn^{2+} sintered at 1380 °C for 1 hour in N_2 (after thermal etching).

4. Conclusions

4.1 Ceramic Ink Preparation

An approach to the preparation of BaTiO₃ inks for making a thick film base for subsequent combinatorial library fabrication was developed. Both Vibro and Dyno mills were found effective in powder regrinding processing however Vibro milling can reach finer particle size characteristics. The performance of ten candidate dispersants was evaluated using sedimentation tests and Darvan 821A at 3 wt.% of ceramic powder was determined as the prime dispersant for preparing the stable aqueous based BT dispersion.

4.2 Control of Shape of Droplet Drying Pattern

Drying of sessile droplets of concentrated suspension is of great complexity, involving Brownian motion, sedimentation, capillary flow, Marangoni flow, phase transitions, interaction between particles and flocculation. However, the capillary flow is a dominant force in determining the drying pattern of aqueous dispersions among all other factors. Uniform structure with well-finished surface was obtained by adding a thixotropic agent to the printing BT inks. The thixotropic agent is probably effective in stopping or weakening the lateral flows inside drops because it helps to form the sessile drops into a viscous gel state during evaporation. The porous structures of the drying residues from BT concentrated dispersion were also characterized. BaTiO₃ base discs were produced by a dip-pen printing technique using the inks described above.

4.3 Investigation of Dopant Distribution in Porous BT Base via a Droplet-doping Method

A novel high-throughput doping technique for BT-based PTCR ceramics was demonstrated. The droplet-doping method was performed by infiltrating liquid dopant precursors on the porous BT base discs. The method eliminates the multiple steps in traditional sample preparation; mixing, drying, calcination, regrinding, drying, pressing and sintering but as with all high-throughput operations there is a compromise between compositional exactitude and sample processing speed. The factors including liquid infiltration pattern in porous substrate, capillary evaporative flow and flow of molten dopant salt hydrate which could affect the uniformity of dopant salt in the final sample were investigated. Erbium-doped and Yttrium-doped BT were fabricated using this combinatorial technique. Different compositional characterization methods including EDS and WDS were used to assess the distribution of dopant through the body of the sample discs. An acceptably uniform distribution of dopant in trace-doped BT ceramics produced by this droplet-doping method can be achieved.

4.4 Heating Control Unit Construction and Furnace Calibration

A PC-controlled furnace system including a heating control unit and an operational interface was developed. This automatic heating unit was calibrated in a temperature range of 20-300 °C. The temperature gradient between the inner furnace and the surface of the sample that was placed at the furnace centre was investigated

4.5 High-throughput Arrayed Testing System

An in-house multiple sample measurement jig with a capacity of 20 samples, was designed and assembled for high throughput resistivity-temperature measurement. A PC-controlled r/T measuring panel was also developed. The validity and accuracy of this integrated heating and testing system was examined.

4.6 Fabrication of La-doped BT Exhibiting PTCR Property

The room temperature conductivity of donor-doped BT is influenced by a broad variety of factors including impurities in the starting powders, cation stoichiometric variation, dopant additive attributes, firing parameters and nature of the external/internal defects etc. BT powder from different sources used as a starting powder was doped with lanthanum as a donor dopant via conventional SSR route. The corresponding PTCR profiles of samples after sintering in air were compared.

The PTCR behaviour of the semiconducting BT ceramics is closely related to the microstructure of the samples. The atmosphere with relatively low oxygen partial pressure during sintering, e.g. applying N_2 flow, can effectively reduce the room-temperature resistivity of La-doped BT samples where the anomalous grain growth was found to occur. In-Ga alloy was selected as the electrode material.

Library of La-doped BT was made with vary doping concentration in the range of 0.1-0.8 mol.% in steps of 0.1. XRD and electrical measurements showed evidence of the changes in structure and PTCR profiles with the change in composition and were closely matched to previously published data for samples made by conventional ceramic routes. The procedure, thus validated, has the potential to deliver dopant-

doped BT-based PTCR libraries rapidly with a very wide range of dopant mixtures and concentrations for electrical property measurement and deserves to be applied to other doped ceramic systems.

4.7 High-throughput Fabrication of Donor-acceptor Co-doped BT Libraries Exhibiting PTCR Property

As a proof of principle, libraries of Er-Mn and Y-Mn codoped BT discs were manufactured by HT method with varying donor content in the range of 0.1 to 0.8 mol.% in steps of 0.1 with a fixed Mn as acceptor content of 0.02 mol.%. Fired at 1380 °C for 1h in N₂, the samples appeared well sintered. r/T measurements (25-300°C) showed all the co-doped BT samples exhibited the expected PTCR property and presented evidence of room-temperature resistivity and PTCR jump ratio trends with change in donor composition corresponding to expected values. Despite the inherent errors in such fabrication and measurements, these results demonstrate that the Er-Mn and Y-Mn co-doped BT libraries produced by the HT method exhibit clear evidence of PTCR property variations consistent with change in donor concentration and values close to those reported in the literature.

This study has shown the viability of producing donor-doped BT PTCR materials with varying donor concentration by a combination high-throughput technology of dip-pen printing and rapid droplet-doping. The small individual samples (~3 mm diameter) that make up the combinatorial libraries can be measured to within a degree of accuracy acceptable for the characterization of combinatorial searches.

5. Suggestions for Future Work

1. **Automation production of BT-based PTCR libraries using LUSI system.** The London University Search Instrument (LUSI) has already successfully presented the capability of mass production of thick film ceramic libraries.^{40, 102, 104} It only needs a minor modification to integrate the droplet-printing part into the whole production system which the corresponding schematic structure as displayed in Figure 5.1. Stages A and B demonstrate the implementation of this high throughput fabrication method for producing the BT base discs on the LUSI printer: stage A shows the printing of the BT suspension and in stage B it is allowed to dry. Stage C illustrates infiltrating liquid dopant precursor into the BT base disc. In order to achieve a homogeneous distribution of dopant solution throughout the body of the porous base, the volume of the dopant solution must be equal to the total volume of the pores in the base which is determined by its porosity. Stage D shows the firing process and the procedure for applying electrodes on sample surfaces is presented in stage E.
2. **Mass production of combinatorial libraries of doped BT PTCR materials and high-throughput screening of PTCR properties and discovery of new BT-based PTCR ceramics with promising properties.** The principle of making BT-based PTCR ceramics via combinatorial method has been proven. More libraries should be fabricated containing a vast variety of dopant selection and in a broader range of doping concentration. The corresponding composition-structure-property relationships can be found. A data mining technique needs to be developed in such informatics research.
3. **Investigation on other electrical properties of the BT-based PTCR materials.** Only the r/T curve of the BT-based PTCR samples via HT method was measured

in this work. In order to create a complete image of the PTCR profiles of the doped BT samples, current/voltage characteristic, voltage dependence of resistivity and frequency dependence of resistivity need to be screened.

4. **To seek possible correlations between sintering parameters and electrical performance properties.** It was observed that the PTCR features of donor-doped BT samples are readily influenced by the firing parameters particularly the sintering atmosphere. Future research on building systematic global composition-structure-property maps for BT-based PTCR materials should include the variation resulting from the change of heat treatment.
5. **Investigation on other low level dopant ceramic systems.** Currently, BT-based PTCR ceramics which is subjected to low level of dopant doing (<1 mol.%) are investigated. Other systems such as ZnO-based varistors, Al₂O₃-based transparent ceramics, TiO₂-based catalysts etc. could be explored. Multi-component starting powder system for various applications can also be investigated.
6. **To optimize the drying pattern of sessile droplets.** The structure uniformity of the as-dried disc is critical for subsequent doping and measuring procedures in this work. More studies need to be done to improve the structural homogeneity by making a convex disc with very small curvature and reduce the variations between the individuals within the same batch.
7. **Investigation of distribution of dopant salt in the body of the base.** More accurate characterization tools such as XPS etc. may be needed for investigation of the dopant compositional distribution throughout the BT body. More in depth analytical experiments (such as quantitative analysis of dopant distribution under different circumstances in the way of droplet-doping proceeding described in Section 3.3.5.) are required.

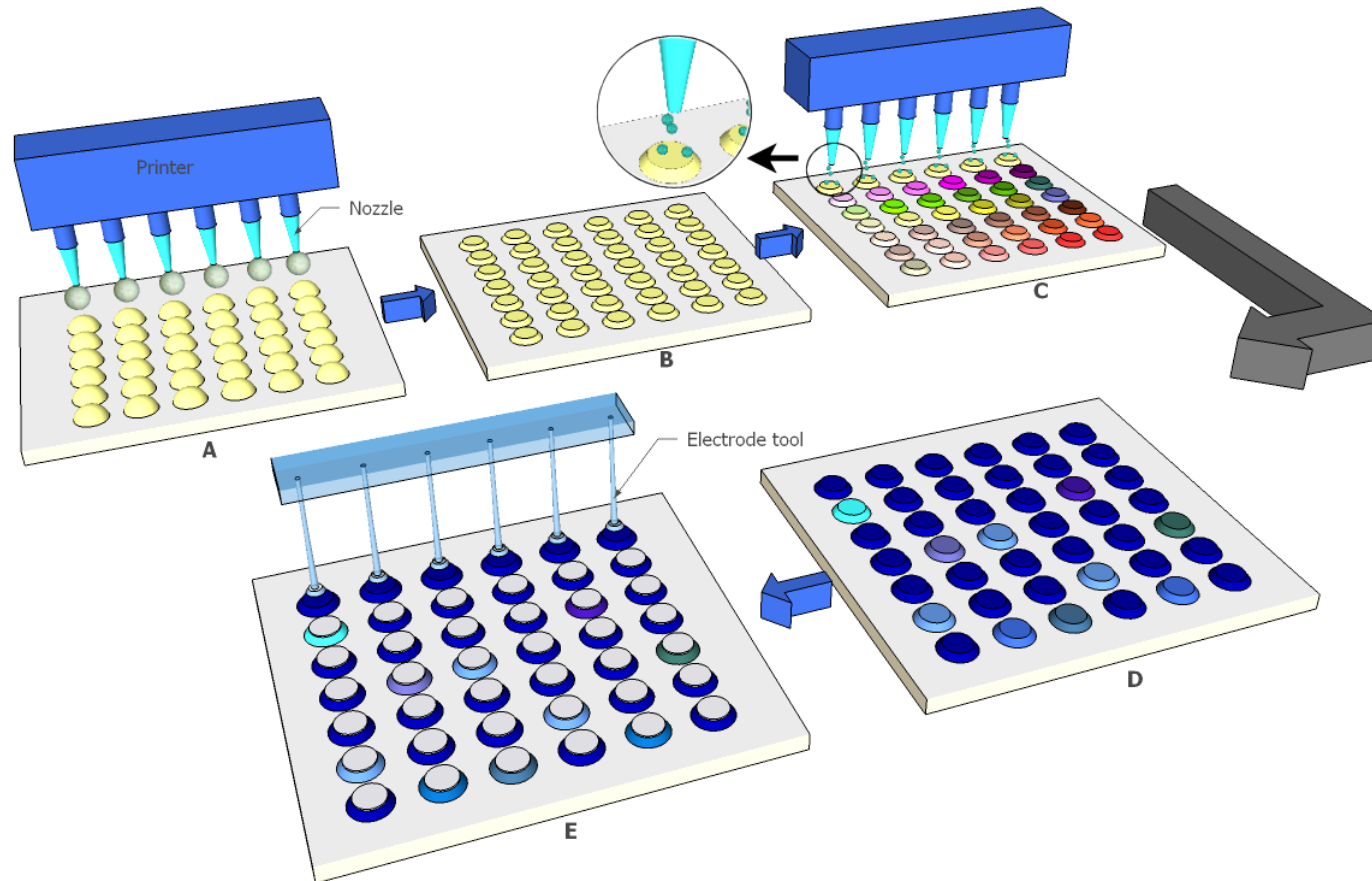


Figure 5.1 Schematic layout of the fabrication method for high throughput discovery of donor-doped BT PTCR ceramics showing the following stages: droplet-printing (A), drying and debinding (B), droplet-doping (C), sintering (D) application of electrode (E).

6. References

- 1 J. C. Phillips, *Physics of High-Tc Superconductors*. 1989, Washington DC: Academic Press. pp.60-61.
- 2 Y. T. Oganessian, F. S. Abdullin, P. D. Bailey, D. E. Benker, M. E. Bennett, S. N. Dmitriev, J. G. Ezold, J. H. Hamilton, R. A. Henderson, M. G. Itkis, Y. V. Lobanov, A. N. Mezentsev, K. J. Moody, S. L. Nelson, A. N. Polyakov, C. E. Porter, A. V. Ramayya, F. D. Riley, J. B. Roberto, M. A. Ryabinin, K. P. Rykaczewski, R. N. Sagaidak, D. A. Shaughnessy, I. V. Shirokovsky, M. A. Stoyer, V. G. Subbotin, R. Sudowe, A. M. Sukhov, Y. S. Tsyganov, V. K. Utyonkov, A. A. Voinov, G. K. Vostokin, and P. A. Wilk, Synthesis of a New Element with Atomic Number Z=117, *Physical Review Letters*, **104**(14): 142502, (2010).
- 3 K. Kennedy, T. Stefansky, G. Davy, V. F. Zackay, and E. R. Parker, Rapid method for determining ternary-alloy phase diagrams, *Journal of Applied Physics*, **36**(12): 3808-3810, (1965).
- 4 J. J. Hanak, The 'Multiple-Sample Concept' in materials research: synthesis, compositional analysis and testing of entire multicomponent system, *Journal of Materials Science*, **5**: 964-971, (1970).
- 5 J. K. Scott and G. P. Smith, Searching for peptide ligands with an epitope library, *Science*, **249**: 386-390, (1990).
- 6 S. P. A. Fodor, J. L. Read, C. Pirrung, L. Stryer, and A. T. Lu, Light-directed, spatially addressable parallel chemical synthesis, *Science*, **251**: 767-773, (1991).
- 7 K. S. Lam, S. E. Salmon, E. M. Hersh, V. Hruby, and M. Kazmierski, A new type of synthetic peptide library for identifying ligand-binding activity, *Nature*, **354**: 82-84, (1991).
- 8 R. Hoogenboom, M. A. R. Meier, and U. S. Schubert, Combinatorial methods, automated synthesis and high-throughput screening in polymer research: past and present, *Macromolecular Rapid Communications*, **24**(1): 15-32, (2003).
- 9 E. W. McFarland and W. H. Weinberg, Combinatorial approaches to materials discovery, *Trends in Biotechnology*, **17**: 107-115, (1999).
- 10 B. Gutte and R. B. Merrifield, The total synthesis of an enzyme with ribonuclease A activity, *Journal of the American Chemical Society*, **91**(2): 501-2, (1969).

- 11 A. Furka, F. Sebestyén, M. Asgedom, and G. Dibo, General-method for rapid synthesis of multicomponent peptide mixtures, *International Journal of Peptide and Protein Research*, **37**(6): 487-493, (1991).
- 12 J. Klein, T. Zech, J. M. Newsam, and S. A. Schunk, Application of a novel split&pool-principle for the fully combinatorial synthesis of functional inorganic materials, *Applied Catalysis A-General*, **254**(1): 121-131, (2003).
- 13 N. Gochman, Future directions for automated analysis, *Med Instrum*, **8**(1): 41-3, (1974).
- 14 E. Danielson, J. H. Golden, E. W. McFarland, C. M. Reaves, W. H. Weinberg, and X. D. Wu, A combinatorial approach to the discovery and optimization of luminescent materials, *Nature*, **389**(6654): 944-948, (1997).
- 15 E. Danielson, M. Devenney, D. M. Giaquinta, J. H. Golden, R. C. Haushalter, E. W. McFarland, D. M. Poojary, C. M. Reaves, W. H. Weinberg, and X. D. Wu, A rare-earth phosphor containing one-dimensional chains identified through combinatorial methods, *Science*, **279**(5352): 837-839, (1998).
- 16 W. H. Weinberg, B. Jandeleit, K. Self, and H. Turner, Combinatorial methods in homogeneous and heterogeneous catalysis, *Current Opinion in Solid State & Materials Science*, **3**(1): 104-110, (1998).
- 17 F. C. Moates, M. Somani, J. Annamalai, J. T. Richardson, D. Luss, and R. C. Willson, Infrared thermographic screening of combinatorial libraries of heterogeneous catalysts, *Industrial & Engineering Chemistry Research*, **35**(12): 4801-4803, (1996).
- 18 E. D. Isaacs, M. Marcus, G. Aepli, X. D. Xiang, X. D. Sun, P. Schultz, H. K. Kao, G. S. Cargill, and R. Haushalter, Synchrotron x-ray microbeam diagnostics of combinatorial synthesis, *Applied Physics Letters*, **73**(13): 1820-1822, (1998).
- 19 X. L. Weng, J. K. Cockcroft, G. Hyett, M. Vickers, P. Boldrin, C. C. Tang, S. P. Thompson, J. E. Parker, J. C. Knowles, I. Rehman, I. Parkin, J. R. G. Evans, and J. A. Darr, High-throughput continuous hydrothermal synthesis of an entire nanoceramic phase diagram, *Journal of Combinatorial Chemistry*, **11**(5): 829-834, (2009).
- 20 S. Roncallo, O. Karimi, K. D. Rogers, J. M. Gregoire, D. W. Lane, J. J. Scragg, and S. A. Ansari, High throughput X-ray diffraction analysis of combinatorial polycrystalline thin film libraries, *Analytical Chemistry*, **82**(11): 4564-4569, (2010).

- 21 Y. Lu, T. Wei, F. Duewer, P. G. Schultz, and X. D. Xiang, Nondestructive imaging of dielectric-constant profiles and ferroelectric domains with a scanning-tip microwave near-field microscope, *Science*, **276**: 2004-06, (1997).
- 22 C. Gao, F. Duewer, and X. D. Xiang, Quantitative microwave evanescent microscopy, *Applied Physics Letters*, **75**: 3005-07, (1999).
- 23 T. Fukumura, M. Ohtani, M. Karwasaki, Y. Okimoto, and H. Koinuma, Rapid construction of a phase diagram of doped Mott insulators with a composition-spread approach *Applied Physics Letters*, **77**(21): 3426-28 (2000).
- 24 Y. K. Yoo, T. Ohnishi, G. Wang, F. Duewer, and X. D. Xiang, Continuous mapping of structure-property relations in $\text{Fe}_{1-x}\text{Ni}_x$ metallic alloys fabricated by combinatorial synthesis, *Intermetallics*, **9**(7): 541-545 (2001).
- 25 A. Pross, A. I. Crisan, S. J. Bending, V. Mosser, and M. Konczykowski, Second-generation quantum-well sensors for room-temperature scanning Hall probe microscopy, *Journal of Applied Physics*, **97**(9): 4, (2005).
- 26 Q. Y. Lu, C. C. Chen, and A. deLozanne, Observation of magnetic domain behavior in colossal magnetoresistive materials with a magnetic force microscope, *Science*, **276**(5321): 2006-2008, (1997).
- 27 X. D. Xiang, X. Sun, G. Briceno, Y. Lou, K. A. Wang, H. Chang, W. G. WallaceFreedman, S. W. Chen, and P. G. Schultz, A combinatorial approach to materials discovery, *Science*, **268**: 1738-40, (1995).
- 28 A. W. Sleight, Chemistry of high-temperature superconductors, *Science*, **242**(4885): 1519-1527, (1988).
- 29 G. Logvenov, I. Sveklo, and I. Bozovic, Combinatorial molecular beam epitaxy of $\text{La}_{2-x}\text{Sr}_x\text{CuO}_{4+\delta}$, *Physica C-Superconductivity and Its Applications*, **460**: 416-419, (2007).
- 30 G. Briceno, H. Y. Chang, X. D. Sun, P. G. Schultz, and X. D. Xiang, A class of cobalt oxide magnetoresistance materials discovered with combinatorial synthesis, *Science*, **270**(5234): 273-275, (1995).
- 31 H. Kionuma, Y. Matsumoto, M. Murakami, T. Shono, T. Hasegawa, T. Fukumura, M. Kawasaki, P. Ahmet, T. Chikyow, and S. Y. Kioshihara, Room-temperature ferromagnetism in transparent transition metal-doped titanium dioxide *Science*, **291**: 854-856, (2001).
- 32 T. Dietl, H. Ohno, F. Matsukura, J. Cibert, and D. Ferrand, Zener model description of ferromagnetism in zinc-blende magnetic semiconductors, *Science*,

- 287**(5455): 1019-1022, (2000).
- 33 F. Tsui, L. He, L. Ma, A. Tkachuk, Y. S. Chu, K. Nakajima, and T. Chikyow, Novel germanium-based magnetic semiconductors, *Physical Review Letters*, **91**(17): 177203, (2003).
- 34 I. Takeuchi, O. O. Famodu, J. C. Read, M. A. Aronova, K. S. Chang, and A. Orozco, Identification of novel compositions of ferromagnetic shape-memory alloys using composition spreads, *Nature Materials*, **2**(3): 180-184 (2003).
- 35 T. Wei, W. G. Wallace-Freedman, P. G. Schultz, and X. D. Xiang, Scanning tip microwave near-field microscope *Applied Physics Letters*, **68**(24): 3506-3508 (1996).
- 36 C. Gao, T. Wei, F. Duewer, Y. L. Lu, and X. D. Xiang, High spatial resolution quantitative microwave impedance microscopy by a scanning tip microwave near-field microscope, *Applied Physics Letters*, **71**: 1872-74, (1997).
- 37 R. B. van Dover, L. D. Schneemeyer, and R. M. Fleming, Discovery of a useful thin-film dielectric using a composition-spread approach, *Nature*, **392**(6672): 162-164, (1998).
- 38 R. B. van Dover and L. F. Schneemeyer, The codeposited composition spread approach to high-throughput discovery/exploration of inorganic materials, *Macromolecular Rapid Communications*, **25**(1): 150-157, (2004).
- 39 H. Chang, C. Gao, I. Takeuchi, Y. Yoo, J. Wang, P. G. Schultz, and X. D. Xiang, Combinatorial synthesis and high throughput evaluation of ferroelectric/dielectric thin-film libraries for microwave applications, *Applied Physics Letters*, **72**(17): 2185-17, (1998).
- 40 R. C. Pullar, Y. Zhang, L. F. Chen, S. F. Yang, J. R. G. Evans, P. K. Petrov, A. N. Salak, D. A. Kiselev, A. L. Kholkin, V. M. Ferreira, and N. M. Alford, Manufacture and measurement of combinatorial libraries of dielectric ceramics - Part II. Dielectric measurements of $Ba_{1-x}Sr_xTiO_3$ libraries, *Journal of the European Ceramic Society*, **27**(16): 4437-4443, (2007).
- 41 X. D. Sun and X. D. Xiang, New phosphor $(Gd_{2-x}Zn_x)O_{3-\delta} : Eu^{3+}$ with high luminescent efficiency and superior chromaticity *Applied Physics Letters*, **72**(5): 525-527 (1998).
- 42 J. S. Wang, Y. Yoo, C. Gao, I. Takenchi, X. D. Sun, H. Y. Chang, P. G. Schultz, and X. D. Xiang, Identification of a blue photoluminescent composite material from a combinatorial library *Science*, **279**: 1712-14, (1998).
- 43 X. D. Sun, K. A. Wang, Y. Yoo, W. G. Wallace-Freedman, C. Gao, X. D.

- Xiang, and P. G. Schultz, Solution-phase synthesis of luminescent materials libraries, *Advanced Materials*, **9**: 1046-49, (1997).
- 44 L. Luo, Z. H. Xiong, N. G. Zhou, and L. Zhou, Structure and luminescence properties of $Gd_{1-x}Al_yO_z:Eu_x$ gradational combinatorial material chips, *Rare Metal Materials and Engineering*, **39**(7): 1260-1264, (2010).
- 45 T. Lin, S. Kellici, K. Gong, K. Thompson, J. R. G. Evans, X. Wang, and J. A. Darr, Rapid automated materials synthesis instrument: exploring the composition and heat-treatment of nanoprecursors toward low temperature red phosphors, *Journal of Combinatorial Chemistry*, **12**(3): 383-92, (2010).
- 46 R. Thomas, J. A. Moulijn, V. H. J. Debeer, and J. Medema, Structure-metathesis-activity relations of silica supported molybdenum and tungsten-oxide, *Journal of Molecular Catalysis*, **8**(1-3): 161-174, (1980).
- 47 R. J. Hendershota, W. B. Rogersa, C. M. Snively, B. A. Ogunnaikea, and J. Lauterbach, Development and optimization of NO_x storage and reduction catalysts using statistically guided high-throughput experimentation *Catalysis Today*, **98**(3): 375-385, (2004).
- 48 N. Takahashia, H. Shinjoha, T. Iijimaa, T. Suzukia, K. Yamazakia, K. Yokota, H. Suzuki, and N. Miyoshi, The new concept 3-way catalyst for automotive lean-burn engine: NO_x storage and reduction catalyst, *Catalysis Today*, **27**(1-2): 63-69, (1996).
- 49 R. Vijay, R. J. Hendershot, S. M. Rivera-Jiménez, W. B. Rogers, B. J. Feist, C. M. Snively, and J. Lauterbach, Noble metal free NO_x storage catalysts using cobalt discovered via high-throughput experimentation, *Catalysis Communications*, **6**(2): 167-171, (2005).
- 50 D. C. Webster and M. A. R. Meier, *Polymer libraries: preparation and applications*, in *Polymer Libraries*. 2010, Springer-Verlag Berlin: Berlin. pp. 1-15.
- 51 J. T. Cabral, S. D. Hudson, C. Harrison, and J. F. Douglas, Frontal photopolymerization for microfluidic applications *Langmuir*, **20**(23): 10020-29, (2004).
- 52 Z. T. Cygan, J. T. Cabral, K. L. Beers, and E. J. Amis, Microfluidic platform for the generation of organic-phase microreactors *Langmuir*, **21**(8): 3629-34, (2005).
- 53 H. Walter, G. Basset, T. Beierlein, A. Von Muhlenen, and G. Nisato, Combinatorial approach for fast screening of functional materials, *Journal of Polymer Science Part B-Polymer Physics*, **48**(14): 1587-1593, (2010).

- 54 H. Sirringhaus, T. Kawase, R. H. Friend, T. Shimoda, W. Wu, and E. P. Woo, High-resolution inkjet printing of all-polymer transistor circuits, *Science*, **290**: 2123-26, (2000).
- 55 K. Fujimoto, K. Takada, T. Sasaki, and M. Watanabe, Combinatorial approach for powder preparation of pseudo-ternary system $\text{LiO}_{0.5}\text{-X-TiO}_2$ (X: $\text{FeO}_{1.5}$, $\text{CrO}_{1.5}$ and NiO), *Applied Surface Science*, **223**(1-3): 49-53, (2004).
- 56 K. Takada, K. Fujimoto, T. Sasaki, and M. Watanabe, Combinatorial electrode array for high-throughput evaluation of combinatorial library for electrode materials, *Applied Surface Science*, **223**(1-3): 210-213, (2004).
- 57 J. S. Thorne, R. J. Sanderson, J. R. Dahn, and R. A. Dunlap, Combinatorial study of the Sn-Cu-C System for Li-Ion battery negative electrode materials, *Journal of the Electrochemical Society*, **157**(10): A1085-A1091, (2010).
- 58 E. Reddington, A. Sapienza, B. Gurau, R. Viswanathan, S. Sarangapani, E. S. Smotkin, and T. E. Mallouk, Combinatorial electrochemistry: a highly parallel, optical screening method for discovery of better electrocatalysts, *Science*, **280**: 1735-37, (1998).
- 59 K. Yaccato, R. Carhart, A. Hagemeyer, M. Herrmann, A. Lesik, P. Strasser, A. Volpe, H. Turner, H. Weinberg, R. K. Grasselli, C. J. Brooks, and J. M. Pigos, High throughput discovery of families of high activity WGS catalysts: Part I - history and methodology, *Combinatorial Chemistry & High Throughput Screening*, **13**(4): 318-330, (2010).
- 60 R. Cremer and D. Neuschütz, Optimization of (Ti,Al)N hard coatings by a combinatorial approach, *International Journal of Inorganic Materials*, **3**(8): 1181-1184, (2001).
- 61 G. Frenzer, A. Frantzen, D. Sanders, U. Simon, and W. F. Maier, Wet chemical synthesis and screening of thick porous oxide films for resistive gas sensing applications, *Sensors*, **6**(11): 1568-1586, (2006).
- 62 U. Simon, D. Sanders, J. Jockel, and T. Brinz, Setup for high-throughput impedance screening of gas-sensing materials, *Journal of Combinatorial Chemistry*, **7**(5): 682-687, (2005).
- 63 R. A. Potyrailo and V. M. Mirsky, Combinatorial and high-throughput development of sensing materials: The first 10 years, *Chemical Reviews*, **108**(2): 770-813, (2008).
- 64 C. Suh and K. Rajan, Combinatorial design of semiconductor chemistry for

- bandgap engineering: "virtual" combinatorial experimentation, *Applied Surface Science*, **223**: 148-158, (2004).
- 65 C. Suh, A. Rajagopalan, X. Li, and K. Rajan. *Combinatorial materials design through database science*. in *Symposium on Combinatorial and Artificial Intelligence Methods in Materials Science II held at the 2003 MRS Fall Meeting*. 2003. Boston, MA: Materials Research Society. **Vol. 2**. pp. 333-341
- 66 D. J. Scott, S. Manos, P. V. Coveney, J. C. H. Rossiny, S. Fearn, J. A. Kilner, R. C. Pullar, N. M. N. Alford, A. K. Axelsson, Y. Zhang, L. Chen, S. Yang, J. R. G. Evans, and M. T. Sebastian, Functional ceramic materials database: An online resource for materials research, *Journal of Chemical Information and Modeling*, **48**(2): 449-455, (2008).
- 67 A. Wagendristel and Y. Wang, *An Introduction to Physics and Technology of Thin Film*. 1994, Singapore: World Scientific Publishing Co. Pte. Ltd. pp.156-198.
- 68 M. de Keijser, D. M. de Leeuw, P. J. van Veldhoven, A. E. M. De Veirman, D. G. Neerincx, and G. J. M. Dormans, The structure of heteroepitaxial lead titanate layers grown by organometallic chemical vapour deposition, *Thin Solid Films*, **266**(2): 157-167, (1995).
- 69 J. E. Mahan, *Physical Vapor Deposition of Thin Films*. 2000, New York: John Wiley & Sons, Inc. pp.35-49.
- 70 J. Luyten, J. Coymans, C. Smolders, S. Vercauteren, E. F. Vansant, and R. Leysen, Shaping of multilayer ceramic membranes by dip coating, *Journal of the European Ceramic Society*, **17**(2-3): 273-279, (1997).
- 71 E. Dien, J. B. Briot, M. Lejeune, and A. Smith, Relationship between processing and electrical behavior of BST films deposited by spin coating, *Journal of the European Ceramic Society*, **19**(6-7): 1349-1352, (1999).
- 72 Y. M. Ai, Y. Liu, T. H. Cui, and K. Varahramyan, Thin film deposition of an n-type organic semiconductor by ink-jet printing technique, *Thin Solid Films*, **450**(2): 312-315, (2004).
- 73 B. A. Ridley, B. Nivi, and J. M. Jacobson, All-inorganic field effect transistors fabricated by printing, *Science*, **286**(5440): 746-749, (1999).
- 74 S. Guerin and B. E. Hayden, Physical vapor deposition method for the high-throughput synthesis of solid-state material libraries, *Journal of Combinatorial Chemistry*, **8**(1): 66-73, (2006).
- 75 X. D. Xiang and P. G. Schultz, The combinatorial synthesis and evaluation of

- functional materials, *Physica C*, **282-287**: 428-430, (1997).
- 76 T. Vossmeier, S. Jia, E. DeLonno, M. R. Diehl, S. H. Kim, X. Peng, A. P. Alivisatos, and J. R. Heath, Combinatorial approaches toward patterning nanocrystals, *Journal of Applied Physics*, **84**: 3664-70, (1998).
- 77 N. C. Woo, B. G. Ng, and R. B. van Dover, High-throughput combinatorial study of local stress in thin film composition spreads, *Review of Scientific Instruments*, **78**(7): 5, (2007).
- 78 T. X. Sun, Combinatorial search for advanced luminescence materials, *Biotechnology and Bioengineering*, **61**: 193-201, (1999).
- 79 C. Schmitz, M. Thelakkat, and H. W. Schmidt, A combinatorial study of the dependence of organic LED characteristics on layer thickness, *Advanced Materials*, **11**: 821-826, (1999).
- 80 C. Schmitz, P. Posch, M. Thelakkat, and H. W. Schmidt, Efficient screening of electron transport materials in multi-layer organic light emitting diodes by combinatorial methods, *Physical Chemistry Chemical Physics*, **1**: 1777-81, (1999).
- 81 S. Pessaud, F. Gervais, C. Champeaux, P. Marchet, A. Catherinot, M. Licheron, J. L. Longuet, and F. Ravel, Combinatorial solid state chemistry by multitarget laser ablation: a way for the elaboration of new superconducting cuprates thin film, *Materials Science and Engineering*, **B60**: 205-211, (1999).
- 82 H. M. Christen, I. Ohkubo, C. M. Rouleau, G. E. Jellison, A. A. Puretzky, D. B. Geohegan, and D. H. Lowndes, A laser-deposition approach to compositional-spread discovery of materials on conventional sample sizes, *Measurement Science & Technology*, **16**(1): 21-31, (2005).
- 83 S. Groudeva-Zotova, H. Karl, A. Savan, J. Feydt, B. Wehner, T. Walther, N. Zotov, B. Stritzker, and A. Ludwig, Structural and magnetic characteristics of FeCo thin films modified by combinatorial ion implantation, *Thin Solid Films*, **495**(1-2): 169-174, (2006).
- 84 I. Grosshans, H. Karl, and B. Stritzker. *Advanced apparatus for combinatorial synthesis of buried II-VI nanocrystals by ion implantation*. in *Spring Meeting of the European-Materials-Research-Society (E-MRS)*. 2002. Strasbourg, France: Elsevier Science Sa pp. 212-215
- 85 H. Koinuma, T. Koida, T. Ohnishi, D. Komiyama, M. Lippmaa, and M. Kawasaki, Parallel fabrication of artificially designed superlattices by combinatorial laser MBE, *Applied Physics A: Materials Science & Processing*, **69**: S29-S31, (1999).

- 86 Z. W. Jin, M. Murakami, T. Fukumura, Y. Matsumoto, A. Ohtomo, M. Kawasaki, and H. Koinuma, Combinatorial laser MBE synthesis of 3d ion doped epitaxial ZnO thin films, *Journal of Crystal Growth*, **214**: 55-58, (2000).
- 87 T. Ohsawa, K. Nakajima, Y. Matsumoto, and H. Koinuma, Combinatorial discovery of anomalous substrate effect on the photochemical properties of transition metal-doped epitaxial SrTiO₃ heterostructures, *Applied Surface Science*, **252**(7): 2603-2607, (2006).
- 88 H. Chang, I. Takeuchi, and X. D. Xiang, A low-loss composition region identified from a thin-film composition spread of (Ba_{1-x-y}Sr_xCa_y) TiO₃, *Applied Physics Letters*, **74**(8): 1165-1167, (1999).
- 89 A. Ludwig, Combinatorial fabrication of magnetic multilayer films, *Applied Surface Science*, **223**(1-3): 78-83, (2004).
- 90 E. Litborn, M. Stjernstrom, and J. Roeraade, Nonolitre filtration based on piezoelectric drop-on-demand technology and laser-induced fluorescence detection, *Analytical Chemistry*, **70**: 4847-52, (1998).
- 91 J. R. G. Evans, M. J. Edirisinghe, P. V. Coveney, and J. Eames, Combinatorial searches of inorganic materials using the ink-jet printer: Science, Philosophy, and Technology, *Journal of the European Ceramic Society*, **21**: 2291-99, (2001).
- 92 M. M. Mohebi and J. R. G. Evans, Combinatorial ink-jet printer for ceramics: calibration, *Journal of the American Ceramic Society*, **86**(10): 1654-61, (2003).
- 93 J. S. Reed, *Principles of Ceramic Processing*. 1995, New York: John Wiley & Sons. pp.496-521.
- 94 G. N. Howatt, *Method of producing high-dielectric high-insulation ceramic plates*. U.S. Patent 2582993. 29th October. 1948.
- 95 G. N. Howatt, R. G. Breckenridge, and J. M. Brownlow, Fabrication of thin ceramic sheets for capacitors, *Journal of the American Ceramic Society*, **30**(8): 237-242, (1947).
- 96 R. E. Mistler, Tape casting: past, present, potential, *American Ceramic Society Bulletin*, **77**(N10): 82-86, (1998).
- 97 G. Y. Onoda and L. L. Hench, *Ceramic Processing before Firing*. 1978, New York: John Wiley & Sons, Inc. pp.142-168.
- 98 J. Yoo, K. M. Cho, W. S. Bae, M. Cima, and S. Suresh, Transformation-toughened ceramic multilayers with compositional gradients, *Journal of the American Ceramic Society*, **81**(1): 21-32, (1998).

- 99 J. Moon, A. C. Caballero, L. Hozer, Y. M. Chiang, and M. J. Cima, Fabrication of functionally graded reaction infiltrated SiC-Si composite by three-dimensional printing (3DP (TM)) process, *Materials Science and Engineering a-Structural Materials Properties Microstructure and Processing*, **298**(1-2): 110-119, (2001).
- 100 S. F. Yang and J. R. G. Evans, Device for preparing combinatorial libraries in powder metallurgy, *Journal of Combinatorial Chemistry*, **6**(4): 549-555, (2004).
- 101 T. A. Stegk, R. Janssen, and G. A. Schneider, High-throughput synthesis and characterization of bulk ceramics from dry powders, *Journal of Combinatorial Chemistry*, **10**(2): 274-279, (2008).
- 102 L. Chen, Y. Zhang, S. Yang, and J. R. G. Evans, Protocols for printing thick film ceramic libraries using the London University Search Instrument (LUSI), *Review of Scientific Instruments*, **78**(7): 2210-2215, (2007).
- 103 J. C. H. Rossiny, S. Fearn, J. A. Kilner, Y. Zhang, and L. Chen, Combinatorial searching for novel mixed conductors, *Solid State Ionics*, **177**(19-25): 1789-1794, (2006).
- 104 R. C. Pullar, Y. Zhang, L. F. Chen, S. F. Yang, J. R. G. Evans, and N. M. Alford, Manufacture and measurement of combinatorial libraries of dielectric ceramics - Part I: Physical characterisation of $Ba_{1-x}Sr_xTiO_3$ libraries, *Journal of the European Ceramic Society*, **27**: 3861-3865, (2007).
- 105 R. C. Pullar, Y. Zhang, L. Chen, S. Yang, J. R. G. Evans, A. N. Salak, D. A. Kiselev, A. L. Kholkin, V. M. Ferreira, and N. M. Alford, Dielectric measurements on a novel $Ba_{1-x}Ca_xTiO_3$ (BCT) bulk ceramic combinatorial library, *Journal of Electroceramics*, **22**(1): 245-251, (2009).
- 106 E. Sachs, M. Cima, and P. Williams, Three-dimensional printing: rapid tooling and prototypes directly from a CAD model, *Journal of Engineering for Industry-transactions of the ASME*, **114**(4): 481-488, (1992).
- 107 D. T. Pham and R. S. Gault, A comparison of rapid prototyping technologies, *Int. J. Machine Tools Manufacture*, **38**: 1257-87, (1998).
- 108 R. Danzebrink and M. A. Aegerter, Deposition of micropatterned coating using an ink-jet technique, *Thin Solid Films*, **351**: 115-118, (1999).
- 109 X. Ding, L. Yongxiang, and W. Dong, Fabrication of $BaTiO_3$ dielectric films by direct ink-jet printing, *Ceramics International*, **30**: 1885-87, (2004).
- 110 M. Mott, J. H. Song, and J. R. G. Evans, Microengineering of ceramics by

- direct ink-jet printing, *Journal of the American Ceramic Society*, **82**(7): 1653-58, (1999).
- 111 X. Zhao, J. R. G. Evans, and M. J. Edirisinghe, Ink-jet printing of ceramic pillar arrays, *Journal of Materials Science*, **37**: 1987-92, (2002).
- 112 X. Zhao, J. R. G. Evans, and M. J. Edirisinghe, Formulation of ceramic ink for a wide-array drop-on-demand ink-jet printer, *Ceramics International*, **29**: 887-892, (2003).
- 113 P. F. Blazdell and J. R. G. Evans, Preparation of ceramic inks for solid freeforming using a continuous jet printer, *Journal of Materials Synthesis and Processing*, **7**(6): 349-356, (1999).
- 114 W. D. Teng, M. J. Edirisinghe, and J. R. G. Evans, Optimization of dispersion and viscosity of a ceramic jet printing ink, *Journal of the American Ceramic Society*, **80**: 486-494, (1997).
- 115 S. Sumita, W. E. Rhine, and H. K. Bowen, Effect of organic dispersants on the dispersion, packing, and sintering of alumina, *Journal of the American Ceramic Society*, **74**(9): 2189-96, (1991).
- 116 W. D. Teng and M. J. Edirisinghe, Development of ceramic inks for direct continuous jet printing, *Journal of the American Ceramic Society*, **81**(4): 1033-36, (1998).
- 117 J. H. Song, M. J. Edirisinghe, and J. R. G. Evans, Formulation and multilayer jet printing of ceramic inks, *Journal of the American Ceramic Society*, **82**(12): 3374-80, (1999).
- 118 P. Blazdell, Solid free-forming of ceramics using a continuous jet printer, *Journal of Materials Processing Technology*, **137**: 49-54, (2003).
- 119 S. L. Zoltan, *Pulse droplet ejection system*. U.S. Patent 3683212. 9th September. 1974.
- 120 E. L. Kyser and S. B. Sears, *Method and apparatus for recording with writing fluids and drop projection means therefore*. U.S. Patent 3946398. 29th June. 1976.
- 121 J. E. Fromm, Numerical calculation of the fluid dynamics of drop-on-demand jets, *IBM J. Res. Dev.*, **28**(3): 322-33, (1984).
- 122 T. Wang and B. Derby, Ink-jet printing and sintering of PZT, *Journal of the American Ceramic Society*, **88**(8): 2053-2058, (2005).
- 123 K. A. M. Seerden, N. Reis, and J. R. G. Evans, Ink-jet printing of wax-based alumina suspensions, *Journal of the American Ceramic Society*, **84**(11): 2514-20,

- (2001).
- 124 N. Reis, C. Ainsley, and B. Derby, Digital microfabrication of ceramic components, *American Ceramic Society Bulletin*, **82**(9): 6-11, (2003).
- 125 P. L. Hue, Progress and trends in ink-jet printing technology, *The Journal of Imaging Science and Technology*, **42**(1): 49-62, (1998).
- 126 T. Agui and M. Nakajima, Drop formation characteristics of electrostatic ink jet using water-based ink, *IEEE Transactions on Electron Devices*, **24**(3): 262-266, (1977).
- 127 H. Kawamoto, S. Umezu, and R. Koizumi, Fundamental investigation on electrostatic ink jet phenomena in pin-to-plate discharge system, *The Journal of Imaging Science and Technology*, **49**(1): 19-27, (2005).
- 128 B. Bugarski, Q. L. Li, and D. Poncelet, Electrostatic droplet generation : mechanism of polymer droplet formation, *AIChE Journal*, **40**(6): 1026-31, (1994).
- 129 S. A. Elrod, B. Handimioglu, and E. Richley, Nozzleless droplet formation with focused acoustic beam, *Journal of Applied Physics*, **65**(9): 3441-47, (1989).
- 130 D. Huang and E. S. Kim, Micromachined acoustic-wave liquid ejector, *Journal of Microelectromechanical System*, **10**(3): 442-449, (2001).
- 131 C. Hull, *Apparatus for production of Three-dimensional Objects by Stereolithography*. U. S. Pat. No. 4575330. 8th August. 1986.
- 132 M. L. Griffith and J. W. Halloran, Freeform fabrication of ceramics via stereolithography, *Journal of the American Ceramic Society*, **79**(10): 2601-08, (1992).
- 133 S. C. Ventura, S. C. Narang, and S. Sharma. *A new SFF process for functional ceramic components*. in *Solid Freeform Fabrication Symposium Proceedings*. 1996. Austin pp. 327-334
- 134 S. Bose, S. Sugaira, and A. Bandyopadhyay, Processing of controlled porosity ceramic structures via fused deposition, *Scripta Materialia*, **41**(9): 1009-1014, (1999).
- 135 M. K. Agarwala, A. Bandyopadhyay, and A. Safari, FDC, rapid fabrication of structural components, *American Ceramic Society Bulletin*, **75**(11): 60-65, (1996).
- 136 M. A. Jafari and W. Han, A novel system for fused deposition of advanced multiple ceramics, *Rapid Prototyping Journal*, **6**(3): 161-175, (2000).
- 137 I. Grida and J. R. G. Evans, Extrusion freeforming of ceramics through fine nozzles, *Journal of the European Ceramic Society*, **23**: 629-635, (2003).
- 138 X. S. Lu, Y. Lee, S. F. Yang, Y. Hao, J. R. G. Evans, and C. G. Parini, Fine

- lattice structures fabricated by extrusion freeforming: Process variables, *Journal of Materials Processing Technology*, **209**(10): 4654-4661, (2009).
- 139 X. S. Lu, Y. Lee, S. F. Yang, Y. Hao, J. R. G. Evans, and C. G. Parini, Solvent-based paste extrusion solid freeforming, *Journal of the European Ceramic Society*, **30**(1): 1-10, (2010).
- 140 J. Beaman and C. R. Deckard, *Selected laser sintering with assisted power handling*. US Patent No. 4,938,816. June 3. 1990.
- 141 J. L. Song, Y. T. Li, and Q. L. Deng, Rapid prototyping manufacturing of silica sand patterns based on selective laser sintering, *Journal of Materials Processing Technology*, **187**: 614-618, (2007).
- 142 B. Caulfield, P. E. Mchugh, and S. Lohfeld, Dependence of mechanical properties of polyamide components on build parameters in the SLS process, *Journal of Materials Processing Technology*, **182**: 477-488, (2007).
- 143 E. Berry, J. M. Brown, and M. Connell, Preliminary experience with medical applications of rapid prototyping by selective laser sintering, *Medical Engineering and Physics*, **19**(1): 90-96, (1997).
- 144 J. M. Williams, A. Adewunmi, and R. M. Schek, Bone tissue engineering using polycaprolactone scaffolds fabricated via selective laser sintering, *Biomaterials*, **26**: 4817-27, (2005).
- 145 D. W. Richerson, *Modern Ceramic Engineering: Properties, Processing, and Use in Design*. 1992, New York: M. Dekker. pp.347-355.
- 146 G. W. Scherer, Theory of drying, *Journal of the American Ceramic Society*, **73**(1): 3-14, (1990).
- 147 S. Ghosal, A. Emami-Naeini, Y. P. Harn, B. S. Draskovich, and J. P. Pollinger, A physical model for the drying of gelcast ceramics, *Journal of the American Ceramic Society*, **82**(3): 513-520, (1999).
- 148 J. A. Lewis, K. A. Blackman, A. L. Ogden, J. A. Payne, and L. F. Francis, Rheological property and stress development during drying of tape-cast ceramic layers, *Journal of the American Ceramic Society*, **79**(12): 3225-3234, (1996).
- 149 R. C. Chiu, T. J. Garino, and M. J. Cima, Drying of granular ceramic films I. Effect of processing variables on cracking behaviour, *Journal of the American Ceramic Society*, **76**(9): 2257-2264, (1993).
- 150 M. Descamps, M. Mascart, B. Thierry, and D. Leger, How to control cracking of tape-cast sheets, *American Ceramic Society Bulletin*, **74**(3): 89-92, (1995).

- 151 E. Streicher, T. Chartier, and P. Boch, Study of cracking and microstructural evolution during drying of tape-cast aluminum nitride sheets, *Journal of Materials Science*, **26**(6): 1659-1665, (1991).
- 152 R. C. Chiu and M. J. Cima, Drying of granular ceramic films II. Drying stress and saturation uniformity, *Journal of the American Ceramic Society*, **76**(11): 2769-2777, (1993).
- 153 D. M. Holmes, R. V. Kumar, and W. J. Clegg, Cracking during lateral drying of alumina suspensions, *Journal of the American Ceramic Society*, **89**(6): 1908-1913, (2006).
- 154 N. D. Denkov, O. D. Velez, P. A. Kralchevsky, I. B. Ivanov, H. Yoshimura, and K. Nagayama, Mechanism of formation of 2-dimensional crystals from latex-particles on substrates, *Langmuir*, **8**(12): 3183-3190, (1992).
- 155 E. Adachi, A. S. Dimitrov, and K. Nagayama, Stripe patterns formed on a glass-surface during droplet evaporation, *Langmuir*, **11**(4): 1057-1060, (1995).
- 156 S. D. Fitzgerald and A. W. Woods, The instability of a vaporization front in hot porous rock, *Nature*, **367**(6462): 450-453, (1994).
- 157 J. Feng, A. Yekta, and M. A. Winnik, Direct non-radiative energy transfer across a sharp polymer interface, *Chemical Physics Letters*, **260**(1-2): 296-301, (1996).
- 158 R. D. Deegan, O. Bakajin, T. F. Dupont, G. Huber, S. R. Nagel, and T. A. Witten, Capillary flow as the cause of ring stains from dried liquid drops, *Nature*, **389**(6653): 827-829, (1997).
- 159 A. F. Routh and W. B. Russel, Horizontal drying fronts during solvent evaporation from latex films, *Aiche Journal*, **44**(9): 2088-2098, (1998).
- 160 F. Parisse and C. Allain, Shape changes of colloidal suspension droplets during drying, *Journal De Physique II*, **6**(7): 1111-1119, (1996).
- 161 F. Parisse and C. Allain, Drying of colloidal suspension droplets: Experimental study and profile renormalization, *Langmuir*, **13**(14): 3598-3602, (1997).
- 162 E. Ciampi, U. Goerke, J. L. Keddie, and P. J. McDonald, Lateral transport of water during drying of alkyd emulsions, *Langmuir*, **16**(3): 1057-1065, (2000).
- 163 J. Conway, H. Korn, and M. R. Fisch, Evaporation kinematics of polystyrene bead suspensions, *Langmuir*, **13**(3): 426-431, (1997).
- 164 R. D. Deegan, Pattern formation in drying drops, *Physical Review E*, **61**(1):

- 475-485, (2000).
- 165 R. D. Deegan, O. Bakajin, T. F. Dupont, G. Huber, S. R. Nagel, and T. A. Witten, Contact line deposits in an evaporating drop, *Physical Review E*, **62**(1): 756-765, (2000).
- 166 I. Ueno and K. Kochiya, Effect of evaporation and solutocapillary-driven flow upon motion and resultant deposition of suspended particles in volatile droplet on solid substrate, *Advances in Space Research*, **34**: 450-454, (2007).
- 167 L. E. Scriven and C. V. Sternling, The Marangoni Effects, *Nature*, **187**(4733): 186-188, (1960).
- 168 H. Hu and R. G. Larson, Analysis of the effects of Marangoni stresses on the microflow in an evaporating sessile droplet, *Langmuir*, **21**(9): 3972-3980, (2005).
- 169 H. Hu and R. G. Larson, Marangoni effect reverses coffee-ring depositions, *Journal of Physical Chemistry B*, **110**(14): 7090-7094, (2006).
- 170 S. G. Yiantsios and B. G. Higgins, Marangoni flows during drying of colloidal films, *Physics of Fluids*, **18**(8), (2006).
- 171 E. Tekin, B. J. de Gans, and U. S. Schubert, Ink-jet printing of polymers - from single dots to thin film libraries, *Journal of Materials Chemistry*, **14**(17): 2627-2632, (2004).
- 172 R. Blossey and A. Bosio, Contact line deposits on cDNA microarrays: A "twin-spot effect", *Langmuir*, **18**(7): 2952-2954, (2002).
- 173 V. Dugas, J. Broutin, and E. Souteyrand, Droplet evaporation study applied to DNA chip manufacturing, *Langmuir*, **21**(20): 9130-9136, (2005).
- 174 M. D. Haw, M. Gillie, and W. C. K. Poon, Effects of phase behaviour on the drying of colloidal suspensions, *Langmuir*, **18**(5): 1626-1633, (2002).
- 175 B. J. de Gans and U. S. Schubert, Inkjet printing of well-defined polymer dots and arrays, *Langmuir*, **20**(18): 7789-7793, (2004).
- 176 J. Park and J. Moon, Control of colloidal particle deposit patterns within picoliter droplets ejected by ink-jet printing, *Langmuir*, **22**(8): 3506-3513, (2006).
- 177 F. Golestanifard, S. Azimi, and K. J. D. Mackenzie, Oxygen evolution during the formation and sintering of nickel manganese oxide spinels for thermistor applications, *Journal of Materials Science*, **22**(8): 2847-2851, (1987).
- 178 G. de Gyorgyfalva, A. N. Nolte, and I. M. Reaney, Correlation between microstructure and conductance in NTC thermistors produced from oxide powders, *Journal of the European Ceramic Society*, **19**(6-7): 857-860, (1999).

- 179 A. Feltz, Perovskite forming ceramics of the system $(\text{Sr}_x\text{La}_{1-x}\text{Ti}_x\text{plusYCo}_y\text{Co}_{1-x-2y}\text{O}_3)\text{-Co-IV-Co-II-O-III}$ for NTC thermistor applications, *Journal of the European Ceramic Society*, **20**(14-15): 2367-2376, (2000).
- 180 A. J. Moulson and J. M. Herbert, *Electroceramics: Materials, Properties, Applications. 2nd Edition* 2003, Chichester: John Wiley & Sons, Ltd. pp.167-173.
- 181 R. Schmidt, A. Stiegelschmitt, A. Roosen, and A. W. Brinkman, Screen printing of co-precipitated $\text{NiMn}_2\text{O}_{4+\delta}$ for production of NTCR thermistors, *Journal of the European Ceramic Society*, **23**(10): 1549-1558, (2003).
- 182 R. Legros, R. Metz, and A. Rousset, Structural properties of nickel manganite $\text{Ni}_x\text{Mn}_{3-x}\text{O}_4$ with $0.5 \leq x \leq 1$, *Journal of Materials Science*, **25**(10): 4410-4414, (1990).
- 183 K. Park and D. Y. Bang, Electrical properties of Ni-Mn-Co-(Fe) oxide thick film NTC thermistors prepared by screen printing, *Journal of Materials Science-Materials in Electronics*, **14**: 81-87, (2003).
- 184 R. Metz, Electrical properties of NTC thermistors made of manganite ceramics of general spinel structure: $\text{Mn}_{3-x-x'}\text{M}_x\text{N}_{x'}\text{O}_4$ ($0 \leq x \text{ plus } x' \leq 1$; M and N being Ni, Co or Cu). Aging phenomenon study, *Journal of Materials Science*, **35**(18): 4705-4711, (2000).
- 185 J. L. M. De Vidales, P. Garcia-Chain, R. M. Rojas, E. Vila, and O. Garcia-Martinez, Preparation and characterization of spinel-type Mn Ni Co O negative temperature coefficient ceramic thermistors, *Journal of Materials Science*, **33**(6): 1491-1496, (1998).
- 186 K. Park, Fabrication and electrical properties of Mn-Ni-Co-Cu-Si oxides negative temperature coefficient thermistors, *Journal of the American Ceramic Society*, **88**(4): 862-866, (2005).
- 187 A. Feltz and W. Polzl, Spinel forming ceramics of the system $\text{Fe}_x\text{Ni}_y\text{Mn}_{3-x-y}\text{O}_4$ for high temperature NTC thermistor applications, *Journal of the European Ceramic Society*, **20**(14-15): 2353-2366, (2000).
- 188 K. Park, Structural and electrical properties of $\text{FeMg}_{0.7}\text{Cr}_{0.6}\text{Co}_{0.7-x}\text{Al}_x\text{O}_4$ ($0 \leq x \leq 0.3$) thick film NTC thermistors, *Journal of the European Ceramic Society*, **26**(6): 909-914, (2006).
- 189 S. Jagtap, S. Rane, S. Gosavi, and D. Amalnerkar, Preparation, characterization and electrical properties of spinel-type environment friendly thick film NTC thermistors, *Journal of the European Ceramic Society*, **28**(13): 2501-2507,

- (2008).
- 190 D. Y. Wang and K. Umeya, Electrical properties of PTCR barium titanate, *Journal of the American Ceramic Society*, **73**(3): 669-677, (1990).
- 191 J. Qi, Z. Gui, Y. Wang, Q. Zhu, Y. Wu, and L. Li, The PTCR effect in BaTiO₃ ceramics modified by donor dopant, *Ceramics International*, **28**(2): 141-143, (2002).
- 192 C. K. Liang and C. C. Tsai, Evaluation of a novel PTC thermistor for telecom overcurrent protection, *Sensors and Actuators a-Physical*, **121**(2): 443-449, (2005).
- 193 S. Jayanthi and T. R. N. Kutty, Effect of segregative additives on the positive temperature coefficient in resistance characteristics of n-BaTiO₃ ceramics, *Journal of Materials Science-Materials in Electronics*, **17**(11): 883-897, (2006).
- 194 T. Shimada, K. Touji, Y. Katsuyama, H. Takeda, and T. Shiosaki, Lead free PTCR ceramics and its electrical properties, *Journal of the European Ceramic Society*, **27**(13-15): 3877-3882, (2007).
- 195 B. Huybrechts, K. Ishizaki, and M. Takata, The positive temperature-coefficient of resistivity in barium titanate, *Journal of Materials Science*, **30**(10): 2463-2474, (1995).
- 196 J. Nowotny and M. Rekas, Positive temperature-coefficient of resistivity for BaTiO₃-based materials, *Ceramics International*, **17**(4): 227-241, (1991).
- 197 E. Brzozowski and M. S. Castro, Conduction mechanism of barium titanate ceramics, *Ceramics International*, **26**(3): 265-269, (2000).
- 198 O. Saburi, Semiconducting bodies in the family of barium titanates, *Journal of the American Ceramic Society*, **44**(2): 54-63, (1961).
- 199 T. Ota and I. Yamai, Positive-temperature-coefficient effect in graphite cristobalite composites, *Journal of the American Ceramic Society*, **75**(7): 1772-1776, (1992).
- 200 D. Lisjak, M. Drogenik, and D. Kolar, Composite ceramics with a positive temperature coefficient of electrical resistivity effect, *Journal of Materials Research*, **15**(2): 417-428, (2000).
- 201 T. R. Shrout, D. Moffatt, and W. Huebner, Composite PTCR thermistors utilizing conducting borides, silicides, and carbide powders, *Journal of Materials Science*, **26**(1): 145-154, (1991).
- 202 S. Hirano and A. Kishimoto, Effect of heating rate on positive-temperature-coefficient-of-resistivity behaviour of conductive composite thin films, *Applied Physics Letters*, **73**(25): 3742-3744, (1998).

- 203 B. C. Hendrix, X. Wang, W. Chen, and W. Q. Cui, Understanding doped V_2O_3 as a functional positive temperature-coefficient material, *Journal of Materials Science-Materials in Electronics*, **3**(2): 113-119, (1992).
- 204 H. R. Kokabi, M. Rapeaux, J. A. Aymami, and G. Desgardin, Electrical characterization of PTC thermistor based on chromium doped vanadium sesquioxide, *Materials Science and Engineering B*, **38**(1-2): 80-89, (1996).
- 205 B. M. Kulwicki, *Advances in Ceramics*. Vol. 1. 1981, Columbus, OH: American Ceramic Society pp.138-139.
- 206 L. A. Xue, Y. Chen, and R. J. Brook, The influence of ionic-radii on the incorporation of trivalent dopants into $BaTiO_3$, *Materials Science and Engineering B-Solid State Materials for Advanced Technology*, **1**(2): 193-201, (1988).
- 207 Y. S. Jung, E. S. Na, U. Paik, J. Lee, and J. Kim, A study on the phase transition and characteristics of rare earth elements doped $BaTiO_3$, *Materials Research Bulletin*, **37**(9): 1633-1640, (2002).
- 208 M. D. Glinchuk, I. P. Bykov, S. M. Kornienko, V. V. Laguta, A. M. Slipenyuk, A. G. Bilous, O. I. V'Yunov, and O. Z. Yanchevskii, Influence of impurities on the properties of rare-earth-doped barium-titanate ceramics, *Journal of Materials Chemistry*, **10**(4): 941-947, (2000).
- 209 O. Saburi, Properties of semiconductive barium titanates, *Journal of the Physical Society of Japan*, **14**: 1159-1174, (1959).
- 210 W. Heywang, Resistivity anomaly in doped barium titanate, *Journal of the American Ceramic Society*, **47**(10): 484-490, (1964).
- 211 W. T. Peria, W. R. Bratschun, and R. D. Fenity, Possible explanation of positive temperature coefficient in resistivity of semiconducting ferroelectrics, *Journal of the American Ceramic Society*, **44**(5): 249-250, (1961).
- 212 G. H. Jonker, Some aspects of semiconducting barium titanate, *Solid-State Electronics* **7**(12): 895-903, (1964).
- 213 H. D. Megaw, Crystal structure of barium titanium oxide and other double oxides of perovskite type, *Trans. Faraday Soc.*, **42A**: 224-31, (1946).
- 214 G. Goodman, Electrical conduction anomaly in samarium doped barium titanate, *Journal of the American Ceramic Society*, **46**(1): 48-54, (1963).
- 215 D. C. Sinclair and A. R. West, Impedance and modulus spectroscopy of semiconducting $BaTiO_3$ showing positive temperature-coefficient of resistance, *Journal of Applied Physics*, **66**(8): 3850-3856, (1989).

- 216 H. M. Alallak, A. W. Brinkman, G. J. Russell, A. W. Roberts, and J. Woods, The effect of donor dopant concentration on the room temperature resistivity of BaTiO₃ ceramics with positive temperature coefficients of resistance, *Journal of Physics D-Applied Physics*, **21**(7): 1226-1233, (1988).
- 217 W. Preis, A. Burgermeister, W. Sitte, and P. Supancic, Bulk and grain boundary resistivities of donor-doped barium titanate ceramics, *Solid State Ionics*, **173**(1-4): 69-75, (2004).
- 218 B. Huybrechts, K. Ishizaki, and M. Takata, Experimental evaluation of the acceptor-states compensation in positive-temperature-coefficient-type barium titanate, *Journal of the American Ceramic Society*, **75**(3): 722-724, (1992).
- 219 M. A. Zubair and C. Leach, Modeling the resistance-temperature characteristic of a positive temperature coefficient thermistor, using experimentally determined permittivity data, *Applied Physics Letters*, **91**(8): Article Number: 082105, (2007).
- 220 T. Miki, A. Fujimoto, and S. Jida, An evidence of trap activation for positive temperature coefficient of resistivity in BaTiO₃ ceramics with substitutional Nb and Mn as impurities, *Journal of Applied Physics*, **83**(3): 1592-1603, (1998).
- 221 A. B. Alles, V. R. W. Amarakoon, and V. L. Burdick, Positive temperature-coefficient of resistivity effect in undoped, atmospherically reduced barium titanate, *Journal of the American Ceramic Society*, **72**(1): 148-151, (1989).
- 222 S. Jiang, D. Zhou, S. Gong, and X. Guan, Effect of heat-treatment under oxygen atmosphere on the electrical properties of BaTiO₃ thermistor, *Microelectronic Engineering*, **66**(1-4): 896-903, (2003).
- 223 N. Hideaki, M. Kenjiro, S. Yukio, and K. Makoto, Influence of Ba/Ti ratio on the positive temperature coefficient of resistivity characteristics of Ca-doped semiconducting BaTiO₃ fired in reducing atmosphere and reoxidized in air, *Journal of the American Ceramic Society*, **90**(6): 1817-1821, (2007).
- 224 J. Daniels, K. H. Hardtl, D. Hennings, and R. Wernicke, Defect chemistry and electrical-conductivity of doped barium titanate ceramics, *Philips Research Reports*, **31**(6): 487-488, (1976).
- 225 G. H. Jonker and E. E. Havinga, The influence of foreign ions on the crystal lattice of barium titanate, *Materials Research Bulletin*, **17**(3): 345-350, (1982).
- 226 H. M. Chan, M. P. Harmer, and D. M. Smyth, Compensating defects in highly donor-doped BaTiO₃, *Journal of the American Ceramic Society*, **69**(6): 507-510,

- (1986).
- 227 M. T. Buscaglia, V. Buscaglia, M. Viviani, and P. Nanni, Atomistic simulation of dopant incorporation in barium titanate, *Journal of the American Ceramic Society*, **84**(2): 376-384, (2001).
- 228 D. M. Smyth, The defect chemistry of donor-doped BaTiO₃: A rebuttal, *Journal of Electroceramics*, **9**(3): 179-186, (2002).
- 229 H. T. Langhammer, M. Drofenik, K. H. Felgner, and H. P. Abicht, Investigation of semiconducting barium titanate ceramics by oxygen coulometry, *Journal of Electroceramics*, **13**(1-3): 793-797, (2004).
- 230 H. T. Langhammer, Q. M. Song, K. H. Felgner, and H. P. Abicht, Investigations on the defect chemistry and the sintering of barium titanate ceramics by oxygen coulometry, *Solid State Sciences*, **4**(2): 197-203, (2002).
- 231 D. Makovec and M. Drofenik, Microstructural changes during the reduction/reoxidation process in donor-doped BaTiO₃ ceramics, *Journal of the American Ceramic Society*, **83**(10): 2593-2599, (2000).
- 232 O. I. V'Yunov, L. L. Kovalenko, A. G. Belous, and V. N. Belyakov, Oxidation of reduced Y-doped semiconducting barium titanate ceramics, *Inorganic Materials*, **41**(1): 87-93, (2005).
- 233 F. D. Morrison, A. M. Coats, D. C. Sinclair, and A. R. West, Charge compensation mechanisms in La-doped BaTiO₃, *Journal of Electroceramics*, **6**(3): 219-232, (2001).
- 234 F. D. Morrison, D. C. Sinclair, and A. R. West, Doping mechanisms and electrical properties of La-doped BaTiO₃ ceramics, *International Journal of Inorganic Materials*, **3**(8): 1205-1210, (2001).
- 235 F. D. Morrison, D. C. Sinclair, and A. R. West, An alternative explanation for the origin of the resistivity anomaly in La-doped BaTiO₃, *Journal of the American Ceramic Society*, **84**(2): 474-476, (2001).
- 236 H. Beltran, E. Cordoncillo, P. Escribano, D. C. Sinclair, and A. R. West, Oxygen loss, semiconductivity, and positive temperature coefficient of resistance behavior in undoped cation-stoichiometric BaTiO₃ ceramics, *Journal of Applied Physics*, **98**(9): Article Number: 094102, (2005).
- 237 D. Makovec, N. Ule, and M. Drofenik, Positive temperature coefficient of resistivity effect in highly donor-doped barium titanate, *Journal of the American Ceramic Society*, **84**(6): 1273-1280, (2001).

- 238 W. Hayes and A. M. Stoneham, *Defects and Defect Processes in Nonmetallic Solids*. 1985, London: John Wiley & Sons, Inc. pp.116-133.
- 239 M. A. Zubair and C. Leach, The effect of SiO₂ addition on the development of low- Σ grain boundaries in PTC thermistors, *Journal of the European Ceramic Society*, **30**(1): 107-112, (2010).
- 240 R. Freer and C. Leach, Local properties of grain boundaries in semiconducting ceramics, *Solid State Ionics*, **173**(1-4): 41-50, (2004).
- 241 F. D. Morrison, D. C. Sinclair, and A. R. West, Characterization of lanthanum-doped barium titanate ceramics using impedance spectroscopy, *Journal of the American Ceramic Society*, **84**(3): 531-538, (2001).
- 242 L. Affleck, J. Seaton, and C. Leach, Characterisation of the R-T response of BaTiO₃ thermistors on three different length scales, *Journal of the European Ceramic Society*, **27**(12): 3439-3444, (2007).
- 243 P. Fiorenza, R. Lo Nigro, P. Delugas, V. Raineri, A. G. Mould, and D. C. Sinclair, Direct imaging of the core-shell effect in positive temperature coefficient of resistance-BaTiO₃ ceramics, *Applied Physics Letters*, **95**(14): article No. 142904, (2009).
- 244 D. Makovec, Z. Samardzija, and M. Drofenik, Solid solubility of holmium, yttrium, and dysprosium in BaTiO₃, *Journal of the American Ceramic Society*, **87**(7): 1324-1329, (2004).
- 245 H. Ueoka, Doping effects of transition-elements on PTC anomaly of semiconductive ferroelectric ceramics, *Ferroelectrics*, **7**(1-4): 351-353, (1974).
- 246 T. Murakami, T. Miyashita, M. Nakahara, and E. Sekine, Effect of rare-earth ions on electrical conductivity of BaTiO₃ ceramics, *Journal of the American Ceramic Society*, **56**(6): 294-297, (1973).
- 247 V. J. Tennery and R. L. Cook, Investigation of rare-earth doped barium titanate, *Journal of the American Ceramic Society*, **44**(4): 187-193, (1961).
- 248 J. G. Stark, *Chemistry Data Book*. 1984, London: John Murray Ltd. pp.28-29.
- 249 J. G. Kim, W. P. Tai, and J. G. Ha, PTCR characteristics and fabrication of porous, Sb-doped BaTiO₃ ceramics, *Journal of Porous Materials*, **10**(1): 69-74, (2003).
- 250 E. Brzozowski, A. C. Caballero, M. Villegas, M. S. Castro, and J. F. Fernandez, Effect of doping method on microstructural and defect profile of Sb-BaTiO₃, *Journal of the European Ceramic Society*, **26**(12): 2327-2336, (2006).

- 251 D. Zhou, M. Cao, and S. Gong, A novel method of preparing $\text{Ba}_{0.96}\text{Ca}_{0.04}\text{Ti}_{1.02}\text{O}_3$ ceramics with low room temperature resistivity, *Materials Science and Engineering B*, **99**(1-3): 399-402, (2003).
- 252 Z. C. Li and B. Bergman, Electrical properties and ageing characteristics of BaTiO_3 ceramics doped by single dopants, *Journal of the European Ceramic Society*, **25**(4): 441-445, (2005).
- 253 F. D. Morrison, D. C. Sinclair, and A. R. West, Electrical and structural characteristics of lanthanum-doped barium titanate ceramics, *Journal of Applied Physics*, **86**(11): 6355-6366, (1999).
- 254 M. Cernea, O. Monnereau, P. Llewellyn, L. Tortet, and C. Galassi, Sol-gel synthesis and characterization of Ce doped- BaTiO_3 , *Journal of the European Ceramic Society*, **26**(15): 3241-3246, (2006).
- 255 Z. A. Nemati, M. Tabibazar, and M. R. Deguire, The effects of cerium doping on the resistivity of PTCR barium lead titanate, *British Ceramic Transactions*, **92**(3): 109-113, (1993).
- 256 S. B. Desu and D. A. Payne, Interfacial segregation in perovskites: 3. microstructure and electrical properties, *Journal of the American Ceramic Society*, **73**(11): 3407-3415, (1990).
- 257 Z. C. Li, H. Zhang, X. D. Zou, and B. Bergman, Synthesis of Sm-doped BaTiO_3 ceramics and characterization of a secondary phase, *Materials Science and Engineering B-Solid State Materials for Advanced Technology*, **116**(1): 34-39, (2005).
- 258 N. Motohira, H. Okamoto, Y. Nakamura, A. Kishimoto, M. Miyayama, and H. Yanagida, Single crystal growth and electrical properties of lanthanum- and gadolinium-doped BaTiO_3 , *Journal of the Ceramic Society of Japan*, **104**(4): 273-276, (1996).
- 259 H. Y. Miao, M. Dong, G. Q. Tan, and Y. P. Pu, Doping effects of Dy and Mg on BaTiO_3 ceramics prepared by hydrothermal method, *Journal of Electroceramics*, **16**(4): 297-300, (2006).
- 260 W. H. Lee, W. A. Groen, H. Schreinemacher, and D. Hennings, Dysprosium doped dielectric materials for sintering in reducing atmospheres, *Journal of Electroceramics*, **5**(1): 31-36, (2000).
- 261 A. Al-Shahrani and S. Abboudy, Positive temperature coefficient in Ho-doped BaTiO_3 ceramics, *Journal of Physics and Chemistry of Solids*, **61**(6): 955-959, (2000).

- 262 F. G. Chang, T. Li, Y. X. Ge, Z. P. Chen, Z. S. Liu, and X. P. Jing, Electrical properties and positron annihilation study of $(\text{Ba}_{1-x}\text{Ho}_x)\text{TiO}_3$ ceramics, *Journal of Materials Science*, **42**(17): 7109-7115, (2007).
- 263 S. K. Jo, Y. H. Han, and K. H. Choi, Effects of oxygen partial pressure control on the microstructure and PTCR properties of Ho doped BaTiO_3 , *Journal of Materials Science*, **42**(16): 6696-6700, (2007).
- 264 Y. Liu and A. R. West, Ho-doped BaTiO_3 : Polymorphism, phase equilibria and dielectric properties of $\text{BaTi}_{1-x}\text{Ho}_x\text{O}_{3-x/2}$: $0 \leq x \leq 0.17$, *Journal of the European Ceramic Society*, **29**(15): 3249-3257, (2009).
- 265 M. Viviani, M. T. Buscaglia, V. Buscaglia, L. Mitoseriu, A. Testino, P. Nanni, and D. Vladikova, Analysis of conductivity and PTCR effect in Er-doped BaTiO_3 ceramics, *Journal of the European Ceramic Society*, **24**(6): 1221-1225, (2004).
- 266 M. T. Buscaglia, M. Viviani, V. Buscaglia, C. Bottino, and P. Nanni, Incorporation of Er^{3+} into BaTiO_3 , *Journal of the American Ceramic Society*, **85**(6): 1569-1575, (2002).
- 267 D. J. Wang, Z. L. Gui, and L. T. Li, Preparation and electrical properties of semiconducting strontium-lead titanate PTCR ceramics, *Journal of Materials Science-Materials in Electronics*, **8**(4): 271-276, (1997).
- 268 S. W. Ding, G. Jia, J. Wang, and Z. Y. He, Electrical properties of Y- and Mn-doped BaTiO_3 -based PTC ceramics, *Ceramics International*: 321, (2007).
- 269 J. Zhi, A. Chen, Y. Zhi, P. M. Vilarinho, and J. L. Baptista, Incorporation of yttrium in barium titanate ceramics, *Journal of the American Ceramic Society*, **82**(5): 1345-1348, (1999).
- 270 Y. Wang, L. Li, J. Qi, and Z. Gui, Ferroelectric characteristics of ytterbium-doped barium zirconium titanate ceramics, *Ceramics International*, **28**(6): 657-661, (2002).
- 271 W. H. Tzing and W. H. Tuan, Effect of NiO addition on the sintering and grain growth behaviour of BaTiO_3 , *Ceramics International*, **25**(1): 69-75, (1999).
- 272 H. T. Langhammer, T. Müller, R. Böttcher, V. Mueller, and H. P. Abicht, Copper-doped hexagonal barium titanate ceramics, *Journal of the European Ceramic Society*, **24**(6): 1489-1492, (2004).
- 273 S. H. Yoon, K. H. Lee, and H. Kim, Effect of acceptors on the segregation of donors in niobium-doped barium titanate positive temperature coefficient resistors, *Journal of the American Ceramic Society*, **83**(10): 2463-2472, (2000).

- 274 G. Er, S. Ishida, and N. Takeuchi, Durability of Nb-(Fe,Mn)-codoped PTCR BaTiO₃ ceramics to reducing atmosphere, *Journal of the Ceramic Society of Japan*, **106**(5): 470-476, (1998).
- 275 B. Cui, P. Yu, J. Tian, and Z. Chang, Preparation and characterization of Co-doped BaTiO₃ nanosized powders and ceramics, *Materials Science and Engineering: B*, **133**(1-3): 205-208, (2006).
- 276 D. K. Lee, H. I. Yoo, and K. D. Becker, Nonstoichiometry and defect structure of Mn-doped BaTiO_{3-δ}, *Solid State Ionics*, **154**: 189-193, (2002).
- 277 J. H. Lee, S. H. Kim, and S. H. Cho, Valence change of Mn ions in BaTiO₃-based PTCR materials, *Journal of the American Ceramic Society*, **78**(10): 2845-2848, (1995).
- 278 O. I. V'Yunov, L. L. Kovalenko, and A. G. Belous, Electrical properties of BaTi_{1-x}M_xO₃ (M= Nb, Ta, Mo, W) ceramics, *Inorganic Materials*, **42**(12): 1363-1368, (2006).
- 279 N. Maso, H. Beltran, E. Cordoncillo, A. A. Flores, P. Escribano, D. C. Sinclair, and A. R. West, Synthesis and electrical properties of Nb-doped BaTiO₃, *Journal of Materials Chemistry*, **16**(30): 3114-3119, (2006).
- 280 X. Wang, H. L. W. Chan, and C. Choy, Positive temperature coefficient of resistivity effect in niobium-doped barium titanate ceramics obtained at low sintering temperature, *Journal of the European Ceramic Society*, **24**(6): 1227-1231, (2004).
- 281 N. Maso, H. Beltran, E. Cordoncillo, D. C. Sinclair, and A. R. West, Polymorphism and dielectric properties of Nb-doped BaTiO₃, *Journal of the American Ceramic Society*, **91**(1): 144-150, (2008).
- 282 M. T. Buscaglia, V. Buscaglia, M. Viviani, and P. Nanni, Atomistic simulation of dopant incorporation in barium titanate, *Journal of the American Ceramic Society*, **84**(2): 376-84, (2001).
- 283 Y. Tsur, T. D. Dunbar, and C. A. Randall, Crystal and defect chemistry of rare earth cations in BaTiO₃, *Journal of Electroceramics*, **7**(1): 25-34, (2001).
- 284 T. D. Dunbar, W. L. Warren, B. A. Tuttle, C. A. Randall, and Y. Tsur, Electron paramagnetic resonance investigations of lanthanide-doped barium titanate: dopant site occupancy, *Journal of Physical Chemistry B*, **108**(3): 908-917, (2004).
- 285 D. Makovec, Z. Samardzija, and M. Drogenik, The solid solubility of holmium in BaTiO₃ under reducing conditions, *Journal of the American Ceramic Society*, **89**(10): 3281-3284, (2006).

- 286 S. B. Desu and D. A. Payne, Interfacial segregation in perovskites: 2. experimental evidence, *Journal of the American Ceramic Society*, **73**(11): 3398-3406, (1990).
- 287 S. B. Desu and D. A. Payne, Interfacial segregation in perovskites: 4. internal boundary layer devices, *Journal of the American Ceramic Society*, **73**(11): 3416-3421, (1990).
- 288 C. J. Peng and H. Y. Lu, Compensation effect in semiconducting barium titanate, *Journal of the American Ceramic Society*, **71**(1): C44-C46, (1988).
- 289 C. J. Ting, C. J. Peng, H. Y. Lu, and S. T. Wu, Lanthanum-magnesium and lanthanum-manganese donor-acceptor-codoped semiconducting barium titanate, *Journal of the American Ceramic Society*, **73**(2): 329-334, (1990).
- 290 J. Seaton and C. Leach, Local property measurement in PTC thermistors, *Acta Materialia*, **51**(20): 6027-6034, (2003).
- 291 P.-J. Wang, Z.-Q. Zeng, Z.-L. Gui, and L.-T. Li, Strontium-lead titanate ceramics with positive temperature coefficient of resistance, *Materials Letters*, **30**(4): 275-277, (1997).
- 292 J. Zhao, L. Li, and Z. Gui, A study of V-shaped PTC behaviour of $\text{Sr}_{0.4}\text{Pb}_{0.6}\text{TiO}_3$ ceramics, *Journal of the European Ceramic Society*, **22**(7): 1171-1175, (2002).
- 293 J. Zhao, L. Li, and Z. Gui, Influence of lithium modification on the properties of Y-doped $\text{Sr}_{0.5}\text{Pb}_{0.5}\text{TiO}_3$ thermistors, *Sensors and Actuators A: Physical*, **95**(1): 46-50, (2001).
- 294 C. Chou, H. Chang, I. Lin, and B. Shaw, Microscopic examination of the microwave sintered $(\text{Pb}_{0.6}\text{Sr}_{0.4})\text{TiO}_3$ positive-temperature-coefficient resistor materials, *Japanese Journal of Applied Physics* **37**: 5269-5272, (1998).
- 295 D. Völtzke, H. P. Abicht, E. Pippel, and J. Woltersdorf, Ca-containing additives in PTC- BaTiO_3 ceramics: effects on the microstructural evolution, *Journal of the European Ceramic Society*, **20**(11): 1663-1669, (2000).
- 296 S. Anwar, P. R. Sagdeo, and N. P. Lalla, Ferroelectric relaxor behavior in hafnium doped barium-titanate ceramic, *Solid State Communications*, **138**(7): 331-336, (2006).
- 297 M. Kumar, A. Garg, R. Kumar, and M. C. Bhatnagar, Structural, dielectric and ferroelectric study of $\text{Ba}_{0.9}\text{Sr}_{0.1}\text{Zr}_x\text{Ti}_{1-x}\text{O}_3$ ceramics prepared by the sol-gel method, *Physica B-Condensed Matter*, **403**(10-11): 1819-1823, (2008).

- 298 S. G. Lu, Z. K. Xu, and H. Chen, Tunability and relaxor properties of ferroelectric barium stannate titanate ceramics, *Applied Physics Letters*, **85**(22): 5319-5321, (2004).
- 299 Z. Yu, C. Ang, R. Y. Guo, and A. S. Bhalla, Ferroelectric-relaxor behavior of Ba(Ti_{0.7}Zr_{0.3})O₃ ceramics, *Journal of Applied Physics*, **92**(5): 2655-2657, (2002).
- 300 V. V. Shvartsman, W. Kleemann, J. Dec, Z. K. Xu, and S. G. Lu, Diffuse phase transition in BaTi_{1-x}Sn_xO₃ ceramics: An intermediate state between ferroelectric and relaxor behavior, *Journal of Applied Physics*, **99**(12): Article Number: 124111, (2006).
- 301 N. H. Chan and D. M. Smyth, Defect chemistry of donor-doped BaTiO₃, *Journal of the American Ceramic Society*, **67**(4): 285-288, (1984).
- 302 F. A. Selmi and V. R. W. Amarakoon, Sol-gel coating of powders for processing electronic ceramics, *Journal of the American Ceramic Society*, **71**(11): 934-937, (1988).
- 303 M. Viviani, P. Nanni, M. T. Buscaglia, M. Leoni, V. Buscaglia, and L. Centurioni, Impedance spectroscopy of n-doped (Ba,Sr)TiO₃ ceramics prepared by modified low temperature aqueous synthesis, *Journal of the European Ceramic Society*, **19**(6-7): 781-785, (1999).
- 304 H. Yaseen, S. Baltianski, and Y. Tsur, Effect of incorporating method of niobium on the properties of doped barium titanate ceramics, *Journal of the American Ceramic Society*, **89**(5): 1584-1589, (2006).
- 305 B. Cui, P. Yu, J. Tian, H. Guo, and Z. Chang, Preparation and characterization of niobium-doped barium titanate nanocrystalline powders and ceramics, *Materials Science and Engineering: A*, **454-455**: 667-672, (2007).
- 306 V. N. Shut, S. V. Kostomarov, and A. V. Gavrilov, PTCR ceramics produced from oxalate-derived barium titanate, *Inorganic Materials*, **44**(8): 905-910, (2008).
- 307 N. Mukherjee, R. D. Roseman, and Q. Zhang, Sintering behavior and PTCR properties of stoichiometric blend BaTiO₃, *Journal of Physics and Chemistry of Solids*, **63**(4): 631-638, (2002).
- 308 B. K. Park, J. H. Lee, D. Y. Kim, and N. M. Hwang, Positive temperature coefficient of resistance effect in heavily niobium-doped barium titanate by the growth of the double-twinned seeds, *Journal of the American Ceramic Society*, **84**(11): 2707-2709, (2001).
- 309 J. Qi, Z. Gui, Y. Wu, and L. Li, Positive temperature coefficient resistance

- effect in $\text{Ba}_{1-x}\text{Sr}_x\text{TiO}_3$ ceramics modified with Bi_2O_3 and PbO by vapour doping method, *Journal of Materials Research*, **14**(8): 3328-29, (1999).
- 310 S. Chatterjee and H. S. Maiti, A novel method of doping PTC thermistor sensor elements during sintering through diffusion by vapour phase, *Materials Chemistry and Physics*, **67**(1-3): 294-297, (2001).
- 311 J. Qi, Z. Gui, Q. Zhu, Y. Wang, Y. Wu, and L. Li, Doping behavior of CdO in BaTiO_3 -based PTCR ceramics, *Sensors and Actuators A: Physical*, **100**(2-3): 244-246, (2002).
- 312 J. Qi, Z. Gui, Y. Wu, and L. Li, Influence of manganese on PTCR effect in BaTiO_3 -based ceramics doped with Bi_2O_3 vapour, *Materials Chemistry and Physics*, **73**(1): 97-100, (2002).
- 313 S. R. Syrtsov, V. N. Shut, and I. F. Kashevich, Positive temperature coefficient of resistivity in thin films of barium titanate, *Materials Science in Semiconductor Processing*, **5**: 223-225, (2003).
- 314 L. Yan, H. B. Lu, Z. H. Chen, S. Y. Dai, Y. L. Zhou, and G. Z. Yang, Characteristics of $\text{BaNb}_x\text{Ti}_{1-x}\text{O}_3$ thin films grown by laser molecular beam epitaxy, *Journal of Crystal Growth*, **244**(3-4): 225-228, (2002).
- 315 N. Lemee, C. Dubourdieu, G. Delabouglise, J. P. Senateur, and F. Laroudie, Semiconductive Nb-doped BaTiO_3 films grown by pulsed injection metalorganic chemical vapor deposition, *Journal of Crystal Growth*, **235**(1-4): 347-351, (2002).
- 316 D. Nagano, H. Funakubo, K. Shinozaki, and N. Mizutani, Electrical properties of semiconductive Nb-doped BaTiO_3 thin films prepared by metal-organic chemical-vapor deposition, *Applied Physics Letters*, **72**(16): 2017-2019, (1998).
- 317 Y. Shao, R. A. Hughes, A. Dabkowski, G. Radtke, W. H. Gong, J. S. Preston, and G. A. Botton, Structural and transport properties of epitaxial niobium-doped BaTiO_3 films, *Applied Physics Letters*, **93**(19): 3, (2008).
- 318 E. Arveux, S. Payan, M. Maglione, and A. Klein, Surface segregation in Nb-doped BaTiO_3 films, *Applied Surface Science*, **256**(21): 6228-6232, (2010).
- 319 S. Chatterjee, K. Sengupta, and H. S. Maiti, A miniature PTC thermistor based sensor element fabricated by tape casting technique, *Sensors and Actuators B: Chemical*, **60**(2-3): 155-160, (1999).
- 320 D. Zhou, Z. Zheng, S. Gong, G. Huang, and Y. Hu, The influence of shaping process on microstructure and properties of BaTiO_3 -based chip thermistors, *Ceramics International*, **32**(7): 839-842, (2006).

- 321 H. A. Sauer and J. R. Fisher, Processing of positive temperature coefficient thermistors, *Journal of the American Ceramic Society*, **43**(6): 297-301, (1960).
- 322 J. B. MacChesney and J. F. Potter, Factors and mechanisms affecting the positive temperature coefficient of resistivity of barium titanate, *Journal of the American Ceramic Society*, **48**(2): 81-88, (1965).
- 323 B. C. LaCourse and V. R. W. Amarakoon, Characterization of the firing schedule for positive temperature coefficient of resistance BaTiO₃, *Journal of the American Ceramic Society*, **78**(12): 3352-3356, (1995).
- 324 D. C. Sinclair and A. R. West, Effect of atmosphere on the PTCR properties of BaTiO₃ ceramics, *Journal of Materials Science*, **29**(23): 6061-6068, (1994).
- 325 M. Ozawa and S. Suzuki, Influence of heat treatment with nitrogen in positive-temperature-coefficient-type BaTiO₃, *Journal of Materials Science Letters*, **16**(7): 545-546, (1997).
- 326 M. Kuwabara, H. Matsuda, N. Kurata, and E. Matsuyama, Shift of the curie point of barium titanate ceramics with sintering temperature, *Journal of the American Ceramic Society*, **80**(10): 2590-2596, (1997).
- 327 R. N. Basu and H. S. Maiti, Effect of sintering time on the resistivity of semiconducting BaTiO₃ ceramics, *Materials Letters*, **5**(3): 99-102, (1987).
- 328 M. Kahn, Effect of heat-treatment on PTCR anomaly in semiconducting barium titanate, *American Ceramic Society Bulletin*, **50**(8): 676-677, (1971).
- 329 M. A. Zubair and C. Leach, The influence of cooling rate and SiO₂ additions on the grain boundary structure of Mn-doped PTC thermistors, *Journal of the European Ceramic Society*, **28**(9): 1845-1855, (2008).
- 330 M. A. Zubair and C. Leach, Modeling the effect of SiO₂ additions and cooling rate on the electrical behavior of donor-acceptor codoped positive temperature coefficient thermistors, *Journal of Applied Physics*, **103**(12): Article Number:123713, (2008).
- 331 P. Bomlai, N. Sirikulrat, and T. Tunkasiri, Effect of heating rate on the properties of Sb and Mn-doped barium strontium titanate PTCR ceramics, *Materials Letters*, **59**(1): 118-122, (2005).
- 332 G. S. Liu and R. D. Roseman, Secondary thermal treatment effect on PTCR BaTiO₃, *Journal of Materials Science Letters*, **18**(22): 1875-1878, (1999).
- 333 S. Jida, T. Suemasu, and T. Miki, Effect of microwave heating on BaTiO₃ : Nb ceramics with positive temperature coefficient of resistivity, *Journal of Applied*

- Physics*, **86**(4): 2089-2094, (1999).
- 334 T.-F. Lin, C.-T. Hu, and I. N. Lin, Influence of stoichiometry on the microstructure and positive temperature coefficient of resistivity of semiconducting barium titanate ceramics, *Journal of the American Ceramic Society*, **73**(3): 531-536, (1990).
- 335 P. Knauth, Ionic and electronic conduction in nanostructured solids: Concepts and concerns, consensus and controversies, *Solid State Ionics*, **177**: 2495-2502, (2006).
- 336 J. Daniels, K. H. Hardtl, and R. Wernicke, PTC effect of barium titanate, *Philips Technical Review*, **38**(3): 73-82, (1979).
- 337 B. D. Begg, E. R. Vance, and J. Nowotny, Effect of particle size on the room-temperature crystal structure of barium titanate, *Journal of the American Ceramic Society*, **77**(12): 3186-3192, (1994).
- 338 M. Yashima, T. Hoshina, D. Ishimura, S. Kobayashi, W. Nakamura, T. Tsurumi, and S. Wada, Size effect on the crystal structure of barium titanate nanoparticles, *Journal of Applied Physics*, **98**(1): Article Number: 014313, (2005).
- 339 M. B. Park, N. H. Cho, C. D. Kim, and S. K. Lee, Phase transition and physical characteristics of nanograined BaTiO₃ ceramics synthesized from surface-coated nanopowders, *Journal of the American Ceramic Society*, **87**(3): 510-512, (2004).
- 340 C. S. Hwang, B. T. Lee, H. J. Cho, K. H. Lee, C. S. Kang, H. Hideki, S. I. Lee, and M. Y. Lee, A positive temperature coefficient of resistivity effect from a paraelectric Pt/(Ba_{0.5}Sr_{0.5})TiO₃/IrO₂ thin-film capacitor, *Applied Physics Letters*, **71**(3): 371-373, (1997).
- 341 W. F. Qin, J. Zhu, J. Xiong, J. L. Tang, W. J. Jie, X. H. Wei, Y. Zhang, and Y. R. Li, Electrical behavior of Y-doped Ba_{0.6}Sr_{0.4}TiO₃ thin films, *Journal of Materials Science-Materials in Electronics*, **18**(12): 1217-1220, (2007).
- 342 M. Okano, Y. Watanabe, and S. W. Cheong, Nonlinear positive temperature coefficient of resistance of BaTiO₃ film, *Applied Physics Letters*, **82**(12): 1923-1925, (2003).
- 343 M. Kuwabara, Effect of microstructure on the PTCR effect in semiconducting barium titanate ceramics, *Journal of the American Ceramic Society*, **64**(11): 639-644, (1981).
- 344 R. D. Roseman and N. Mukherjee, PTCR effect in BaTiO₃: Structural aspects

- and grain boundary potentials, *Journal of Electroceramics*, **10**(2): 117-135, (2003).
- 345 D. L. Zhang, D. X. Zhou, S. L. Jiang, X. Wang, and S. P. Gong, Effects of porosity on the electrical characteristics of current-limiting BaTiO₃-based positive-temperature-coefficient (PTC) ceramic thermistors coated with electroless nickel-phosphorous electrode, *Sensors and Actuators a-Physical*, **112**(1): 94-100, (2004).
- 346 J.-G. Kim, Synthesis of porous (Ba,Sr)TiO₃ ceramics and PTCR characteristics, *Materials Chemistry and Physics*, **78**(1): 154-159, (2002).
- 347 A. Hasegawa, S. Fujitsu, K. Koumoto, and H. Yanagida, The enhanced penetration of oxygen along the grain-boundary in semiconducting barium titanate, *Japanese Journal of Applied Physics*, **30**(6): 1252-1255, (1991).
- 348 G. S. Liu and R. D. Roseman, Effect of BaO and SiO₂ addition on PTCR BaTiO₃ ceramics, *Journal of Materials Science*, **34**(18): 4439-4445, (1999).
- 349 M. Drofenik, D. Makovec, I. Zajc, and H. T. Langhammer, Anomalous grain growth in donor-doped barium titanate with excess barium oxide, *Journal of the American Ceramic Society*, **85**(3): 653-660, (2002).
- 350 Z. He, J. Ma, Y. Qu, and X. Feng, Effect of additives on the electrical properties of a (Ba_{0.92}Sr_{0.08})TiO₃-based positive temperature coefficient resistor, *Journal of the European Ceramic Society*, **22**(13): 2143-2148, (2002).
- 351 Z. M. He, J. Ma, Y. F. Qu, and C. G. Wang, Compositional and processing effects on electrical properties of (Ba_{0.85}Pb_{0.15})TiO₃-based positive temperature coefficient resistors, *Journal of the European Ceramic Society*, **24**(14): 3617-3622, (2004).
- 352 H. Mimi, K. Mihara, Y. Sakabe, and M. Kuwabara, Preparation of multilayer semiconducting BaTiO₃ ceramics co-fired with Ni inner electrodes, *Japanese Journal of Applied Physics Part 1-Regular Papers Brief Communications & Review Papers*, **46**(10A): 6715-6718, (2007).
- 353 A. Kanda, S. Tashiro, and H. Igarashi, Effect of firing atmosphere on electrical properties of multilayer semiconducting ceramics having positive temperature coefficient of resistivity and Ni-Pd internal electrodes, *Japanese Journal of Applied Physics*, **33**: 5431-5434, (1994).
- 354 H. Takeda, W. Aoto, and T. Shiosaki, BaTiO₃-(Bi_{1/2}Na_{1/2})TiO₃ solid-solution semiconducting ceramics with T_c > 130°C, *Applied Physics Letters*, **87**(10): Article Number: 102104, (2005).
- 355 B. J. Chu, D. R. Chen, G. R. Li, and Q. R. Yin, Electrical properties of

- $\text{Na}_{1/2}\text{Bi}_{1/2}\text{TiO}_3\text{-BaTiO}_3$ ceramics, *Journal of the European Ceramic Society*, **22**(13): 2115-2121, (2002).
- 356 P. h. Xiang, H. Harinaka, H. Takeda, T. Nishida, K. Uchiyama, and T. Shiosaki, Annealing effects on the characteristics of high T_c lead-free barium titanate-based positive temperature coefficient of resistivity ceramics, *Journal of Applied Physics*, **104**(9): Article Number: 094108, (2008).
- 357 P. H. Xiang, H. Takeda, and T. Shiosaki, Characterization of manganese-doped $\text{BaTiO}_3\text{-(Bi}_{1/2}\text{Na}_{1/2})\text{TiO}_3$ positive temperature coefficient of resistivity ceramics using impedance spectroscopy, *Journal of Applied Physics*, **103**(6): Article Number: 064102, (2008).
- 358 J. F. Wei, Y. P. Pu, Y. Q. Mao, and J. F. Wang, Effect of the Reoxidation on Positive Temperature Coefficient Behavior of $\text{BaTiO}_3\text{-Bi}_{0.5}\text{Na}_{0.5}\text{TiO}_3$, *Journal of the American Ceramic Society*, **93**(6): 1527-1529, (2010).
- 359 S. L. Leng, G. R. Li, L. Y. Zheng, T. B. Wang, and Q. R. Yin, Synthesis of Y-doped $\text{BaTiO}_3\text{-(Bi}_{1/2}\text{K}_{1/2})\text{TiO}_3$ lead-free positive temperature coefficient of resistivity ceramics and their PTC effects, *Journal of the American Ceramic Society*, **92**(11): 2772-2775, (2009).
- 360 H. Takeda, H. Harinaka, T. Shiosaki, M. A. Zubair, C. Leach, R. Freer, T. Hoshina, and T. Tsurumi, Fabrication and positive temperature coefficient of resistivity properties of semiconducting ceramics based on the $\text{BaTiO}_3\text{-(Bi}_{1/2}\text{K}_{1/2})\text{TiO}_3$ system, *Journal of the European Ceramic Society*, **30**(2): 555-559, (2010).
- 361 R. L. Brutchey, G. S. Cheng, Q. Gu, and D. E. Morse, Positive temperature coefficient of resistivity in donor-doped BaTiO_3 ceramics derived from nanocrystals synthesized at low temperature, *Advanced Materials*, **20**(5): 1029-1032, (2008).
- 362 Z. Cai, X. Li, Q. Hu, and X. Zeng, Laser sintering of thick-film PTC thermistor paste deposited by micro-pen direct-write technology, *Microelectronic Engineering*, **86**(1): 10-15, (2009).
- 363 L. M. McDowellboyer, J. R. Hunt, and N. Sitar, Particle-transport through porous-media, *Water Resources Research*, **22**(13): 1901-1921, (1986).
- 364 D. Or, Scaling of capillary, gravity and viscous forces affecting flow morphology in unsaturated porous media, *Advances in Water Resources*, **31**(9): 1129-1136, (2008).
- 365 Y. Zevi, A. Dathe, J. F. McCarthy, B. K. Richards, and T. S. Steenhuis,

- Distribution of colloid particles onto interfaces in partially saturated sand, *Environmental Science & Technology*, **39**(18): 7055-7064, (2005).
- 366 R. J. Glass, J. R. Brainard, and T. C. J. Yeh, Infiltration in unsaturated layered fluvial deposits at Rio Bravo: Macroscopic anisotropy and heterogeneous transport, *Vadose Zone Journal*, **4**(1): 22-31, (2005).
- 367 G. Wagner, A. Birovljev, P. Meakin, J. Feder, and T. Jossang, Fragmentation and migration of invasion percolation clusters: Experiments and simulations, *Physical Review E*, **55**(6): 7015-7029, (1997).
- 368 Y. Meheust, G. Lovoll, K. J. Maloy, and J. Schmittbuhl, Interface scaling in a two-dimensional porous medium under combined viscous, gravity, and capillary effects, *Physical Review E*, **66**(5): 12, (2002).
- 369 E. Aker, K. J. Maloy, and A. Hansen, Dynamics of stable viscous displacement in porous media, *Physical Review E*, **61**(3): 2936-2946, (2000).
- 370 S. J. Ianson and W. D. Hoff, Water-movement in porous building materials 8. effects of evaporative drying on height of capillary rise equilibrium in walls, *Building and Environment*, **21**(3-4): 195-200, (1986).
- 371 I. Ioannou, C. Hall, M. A. Wilson, W. D. Hoff, and M. A. Carter, Direct measurement of the wetting front capillary pressure in a clay brick ceramic, *Journal of Physics D-Applied Physics*, **36**(24): 3176-3182, (2003).
- 372 R. K. Holman, M. J. Cima, S. A. Umland, and E. Sachs, Spreading and infiltration of inkjet-printed polymer solution droplets on a porous substrate, *Journal of Colloid and Interface Science*, **249**(2): 432-440, (2002).
- 373 G. Desie, G. Deroover, F. De Voeght, and A. Soucemarianadin, Printing of dye and pigment-based aqueous inks onto porous substrates, *Journal of Imaging Science and Technology*, **48**(5): 389-397, (2004).
- 374 R. Somasundaram, R. Kanagaraj, and P. Kalakkath, Dynamic characteristics of drop-substrate Interactions in direct ceramic ink-jet printing using high speed imaging system, *Defence Science Journal*, **59**(6): 675-682, (2009).
- 375 W. C. Tu and F. F. Lange, Liquid precursor infiltration processing of powder compacts .1. Kinetic studies and microstructure development, *Journal of the American Ceramic Society*, **78**(12): 3277-3282, (1995).
- 376 J. G. Duh and J. U. Wan, Liquid infiltration in ZrO₂ ceramics, *Journal of Materials Science Letters*, **12**(7): 473-475, (1993).
- 377 S. J. Glass and D. J. Green, Surface modification of ceramics by partial

- infiltration, *Advanced Ceramic Materials*, **2**(2): 129-131, (1987).
- 378 S. Pratapa, I. M. Low, and B. H. O'Connor, Infiltration-processed, functionally graded aluminium titanate zirconia-alumina composite - Part I - Microstructural characterization and physical properties, *Journal of Materials Science*, **33**(12): 3037-3045, (1998).
- 379 A. Zadrazil, F. Stepanek, and O. K. Matar, Droplet spreading, imbibition and solidification on porous media, *Journal of Fluid Mechanics*, **562**: 1-33, (2006).
- 380 R. Lenormand, Liquids in porous-media, *Journal of Physics: Condensed Matter* **2**: SA79-SA88, (1990).
- 381 N. C. Wardlaw and Y. Li, Fluid topology, pore-size and aspect ratio during imbibition, *Transport in Porous Media*, **3**(1): 17-34, (1988).
- 382 E. L. Hinrichsen, K. J. Maloy, J. Feder, and T. Jossang, Self-similarity and structure of DLA and viscous fingering clusters, *Journal of Physics a-Mathematical and General*, **22**(7): L271-L277, (1989).
- 383 P. Meakin, J. Feder, V. Frette, and T. Jossang, Invasion percolation in a destabilizing gradient, *Physical Review A*, **46**(6): 3357-3368, (1992).
- 384 M. J. Blunt and H. Scher, Pore-level modeling of wetting, *Physical Review E*, **52**(6): 6387-6403, (1995).
- 385 N. Alleborn and H. Raszillier, Spreading and sorption of a droplet on a porous substrate, *Chemical Engineering Science*, **59**(10): 2071-2088, (2004).
- 386 V. M. Starov, S. R. Kostvintsev, V. D. Sobolev, M. G. Velarde, and S. A. Zhdanov, Spreading of liquid drops over dry porous layers: Complete wetting case, *Journal of Colloid and Interface Science*, **252**(2): 397-408, (2002).
- 387 V. M. Starov, S. A. Zhdanov, and M. G. Velarde, Spreading of liquid drops over thick porous layers: Complete wetting case, *Langmuir*, **18**(25): 9744-9750, (2002).
- 388 W. C. Tu and F. F. Lange, Liquid precursor infiltration processing of powder compacts .2. Fracture toughness and strength, *Journal of the American Ceramic Society*, **78**(12): 3283-3289, (1995).
- 389 R. J. Darby, I. Farnan, and R. V. Kumar, Method for making minor dopant additions to porous ceramics, *Advances in Applied Ceramics*, **108**(8): 506-508, (2009).
- 390 G. D. Parfitt, *Dispersion of powders in liquids with special reference to pigments*. 1969, Amsterdam: Elsevier. pp.165-200.

- 391 P. Pei, D. Minor, and G. Y. Onoda, *Laboratory techniques for bulk density measurement*, in *Advances in Process Measurements for the Ceramic Industry*, A. Jilavenkatesa and G.Y. Onada, Editors. 1999, The American Ceramic Society: Westerville. pp. 293-306.
- 392 P. J. Goodhew, J. Humphreys, and R. Beanland, *Electron Microscopy and Analysis*. 2001, London: Taylor & Francis Inc.
- 393 F. D. Morrison, *Synthesis and electrical characterisation of lanthanum doped barium titanate*. 1999, PhD dissertation, University of Aberdeen: Aberdeen. pp. 34-35.
- 394 S. Urek, M. Drofenik, and D. Makovec, Sintering and properties of highly donor-doped barium titanate ceramics, *Journal of Materials Science*, **35**(4): 895-901, (2000).
- 395 M. M. Mohebi, *An ink-jet printer for ceramic combinatorial libraries and functional gradients*. 2003, PhD dissertation, Queen Mary, University of London: London. pp. 183-187.
- 396 L. Bergstrom, Colloidal processing of a very fine BaTiO₃ powder-Effect of particle interactions on the suspension properties, consolidation and sintering behavior, *Journal of the American Ceramic Society*, **80**(2): 291-300, (1997).
- 397 S. Mizuta, M. Parish, and H. K. Bowen, Dispersion of BaTiO₃ powders (part I), *Ceramic International*, **10**(2): 43-48, (1984).
- 398 J. A. Bzdawka and D. T. Haworth, The dispersion of barium titanium oxide in water and methylisobutylketone, *Journal of Dispersion Science and Technology*, **1**(3): 323-340, (1980).
- 399 Z. Chen, T. A. Ring, and J. Lemaitre, Stabilization and processing of aqueous BaTiO₃ suspension with polyacrylic acid, *Journal of the American Ceramic Society*, **75**(12): 3201-208, (1992).
- 400 S. Bhattacharjee, M. K. Pria, and H. S. Maiti, Polyvinyl butyral as a dispersant for barium titanate in a non-aqueous suspension, *Journal of Materials Science*, **28**: 6490-495, (1993).
- 401 A. W. M. L. De and W. P. T. Derks, Colloidal stabilization of BaTiO₃ with poly(vinyl alcohol) in water, *Colloids and Surfaces A*, **71**: 147-153, (1993).
- 402 R. Blanco-Lopez and F. L. Riley, Polymeric stabilization of aqueous suspensions barium titanate. Part I: Effect of pH., *Journal of the European Ceramic Society*, **20**: 1579-1586, (2000).

- 403 R. Blanco-Lopez and F. L. Riley, Polymeric stabilization of aqueous suspensions barium titanate. Part II: Effect of polyelectrolyte concentration, *Journal of the European Ceramic Society*, **20**: 1587-1594, (2000).
- 404 J.-H. Jean and H.-R. Wang, Effect of solids loading, pH, and polyelectrolyte addition on the stabilization of concentrated aqueous BaTiO₃ suspensions, *Journal of the American Ceramic Society*, **83**(2): 277-80, (2000).
- 405 H. Rashid, B. Y. Tay, and M. J. Edirisinghe, Dispersion of ceramic ink using an ultrasonic disruptor, *Journal of Materials Science Letters*, **19**(9): 799-801, (2000).
- 406 Z.-G. Shen, J.-F. Chen, H.-k. Zou, and J. Yun, Dispersion of nanosized aqueous suspensions of barium titanate with ammonium polyacrylate, *Journal of Colloid and Interface Science*, **275**: 158-164, (2004).
- 407 L. Guo, Y. Zhang, N. Uchida, and K. Uematsu, Adsorption effects on the rheological properties of aqueous alumina suspensions with polyelectrolyte, *Journal of the American Ceramic Society*, **81**(3): 549-556, (1998).
- 408 Y. Zhang, L. F. Chen, S. F. Yang, and J. R. G. Evans, Preparation of ceramic well plates for combinatorial methods using the morphogenic effects of droplet drying, *Journal of the American Ceramic Society*, **89**(12): 3858-3860, (2006).
- 409 L. F. Chen and J. R. G. Evans, Arched structures created by colloidal droplets as they dry, *Langmuir*, **25**(19): 11299-11301, (2009).
- 410 D. H. Yoon and B. I. Lee, Processing of barium titanate tapes with different binders for MLCC applications - Part I: Optimization using design of experiments, *Journal of the European Ceramic Society*, **24**(5): 739-752, (2004).
- 411 Y. Zhang, L. Chen, S. Yang, and J. R. G. Evans, Control of particle segregation during drying of ceramic suspension droplets, *Journal of the European Ceramic Society*, **27**(5): 2229-2235, (2007).
- 412 J. J. Guo and J. A. Lewis, Aggregation effects on the compressive flow properties and drying behavior of colloidal silica suspensions, *Journal of the American Ceramic Society*, **82**(9): 2345-2358, (1999).
- 413 A. Kristoffersson, E. Roncari, and C. Galassi, Comparison of different binders for water-based tape casting of alumina, *Journal of the European Ceramic Society*, **18**(14): 2123-2131, (1998).
- 414 R. C. Chiu and M. J. Cima, Drying of granular ceramic films 2. drying stress and saturation uniformity, *Journal of the American Ceramic Society*, **76**(11): 2769-2777, (1993).

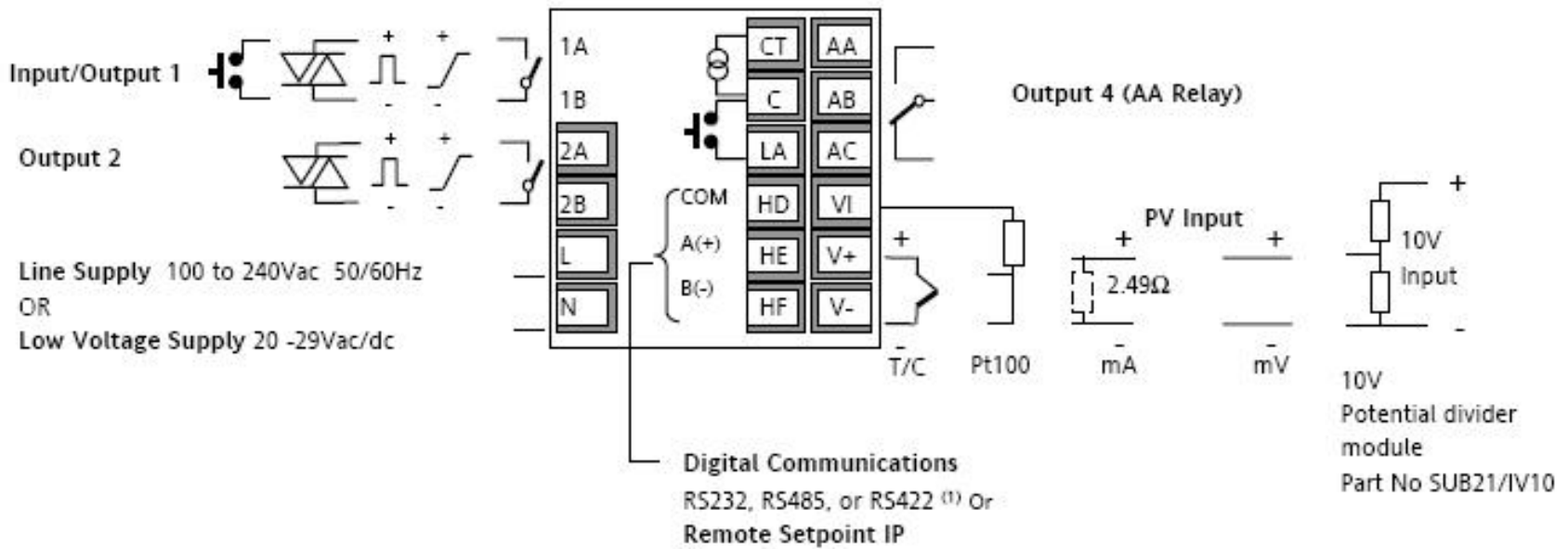
- 415 H. Hu and R. G. Larson, Evaporation of a sessile droplet on a substrate, *Journal of Physical Chemistry B*, **106**(6): 1334-1344, (2002).
- 416 E. R. Weeks, *Soft jammed materials*, in *Statistical Physics of Complex Fluids*, S. Maruyama and M. Tokuyama, Editors. 2007, Tohoku University Press: Sendai. pp. 2-10 -- 2-16.
- 417 A. H. Cottrell, *The Mechanical Properties of Matter*. 1981, New York: John Wiley & Sons. Inc. pp.27-28.
- 418 P. N. Segre, F. Liu, P. Umbanhowar, and D. A. Weitz, An effective gravitational temperature for sedimentation, *Nature*, **409**(6820): 594-597, (2001).
- 419 I. Santacruz, M. I. Nieto, J. Binner, and R. Moreno, Gel casting of aqueous suspensions of BaTiO₃ nanopowders, *Ceramics International*, **35**(1): 321-326, (2009).
- 420 R. Eötvös, Ueber den Zusammenhang der Oberflächenspannung der Flüssigkeiten mit ihrem Molecular Volumen, *Annalen Der Physik Und Chemie*, **27**: 448-459, (1886).
- 421 T. Boeck and A. Thess, Inertial Benard-Marangoni convection, *Journal of Fluid Mechanics*, **350**: 149-175, (1997).
- 422 J. Wang and J. R. G. Evans, Segregation in multicomponent ceramic colloids during drying of droplets, *Physical Review E*, **73**(2): Article Number: 021501, (2006).
- 423 G. E. Fair and F. F. Lange, Effect of interparticle potential on forming solid, spherical agglomerates during drying, *Journal of the American Ceramic Society*, **87**(1): 4-9, (2004).
- 424 J. Wang and J. R. G. Evans, Drying behaviour of droplets of mixed powder suspensions, *Journal of the European Ceramic Society*, **26**(15): 3123-3131, (2006).
- 425 Z. Sofer, P. Tresnáková, J. Spirková, S. Rubás, and M. Kalábová, Synthesis of Er-complexes for photonic applications, *Journal of Physics and Chemistry of Solids*, **68**(5-6): 1272-1275, (2007).
- 426 H. Beltran, E. Cordoncillo, P. Escribano, D. C. Sinclair, and A. R. West, Insulating properties of lanthanum-doped BaTiO₃ ceramics prepared by low-temperature synthesis, *Journal of the American Ceramic Society*, **87**(11): 2132-2134, (2004).
- 427 D. R. Lide, ed. *CRC Handbook of Chemistry and Physics (82nd Edn.)*. 2001, CRC Press, Inc.: Boca Raton. pp. 8:107-111.
- 428 M. Denesuk, B. J. J. Zelinski, N. J. Kreidl, and D. R. Uhlmann, Dynamics of

- incomplete wetting on porous materials, *Journal of Colloid and Interface Science*, **168**(1): 142-151, (1994).
- 429 D. R. Lide, ed. *CRC Handbook of Chemistry and Physics (82nd Edn.)*. 2001, CRC Press, Inc.: Boca Raton. pp. 6-3.
- 430 R. C. Daniel and J. C. Berg, Spreading on and penetration into thin, permeable print media: Application to ink-jet printing, *Advances in Colloid and Interface Science*, **123**: 439-469, (2006).
- 431 M. Dong and I. Chatzis, Effect of capillary pressure on wetting film imbibition ahead of main liquid-gas displacement front in porous media, *Petroleum Science and Technology*, **28**(9): 955-968, (2010).
- 432 L. Furuberg, J. Feder, A. Aharony, and T. Jossang, Dynamics of invasion percolation, *Physical Review Letters*, **61**(18): 2117-2120, (1988).
- 433 Y. Y. Zhang, M. Shariati, and Y. C. Yortsos. *The spreading of immiscible fluids in porous media under the influence of gravity*. in *Symposium on Environmental Models and Experiments Envisioning Tomorrow (EnviroMEET 98)*. 1998. Irvine, California: Kluwer Academic Publ pp. 117-140
- 434 I. V. Koptuyug, S. I. Kabanikhin, K. T. Iskakov, V. B. Fenelonov, L. Y. Khitrina, R. Z. Sagdeev, and V. N. Parmon, A quantitative NMR imaging study of mass transport in porous solids during drying, *Chemical Engineering Science*, **55**(9): 1559-1571, (2000).
- 435 M. Kuntz and P. Lavallee, Experimental evidence and theoretical analysis of anomalous diffusion during water infiltration in porous building materials, *Journal of Physics D-Applied Physics*, **34**: 2547-2554, (2001).
- 436 J. Emsley, *The Elements*. 1998, Oxford: Clarendon Press. pp.72-73.
- 437 J. M. Wan and T. K. Tokunaga, Film straining of colloids in unsaturated porous media: Conceptual model and experimental testing, *Environmental Science & Technology*, **31**(8): 2413-2420, (1997).
- 438 N. Weisbrod, M. R. Niemet, and J. S. Selker, Imbibition of saline solutions into dry and prewetted porous media, *Advances in Water Resources*, **25**(7): 841-855, (2002).
- 439 M. J. Nicholl and R. J. Glass, Infiltration into an analog fracture: Experimental observations of gravity-driven fingering, *Vadose Zone Journal*, **4**(4): 1123-1151, (2005).
- 440 L. Pel, K. Kopinga, and E. F. Kaasschieter, Saline absorption in calcium-

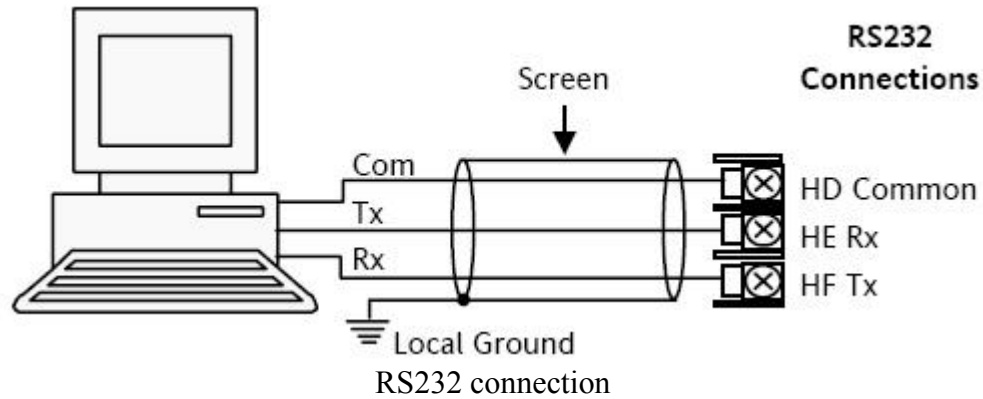
- silicate brick observed by NMR scanning, *Journal of Physics D-Applied Physics*, **33**(11): 1380-1385, (2000).
- 441 Y. T. Puyate and C. J. Lawrence, Wick action at moderate Peclet number, *Physics of Fluids*, **10**(8): 2114-2116, (1998).
- 442 A. G. Yiotis, I. N. Tsimpanogiannis, A. K. Stubos, and Y. C. Yortsos, Pore-network study of the characteristic periods in the drying of porous materials, *Journal of Colloid and Interface Science*, **297**(2): 738-748, (2006).
- 443 H. P. Huinink, L. Pel, and M. A. J. Michels, How ions distribute in a drying porous medium: A simple model, *Physics of Fluids*, **14**(4): 1389-1395, (2002).
- 444 E. Pert, Y. Carmel, A. Birnboim, T. Olorunyolemi, D. Gershon, J. Calame, I. K. Lloyd, and O. C. Wilson, Temperature measurements during microwave processing: The significance of thermocouple effects, *Journal of the American Ceramic Society*, **84**(9): 1981-1986, (2001).
- 445 M. Fokine, High temperature miniature oven with low thermal gradient for processing fiber Bragg gratings, *Review of Scientific Instruments*, **72**(8): 3458-3461, (2001).
- 446 J. M. Pickering, B. E. Schwab, and A. D. Johnston, Off-center hot spots: Double thermocouple determination of the thermal gradient in a 1.27cm (1/2in) CaF₂ piston-cylinder furnace assembly, *American Mineralogist*, **83**(3-4): 228-235, (1998).
- 447 J. A. Dalton and F. G. F. Gibb, Temperature gradients in large cold-seal pressure vessels, *Mineralogical Magazine*, **60**(399): 337-345, (1996).
- 448 J. B. Ferguson, Temperature uniformity in an electric furnace, *Physical Review*, **12**: 81-94, (1918).
- 449 S. Benkhof, *PTC Thermistors*. 2007, Siemens Matsushita Components. pp. 19-24.
- 450 H. Ihrig, PTC effect in BaTiO₃ as a function of doping with 3d elements, *Journal of the American Ceramic Society*, **64**(10): 617-620, (1981).
- 451 M. Drogenik, Oxygen partial pressure and grain growth in donor-doped BaTiO₃, *Journal of the American Ceramic Society*, **70**(5): 311-314, (1987).
- 452 M. M. Gallego and A. R. West, Effect of annealing treatments on positive temperature coefficient of resistance properties of barium titanate ceramics and a new model for the positive temperature coefficient of resistance effect, *Journal of Applied Physics*, **90**(1): 394-403, (2001).
- 453 D. P. Cann and C. A. Randall, Electrode effects in positive temperature

- coefficient and negative temperature coefficient devices measured by complex-plane impedance analysis, *Journal of Applied Physics*, **80**(3): 1628-1632, (1996).
- 454 M. Wegmann, R. Bronnimann, F. Clemens, and T. Graule, Barium titanate-based PTCR thermistor fibers: Processing and properties, *Sensors and Actuators a-Physical*, **135**(2): 394-404, (2007).
- 455 S. Urek and M. Drofenik, PTCR behaviour of highly donor doped BaTiO₃, *Journal of the European Ceramic Society*, **19**(6-7): 913-916, (1999).
- 456 C. A. Kleint, U. Stopel, and A. Rost, X-ray-diffraction and conductivity investigation of lanthanum-doped barium titanate ceramics, *Physica Status Solidi a-Applied Research*, **115**(1): 165-172, (1989).
- 457 F. D. Morrison, D. C. Sinclair, J. M. S. Skakle, and A. R. West, Novel doping mechanism for very-high-permittivity barium titanate ceramics, *Journal of the American Ceramic Society*, **81**(7): 1957-1960, (1998).
- 458 S. W. Ding, G. Jia, J. Wang, and Z. Y. He, Electrical properties of Y- and Mn-doped BaTiO₃-based PTC ceramics, *Ceramics International*, **34**(8): 2007-2010, (2008).
- 459 P. Blanchart, J. F. Baumard, and P. Abelard, Effects of yttrium doping on the grain and grain-boundary resistivities of BaTiO₃ for positive temperature-coefficient thermistors, *Journal of the American Ceramic Society*, **75**(5): 1068-1072, (1992).
- 460 J. Illingsworth, H. M. Alallak, A. W. Brinkman, and J. Woods, The influence of Mn on the grain-boundary potential barrier characteristics of donor-doped BaTiO₃ ceramics, *Journal of Applied Physics*, **67**(4): 2088-2092, (1990).
- 461 E. Brzozowski and M. S. Castro, Grain growth control in nb-doped BaTiO₃, *Journal of Materials Processing Technology*, **168**(3): 464-470, (2005).
- 462 H. J. Hagemann and H. Ihrig, Valence change and phase-stability of 3D-doped BaTiO₃ annealed in oxygen and hydrogen, *Physical Review B*, **20**(9): 3871-3878, (1979).












Appendix A Terminal layout of temperature controller (Eurotherm 3216) and RS232 connection



Terminal layout of temperature controller



Appendix B SubVI used in LabVIEW program

	SubVI icon	Name of functional module
1		Close program
2		Configure keylock
3		Configure instrument mode
4		Acknowledge alarm
5		Set controller mode
6		Set setpoint value
7		Read process variables
8		Read processor utilization factor
9		Read alarm notification
10		Error message
11		Create file